Search for the sources of ultra-high energy cosmic rays with the Pierre Auger Observatory

Von der Fakultät für Mathematik, Informatik und Naturwissenschaften der RWTH Aachen University zur Erlangung des akademischen Grades eines Doktors der Naturwissenschaften genehmigte Dissertation

vorgelegt von

Markus Lauscher, M.Sc. RWTH

aus Rohren

Berichter: Universitätsprofessor Dr. rer. nat. Thomas Hebbeker
Universitätsprofessor Dr. rer. nat. Christopher Wiebusch

Tag der mündlichen Prüfung: 02.12.2016

Erstgutachter und Betreuer

Prof. Dr. Thomas Hebbeker
III. Physikalisches Institut A
RWTH Aachen

Zweitgutachter

Prof. Dr. Christopher Wiebusch
III. Physikalisches Institut B
RWTH Aachen

Contents

1. Introduction

The observation that the earth is constantly hit by highly energetic particles, nowadays referred to as cosmic rays, dates back to the year 1912 and to Victor Hess and his balloon flight experiments. In 1938, by using distant coincidence detectors, Pierre Auger realised that the impact of these cosmic rays create cascades of particles in the form of extensive air showers in the atmosphere.

Ever since cosmic rays have been extensively studied using these extensive air showers to reconstruct their properties. However, the most energetic of these particles, ranging from 10^{18} eV to over 10^{20} eV, still pose many questions - first and foremost: What is their origin?

One way to address this question is to analyse their measured arrival directions at earth in search for possible source regions in, and more likely, outside of our galaxy. This is challenging, as cosmic rays are charged nuclei and are hence deflected by magnetic fields in and between galaxies. This deflection becomes even stronger in the case of heavy nuclei. This leads to a largely isotropic distributions of their arrival directions at earth.

In this work two approaches are used to address this challenge. First a Needlet Wavelet based analysis method is used to search for patterns in the arrival distribution of these ultra-high energy cosmic rays (UHECRs), measured at the worlds largest observatory for UHECRs: The Pierre Auger Observatory in Argentina. This technique was originally introduced to search for structures in the, also highly isotropic, cosmic microwave background.

The second approach lies in the currently undergoing upgrade of the Pierre Auger Observatory. One goal of the upgrade is to achieve the capability of measuring the mass composition of cosmic rays on an event by event basis. Currently this is only possible on a statistical basis. This would allow future searches for patterns in the measured arrival directions to be restricted to the lightest and hence least deflected cosmic rays. One necessary component of this upgrade is the deployment of a new detector with efficient, robust and cost-effective light sensors with a sufficient dynamic range. Silicon-Photomultipliers (SiPMs) are a recent form of semiconductor light detectors that could fulfil these requirements. To establish this it is necessary to characterise their response to a wide range of light fluxes and to be able to reconstruct the incident signal from their response. In this work a dedicated technique to achieve this characterisation and reconstruction is developed.

This work is structured as follows. In chapter 2 an introduction to cosmic rays is given. This includes a description of their properties, observational techniques using extensive air showers, the effect galactic and extra-galactic magnetic fields have on their propagation and an overview over the current status in search for patterns in their measured arrival directions.

In chapter 3 the Pierre Auger Observatory, the techniques used to reconstruct the properties of observed cosmic rays and the components of the upgrade of the Pierre Auger Observatory: AugerPrime are described.

Chapter 4 details a technique to fully characterise the response of SiPMs, from very low light fluxes up to saturation, and describes a method to reconstruct the incident signal from their response.

The main part of this work consists in the analysis of the measured arrival directions at the Pierre Auger Observatory. The Wavelet analysis method used to analyse the arrival directions is described in chapter 5.

In chapter 6 the optimal choice of the free parameters of the analysis method is determined and its sensitivity is compared to another commonly used analysis method: The angular power spectrum.

Chapter 7 gives an overview on the used data set and the applied corrections to ensure no artificial patterns are introduced in the analysis.

Finally, the method is applied to the data in chapter 8. In the first step a search for patterns of any angular scale in the data is performed. As this leads to the detection of a dipolar pattern this pattern is fully characterised in the second step. Lastly, the analysis is restricted to a portion of the sky to study possible signals from Centaurus A, the active galactic nuclei closest to earth and a suspected source of UHECRs.

This thesis ends in chapter 9 with a summary of all obtained results.

2. Ultra-High Energy Cosmic Rays

In this chapter we give a general overview over ultra-high energy cosmic rays (UHECRs). We begin with a general description of their properties and the energy spectrum at earth in section 2.1. Afterwards, in section 2.2, we describe the extensive air showers they cause in the atmosphere. In the following, we discuss possible origins for cosmic rays within our galaxy in section 2.3 and of even higher energy cosmic rays from outside our galaxy in section 2.3. This includes a discussion of the magnetic fields the cosmic rays propagate through their way to earth. Finally, we describe the status of the search for patterns, and hence possible origins, in the observed arrival directions of UHECRs at earth in section 2.5.

2.1. Introduction

The observation that the earth is constantly hit by high-energy particles dates back over 100 years to Victor Hess and his balloon flights. Today, they are referred to as cosmic rays and have been studied extensively ever since. Cosmic rays are defined as charged particles that originate from outside the solar system and range from kinetic energies E of 10^6 eV to above 10^{20} eV [1].

The focus in this work is on ultra-high energy cosmic rays (UHECRs). While there is no clear demarcation where the ultra-high energy range starts, we refer to cosmic rays with energies E above 10^{18} eV (= 1 EeV) as UHECRs. For low energies E the cosmic ray flux is modulated by the sun but above $E \approx 10^{11}$ eV the spectrum $\mathrm{d}N/\mathrm{d}E$ of cosmic rays can be approximated by a power law

$$\mathrm{d}N/\mathrm{d}E \propto E^{-\gamma} \tag{2.1}$$

with spectral index $\gamma \approx 2.7$ [1]. The power law has a very steep slope and hence the flux falls rapidly with the energy. While the rate is around one particle per square metre and second at 10^{12} eV, it drops to one particle per square kilometre and year around 10^{18} eV and even down to one particle per square kilometre and century around 10^{20} eV. Due to the steeply falling flux a direct observation of UHECRs via satellites is not possible. Instead large, ground based observatories are required which study the extensive air showers which cosmic rays cause in the atmosphere.
To compare experiments of different size and acceptance usually the differential flux Φ of cosmic rays

$$\Phi(E) = \frac{\mathrm{d}N}{\mathrm{d}E \cdot \mathrm{d}A \cdot \mathrm{d}\Omega \cdot \mathrm{d}t} \tag{2.2}$$

is reported. Here N is the number of particles, A the area of the detector, Ω the solid angle and t the active time of the detector. This differential spectrum, as obtained by various measurements, is shown at the top of figure 2.1. At the bottom the spectrum is also shown but weighted with $E^{2.5}$ to enhance particular features of the spectrum: Up to energies of 10^{15} eV, the 'knee', the flux follows a power law with a spectral index of $\gamma = 2.7$ [3]. After the knee the spectrum steepens to an index of $\gamma = 3.1$, a further steepening occurs at the 'second knee' around an energy of $4 \cdot 10^{17}$ eV. Finally at the 'ankle', around energies of $4 \cdot 10^{18}$ eV, the spectrum flattens again with an index of $\gamma = 2.6$ [3]. After around $4 \cdot 10^{19}$ eV a suppression of the flux becomes apparent [1]. Later in the chapter we discuss possible reasons for the observed structures.

Almost all chemical elements have been observed in cosmic rays arriving at earth [2]. Shown in figure 2.2 is the abundance of elements at a kinetic energy around 1 GeV per nucleon, normalised to the abundance of silicon. As a comparison the abundance of elements in the solar system is also shown. On average cosmic rays are composed of mainly nuclei (92%) and electrons (2%) [4]. Of the nuclei protons dominate with 98% followed by helium (15%) and the remainder being heavier elements [4]. However, the composition of UHECRs is still largely unknown. Measurements by the Pierre Auger Collaboration suggest a transition of a proton dominated mixed flux around 10^{18} EeV towards a heavier composition at higher energies [5]. Measurements by the HiRes and Telescope Array Collaboration however suggest a proton composition up to the highest energies [6, 7]. In both cases the interpretation of the achieved results depends on Monte Carlo (MC) simulations which use different models describing the propagation of particles in the air-shower cascade. With the upgrade of the Pierre Auger Observatory a model-independent measurement of the composition could be possible (see section 3.3). In the following we discuss the extensive air showers cosmic rays cause in the atmosphere, and techniques to reconstruct the properties of the arriving cosmic ray particles.

2.2. Extensive Air Showers

When a cosmic ray particle of high energy impacts the atmosphere, it usually undergoes an inelastic scattering with an air molecule. This first interaction creates a multitude of additional particles, which in turn create new particles leading to a self-sustaining cascade. A schematic of this is shown on the left-hand side of figure 2.3. The shower can be considered to consist of three components: an electromagnetic, a hadronic and a pion generated muonic/neutrino component [1]. In the most simple case the primary particle is a photon or an electron and the shower will only consist out of an electromagnetic cascade. In this case the photons produce electron-positron pairs by the interaction with a nucleus N via $\gamma + N \longrightarrow e^+e^- + N$ and the electrons/ positrons generate Bremsstrahlung via $e^\pm + N \rightarrow e^\pm + \gamma + N$. The produced Bremsstrahlung photons can then again create electron-positron pairs and so on. The cascade terminates when the energy of the electrons and positrons drops below the critical energy of $E_C \approx 80\,\mathrm{MeV}$ in air, where they start loosing more energy via ionisation then through radiation [1].

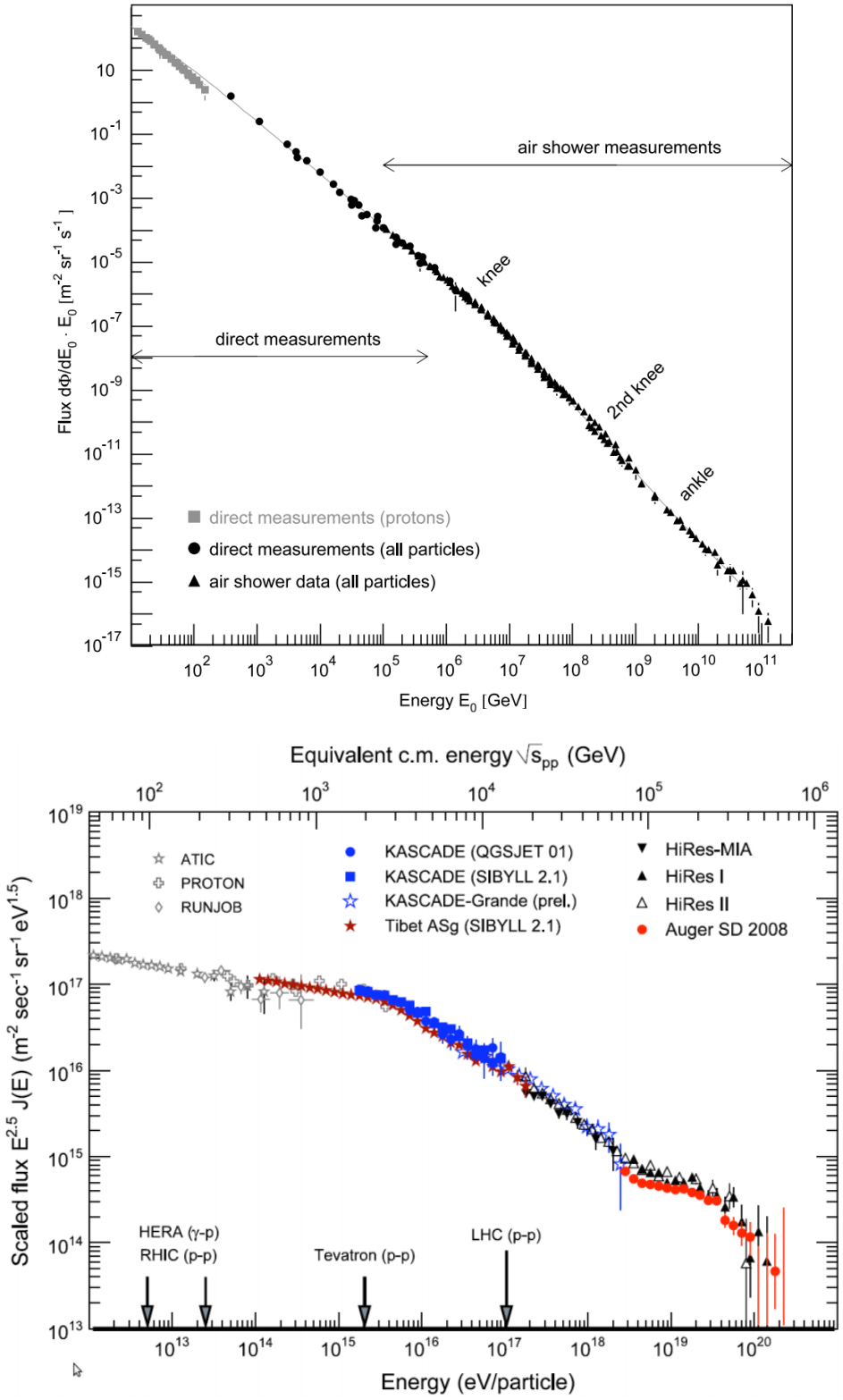

Figure 2.1.: Top: All particle cosmic ray energy spectrum [2]. **Bottom:** All particle cosmic ray energy spectrum scaled with (energy)$^{2.5}$ from [2]. The equivalent centre of mass energy and maximum energy of man-made particle accelerators are also given (bottom). Measurements are from direct satellite measurements as well as ground based experiments. See [2] for details on the experiments.

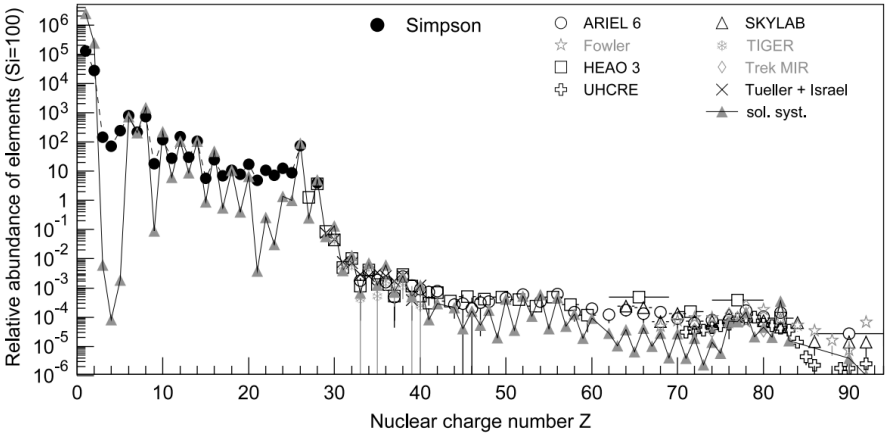

Figure 2.2.: Abundance of elements in cosmic rays at energies around a kinetic energy of 1 GeV per nucleon as a function of their nuclear charge Z. The grey filled, upward pointing triangles show the abundance of elements in the solar system. Taken from [2]. See [2] for details on the experiments.

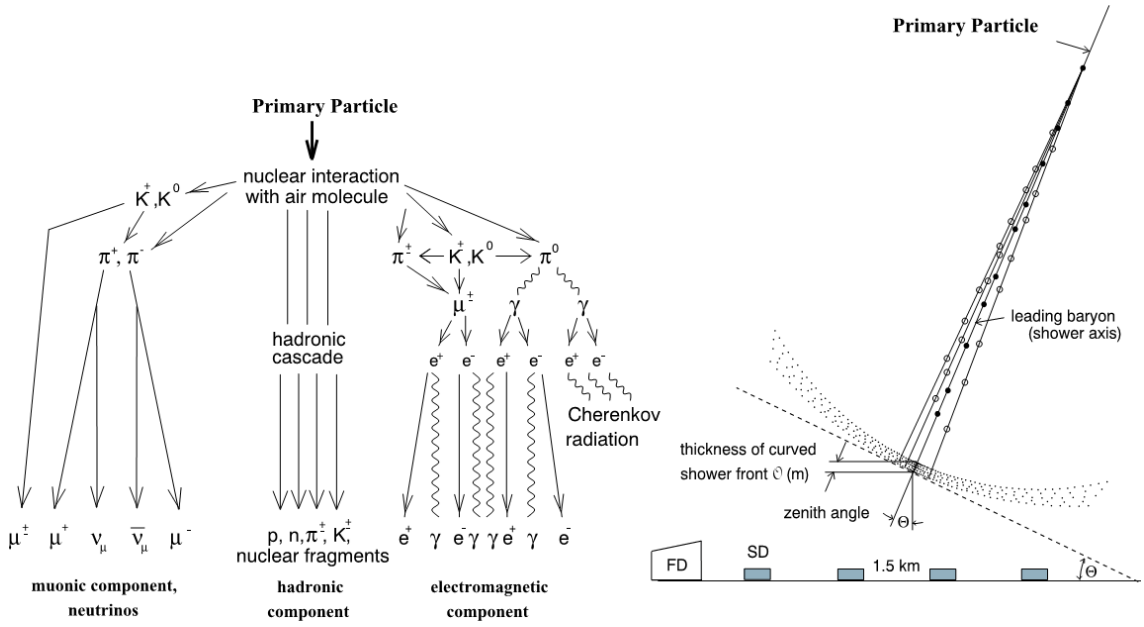

Figure 2.3.: Left: Illustration of the three main components of an extensive air shower. **Right:** Illustration of detection mechanisms. The shower particles form a shower front of several meters thickness and a lateral extend in the order of kilometres. The particles impacting the ground level can be studied by an extensive array of surface detector (SD) stations. The propagation of the particles through the air can be observed via optical, ground based telescopes. This fluorescence detector (FD) stations observe the isotropically emitted fluorescence light caused by the propagation of the electromagnetic cascade through the atmospheric nitrogen. Taken from [8].

In the more general and common case where the primary particle is a nucleus, the first collision will produce new nuclei, neutral and charged pions ($\pi^{\pm}, \pi^{0}$) and kaons ($K^{\pm}, K^{0}_{\mathrm{S/L}}$). These hadrons then collide with further air molecules driving the hadronic component forward, or, depending on their lifetime and density of the atmosphere surrounding them, decay before interacting. For example the charged pions, with a lifetime of $\tau = 2.6 \cdot 10^{-8}\,\mathrm{s}$ [9], decay mainly via $\pi^{\pm} \longrightarrow \mu^{\pm} + \nu$. Especially at higher altitudes with a less dense atmosphere, pions may decay before interacting, giving rise (together with the charged kaons) to the muonic component of the shower [1]. Due to the rather long muon lifetime of $\tau = 2.2 \cdot 10^{-6}\,\mathrm{s}$ and the very low neutrino cross-section these components largely decouple from the shower development.
The produced neutral pions have a very short lifetime of $\tau = 8.4 \cdot 10^{-17}\,\mathrm{s}$ and decay nearly instantly via $\pi^{0} \longrightarrow \gamma + \gamma$ (98.8% of decays) or $\pi^{0} \longrightarrow e^{+}e^{-} + \gamma$ (1.2% of decays) [9] giving rise to the previously described electromagnetic cascade. During the shower development about 85-90% of the energy of the primary particle will be transferred to the electromagnetic component of the shower [1].

On a macroscopic level the shower moves towards the ground with nearly the speed of light. The shower particles form a shower front, with a thickness of up to a few metres, while the lateral extent can reach several kilometres. The air shower ends when the involved particles have insufficient energy to drive the cascade further, or the shower impacts on the ground.

At sea level a 10^{19} eV vertical, proton induced shower, will have around $3{\cdot}10^{10}$ particles. Of these 99% will be photons and electrons/positrons in a 6 to 1 ratio carrying around 85% of the energy. The remaining particles are muons with an energy around 1 GeV and carrying 10% of the energy, pions also with a typical energy of 1 GeV, carrying 4% of the energy. The remainder consists of kaons, neutrinos and baryons [1].

A more detailed discussion of extensive air showers can be found in [10].

2.2.1. Detection Techniques

One method to gain information about the primary particle is to study the absolute number and the distribution of the electrons/positrons and muons on the ground. By measuring the distribution of particles on the ground, together with the information on their arrival time, it is possible to reconstruct the energy of the primary particle, as well as the arrival direction. This method can be dated back to the late 1930s and to P. Auger, who used Wilson chambers and Geiger Müller tubes to study coincidences. He was able to find coincidences from counters separated up to 300 m and concluded that this was due to secondary particles generated by cosmic rays.
With this method, the reconstruction of the energy of the primary particle normally relies on shower simulations, introducing systematic uncertainties on the result. A schematic view of this principle of using the lateral distribution of the ground particles is shown on the right-hand side of figure 2.3.
Another method to gain information about the primary particle is to study the longitudinal shower profile using optical telescopes. Here the electromagnetic component is very significant as it carries about 90% of the cascade components. The longitudinal

profile can be studied using the emission of fluorescence or Cherenkov light the electromagnetic component of the shower causes in the atmosphere. This is also illustrated on the right-hand side of figure 2.3. A detailed over-view on the historical evolution of experiments studying UHECRs and of observational techniques of extensive air showers can be found in [11]. In the next chapter we illustrate both lateral and longitudinal reconstruction techniques using the example of the Pierre Auger Observatory.

2.3. Acceleration and Possible Sources of Cosmic Rays

As described the cosmic ray spectrum follows a power law. To accelerate particles to high energies and to give rise to a power-law spectrum 'stochastic-acceleration' is considered as a likely mechanism. First introduced by Fermi in 1949 [12] and further refined (e.g. [13, 14]) to what is now referred to as 'diffusive shock acceleration'. The general idea is the transfer of energy from a moving shock front to a particle. Such shock fronts can, for example, exist in front of expanding supernova remnants (SNR) as the velocity is much larger than the surrounding interstellar medium [1]. Regardless of the specific nature of the shock front the general idea behind the acceleration is the same. A particle, bound to the shock region of extent r_s by a magnetic filed of strength B, bounces back and forth across the shock front. Each passing of the front leads to an energy gain proportional to β on average, where β is the velocity of the shock front in units of the speed of light or, in a more generalized manner, the 'efficiency' of the accelerator. In the case of a non relativistic moving shock front the energy gain by one pass back and forth through the shock is $\frac{4}{3}\beta$ [10]. During each passing with energy gain $\Delta E = \epsilon E$ there is a chance P_{esc} for the particle to escape the source region. This leads (see e.g. [10]) naturally to a power law spectrum where the number of particles N remaining in the source region with an energy greater E_n is given by

$$N(E_n) \propto \frac{1}{P_{\text{esc}}} \left(\frac{E_n}{E_0}\right)^{-\gamma}. \tag{2.3}$$

With

$$\gamma = \frac{P_{\text{esc}}}{\epsilon}. \tag{2.4}$$

Hillas [15] summarized the maximum achievable energy $E_{\max}$ via this process by

$$E_{\max} = \beta z e \left(\frac{B}{1\mu\text{G}}\right) \left(\frac{r_s}{1\text{kpc}}\right) \text{EeV} \tag{2.5}$$

with Ze being the charge of the accelerated particle. Hence the larger the source region and the larger the magnetic field the higher energies are possible.

Within our galaxy SNR are considered as a likely source for cosmic rays. Indeed, if only 5% - 10% of the kinetic energy in SNR would be transferred to the acceleration of cosmic rays this would be sufficient to explain the observed flux [1].

Using this mechanism a possible explanation of the observed steepening of the cosmic ray flux at the knee could be that here galactic accelerators become insufficient to

accelerate protons to even higher energies. As heavier particles can be accelerated to higher energies, proportional to their charge, the steepening can be explained by the gradual disappearance of elements from the flux until even iron cannot be accelerated to higher energies, here we observe the second knee [1]. In this transition the extra-galactic cosmic ray flux becomes dominant until the spectrum flattens again at the ankle [3]. This rigidity[1] dependent flux change could e.g. explain the obtained flux measurements of the Kascade Collaboration [1, 16]. Another explanation for the features in the flux is a rigidity dependent escape of the particles from the galaxy [3] when the galactic magnetic field is no longer strong enough to contain them.

Much less is known on the origin of extra-galactic cosmic rays which likely dominate the flux above the ankle. In 1984, Hillas [15] summarized the requirements on possible source regions to accelerate cosmic rays to a certain energy in what is now referred to as a 'Hillas diagram'. A modern version of this plots is shown in figure 2.4. As equation 2.5 indicates, only a source region of sufficient size and/or with a sufficient magnetic field is capable to accelerate particles above a certain energy. In the case of figure 2.4 this energy is 100 EeV. As can be seen even for relativistic shocks or highly efficient accelerators (i.e. $\beta = 1$), only few known objects can accelerate iron and even fewer objects protons to such high energies. Rapidly rotating Neutron stars or pulsars and gamma-ray bursts (GRB), despite their relatively small size, posses a high enough magnetic field to be possible sources candidates. Other possible sources are active galactic nuclei (AGN) both in their core region containing super-massive black holes or in the jets they extend over long distances into the galaxy [1]. With exception of the pulsar the source of the energy is accretion of matter onto stars and consequent collapse into a black hole (GRB) or onto a central black hole (AGN). The transfer of angular momentum from this flow forms an accretion disk which can lead to powerful plasma flow perpendicular to the disk (jets). For a more detailed overview on both galactic and extra-galactic sources of UHECRs and acceleration mechanisms see [17, 18].

The last observable feature in the cosmic ray spectrum is a rapid drop or cut-off of the flux near $4 \cdot 10^{19}$ eV. One possible explanation is that here, similar to galactic sources of cosmic rays, the sources of UHECRs reach their maximum energy. As in the case of the knee, this would result in a rigidity dependent cut-off [7]. However, the most prominent explanation for the drop off is the Greisen-Zatsepin-Kuzmin cut-off (GZK cut-off). At energies above about $4{\cdot}10^{19}$ eV photo-hadronic interactions between protons and photons of the cosmic-microwave background lead to the production of pions

$$p\gamma \rightarrow N + n\pi$$

or to the production of e^+e^- pairs

$$p\gamma \rightarrow p + e^+e^-.$$

[1]The rigidity of a particle is its momentum p (or energy E in the relativistic limit) divided by its charge Ze and is an indicator of its resistance to being deflected by a magnetic field. At the same energy, particles with a larger charge will be deflected more strongly.

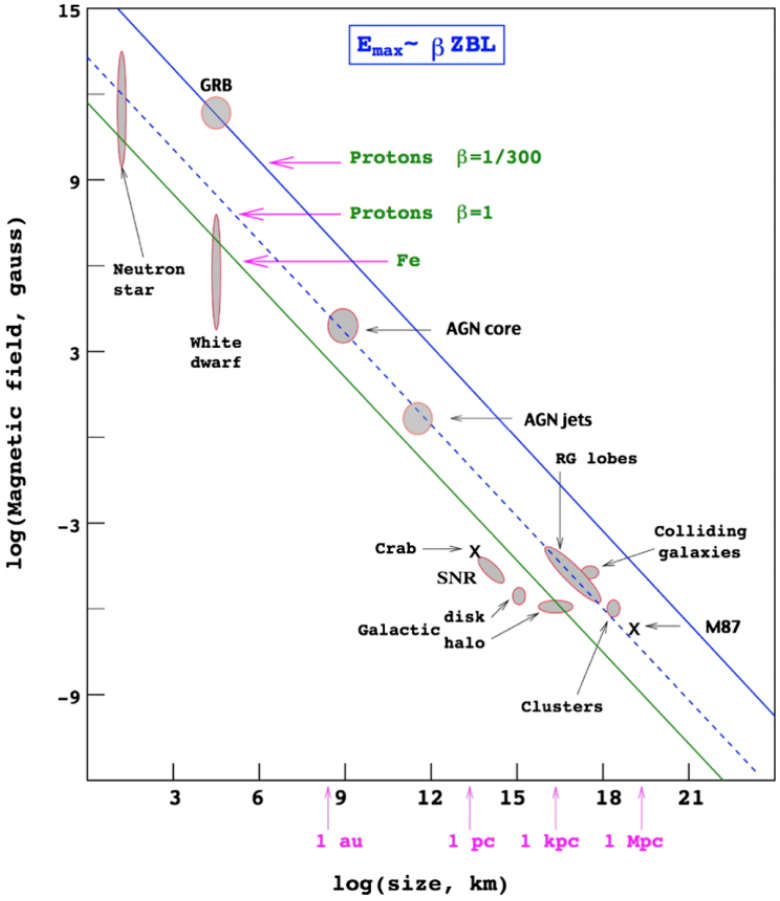

Figure 2.4.: Hillas diagram of possible source regions of UHECRs based on equation 2.5. To accelerate a particle above 100 EeV the source region must lie above the corresponding lines. Taken from [1].

Here N is a nucleon and n the number of produced pions [3]. For heavier nuclei photo-disintegration on cosmic microwave background (CMB) and IR-UV photons can occur and break up nuclei at ultra-high energies. This effect is especially strong for nuclei with a mass number $A < 20$ which cannot travel farther than a few Mpc without disintegrating [3].

As the mass-composition of UHECRs is currently unclear (see section 2.1), an answer on the origin of the cut-off is currently not possible. In the future it could be addressed with the proposed upgrade of the Pierre Auger Observatory (see section 3.3). For an overview on experimental results on UHECRs from the ankle to the cut-off and possible explanations for the cut-off see [7].

2.4. Magnetic Fields

While we outlined possible sources of UHECRs in the previous section to date no sources have been found experimentally. One likely contributor to this observation is the existence of magnetic fields which exist throughout the universe [19]. During propagation to earth UHECRs are deflected by the magnetic fields via the Lorentz force

$$\frac{d\mathbf{p}}{dt} = Z\mathbf{v} \times \mathbf{B}, \tag{2.6}$$

where $\mathbf{p}$ is the relativistic momentum, Z the charge and $\mathbf{v}$ the velocity (approximately the speed of light) of the cosmic ray and $\mathbf{B}$ the magnetic field vector. This leads to a gyroradius r_g of the particle of:

$$r_g \propto \frac{E}{ZeB_\perp}, \tag{2.7}$$

and a deflection angle ϑ of a cosmic ray travelling a distance $D \ll r_g$ of [20]:

$$\vartheta = \frac{D}{r}. \tag{2.8}$$

Hence cosmic rays are deflected with a strength inversely proportional to their rigidity E/Z and thus the deflection depends on the charge and energy of UHECRs.

In general magnetic fields in the universe will not be aligned but are turbulent with only a certain coherence length l_c. If an ensemble of cosmic rays travels from a single source over a certain distance $d \gg l_c$ through a magnetic field with average strength B_{rms} this can be viewed as a directed random walk and will result, with respect to an observer, in an average smearing around the source of:

$$\sigma_{\text{rms}} = 0.87^\circ \left[\frac{41 \text{ EeV}}{E/Z} \frac{B_{\text{rms}}}{5\ \mu\text{G}} \sqrt{\frac{d}{2 \text{ kpc}}} \sqrt{\frac{l_c}{50 \text{ pc}}} \right] \tag{2.9}$$

in the limit of small deflections [21]. Here the units have been chosen relevant to the galactic magnetic field with typical field strengths of a few μG and coherence lengths of up to 100 pc [21]. Equation 8.2 on page 145 uses units more appropriate to extra-galactic magnetic fields.

In the following we give a short overview on the galactic and extra-galactic magnetic fields and their expected effects on the propagation of UHECRs.

2.4.1. The Galactic Magnetic Fields (GMF)

In comparison to the extra-galactic magnetic field (EGMF) (see next section) more is known about the GMF. The currently most advanced, observation based model of the GMF exists in the form of the JF12 model [22, 23]. The model was obtained using synchrotron measurements of the WMAP satellite and Faraday rotation measurements of extragalactic sources. A description of the observational results used and a derivation of the model can be found in [22, 23]. This model will be used in section 8.3 in this

thesis. In the following we give an overview over the components of the model and by proxy an overview of the structure of the GMF.
The model is composed out of three main parts, i) a coherent large-scale field, with disk, halo and out-of-plane components, ii) a random field with spatially-varying field strength and iii) a striated random field [22, 23]. The structure and strength of the field is illustrated in figure 2.5. The coherent large-scale disk field is shown on the top, right-hand side of the figure. Around an inner toroidal core of inner radius of 3 kpc and of an outer radius of 5 kpc the field follows a logarithmic-spiral geometry along and between the spiral arms of the galaxy. The typical strength of this field is around 1 μG. The average strength of the random (turbulent) field also follows this structure as illustrated on the top, left-hand side of figure 2.5. The disc field is super-imposed with an X-shaped field perpendicular to the galaxy and symmetric in azimuth as illustrated at the bottom of figure 2.5. The striated random field is scaled with the strength of the disc field with is aligned either parallel or anti-parallel to it on a scale around 100 pc. The final component is a toroidal halo component [22, 23]. The expected average deflection by this GMF model for cosmic rays, averaged over cosmic rays arriving isotropically at earth, is shown on the bottom, left-hand side of figure 2.6. As can be seen, even for a proton with an energy of 10^{19} eV the average deflection will be around 30° making the identification of UHECRs, especially in case of a heavy composition, challenging. Due to the structure of the GMF the average deflection will depend upon the point of entry in the galaxy as is illustrated at the top, left-hand side of figure 2.6.

2.4.2. The Extra-Galactic Magnetic Field (EGMF)

The origin of EGMF (i.e. magnetic fields between galaxies) are not well known. Some models suggest their origin in the early universe while others see them as originating from magnetic pollution from sources such as galactic winds from jets or radio galaxies or a combination thereof [3]. Similar is the uncertainty on the expected deflection of UHECRs, ranging from expectation of deflections around $10° - 20°$ down to less than a degree for protons with $E > 100$ EeV and sources with a distance up to 100 Mpc [26, 27, 3]. Current upper limits on the average strength of EGMFs are around 1 nG [28] and lower limits down to 10^{-6} nG [29].

An illustration of the expected deflection as a function of rigidity and various field strengths is shown on the bottom, right-hand side of figure 2.6.

2.5. Status of Searches for Anisotropies in the Arrival Directions of UHECRs

In the following we give a short overview on the current status on searches for anisotropies in the arrival directions of UHECRs and hence the search for their sources. We focus on the two current largest UHECRs observatories, the Telescope array and the Pierre Auger Observatory. With the former being located in the northern and the latter in

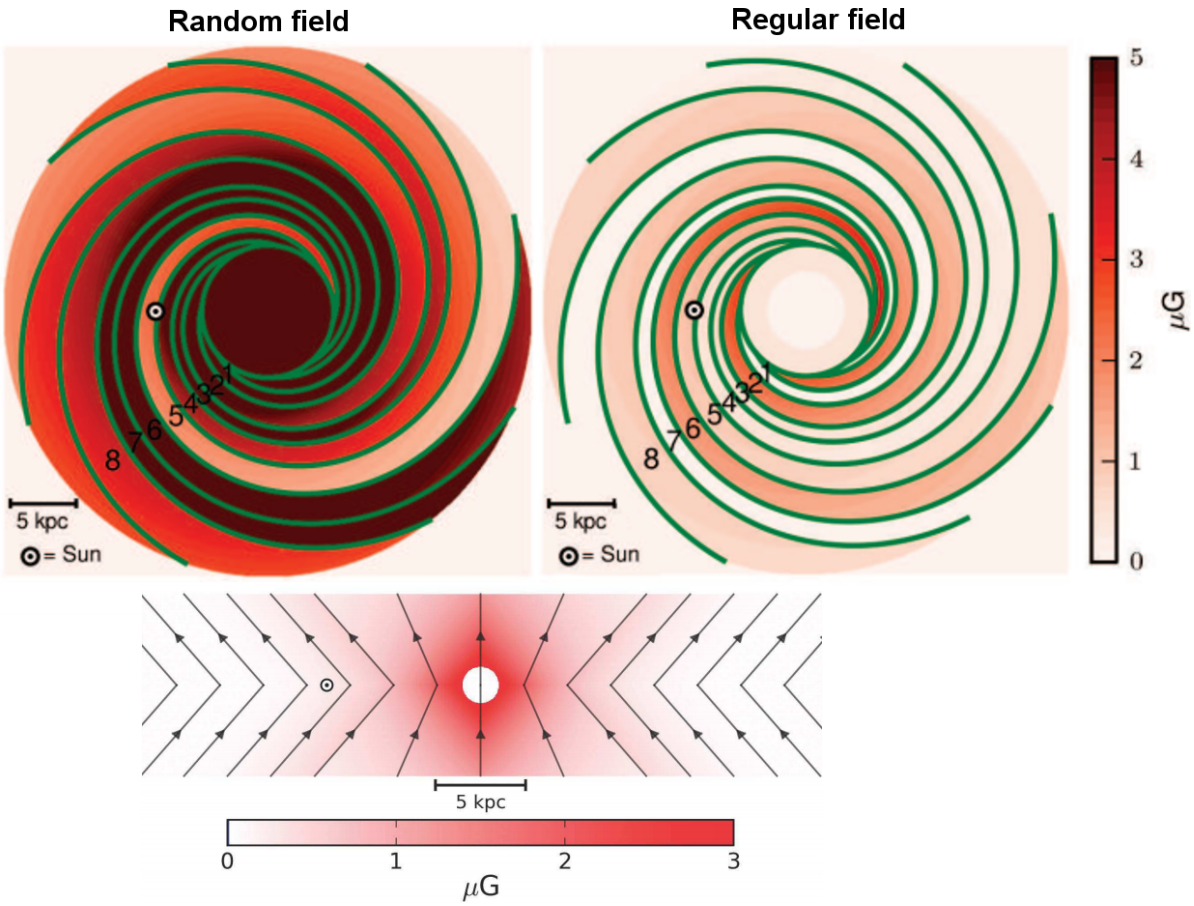

Figure 2.5.: Illustration of the components of the JF12 GMF model. **Top, Left/Right:** Random/Coherent field component and strength. In contrast to the coherent field particles traversing through the random field will be deflected randomly, according to equation 2.9. **Bottom:** X-shaped coherent field shown as a cross-section through the galaxy. The field is symmetrical in azimuth. Modified from [23].

the southern hemisphere they are able the study cosmic rays arriving anywhere (if their data is combined) at earth up to the highest energies.

First we focus on results obtained by the Pierre Auger Observatory. A large scale flux modulation in right ascension (α) [30, 31] and in both declination (δ) and right ascension [32, 33, 31] has been reported by the Pierre Auger Collaboration from the analysis of events with zenith angles smaller than 60°. The amplitude of the modulation is below $\sim 2\%$ at EeV energies, and shows a marginally significant indication of a transition from a direction near $\alpha \simeq 270°$ below 1 EeV, consistent with the direction of the galactic centre, towards directions near $\alpha \simeq 100°$ above 4 EeV. The amplitude increases to several percent around 10 EeV. A more recent report from the Auger Collaboration, extending the maximum zenith angle up to 80° and using events up to the end of 2013, gives a hint of a large-scale dipolar anisotropy for energies $E > 8$ EeV [34]. Under the

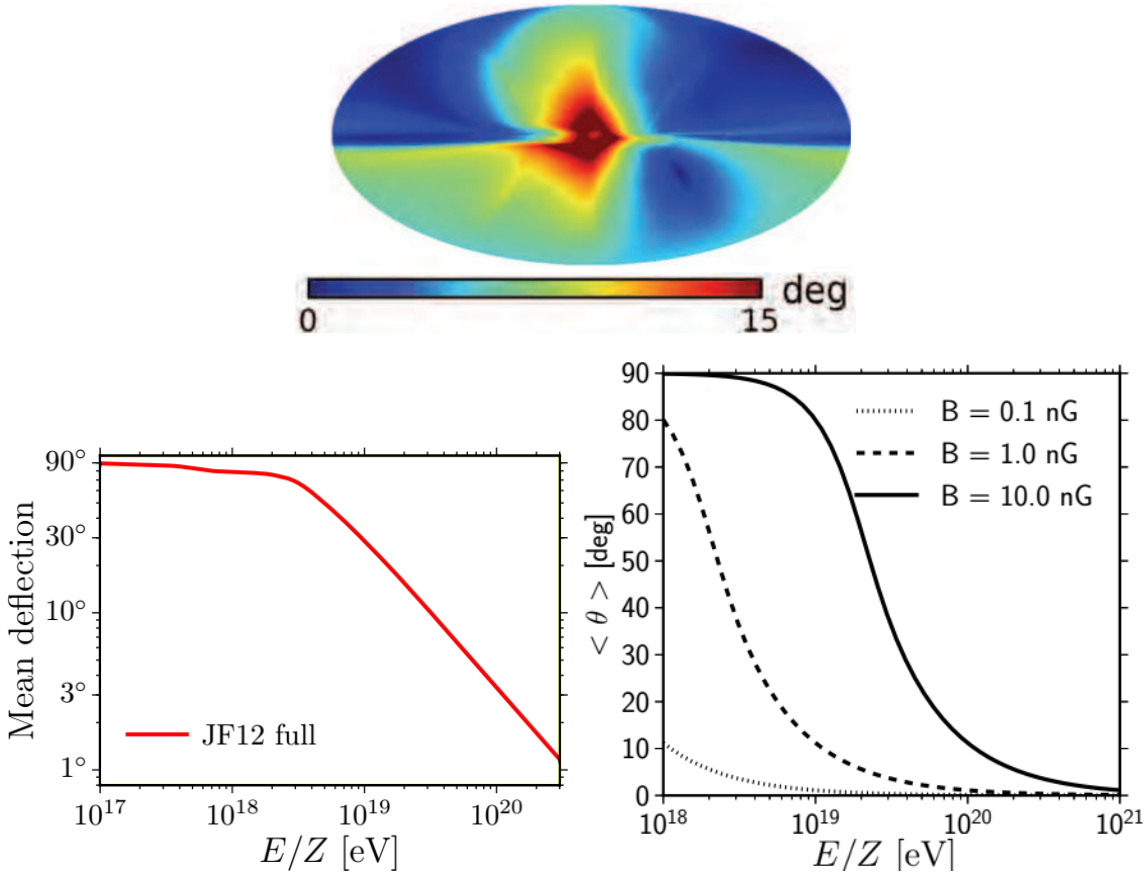

Figure 2.6.: Top: Expected average deflection of 60 EeV protons in the JF12 GMF model, displayed by arrival direction in galactic coordinates. Modified from [23]. **Left, Bottom:** Expected average deflection as a function of particle rigidity in the JF-12 GMF model. Modified from [24]. **Right, Bottom:** Expected average deflection as a function of particle rigidity through an EGMF with a coherence length of 1 Mpc and an observer distance of 10 Mpc. Modified from [25].

assumption that this flux is dominated by a dipole, the results correspond to a dipole with an amplitude of $r = (7.3 \pm 1.5)\%$ directed towards $(\alpha, \delta) = (95° \pm 13°, -39° \pm 13°)$. A smoothed skymap of the data above 8 EeV in [34] is shown on the left-hand side of figure 2.7 indicating the dipolar structure.

At energies above 40 EeV the Pierre Auger Collaboration has searched for intrinsic anisotropies in cosmic rays by using angular auto-correlation and searching for possible excesses in circular windows across the exposed sky. The results of these studies were found to be compatible with an isotropic expectation [35].

The region around the closest AGN to earth - Centaurus A - has also been studied. More specifically the expected vs. observed number of events as a function of the angular distance to Centaurus A and as a function of the energy threshold between 40 and 80 EeV was studied. The largest excess of events was observed at an angular distance of

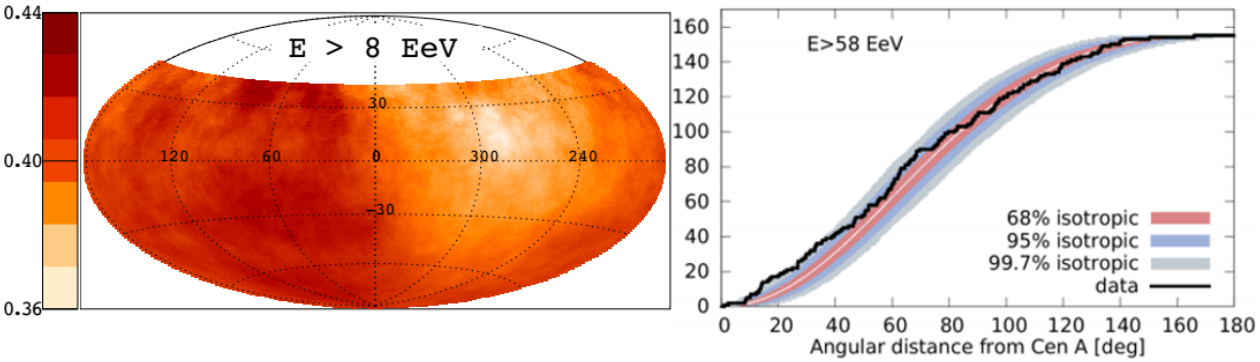

Figure 2.7.: Left: Skymap of arrival directions in equatorial coordinates, measured at the Pierre Auger Observatory with energies greater than 8 EeV, smoothed with a 45° filter [34]. An indication of a dipolar structure can be seen. Modified from [35]. **Right:** Exploration of a possible excess of events at a certain angular distance from Centaurus A using events detected at the Pierre Auger Observatory with an energy greater than 58 EeV. Modified from [35].

15° and for an energy threshold of 58 EeV, with a penalized probability of 1.4% [35]. This is illustrated on the right-hand side of figure 2.7.

The Telescope Array (TA) has recently observed a hotspot in the arrival direction of UHECRs with $E > 57$ EeV with a post-trial probability of 3.7×10^{-4}. The hotspot lies within a 20° circle centred around $(\alpha, \delta) = (147°, 43°)$ [36].

As the Telescope Array and the Pierre Auger Observatory together have access to the complete sky, both collaborations have begun to analyse their combined data. The lower limit of this analysis is due to the full-efficiency threshold of the TA which is at 10 EeV. As both experiments do not necessarily share the same energy calibration an iterative method was used to determine the energy above which events measured by the Auger Observatory were included in the analysis. To find this energy a declination band in the sky, where both experiments are sensitive, was used and the Auger energy threshold was chosen to equalize the flux of both experiments. As a result Auger events with energies greater than 8.8 EeV, in terms of the Auger energy scale, were used in the combined data set [37, 38]. By taking advantage of full sky coverage, the multipole coefficients of the UHECR flux have been measured for the first time [37]. No significant deviation from isotropic expectations was found in the angular power spectrum up to multipoles $\ell = 20$ and upper limits on the dipole and quadrupole moments were reported as a function of the direction in the sky, varying between 8% and 13% for the dipole and between 7.5% and 10% for a symmetric quadrupole. An update of this study [39] above 10 EeV, including one additional year of data recorded at the Telescope Array and extending the zenithal range of the data recorded at the Pierre Auger Observatory up to $\theta = 80°$ reconstructed a dipolar signal with an amplitude of $r = (6.5 \pm 1.9)\,\%$ and a chance probability of 5×10^{-3} with reference to a purely isotropic distribution. No other deviation from isotropy was observed neither on the quadrupolar or on other angular

scales. Due to the full-sky exposure this measurement of the dipole moment does not rely on any assumption on the underlying flux of cosmic rays. Furthermore, the resolution of the quadrupole and higher order moments is the best obtained to present [39].

The origin of the observed dipolar anisotropy is currently unclear. A small dipole pattern of extra-galactic cosmic rays is expected due to our motion with respect to the frame in which they are isotropic. This is referred to as the Compton–Getting effect [40], and has been observed at lower energies, but the effect is expected to be below the 1% level [40, 41]. Due to the inhomogeneous distribution of nearby galaxies, a dipole pattern may also be caused at energies around and above 10^{19} eV [41].

3. The Pierre Auger Observatory

The Pierre Auger Observatory is currently the largest experiment for the observation of UHECRs and can observe cosmic rays with energies from 10^{17} eV to above 10^{20} eV [42]. It is located in the Argentinian pampa near the town of Malargüe. The observatory is a hybrid detector consisting of a surface detector (SD) array of water-Cherenkov detectors and a fluorescence detector (FD). The SD consists of 1600 detector stations, each filled with 12 tonnes of water, positioned in a hexagonal grid with 1500 m spacing. The surface detector uses the distribution and timing of the electrons and muons on the ground to reconstruct the energy of the primary particle and its arrival direction as described in the following. The resulting instrumented area of 3000 km^2 is overlooked by the fluorescence detector. Each of the 27 FD fluorescence telescopes has a field of view (FOV) of 30° x 30°. 24 of these are housed in four telescope buildings, enclosing the array. The remaining three of these are part of the HEAT extension of the Auger Observatory and are located near one of the telescope buildings, Coihueco, in three individual housings which can be tilted upwards by 29° degrees. This allows them to observe showers with a lower energy, down to 10^{17}, which develop higher in the atmosphere [42]. A schematic view of the Auger Observatory is shown in figure 3.1.
The hybrid, i.e. two detector-nature allows to calibrate the SD using a nearly calorimetric measurement of the shower in the atmosphere by the FD. Similarly the reconstruction accuracy of the shower geometry can be significantly enhanced in 'hybrid' events where both the FD and SD observe the same shower.

Unless otherwise noted the information in this chapter are based on [42, 44, 45]. A detailed overview on the observatory operation, monitoring, detector systems and enhancements, reconstruction and performance of the Pierre Auger Observatory can be found in [42].

3.1. The Fluorescence Detector

As mentioned previously each of the regular 24 FD telescopes has a field of view of 30° x 30° with 6 of them housed in the four fluorescence telescope buildings Coihueco, Loma Amarilla, Los Morados and Los Leones. Shown on the top, left-hand side of figure 3.2 is a photograph of the Los Leones building and on the bottom, left-hand side of the figure a schematic view of a single FD telescope is shown. The aperture of the telescope has a diameter of 2.2 m and consists of an optical filter and a corrector ring. After the aperture the light is focussed on the spherical focal surface by a spherical mirror. The focal surface consists of 440 hexagonal camera pixels, each with a field of view of 1.5 °. Every pixel consists of one photomultiplier tube (PMT). The signal of

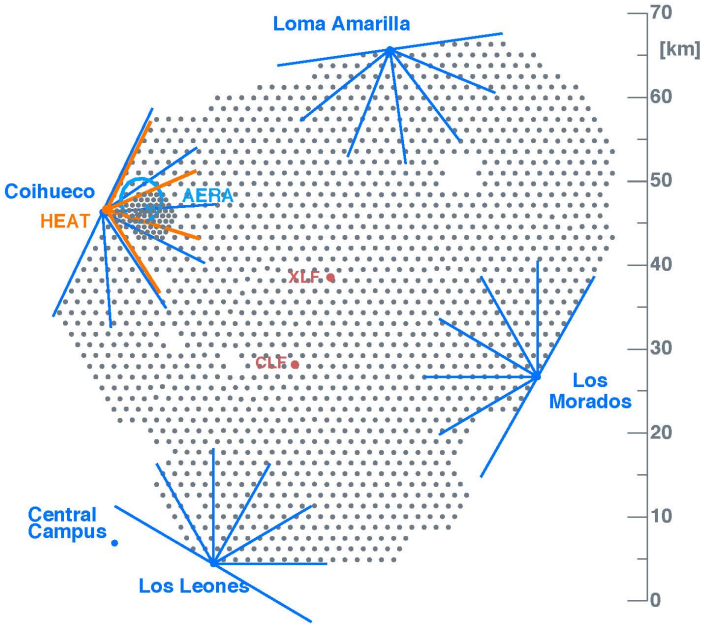

Figure 3.1.: Schematic layout of the Pierre Auger Observatory located near Malargüe, Argentina. Blue and orange dots and lines indicate the position and FOV of the 5 FD detector stations. Red dots indicate the central laser facility (CLF) and extreme laser facility (XLF). The black dots show the SD detector stations, which are more densely placed in the infill-array near Coihueco. Also located there is the AERA radio extension as indicated by the light blue circle. Source: http://augerpc.in2p3.fr/sites/default/files/augerbuilt_3045.jpg.

each pixel is digitised by an analogue to digital converter (ADC) with a sampling rate of 10 MHz. This time resolved signal is used for the reconstruction of first the shower geometry and then secondly the longitudinal shower profile as described in the next section. The 3 HEAT telescopes are functionally identical to the regular FD telescopes with the exception that they are read-out with twice the sampling rate and they can be tilted to observe lower energy showers higher in the atmosphere. With this configuration the FD can observe events from 10^{17} eV up to the highest energies, reaching a trigger efficiency of 100% for energies above 10^{19} eV over the entire array of the surface detector. Since showers can only be observed during clear and moonless nights the duty cycle is around 13%.

More detailed information on the FD can be found in [44].

3.1.1. Reconstruction of FD Events

A shower passing through the atmosphere excites the atmospheric nitrogen. Upon de-excitation the nitrogen emits fluorescence light isotropically. This light can be observed

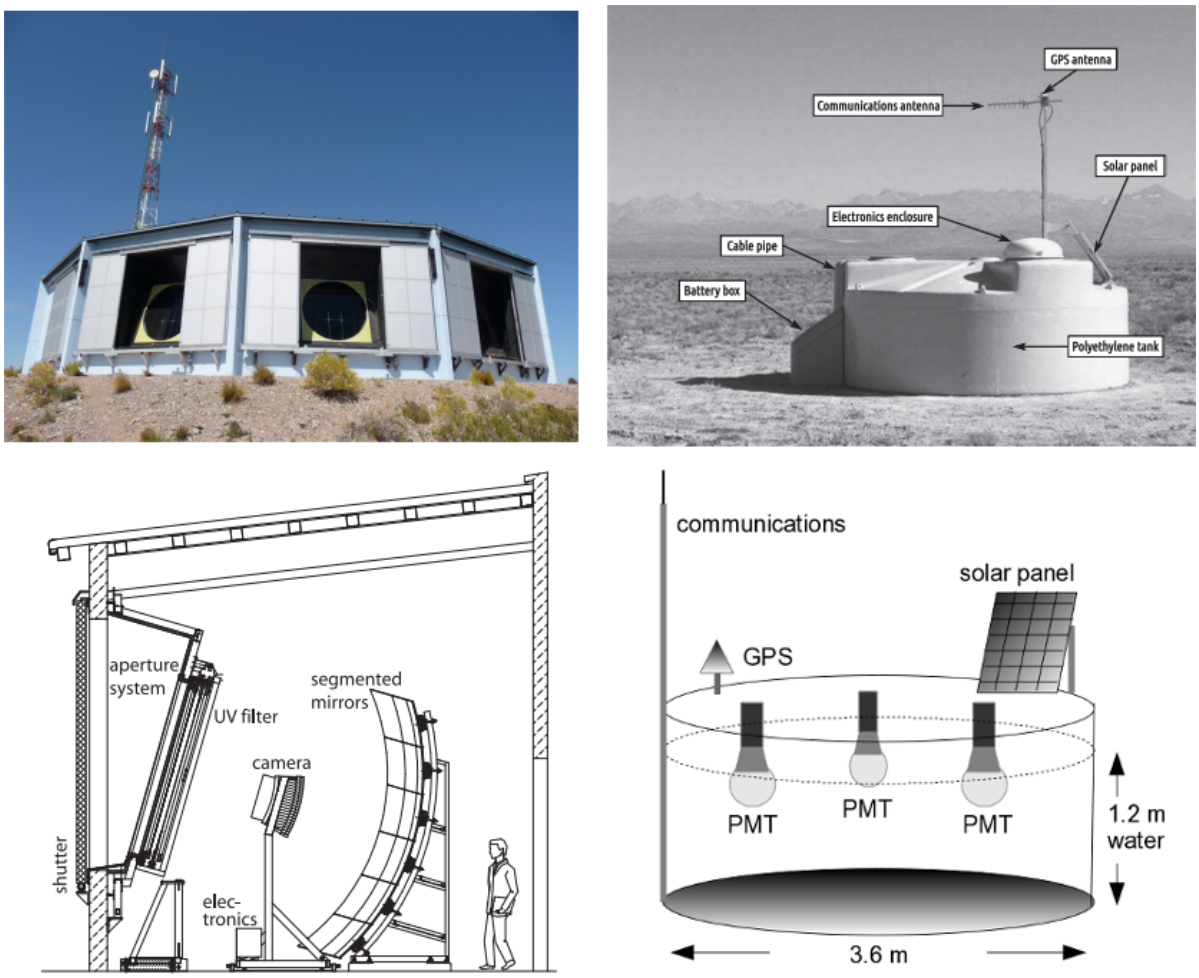

Figure 3.2.: Top, Left: Photograph of the Los Leones telescope building. Shown are the two central telescope apertures [42].
Bottom, Left: Schematic illustration of one FD telescope. The incoming fluorescence light is focused through the aperture onto the segmented mirror and background light is reduced through an UV-pass filter. The camera consists of 440 photomultiplier tubes [42].
Top, Right: Photograph of one SD detector station with its various components outlined [42].
Bottom, Right: Schematic illustration of one SD detector station. The passage of particles from an air shower causes the emission of Cherenkov light in the water within the detector. The walls of the detector are covered with reflective foil to increase the amount of light detected by the PMTs [43].

by the FD telescopes. The passing of a shower through an FD camera is illustrated in the bottom, left-hand side of figure 3.3. The timing of the individual triggering of the respective pixels is colour coded. As the shower moves down in the atmosphere, first the pixels at the top of the camera are hit (due to the optics) and the shower image moves downwards. As camera pixels can also be triggered by other causes certain trigger criteria have to be met (for details see [44]) for a track in the camera to be considered as caused by an air shower. Once a shower has been detected by the FD, its properties can be reconstructed.

The shower forms a shower-detector-plane (SDP) with the telescope as illustrated at the top, left-hand side of figure 3.3. This plane is first determined as the plane through the telescope which most closely contains the pointing directions of the FD pixels centred on the shower axis as illustrated by the fitted line in the bottom, left-hand side of figure 3.3.

Within the SDP the trigger time $t(\chi_i)$ of an individual pixel which observes an angle χ_i with respect to the SDP is related to the closest shower distance R_p of a shower moving with an angle χ_0 with respect to the ground in the SDP:

$$t(\chi_i) = T_0 + \frac{R_p}{c} \tan\left(\frac{\chi_0 - \chi_i}{2}\right). \tag{3.1}$$

Via minimisation using the observed times $t(\chi_i)$ the free parameters R_p, χ_0 and the start time T_0 can be determined. Once the geometry is known, the collected light at the aperture at a given time can be converted to the energy deposited by the shower as a function of the slant depth as illustrated at the top, right-hand side of figure 3.3. To achieve this, the light attenuation from the shower to the telescope needs to be accounted for and all contributing light sources need to be distinguished. This includes the fluorescence light, Cherenkov light and multiply scattered light. Once this is done, the fluorescence light intensity can be related to the deposited energy via the fluorescence yield, which can be measured experimentally in the laboratory [46].

To determine the shower energy a Gaisser-Hillas function

$$f_{\mathrm{gh}}(X) = \left(\frac{\mathrm{d}E}{\mathrm{d}X}\right)_{\max} \left(\frac{X - X_0}{X_{max} - X_0}\right)^{(X_{\max} - X)/\lambda} \exp\left(\frac{X_{\max} - X}{\lambda}\right) \tag{3.2}$$

is fitted to the energy deposit per slant depth ($\mathrm{d}E/\mathrm{d}X$). Here $X_{\max}$ is the position of the shower maximum and X_0 and λ are shape parameters. Finally, the calorimetric energy of the shower is reconstructed by integrating equation 3.2 and correcting for the 'invisible energy' that is carried away by high energy muons and neutrinos.

In the case of the Pierre Auger Observatory the accuracy of the reconstruction of the shower geometry is significantly enhanced in 'hybrid events', for which one or more SD detector stations provide additional information on the position of the shower on the ground. Likewise, the calorimetric measurement of the shower energy by the FD is used to calibrate the energy reconstruction of the SD as illustrated in the bottom, right-hand side of figure 3.2 and as explained in the next section.

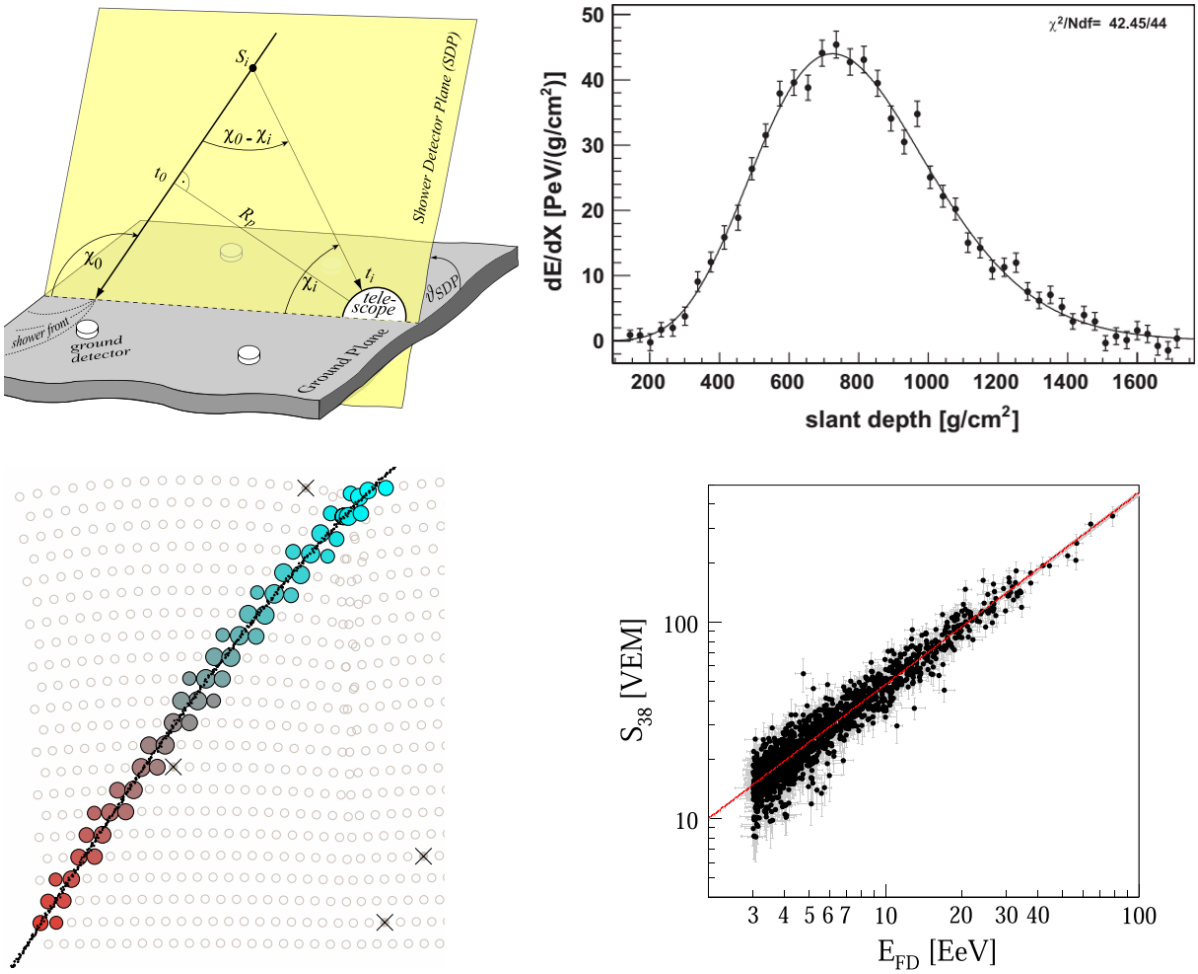

Figure 3.3.: Top, Left: Illustration of the reconstruction of the geometry of the shower from observables of the FD. From the point of view of a telescope the shower moves within a plane the telescope forms with the shower axis: the SDP. For details on the reconstruction see section 3.1.1 [44].
Bottom, Left: Light-track of an air shower observed by two fluorescence telescopes. The trigger time of the individual triggered pixels is colour coded. The shower moves downwards in time with respect to the camera. The black dots indicate the reconstructed shower profile. Individual camera pixels are represented by the hollow circles. Pixels which were triggered but were determined as too far from the shower axis by the reconstruction algorithm or are out of time are marked with an X and are not included in the reconstruction [44].
Top, Right: Reconstructed energy profile from the fluorescence light arriving at the telescopes as a function of the slant depth. The black line illustrates a fit with a Gaisser-Hillas function (see equation 3.2). The reconstructed energy of the shower is $E = (3.0 \pm 0.2) \cdot 10^{19}$ eV [42].
Bottom, Right: Calibration of the SD energy estimator S_{38} (see next section) using the energy $E_{\mathbf{FD}}$ measured by the FD using many hybrid events [42].

3.2. The Surface Detector

Each SD detector station consists of a water tank of 3.6 m diameter and 1.2 m height filled with 12 m^3 of ultra-pure water. All three PMTs of the Photonis XP1805/D1 type are symmetrically distributed and at a distance of 1.2 m from the tank centre and at the top of the tank. These collect the Cherenkov light that is emitted in the water by the relativistic electrons, positrons, muons and photons (that convert to electron-positron pairs in water) from the shower on the ground. To increase the collected light each tank is outlined with highly reflective liner. A photograph and a schematic view of one SD detector station is shown on the top and bottom, right-hand side of figure 3.2. Each detector station operates autonomously using a 10 W solar panel and a battery. Each station has an electronics package consisting of a read-out board for the PMTs, a GPS receiver and a radio transceiver to send the data to communication towers at the FD detector stations which in turn communicate with the central data acquisition system (CDAS) located at the Malargüe Campus. The SD stations are calibrated so that the collected charge of a PMT can be converted to the signal that would be produced from a minimally ionizing muon passing vertically through the detector, called a vertical-equivalent-muon (VEM) [47].

More detailed information on the SD can be found in [45].

3.2.1. Reconstruction of Vertical SD Events

In the following we describe the reconstruction of air showers with a maximum zenith angle of 60°, referred to as 'vertical' showers. The reconstruction of inclined or 'horizontal' showers with zenith angles between 60° and 80° degree differs as explained in the next section and in [48]. In order to identify a signal from a set of stations to be considered to be originating from an air shower, certain trigger-conditions have to be met (for details see [49]). As in the case of the FD the first step in reconstruction is the reconstruction of the geometry of the shower, which is performed in two steps: the determination of the shower origin $\mathbf{x_{sh}}$ and the shower impact on the ground $\mathbf{x_{gr}}$ which together form the shower axis. The first step obtains an approximation of the shower geometry by fitting the start time to the signals t_i in each individual detector station with position $\mathbf{x}_i$ to a shower front approximated as a sphere inflating at the speed of light c:

$$c(t_i - t_0) = |\mathbf{x_{sh}} - \mathbf{x_i}|. \tag{3.3}$$

Here $\mathbf{x_{sh}}$ and t_0 are the mentioned virtual origin and start-time of the shower as illustrated on the top and bottom, left-hand side of figure 3.4.

To obtain the impact point of the shower on the ground, $\mathbf{x_{gr}}$ is obtained by fitting a lateral density function (LDF) to the signal of the stations. An illustration of the footprint of a shower with an energy of (104 ± 11) EeV and a zenith angle of (25.1° ± 0.1°) is shown on the top, right-hand side of figure 3.4 together with the reconstructed shower axis (projected onto the ground). The lateral distribution of the signals is shown on the bottom, right-hand side of the same figure, together with the fitted LDF. The

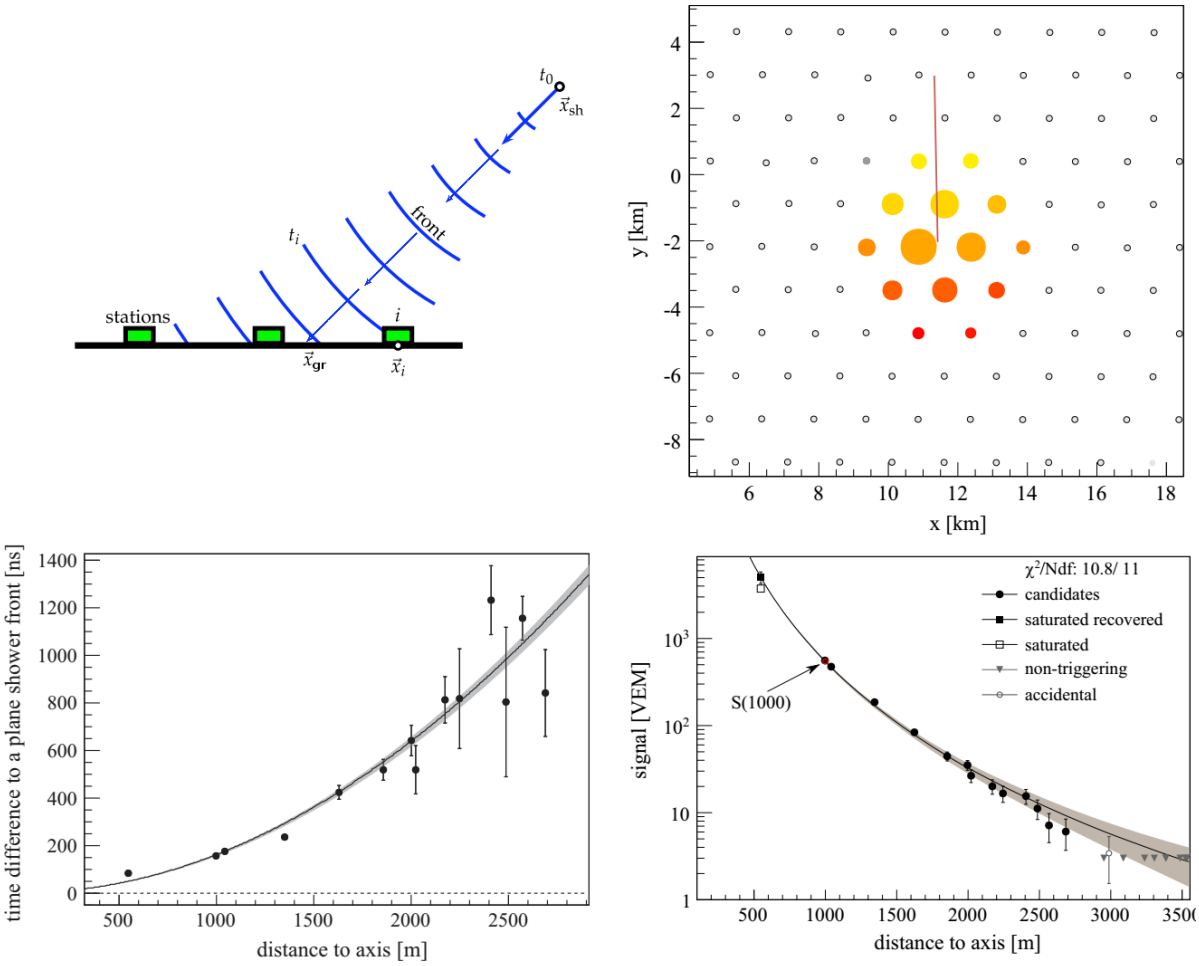

Figure 3.4.: Top, Left: Reconstruction of the shower geometry. Shown is an illustration of the evolution of the spherical shower front, originating from $\mathbf{x_{sh}}$ and at time t_0. These parameters can be determined using the timings of the individual stations i using equation 3.3.
Bottom, Left: Reconstruction of the shower geometry. Dependence of the signal start times (relative to the shower front) on perpendicular distance to the shower axis.
Top, Right: Shower footprint on the ground as viewed by the SD. The time differences are colour coded (yellow early, red late), the size of the coloured stations corresponds to the signal size. The reconstructed shower axis is indicated by the line. The end point of the line marks the impact point of the shower centre on the ground.
Bottom, Right: Fit of the LDF (see equation 3.4) for a single shower to the signal of candidate stations (full circles), as determined by local station trigger. Stations close to the shower axis can saturate due to the high particle density. If the signal can be extracted from the stations (as described in [31]), they are included in the fit (full squares) otherwise they are excluded (empty squares). Stations that have a local trigger but are determined by the reconstruction algorithm as not belonging to the shower are excluded from the fit (empty circles). The probability of stations that could have triggered due to the shower but did not (downward triangles) is also considered by the fit.
Modified from [42].

function used to describe the distribution of the signal, and by proxy the particle density on the ground, is a modified Nishimura-Kamata-Greisen function (NKG) [42, 50, 51]:

$$S(r) = S(r_{\text{opt}}) \left(\frac{r}{r_{\text{opt}}} \right)^{\beta} \left(\frac{r + r_1}{r_{\text{opt}} + r_1} \right)^{\beta+\gamma}. \tag{3.4}$$

here r_{opt} is the optimum distance, specific for the geometry of the array, $r_1 = 700$ m and $S(r_{\text{opt}})$ is an estimate of the shower size and is used later to determine the energy of the shower. For the SD with a spacing of 1.5 km $r_{\text{opt}} = 1000$ m is chosen as this minimises the uncertainty from the choice of parameters for the LDF. The parameter $S(r_{\text{opt}} = 1000$ m) is referred to as $S(1000)$. The parameter β depends on the zenith angle and shower size. For events with only 3 stations β and γ are fixed using a parametrisation obtained by events with a larger number of stations.

With the reconstructed shower origin from the geometrical reconstruction and the shower impact, the shower axis is then given as the line connecting these two points.

With the shower geometry known and the parameter $S(1000)$, which is the signal a detector station 1000 m from the shower centre would measure, the energy of the shower can be reconstructed.

As $S(1000)$ still depends on the zenith angle θ it is transformed to a quantity independent of the zenith angle [42]

$$S_{38} = \frac{S(1000)}{CIC(\theta)}. \tag{3.5}$$

Here the constant intensity cut method

$$CIC(\theta) = 1 + a(\cos^2(\theta) - \cos^2(38^\circ) + b(\cos^2(\theta) - \cos^2(38^\circ))^2 \tag{3.6}$$

[42] is used with the parameters a and b being determined experimentally. Here $CIC(\theta)$ corrects for the attenuation and geometrical effects a shower of given energy experiences in the atmosphere and hence leads to a smaller $S(1000)$ (at a given energy) the larger the zenith angle is. This energy estimator S_{38} is now independent on the zenith angle and corresponds to the signal a shower with $S(1000)$ would have produced had it arrived with a zenith angle of 38°, which is the most common zenith angle in Auger data.

Using high-quality hybrid events, where both reconstructions from the FD and SD exist, the S_{38} parameter is related to the FD energy as shown on the bottom, right-hand side of figure 3.3. This way the calorimetric energy of the FD is used to obtain an energy calibration for SD events, even when the FD does not observe the particular event.

For the vertical events used in this thesis (see chapter 7) the energy resolution is better than 17% and for the horizontal events (see next section) the average SD energy resolution is 19.3% [34]. The systematic uncertainty in the energy due to the FD energy scale, applied to both vertical and horizontal events, is 14% [31].

3.2.2. Reconstruction of Horizontal SD Events

Events with a zenith angle above 60° degree pass a longer way through the atmosphere and hence are observed at a later shower age, i.e. at a later stage of shower development. By the time they are observed the electromagnetic cascade has stopped and most

electrons and positrons are absorbed, so that the muonic component is dominant [48]. The muons traverse a long way through the geomagnetic field introducing an asymmetry in the lateral distribution which needs to be accounted for in the reconstruction. The first step is again the determination of the shower geometry. The origin of the shower is determined as in the case of vertical showers. The impact point of the shower centre on the ground ($\mathbf{x_{gr}}$) is also reconstructed using a LDF. In the case of horizontal showers the LDF is given by [48]:

$$\eta_\mu = N_{19} \cdot \rho_{\mu,19}(\mathbf{x_{gr}}; \theta, \phi) \cdot A_\perp(\theta). \tag{3.7}$$

Here N_{19} is the equivalent to the vertical S_{38} energy estimator and is the relative normalization of a particular event with respect to the muon reference distribution $\rho_{\mu,19}(\mathbf{x_{gr}}; \theta, \phi)$. This reference distribution is obtained using extensive simulations [48] and includes implicitly the local zenith and azimuth angles (θ, ϕ) and the geomagnetic field. $A_\perp$ is the detector area project onto the shower plane. The energy reconstruction is performed by relating N_{19} to the energy measurement of the FD in high quality hybrid events [48]. Detailed information on the reconstruction of horizontal events can be found in [48].

3.2.3. Coverage, Trigger Efficiency and Angular Resolution of the SD

In order to search for patters and deviations from isotropy in the arrival directions of UHECRs it is necessary to know the exposure, i.e. the geometrical coverage of the detector integrated over the active observation time, of the detector to calculate an expectation which distributions of arrival directions are expected, for example in the case of a purely isotropic flux. Due to the limited duty cycle of the FD the calculation of the exposure of the FD usually is determined using extensive MC simulations. However as the SD operates nearly in full time it is possible to calculate the coverage analytically, under certain assumptions.

For a full-time operating detector with full efficiency the relative exposure of the detector, as a function of the declination δ is given by [52]:

$$\omega(\delta) \propto \cos(\alpha_0)\cos(\delta)\sin(\alpha_m) + \alpha_m \sin(a_0)\sin(\delta). \tag{3.8}$$

Here α_m is given by

$$\alpha_m = \begin{cases} 0 & \text{if } \xi > 1 \\ \pi & \text{if } \xi < -1 \\ \cos^{-1}(\xi) & \text{otherwise} \end{cases} \tag{3.9}$$

and [52]

$$\xi = \frac{\cos(\theta_m) - \sin(a_0)\sin(\delta)}{\cos(a_0)\cos(\delta)}. \tag{3.10}$$

Here the latitude[1] of the detector is given by a_0, θ is the zenith and θ_m the maximum zenith angle above which events are not considered. An illustration of this equation is shown in figure 7.1. Unless otherwise noted we refer to this formula if we mention Auger coverage in the following. In order to ensure that measured events indeed follow this formula, even above the energy of reaching full efficiency, certain corrections have to be applied to the observed data. These are described in chapter 7. As the detector is assumed to be operational full-time and hence has no variation in sidereal time there is no dependence on the right-ascension. Full efficiency means that the zenith angle acceptance depends only on the reduced perpendicular detector area given by $\cos(\theta)$ [52]. This is achieved when the SD reaches full trigger efficiency, at which point a shower can be reconstructed, regardless of the geometry. Shown in figure 3.5 is the trigger efficiency of the SD for events up to a maximum zenith angle of 60°. On the left-hand side the expected efficiency is shown based on MC simulations for proton, iron and photon primaries. On the right-hand side the efficiency, averaged over the chemical composition of hadronic showers, based on SD data and hybrid events is shown. As can be seen the array reaches an efficiency above 99% above about 3 EeV. For horizontal events this threshold increases to 4 EeV [53]. In this thesis only events with a minimum energy of 4 EeV will be considered. At full efficiency the detection area per elemental hexagon cell, as illustrated on the right-hand side of figure 3.6, can be calculated from the geometry and is 1.95 km^2. The corresponding aperture for showers with a maximum zenith angle of 60° is $a_{\text{cell}} = 4.58$ km^{2}sr. In the case of a maximum zenith angle of 80° the aperture is $a_{\text{cell}} = 1.95\ \text{km}^2 \int_0^{2\pi} d\phi \int_{0°}^{80°} d\vartheta \cos(\vartheta)\sin(\vartheta) = 5.94$ km^{2}sr. With the knowledge of the active elemental hexagons as a function of time $N_{\text{cell}}(t)$, which is provided by the monitoring, the integrated exposure over a given time can be obtained by integrating $a_{\text{cell}} \cdot N_{\text{cell}}(t)$ over the number of live seconds [49].

A further quantity of interest is the angular resolution of the SD. In theory this quantity would be measured using a known point source of UHECRs. Unfortunately no such known source exists. Another possibility would lie in the exploitation that certain celestial objects, such as the moon or the sun, block UHECRs on their way to earth. Such a blocking would appear as a deficit in a coordinate system centred on the celestial body. As this position is known, this could also be used to determine the angular resolution. However, due to the small size of these objects, this requires a high amount of collected events of a certain quality.
Currently the angular resolution is determined using MC simulations [54]. Shown on the left-hand side of figure 3.5 is the determined angular resolution of the SD using MC simulations as a function of the zenith angle and for a different amount of triggered stations. The angular resolution σ_η is defined so that the angle between a reconstructed event and a given point source would contain 68% of events. If the resolution of the azimuth and zenith angle is given by a 1-D Gaussian with width σ around the equator, the relation between the two resolutions is given by $\sigma_\eta = 1.5 \cdot \sigma$ [54]. As can be seen, the angular resolution depends on the zenith angle and the number of stations used in the

[1]The centre of the Auger Observatory is located at 35.21° southern latitude.

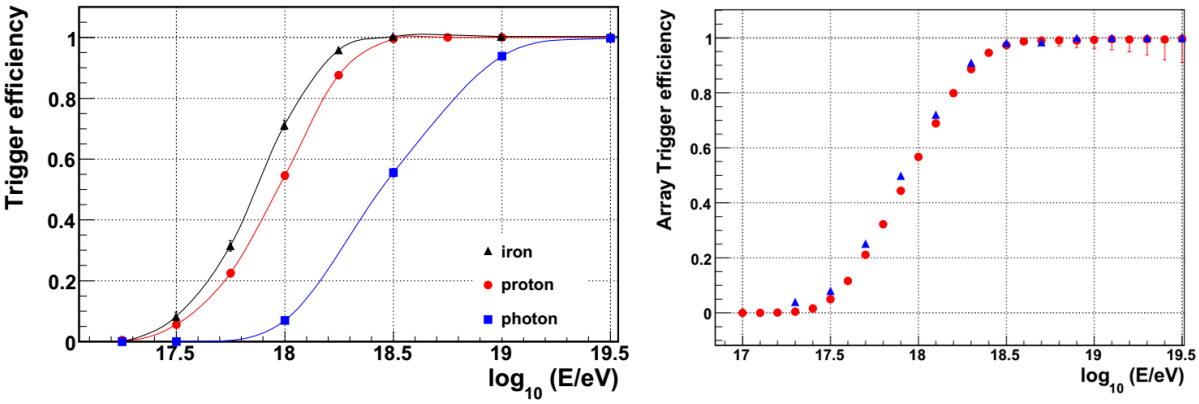

Figure 3.5.: Left: SD trigger efficiency up to zenith angles of 60° as a function of MC energy for protons (circles), iron (triangles) and photons (squares). **Right:** SD trigger efficiency as a function of reconstructed energy derived from SD data (triangles) and hybrid data (circles). As the points are based on measured rather than MC data the composition is unknown. Modified from [49].

reconstruction. Larger zenith angles are generally reconstructed better with an increase in the uncertainty for very inclined showers. Similarly the more stations are part of the reconstruction the lower the uncertainty reaching an angular resolution below 1° with 6 or more stations regardless of the zenith angle. In terms of energy this corresponds to an angular resolution in the order of $\sim 1.5°$ for events with 3 EeV $< E <$ 10 EeV which goes down to $\sim 1°$ for events $E >$ 10 EeV [54].

3.3. AugerPrime

The current Pierre Auger Observatory will be upgraded with new detector components in the next years. The goal of this upgrade is to be capable to have access to the mass composition of cosmic rays on an event by event base. As discussed in the previous chapter, the mass composition can currently only be determined on a statistical basis and under the use of different hadronic interaction models. Based on these techniques there exists a tension between the results from different observatories.

The goal of the upgrade is to determine the mass composition without the reliance on these models. This would allow to determine the cause of the observed flux suppression at the highest energies. It would also be a great benefit in the search of the sources of UHECRs. As particles with a low charge, such as protons, are least deflected by magnetic fields, anisotropy searches could be improved using only such particles [55].

In the following we give an overview on the components of the upgrade based on the preliminary design report [55]. As the report is still preliminary, details may be subject to subsequent change.

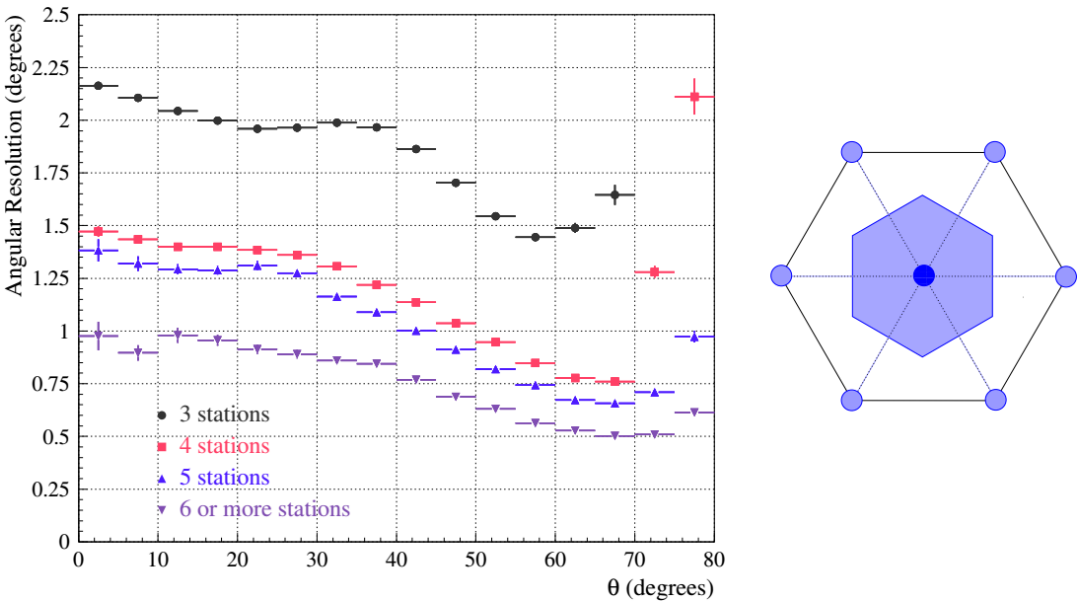

Figure 3.6.: Left: Angular resolution of the SD as a function of the zenith angle and triggered detector stations. The angular resolution σ_η is relative to the spatial angle η between the incident and the reconstructed event. If the resolution on the azimuth and zenith angle is σ around the equator, the relation between them is given by $\sigma_\eta = 1.5 \cdot \sigma$ [54]. **Right:** Scheme of an hexagon of SD stations. The elemental hexagon cell is the one in the middle, coloured, hexagonal box and has an area of 1.95 km^2 [49].

3.3.1. The Surface Scintillator Detectors (SSD)

Each SD detector station will be equipped with a scintillating detector on top. This allows the sampling of the shower particles with two different detectors, thus the measurement of the muonic component of the shower disentangled from the electromagnetic component. This enables an independent access to the primary mass composition as the muon component of an air shower is sensitive to the mass composition of the primary particle (for details see [55]).

The core of the SSD consists of two modules, equipped with 12 plastic scintillator bars each of a total area of 4 m^2 positioned on top of each current SD station as illustrated on the left-hand side of figure 3.7. Wavelength shifting fibres run through the scintillator bars, as illustrated on the right-hand side of figure 3.7. The fibres are all read-out with one PMT per station or, in an alternative configuration, via Silicon-Photomultipliers (SiPMs) (see below). With this setup the light produced by charged particles in the scintillator can be directly compared to the signal in the water-Cherenkov detector (WCD). In the SSD the signal amplitude will be dominated by electrons and positrons while the signal in the WCD will be dominated by photons and muons [55].

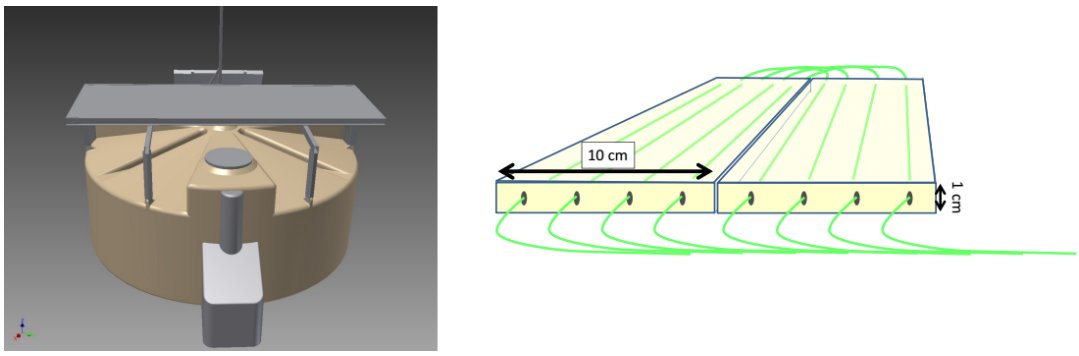

Figure 3.7.: Left: Illustration of the SSD. A plastic scintillator module is positioned on top of the existing SD station [55]. **Right:** Illustration of two plastic scintillator bars. Two modules, each composed of 12 of the illustrated scintillator bars (i.e. 6 times the shown number) are used per station. The plastic scintillator contains wavelength shifting fibres in a 'U-shape' which are all read out with one PMT. The fibres are wavelength shifting to effectively collect the light from the scintillator [55].

3.3.2. Surface Detector Upgrade

The electronics of each SD detector station will be upgraded to read out the current detector station and the new SSD. Additional improvements will include an increase of the sampling rate and an increase of the dynamic range due to the installation of an additional, smaller PMT in the WCD. This addition will reduce the saturation of stations close to the shower core (see the bottom, right-hand side of figure 3.4). Currently the signal information from saturated stations can sometimes be recovered, but only at the expense of an increased uncertainty. The inclusion of an additional, smaller PMT could reduce the fraction of saturated events down to 2% at the highest energies and allows for the measurement of complete signals as close to 300 m from the shower core.

3.3.3. The Underground Muon Detector (UMD)

The current SD infill area of 23.5 km^2 will be equipped with an underground muon detector. As the electro-magnetic component of the shower will be absorbed by the earth, this allows for an independent measurement of the muonic component of the shower and serves as a verification of the upgraded SD stations. The UMD will consist of 61 stations deployed in a 750 m grid in the infill area (see figure 3.1) where the SD station are also more densely spaced. Each detector station will have an instrumented area of 30 m^2 and will be buried at a depth of 1.3 m next to the SD stations. As in the case of the SSD, the particles are detected via modules of plastic scintillator bars read out by an PMT. On the left-hand side of figure 3.8 one such scintillator bar module of 10 m^2 is shown and on the right-hand side an in-field instrumented area of 30 m^2 is shown. Besides as serving as an independent verification of the results of the SSD the spacing of the detectors makes them ideal to study the chemical composition around the energy

Figure 3.8.: Left: Illustration of a 10 m^2 UMD scintillator module. The module consists of 32 scintillator bars read out with 64 optical fibres coming from each side of the module. As shown in the upper left corner the 64 fibres are concentrated to be read out in common [55]. **Right:** Illustration of one UMD station. The scintillator bars are placed underground. The housings contain the electronics and allow access to them. This image contains two 10 m^2 and two 5 m^2 modules, resulting in a total instrumented area of 30 m^2 [55].

region of the ankle in the cosmic ray spectrum (see figure 2.1).

3.3.4. Extended FD Duty Cycle

The operation mode of the FD will be changed to extend the measurements into periods with higher night sky background (e.g. before sunrise and after sunset and during fuller moon phases). This will increase the duty cycle up to 50%. To achieve this goal the gain of the PMTs in the FD telescopes will be reduced during periods of higher brightness to avoid damage of the PMTs.

3.3.5. Photon Detectors for AugerPrime

Currently PMTs are proposed to be used to read out the SSD and the UMD. Another interesting light sensor that could be used in either of these detectors are Silicon-Photomultipliers (SiPMs) which are currently also explored as an option. SiPMs are semiconductor light-detectors that have become increasingly used in high-energy physics. They possess important advantages to PMTs in some cases. They are able to be operated at low operating voltages around 20-100 V, have a very high photon detection efficiency (PDE) of currently up to 50% [56] and can be operated in the presence of high magnetic fields. They are also robust [57], an important feature in field use, and can withstand high light fluxes without being damaged. In comparison to PMTs which require manual labour during assembly they can be produced en masse relatively cheaply [58].

They also come with some disadvantages. Their behaviour depends on the operating temperature but this can be controlled easily using electronics [57]. The most significant challenge in using SiPMs is their dynamic range, which is limited by the number of cells they are composed of. At high light fluxes SiPMs tend to saturate and have a non-linear response to the incoming light flux. This, along with additional challenges which are described in the next chapter, makes the determination of the incoming light-flux on the SiPMs and hence the determination of the signal strength not straightforward [58].

In the next chapter we give an introduction to SiPMs and explore these topics in detail. We present a measurement technique that allows to fully characterise SiPMs up to saturation and to reconstruct the incident photons flux onto the sensor.

4. Dynamic Range Measurements and Calibration of SiPMs

The results of this chapter have already been (partially) published in the following publication:

- T. Bretz, T. Hebbeker, M. Lauscher, L. Middendorf, T. Niggemann, J. Schumacher, M. Stephan, A. Bueno, S. Navas and A.G. Ruiz *Dynamic range measurement and calibration of SiPMs*, Journal of Instrumentation, Volume 11, March 2016, (2016).

This chapter is based on this publication with some additions and modifications by the author of this work. The work in this publication is based on ideas from the author of this work. The measurements used in this work where either performed by the author of this work or under his supervision. More specifically the measurements described in section 4.4.2 were performed by the author of this work, while the remaining measurements were performed at the university of Granada by S. Navas and A.G. Ruiz. The majority of the analyses and text haven been performed and been written by the author of this work. The contained text in the publication was revised and copy-edited by the co-authors of the publication. The author of this work is the corresponding author of this publication.

4.1. Introduction

Silicon Photomultipliers (SiPMs) are semiconductor devices which allow the detection of very low photon fluxes down to the single photon level. In the past years they have been extensively studied and characterised (e.g. [59, 60, 61, 62, 63, 64]). Due to their relative cost-efficiency, high detection efficiency and insensitivity to magnetic fields, they have become of interest in various fields. For example, in medicine they are considered for use in PET scanners [65], in Particle physics as part of an upgrade to the trigger systems in collider experiments [66] and in Astroparticle physics as detectors for Cherenkov [67, 68] and fluorescence light [69] and possible as read-out sensors for scintillators to measure the ground distribution of particles [55] from extensive air showers. Some applications, such as trigger systems, only require that the signal from the SiPM exceeds a certain threshold. Other applications, such as calorimetric measurements of fluorescence and Cherenkov light, require the reconstruction of the absolute light flux incident to the sensor. This is more difficult to achieve when SiPMs are used instead of PMTs. In

the following we describe a method to measure the dynamic range of an SiPM up to saturation, that provides an estimation of the real number of photons impinging onto the device and hence, a calorimetric measurement of the incident energy. In the following, we give a short introduction to SiPMs and elaborate the challenge in the reconstruction of the light flux in more detail.

4.1.1. SiPM Overview

An SiPM is essentially a matrix of self quenching Geiger-mode avalanche photodiodes (GAPDs) (referred to as pixels or *cells*) read-out in common. An avalanche photodiode basically consists out of a semiconductor pn-junction with an externally applied bias-voltage as illustrated in figure 4.1. A detailed introduction on the working principle of pn-junctions and photodiodes can be found in [70] as well as in [58] which also includes a detailed description of SiPMs. An incoming photon can create an electron-hole pair within the depletion zone formed in the contact region of a p- and n-doped semiconductor. The pair is separated by the electric field due to the applied voltage. In the proportional mode the electric field is high enough so that electrons, traversing towards the n-doped end of the junction, can create additional electron-hole pairs on their way through impact ionisation as illustrated on the left-hand side of figure 4.1 [58]. If the bias-voltage is not too high the created holes do not create electron-hole pairs and the multiplication occurs only in the directions the electrons travel and ends intrinsically once the electrons leave the high field region. However, if the photodiode is operated in Geiger-mode both holes and electrons can create further pairs as illustrated on the right-hand side of figure 4.1. The avalanche now diverges and does not end intrinsically. To stop the avalanche "passive-quenching" is used. A high-ohmic resistor, the quenching resistor, is placed in series with the GAPD. During the avalanche the current through the GAPD and hence the voltage drop across the quenching resistor increases. This causes a voltage drop across the GAPD until the voltage falls below a level required to sustain the avalanche and the avalanche ends [58]. An SiPM consists ouf of many GAPDs and their quenching resistors read-out in common as illustrated in figure 4.2. A photograph of an SiPM with an active area of 1x1 mm^2 composed of 100 cells is shown in figure 4.3.

SiPMs are normally operated at a bias-voltage V_{bias} in the order of several tens of volts [58]. The more important quantity is however the over-voltage V_{OV}. This is the voltage the SiPM is operated at above the breakdown voltage V_{break} (i.e. $V_{bias} = V_{break} + V_{OV}$) from which the cells of the SiPM operate in Geiger-mode i.e., where a self sustaining avalanche takes place. The over-voltage usually is in the order of a few volts. When an incoming photon creates an electron-hole pair in a cell and creates an avalanche breakdown this is referred to as the *firing* of a cell. Due to the avalanche, the electron-hole pair is multiplied by a factor $\sim 10^5 - 10^6$ (increasing with V_{OV}), which is referred to as the "gain". Since the cells are read-out in sum, the total output signal of N fired cells is, therefore, on average, N-times the single cell signal.

Each pulse is followed by a dead time due to the finite time taken to quench the

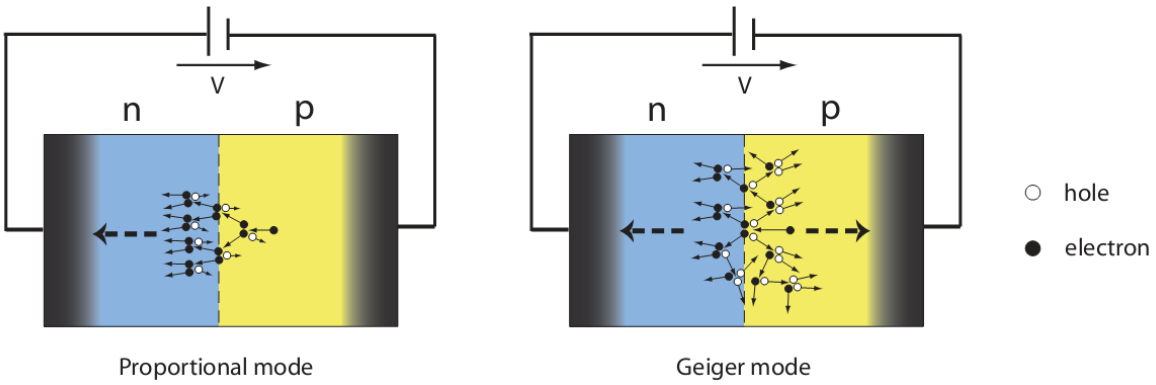

Figure 4.1.: Left/Right: Avalanche development in proportional (left) and in Geiger-mode (right). In proportional mode the APD is biased with a voltage below the breakdown voltage and the avalanche is only driven by electrons, develops only into one direction and ends intrinsically. In Geiger-mode the avalanche is driven in both directions by electrons and holes and hence diverges and needs to be quenched externally [71].

avalanche and reset the cell voltage to its initial bias value. Typical cell "recovery" times are of the order of few tens of nanoseconds depending on the SiPM model (smaller for small cell sizes). If another breakdown occurs in the same cell during the recharge time, the second signal will be of reduced size.

Besides the detection of a photon, a cell-breakdown can also be caused via undesirable effects: thermal excitation and correlated noise in the form of "optical cross-talk" and "after-pulsing". The thermal noise rate usually lies in the order of a few kHz per cell at room temperature. The optical cross-talk is caused by photons generated during the avalanche which nearly simultaneously excite cells surrounding the fired cell [59, 58, 73]. After-pulsing is caused by charge carriers trapped in lattice defects during the avalanche and released at a later time with typical release time constants ranging from a few ten to hundred nanoseconds [59, 58]. Both, correlated and uncorrelated (thermal) noise increase the effective recovery time of the SiPM as each noisy pulse starts the recovery process anew.

In the case of low intensity light fluxes (i.e., when few cells are fired) and negligible noise, even though each cell operates as a binary device, the whole SiPM acts as an analogue detector: the proportionality between the analog output signal and the number of fired cells allows the reconstruction of the number of photons hitting the SiPM active surface ($n_{\gamma,\mathrm{SiPM}}$). Unless the cell is still recharging after a previous avalanche, a new breakdown avalanche will produce the same signal in terms of signal height and generated charge. However, in the event of high intensity light fluxes the calorimetric reconstruction becomes more difficult and the measure of $n_{\gamma,\mathrm{SiPM}}$ degrades due to several factors, among which the cell recovery time, the noise and naturally the finite number

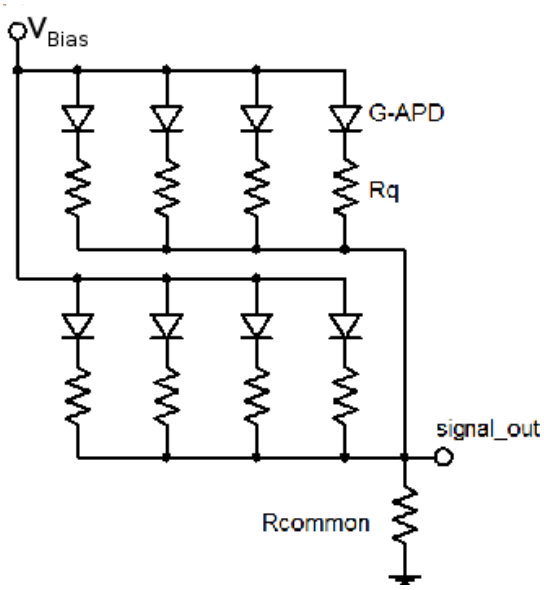

Figure 4.2.: Basic layout of an SiPM. Many GAPDs and their quenching resistors Rq are connected in series and read out via a common load Rcommon.

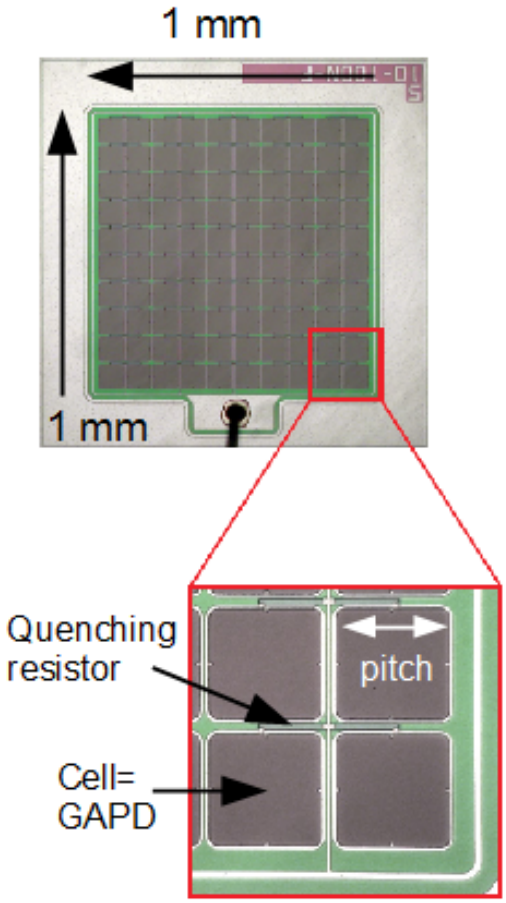

Figure 4.3.: Microscope image of an SiPM composed of 100 cells. (1x1 mm^2, 100 μm cell pitch) [72].

of cells dominate.

4.1.2. The Energy Reconstruction Challenge

The reconstruction of $n_{\gamma,\mathrm{SiPM}}$ from a light pulse is, therefore, not straightforward. Due to the binary nature of each SiPM cell, a simultaneous hit of multiple photons produces the same signal as a single hit in one cell. The result is in a degradation of the energy resolution due to loss of information. Hence, for high light fluxes where multiple photons hit the individual SiPM cells simultaneously or within their recovery time the SiPM output will not be proportional to the incoming light flux. This scenario may appear in short (few nanoseconds) light pulses provided they are intense enough, but also in light pulses of lower intensity, provided they extend over a long time period ($\gtrsim$ cell recovery time). Additionally, correlated noise in the form of cross-talk and after-pulses is present. Hence, even in the absence of thermal noise, the firing of a single cell cannot

be attributed to the detection of a signal photon.

To explore and address these challenges we present in this chapter a measurement of the response (in terms of impinging photons and fired cells) of three different SiPM types to light pulses over a wide range of pulse amplitudes, pulse widths and SiPM over-voltages. By using a calibrated reference sensor, we calculate the average of the total number of photons impinging on the surface of the SiPM. To ensure that all photon and noise signals are included in the response of the SiPM, the integration gate, i.e. the time interval during which the charge is accumulated, is always kept long relative to the varying pulse widths. For each given over-voltage we scan over a wide range of incoming light flux intensities and widths and carefully study the smooth evolution of the SiPM response from linear (low intensity and small width) to saturated. Based on these measurements we present a method which allows to reconstruct the light flux on the SiPM, $n_{\gamma,\mathrm{SiPM}}$.

This chapter is organised as follows. In section 4.2 we describe in detail the experimental setup, aimed to facilitate an easy replication of the presented measurement procedure. In section 4.3 we give a short overview of the required preparatory SiPM measurements, needed to characterise the basic properties of the devices: gain, breakdown voltage and noise rates. The dynamic range measurements and the analysis of the data are depicted in section 4.4. Finally, a discussion and interpretation of the results is given in section 4.5.

4.2. Experimental Setup

The core of the experimental setup (figure 4.4) consists of an integrating sphere (IS)[1] with three ports. A light input optical fiber (IS port 1), a calibrated silicon photodiode[2] (IS port 3) and a SiPM[3] (IS port 2) are coupled to the ports of the sphere. None of the components faces another directly. The used connection circuit of the SiPM is shown in figure 4.5. A low-noise signal amplifier[4] is also connected to the SiPM when a gain measurement is performed. As explained later, this data is acquired with a very low light intensity flux, i.e. with a very small cell occupancy rate down to the level of few *photo-electrons (p.e.)*. These measurements are used to establish the equivalence between "collected charge" and "number of cell breakdowns". The manufacturer states a nominal gain G_{Amp} of 100 for the amplifier which we verified experimentally as shown in figure 4.8 and explained in section 4.4.3. With the mentioned read-out circuit, the SiPM dynamic range measurements (section 4.4.1) are performed, however, *without* the signal amplifier which saturates much earlier than the SiPM, typically if more than ∼10% of

[1] Model IS200 from Thorlabs [74]. Operating range: 250 to 2500 nm.

[2] Model S2281 from Hamamatsu [75]. Sensitive range: 190 to 1100 nm. Active area: 100 mm^2.

[3] The SiPM and the connection circuit are placed together inside a small aluminium box to reduce the electronic noise as much as possible.

[4] Model PS 6954B-100 from Phillips Scientific [76]. Bipolar amplifier 100 kHz to 1.5 GHz with nominal gain ×100.

the cells are fired[5].

These components are held inside a light tight aluminium box which is placed inside a cooling chamber[6] to guarantee a stable temperature environment during data taking. Figure 4.6 shows the data recorded by the internal temperature probe during a long-period stability test performed at a benchmark temperature of 0°C. The systematic offset of the measured average temperature (~ 0.15°C) as well as the quoted temperature fluctuations (below ± 0.1°C) meet the requirements of our measurement. The light source is a blue LED with maximum intensity at a wavelength of 480 nm (FWHM = 10 nm) triggered by a custom-made pulser (section 4.2.1). The peak intensity and time duration of the light shots can be tuned remotely through a software interface installed on a PC connected to the pulser. A single optical fiber is used to guide the light from the LED to the integrating sphere. The current generated in the reference photodiode is measured with a pico-ammeter[7], and it is used to determine the absolute amount of light which reaches the SiPM (section 4.4). The quantum efficiency of the calibrated photodiode is (62±3)% at 480 nm. A remotely controlled, low voltage supply unit[8] is used to apply the SiPM bias voltage V_{bias}.

The final component of the setup is a rack consisting of a number of VME and NIM modules[9], an oscilloscope[10] and a PC for data acquisition and signal processing. The use of the charge accumulated by the Charge-to-Digital Converter (QDC), instead of e.g. ADC traces, allows for simpler measurement setups and the usage of pre-existing SiPM readout chipsets such as the MAROC [82]. Standard LEMO and BNC cables/plugs are used to transmit the signals. The complete system is controlled via software programs to automate the preparatory (section 4.3) and linearity (section 4.4) measurements. This includes the recording of the temperature of the cooling chamber, the setting and recording of the bias voltage of the SiPM and the LED, the time duration of the light pulse (t_{pulse}), and the data acquisition from the pico-ammeter and VME modules.

4.2.1. Custom-made LED Pulser: the "Universal Pulser"

An important aspect of this measurement is to study the response of the SiPM to a given number of photons stretched over the varying time lapse of the light pulse. This requires an LED pulser capable of sustaining the LED bias voltage for short ($\approx$ 10 ns) and long ($\approx$ 100 ns) periods, compared to the cell recovery time of the SiPM. To provide enough light from the LED over a wide range of pulse amplitudes (V_{LED}) and pulse widths (t_{pulse}), a custom made pulser named the "Universal Pulser" was developed at the III Physikalisches Institut A, RWTH Aachen University. It allows to generate LED pulse amplitudes V_{LED} between 0 V and 50 V and pulse widths t_{pulse} between 3 ns and 120 ns, which can be set via PC. An example of superimposed pulses provided

[5]The maximum output signal driven by the amplifier is 2 Volts across a single 50 Ω load [76].
[6]Model CCK-25-100 from DYCOMETAL [77]. Temperature range: −20°C to +100°C.
[7]Model 6485 from Keithley [78].
[8]Model CPX 400 Dual from TT*i* [79].
[9]QDC V965A, ADC V1729, SCALER V560AE, LTD V814B, FanIn/FanOut V925 all from CAEN [80].
[10]Model Waverunner 1600 from LeCroy [81]. 1 GHz bandwidth, 5 GS s^{-1}.

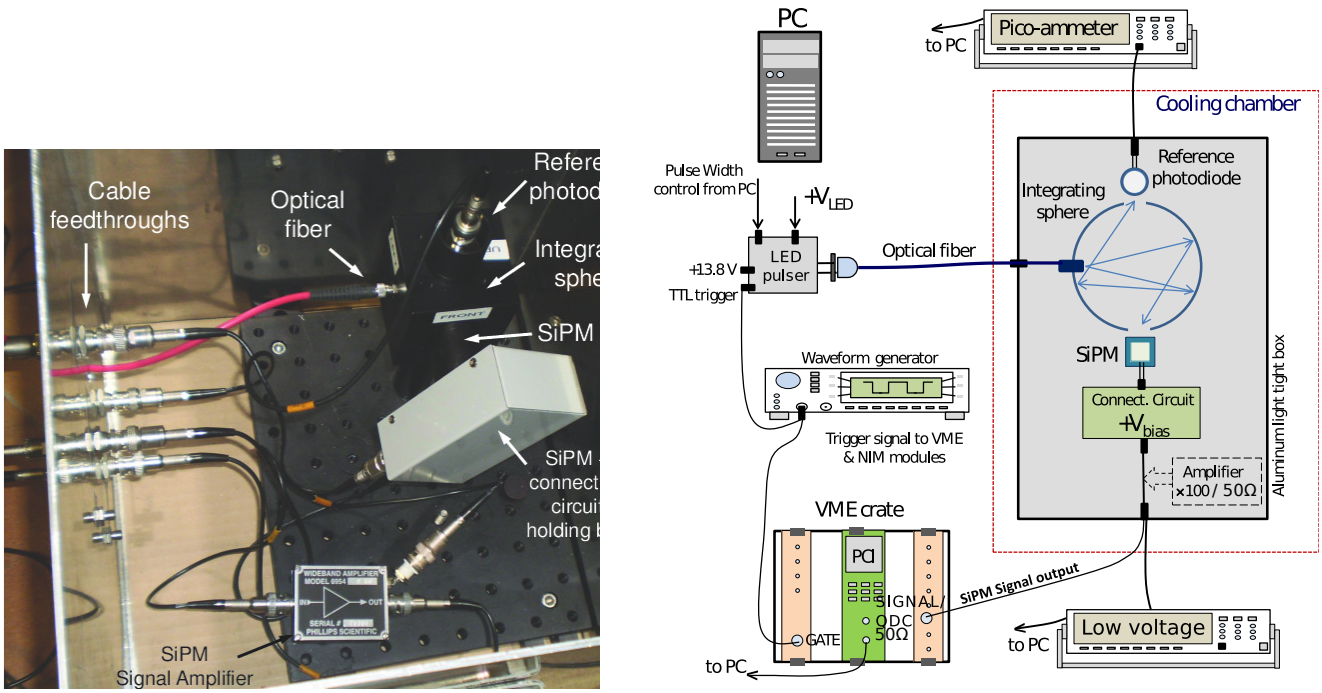

Figure 4.4.: Experimental setup used for SiPM characterisation tests at the University of Granada (see introduction to this chapter). **Left:** photo of the light tight aluminium box holding a three-ports integrating sphere to which the optical fiber, the SiPM and the calibrated photodiode are connected. The SiPM signal amplifier, used only in gain measurements, is also visible. **Right:** Schematic drawing of the full setup. The aluminium box is placed inside a cooling chamber; the LED is triggered by a custom-made pulser; the photodiode signal is read-out by a pico-ammeter; the SiPM signal is integrated by a QDC module (VME).

by the pulser measured with a test probe is shown in figure 4.7. The pulser has a slew rate around 9 V ns^{-1} and, after a small overshoot, delivers a constant voltage to the LED. A constant voltage, even at high amplitudes and pulse widths, is important as this shows that the LED is indeed emitting light for the whole duration of the pulse and not just a short burst followed by a slow recharge. With the high slew rate generated, the maximum amplitude of the pulser can be reached within 5 to 6 ns. A pulse is emitted upon receiving a TTL signal, given by a waveform generator[11] which also works as the general trigger for the data acquisition system. The LED voltage is provided by an external voltage supply unit[12]. We note that permanent operating voltages of up to 50 V are normally not possible with this LED. However, the LED is not damaged due to the low duty cycle with the pulse frequency being of the order of 20 kHz (16 kHz to be precise) in our case. The wide range of possible pulse amplitudes and widths provided

[11]Model TGA 1242 from TTi [79].
[12]Model PLH120-P from TTi [79].

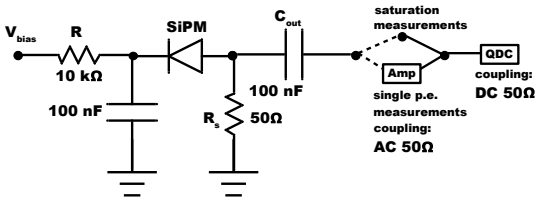

Figure 4.5.: Readout circuit used in the setup as proposed by KETEK [83] and Hamamatsu [84]. The amplifier is only used during the single p.e. level measurements.

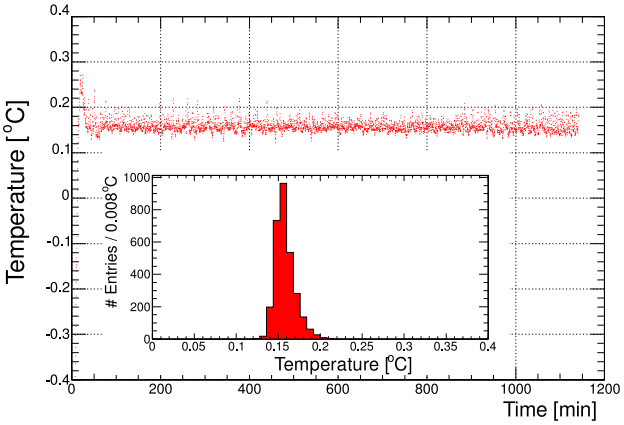

Figure 4.6.: Example of cooling chamber temperature stability over 19 hours of data taking (benchmark temperature 0°C).

by the pulser allows delivering to the SiPM a similar number of photons per pulse either from short but intense light-pulses or from longer but less intense light-pulses (see section 4.4). This allows to evaluate the uniformity of the SiPM response or deviation thereof (i.e. saturation) to the identical number of photons spread over a varying time interval.

4.2.2. Characterised SiPMs

Table 4.1 summarises the main features of the three SiPM models analysed in this work: one manufactured by KETEK [83] and two by Hamamatsu [84]. The three units have the same active area of 3×3 mm^2 but two different cell pitches of 50 and 100 μm resulting in configurations with different number of cells ($N^{\text{cell}} = 3600$ and 900, respectively). They also show different fill factors and cell recharge times. The devices are sensitive to a wide range of photon wavelengths (from ∼300 nm to ∼800 nm) with a peak sensitivity at 420 nm in all cases, which may make them suitable for Cherenkov and fluorescence light detection. One difference between the KETEK and Hamamatsu sensors concerns the breakdown voltage being a factor 2.5 smaller for the former. The dark count rate at the higher over-voltages[13] and room temperature ($20 - 25$°C) ranges between 1 and 10 MHz depending on the type. Typical cross-talk and after-pulse probabilities for the used SiPMs are in the order of a few 10% (see section 4.3 and [63]).

[13] V_{OV} from 1.3 V to 2.5 V, depending on the type.

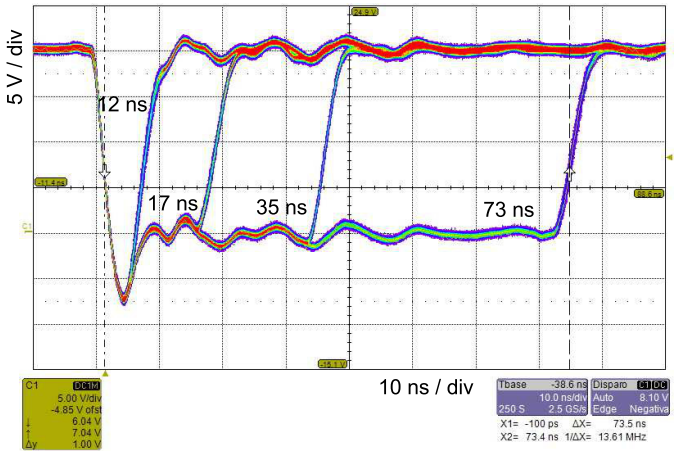

Figure 4.7.: Oscilloscope screenshot of example of pulses produced by the "Universal Pulser". The measurements were performed with the LED attached and using a test probe (÷10, 9.5 pF, 10 MΩ). The pulser achieves a slew rate around 9 V ns^{-1} and, after a small initial overshoot, delivers a constant voltage at the LED. Shown are overlays of pulse widths of 12, 17, 35 and 73 ns FWHM (from left to right).

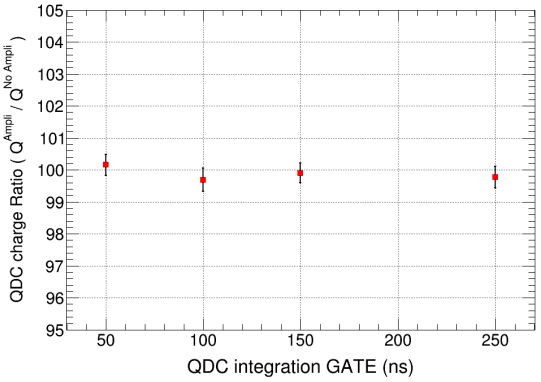

Figure 4.8.: Ratio of the SiPM integrated QDC charge measured with and without signal amplifier. Points correspond to different integration gate lengths and are averaged over several illumination levels. The results are compatible with the nominal gain (×100) provided by the manufacturer.

Table 4.1.: General specifications of the SiPM types characterised in this work (from manufacturer data-sheets [84, 83]). The fill factor refers to the ratio of the sum of the active areas of the cells to the entire area where the cells are contained. The fill factor is less than unity as electrical connection between the cells and the quenching resistor of each cell take up space.

Manufacturer	Type	Active area (mm^2)	Num. cells (N^{cell})	Cell pitch (μm)	Fill factor (%)	Breakdown voltage (V)	Gain (×10^6)
KETEK [83]	PM3350	3×3	3600	50	70	∼27	∼ 2
Hamamatsu [84]	S10362-33-050C	3×3	3600	50	61.5	∼70	∼ 0.8
Hamamatsu [84]	S10362-33-100C	3×3	900	100	78.5	∼70	∼ 2.4

4.3. Preparatory Measurements: Basic SiPM Features

We report here on some measurements which are crucial in understanding fundamental SiPM effects arising later in the dynamic range measurement discussed in section 4.4. The procedure to determine the gain and over-voltage of the devices is briefly illustrated

in section 4.3.1, whereas in section 4.3.2 we summarise the measured dark count rates, cross talk probabilities and other parameters relevant to the SiPM response. These experiments were carried out at low light levels, *with* a signal amplifier [76] and using the read-out circuit recommended by both manufacturers [83, 84] (figure 4.5). This allows the resolution of the number of individual fired cells (c.f. figure 4.9). Then, section 4.3.3 features a series of qualitative tests aiming at understanding the behaviour of the detectors when exposed to a long-lasting and high-amplitude light flux. The same experimental conditions used for the SiPM dynamic range studies was used here. In particular, due to its early saturation[5], the amplifier was removed from the setup and the signal read directly from the SiPM output. While individual cell breakdowns cannot be distinguished this way, a sufficient light flux allows for SiPM signals to be observed on an oscilloscope providing a basis to understand the behaviour of the SiPM in the dynamic range measurements.

4.3.1. Charge per Cell and Breakdown Voltage

The gain of a SiPM is a dimensionless quantity defined as the number of generated election-hole pairs per avalanche of an SiPM cell. Hence it is proportional to the charge produced by a single avalanche in a cell (ΔQ/cell), commonly referred to as *single photoelectron* (*p.e.*) level. Figure 4.9 (left) shows typical waveforms obtained with the oscilloscope when, on average, only a few SiPM cells are hit by photons. Pulses of increasing amplitude corresponding to increasing numbers of fired cells are recognisable. For the dynamic range studies described in this work, the charge per cell at different over-voltages is needed to estimate the number of fired cells from the measured charge spectrum when the SiPM is exposed to high or long light fluxes (section 4.4.3).

In practice, the distance of two adjacent photo-peaks in the QDC charge spectrum (right plot in figure 4.9) gives the charge per cell [63, 64]. The length of the QDC integration gate has to be large enough to capture the complete pulse, avoiding an underestimation of the gain. However, integrating over long gates heavily degrades the resolution of the charge spectrum if the device is very noisy (dark counts and after-pulsing predominantly, see section 4.3.2), making single peaks indistinguishable. The main effect of noise pulses synchronous to the real photon pulses is to change the relative height of the peaks in the charge spectrum, but they have no impact on the mean value of ΔQ/cell. Besides, asynchronous noise pulses also populate the inter-peak region with a rate increasing with the gate size. Hence, the choice of the gate length varies depending on the properties of the SiPM under investigation (noise and pulse duration, mainly). The aim is to have the gate as long as possible to include all of the pulse and correlated noise effects, while still being able to estimate the gain from the QDC charge spectrum. For the KETEK model, a satisfactory multiple peak identification was possible with gate lengths up to $t_{\text{pulse}} = 400$ ns at T = 0°C. Unfortunately no peak identification was possible with the two Hamamatsu SiPMs at this gate length. Instead it was necessary to reduce the gate length to 250 ns and 150 ns when operating with the Hamamatsu -050C and -100C devices respectively due to a higher noise activity (see table 4.2). In any case, the integration of the entire signal for the selected gates is guaranteed, given

the much shorter duration of the generated LED light-pulses (from 12 ns to 73 ns).

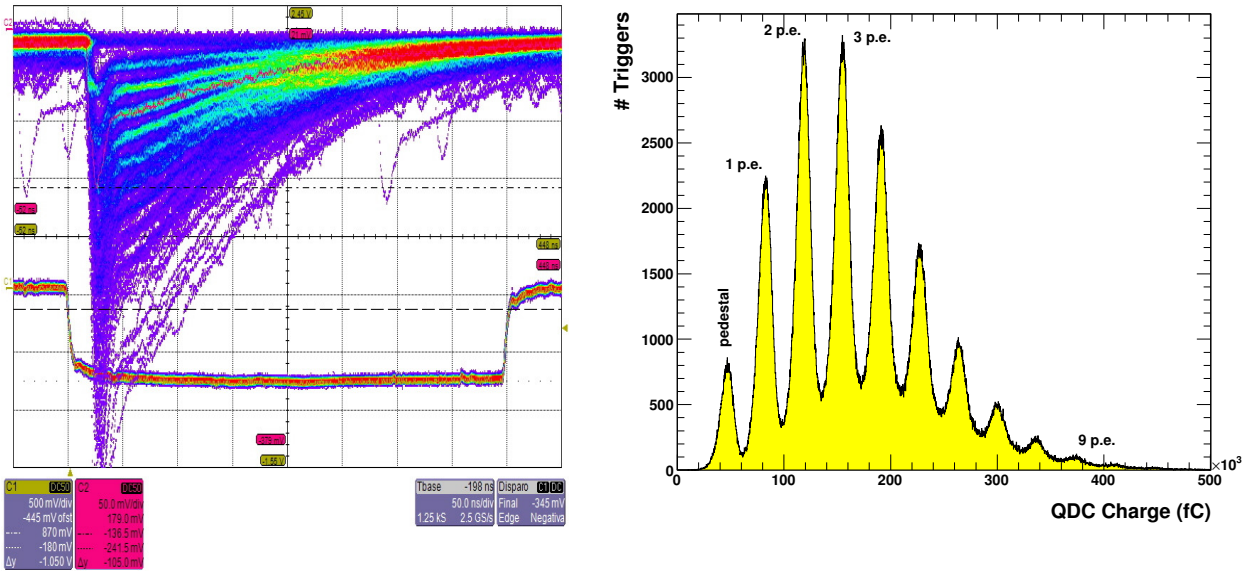

Figure 4.9.: Data from SiPM KETEK type PM3350 (V_{OV} = 2.6 V, T = 0°C, amplifier gain = 100, QDC integration gate 400 ns width exposed to a pulsed, low light-flux. **Left:** oscilloscope picture (50 mV/div, 50 ns/div) of superimposed signal pulses and NIM signal which gates the QDC (lower trace). **Right:** the corresponding charge spectrum (QDC data) from which the average charge per cell is calculated.

It is well known that the breakdown voltage V_{break} of a SiPM (and hence, the gain at a fixed bias Voltage V_{bias}) depend strongly on the temperature due to the interaction of the charge carriers with phonons [85]. To minimise the influence of the temperature on the measured parameters, the sensors were housed inside a cooling chamber[6] and kept at fixed temperature during data taking (±0.15°C stability around benchmark temperature, see figure 4.6). The uncertainty on the reconstruction of the breakdown voltage V_{break} and hence V_{OV} is 0.03 V. An example of the determination of the breakdown voltage is shown in figure 4.10. As the gain depends linearly on the over-voltage the breakdown voltage is obtained by fitting a linear function to the charge per cell breakdown as a function of the bias voltage and then extrapolating to down to a gain of zero as illustrated in figure 4.10. The determined charge per cell breakdown (ΔQ/cell) is later used in equation 4.4.3 to evaluate the number of fired cells of the SiPM in case of the saturation measurements without the amplifier as described in section 4.4.3.

4.3.2. Dark Count Rate and Cross-talk Probability

Even in complete darkness, breakdown of cells can occur in the SiPM due to uncorrelated (random thermal noise) and correlated (cross-talk and after-pulsing) phenomena [59, 58,

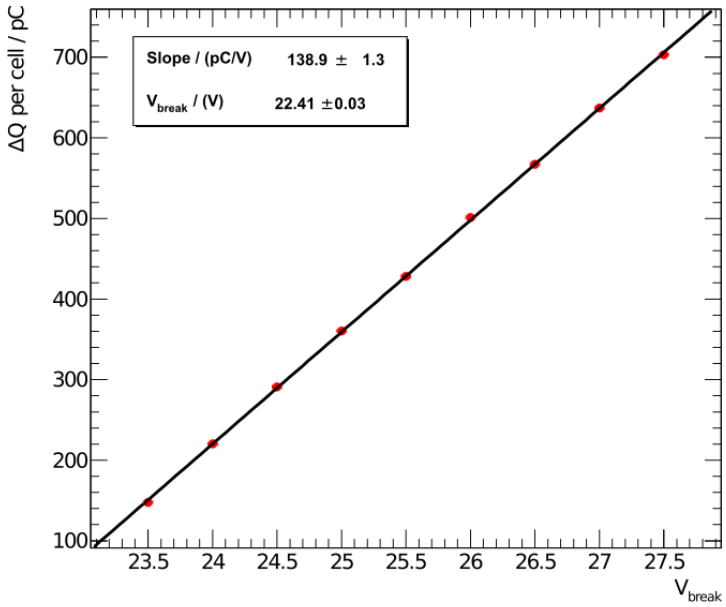

Figure 4.10.: Determination of the breakdown voltage of an SiPM. Data from SiPM KETEK type PM3350 and with the amplifier.

73, 86]. The increased pixel occupancy caused by these hits has two pernicious effects. Firstly, it leads to an overestimation of the photo-detection efficiency and, hence, to a miss-reconstruction of the number of photons. Secondly, it reduces the dynamic range of the sensor. Both, the thermal noise and cross-talk probabilities are expected to rise with the over-voltage (an increase of the trigger probability and gain resulting in the generation of more photons per avalanche) and the former additionally rises with temperature.

The measurements of the thermal noise rate and the optical cross-talk probability are performed in darkness following the method described in [63]. The SiPM signal is amplified and fed into a low threshold discriminator module connected to a scaler[14]. Pulses with amplitudes above a defined threshold level are counted by this module. The crosstalk probability is given by the ratio of pulses over the 1.5 p.e. level to pulses over the 0.5 p.e. level. The results of the measurements are summarised in table 4.2. We also include measurements of the after-pulse probability [63, 87] and recovery time for the same type of SiPM [88].

As can be seen the S10362-33-100C SiPM is by far the 'noisiest' of all studied SiPMs with both a hight crosstalk and after-pulsing probability. Despite its 50 μm cell size the KETEK PM3350 SiPM has the highest cell recovery time of the studied SiPMs.

[14]LTD V814B and SCALER V560 AE from CAEN [80].

Table 4.2.: Summary of the parameters relevant to SiPM saturation for all studied SiPM types. Referenced measurements are for the same type of SiPM. We only quote the cell recovery and not the grid recovery time (see [89] for details).

Over-voltage V_{OV} (V)	Dark Noise ($T = 0°$ C) (kHz)	Cross-talk probability (%)	After-pulse probability (%) [63]	Cell recovery time (ns) [88]
50 μm Hamamatsu - S10362-33-50C				
1.25	1090	10	11	20
1.45	1210	13	18	20
1.65	1540	17	22	20
100 μm Hamamatsu - S10362-33-100C				
0.70	1320	9	17	48
0.90	1660	15	28	48
1.30	2270	29	49	48
50 μm KETEK SiPM - PM3350				
2.10	110	3	-	83
3.10	200	6	≤ 9 [87]	83
4.10	330	10	-	83

4.3.3. Exposing the SiPM to Long-lasting and Intensive Light Fluxes

For the dynamic range measurements we use hereafter unamplified SiPM signals in order to avoid saturation of the amplifier. Illustrations of how the unamplified SiPM signals behave under light of varying pulse heights (V_{LED}) and pulse duration (t_{pulse}) are shown in figure 4.11. Starting with the top left figure of the -050C Hamamatsu SiPM, a steady increase of the maximum amplitude V_{max} with increased V_{LED} , and hence more fired cells, can be observed at a fixed pulse duration of 12 ns. After the voltage reaches V_{max} an exponential recharge back to the baseline is observed. A similar plot but with a pulse width of 73 ns is shown on the top right. At moderate pulse heights ($V_{LED} \lesssim 5$ V) the SiPM does not saturate, the signal reaches V_{max} and smoothly goes back to the baseline. However, at large pulse heights ($V_{LED} \gtrsim 10$ V) the signal saturates and stays almost flat in a plateau until the light pulse ends.
Here the SiPM enters a state of continuous breakdown where the cells break down again (as soon as they are able to) although with a reduced pulse height. The plateau likely represents the limit of how quickly the cells can recharge over their quenching resistors. At low values of V_{LED}, the KETEK SiPM shows a similar behaviour (bottom left) albeit on a slower time scale due to its larger cell recovery time (see table 4.2). However at a high values (bottom right) the plateau only starts after the voltage has already dropped towards the baseline. A visual comparison between the two right-column figures indicates clear differences of the response of the two devices to long-lasting light pulses.

The form of the response of the KETEK SiPM suggests a contribution of more than

one time constant in the recharge process. Indeed in the electrical SiPM model presented in [60] the recharge behaviour is characterised via two exponentials with two different time constants. The first and longer one corresponds to the mentioned cell recovery time and is determined via the quenching resistor and diode capacitance. The second and shorter one is determined by the shunt resistor and parasitic and grid capacitances of the SiPM. However whether this second contribution is observable in a voltage trace depends on the specific values of each SiPM as well as the read out electronics and hence the SiPM type [60]. For a more detailed overview we refer to [60].

4.4. The Dynamic Range: Measurement Procedure and Analysis

4.4.1. General Measurement Setup

The layout of the experimental setup (figure 4.4) is similar to the one used in the preparatory measurements (described in sections 4.3.1 and 4.3.2), with the exception that the signal amplifier is removed. The SiPM signals are now recorded unamplified by the Charge-to-Digital Converter (QDC). A number of data points is acquired changing the three following parameters in an automated way:

- The SiPM over-voltage V_{OV}. For each SiPM several values of V_{OV} (typically in steps of 0.2 V) covering the full range of each individual sensor are selected to study the behaviour of the dynamic range in different gain and noise level scenarios.
- The LED pulse width t_{pulse}. Discrete values between 12 ns and 73 ns (determined by the pulser) are selected to study the dependence of the SiPM response on the pulse length for a given number of photons impinging on the SiPM.
- The LED bias voltage V_{LED}, which is increased from 0 to 50 V in steps of 100 mV, allowing a detailed investigation of the dynamic range and a full scan over a few fired cells up to saturation.

The intensity and the duration of the light pulses are controlled via a program interface between the PC and the Universal Pulser. Figure 4.12 (left) displays the correlation between the LED voltage and the current from the calibrated photodiode (PD) coupled to the integrating sphere. For a given V_{LED}, increasing the length of the light pulse increases the photodiode current, as expected. For instance, the same current (i.e. number of detected photons) of 10 nA can be reached with three combinations of V_{LED} and t_{pulse}. The right panel of figure 4.12 illustrates the distributions of integrated charge measured by the QDC for $t_{pulse} = 12$ ns. Each of the observed Gaussian peaks corresponds to one value of V_{LED}. Even though shown together, the distributions are recorded and analysed

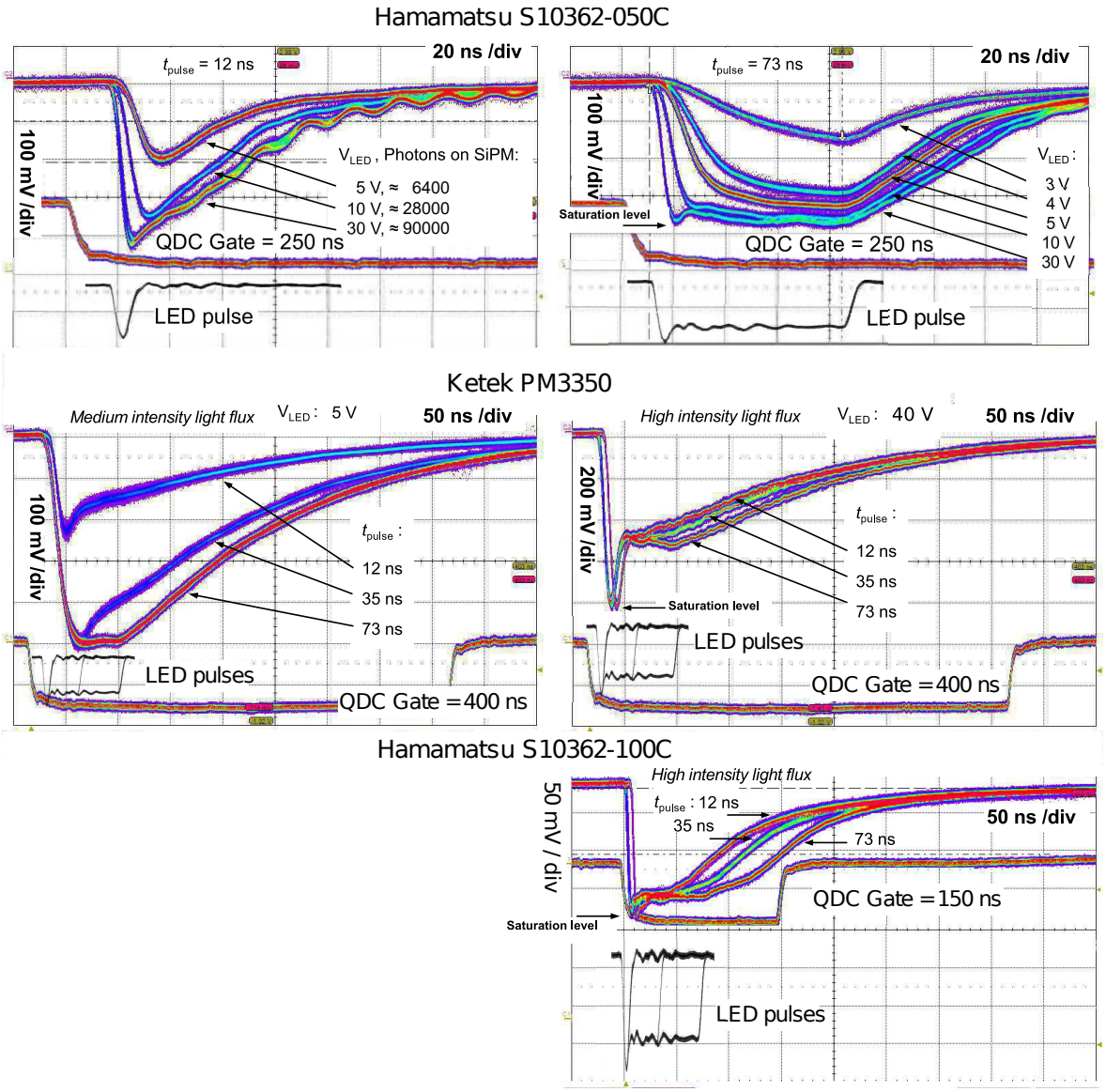

Figure 4.11.: Unamplified response of all SiPM types to light fluxes (with a frequency of 16 kHz) of various pulse widths (duration of the LED pulse t_{pulse}) and pulse heights (V_{LED}). **Top**: Hamamatsu S10362-050C, $V_{\mathrm{bias}} = 70.0$ V, **Middle**: KETEK PM3550, $V_{\mathrm{bias}} = 25.5$ V, **Bottom**: Hamamatsu S10362-100C, $V_{\mathrm{bias}} = 69.3$ V. The rectangular waveforms represents the QDC-gate and the black waveforms the (scaled) LED pulse(s) from figure 4.7.

separately. The non-uniform spacing of the Gaussian peaks, the quick increase of peak density with V_{LED} and the maximum charge reached at the highest LED values give already a qualitative hint of the magnitude of the saturation process.

For each individual combination of V_{LED} and t_{pulse} the automated data acquisition system records roughly 50 measurements of the photodiode current and about 40,000 QDC triggers. The mean and spread of the charge distributions are obtained from Gaussian fits. Moreover, additional "dark"-measurements (LED switched off) are performed

and used in the analysis to correct for the dark noise of the SiPM and dark current of the photodiode.

These measurements provide "photodiode current" data together with distributions of "SiPM charge". However, the "number of photons impinging the SiPM surface" and the "number of SiPM fired cells" are needed to complete the dynamic range characterisation of the devices and to evaluate their calorimetric performances. In order to achieve this objective, the analysis of the recorded raw data follows two basic steps:

1. Conversion of the photodiode current (I_{PD}) to the number of photons impinging on the active surface of the SiPM ($n_{\gamma,\mathrm{SiPM}}$), described in section 4.4.2.

2. Conversion of the mean charge in the charge spectra measured by the QDC (Q_{SiPM}) to the average number of fired cells or number of *effective fired cells* (n_{eff}), explained in section 4.4.3.

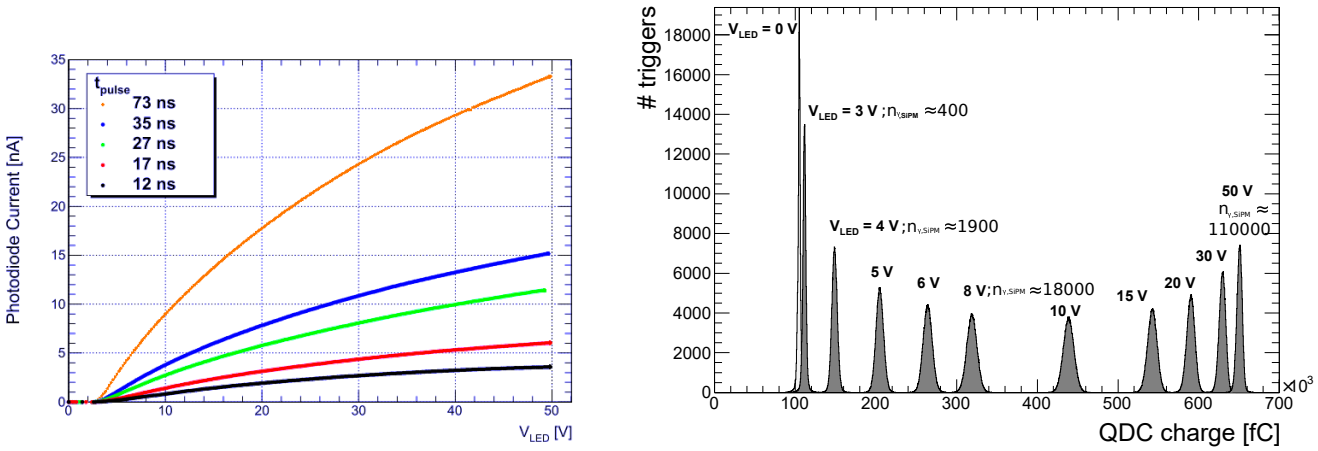

Figure 4.12.: Left: Increase of the photodiode current with the intensity (V_{LED}) of the LED light pulse. Different lines correspond to different values of the pulse duration (t_{pulse}). **Right:** Superposition of QDC charge spectra from a scan on V_{LED} between 0 and 50 V. Although the scan is performed in steps of 0.2 V only selected voltages are shown (t_{pulse} = 12 ns, data from KETEK PM3350, light pulse frequency: 16 kHz).

4.4.2. Conversion of the Photodiode Current to Photons on the SiPM

Using the fact that the quantum efficiency Q_{eff} of the photodiode is known[15], the number of photons impinging on the surface of the photodiode $n_{\gamma,\mathrm{PD}}$ can be obtained via

$$n_{\gamma,\mathrm{PD}} = \frac{\Delta I_{\mathrm{PD}}}{q_e \cdot Q_{eff} \cdot f} \tag{4.1}$$

Here ΔI_{PD} is the difference between the mean photodiode current at a given combination of $\mathrm{V_{LED}}$ and t_{pulse} and the mean photodiode current in darkness (i.e. the pedestal), q_e the elementary charge and f the frequency of the pulser. At low illumination levels, the statistical uncertainty on $n_{\gamma,\mathrm{PD}}$ is dominated by the fluctuations on the measured photodiode current. The next step is to calculate the mean number of photons per pulse impinging on the *active* surface[16] of the SiPM ($n_{\gamma,\mathrm{SiPM}}$). This was also required for the photon detection efficiency measurements (PDE) in [63]. There a similar setup was used, being the only difference that the SiPM was always located behind an aperture, exposing only a fraction of the active detection area. A conversion factor R_{PD} was used to convert the number of photons between the SiPM and the reference sensor ($n_{\gamma,\mathrm{SiPM}} = n_{\gamma,\mathrm{PD}}/R_{\mathrm{PD}}$). This factor is obtained by measuring the photodiode current at a constant light flux at a) the normal position of the diode (IS port 3) without aperture in front ($\Delta I_{\mathrm{PD,w/o\ Aper}}$) and b) at the position of the SiPM (IS port 2) with the aperture in front ($\Delta I_{\mathrm{PD,\ Aper}}$) [63]:

$$R_{\mathrm{PD}} = \frac{\Delta I_{\mathrm{PD,w/o\ Aper}}}{\Delta I_{\mathrm{PD,Aper}}} \tag{4.2}$$

However, for this work it is necessary to illuminate the entire surface of the SiPM and retain the information on the amount of photons impinging on the entire surface. To obtain this information we modify the procedure to determine the correction factor R_{Geo} as follows:

$$R_{\mathrm{Geo}} = \frac{R_{\mathrm{PD}}}{R_{\mathrm{SiPM}}} \tag{4.3}$$

where R_{PD} is obtained from equation 4.2 and R_{SiPM} is the ratio of the SiPM response with and without an aperture in front but measuring in both cases at its normal position on the integrating sphere (IS port 2). This means that both sensors are at the same position and have the same field of view when using the aperture. By taking the ratio of R_{PD} and R_{SiPM} the effect of the (unknown) field of view with the aperture cancels. Now R_{Geo} can be used to convert the number of photons per pulse on the photodiode to the amount of photons impinging on the whole SiPM:

$$n_{\gamma,\mathrm{SiPM}} = \frac{n_{\gamma,\mathrm{PD}}}{R_{\mathrm{Geo}}} \tag{4.4}$$

[15] $Q_{eff}(\lambda)$ was calibrated by the manufacturer with a 3% precision at $\lambda \sim 480$ nm.
[16] The area of the cells including the dead space in-between the cells

The challenge here lies in obtaining an exact (unbiased) measurement of R_{SiPM} which is only determined by the geometry of the setup. The limited dynamic range together with the unavoidable correlated noise of the SiPM (section 4.3.2) make the estimation of R_{SiPM} much more difficult than the geometrical factor of the (linear) photodiode R_{PD}. To test how R_{SiPM} is influenced by these phenomena, we perform multiple measurements at different SiPM over-voltages and LED-voltages. The SiPM signal is amplified and the light level is kept relatively low to achieve well separated charge spectra (as in section 4.3). We use custom made apertures for each SiPM which only expose the active area of each SiPM. If R_{SiPM} is affected by the dynamic range this would manifest in a dependence of R_{SiPM} on the light flux. Likewise a correlated noise effect would show a dependence on the over-voltage because these effects increase with the over-voltage. Moreover, using an additional photodiode we perform further measurements to ensure that the final measured value of R_{Geo} is not influenced by the fact that some aperture measurements require that IS port 3 is closed with an end-cap with possibly different reflective properties than the photodiode which is normally located at this port.

To be more resistant to correlated noise effects we use the Poissonian mean (as in e.g. [63]) to evaluate R_{SiPM}. Assuming that a given charge spectrum (e.g. figure 4.9 right) follows that a Poissonian distribution the Poissonian mean μ can be obtained from the probability $P(\mu, 0)$ that no light has been observed. More specifically μ can be extracted from the number of events in the pedestal N_{Ped} (i.e. the peak where no light has been detected and hence no cell breakdown has occurred) in relation to the total number of events in the spectrum N_{Tot} [63]:

$$
\begin{aligned}
P(\mu, k) &= \frac{\mu^k e^{-\mu}}{k!} && (4.5)\\
\Rightarrow P(\mu, 0) &= e^{-\mu} && (4.6)\\
\Rightarrow \mu &= -\ln(P(\mu, 0)) && (4.7)\\
\Rightarrow \mu &= -\ln\left(\frac{N_{\mathrm{Ped}}}{N_{\mathrm{Tot}}}\right) && (4.8)
\end{aligned}
$$

The advantage of this method is that μ can be calculated without being affected by correlated noise since the pedestal peak of the charge distribution (which corresponds to light flashes not resulting in the detection of a photon) does not contain correlated noise events.

We then obtain R_{SiPM} similar to R_{PD} (equation 4.2):

$$
R_{\mathrm{SiPM}} = \frac{\Delta\mu_{\mathrm{SiPM,w/o\ Aper}}}{\Delta\mu_{\mathrm{SiPM,Aper}}} \tag{4.9}
$$

The subscripts "Aper" and "w/o Aper" again refer to measurements with and without the aperture, respectively. Here $\Delta\mu_{\mathrm{SiPM}} = \mu^{\mathrm{Light}}_{\mathrm{SiPM}} - \mu^{\mathrm{Dark}}_{\mathrm{SiPM}}$ is the difference of the Poissonian mean of the charge spectrum obtained with the LED turned on and off (pedestal). In the measurement $\mu^{\mathrm{Dark}}_{\mathrm{SiPM}}$ is obtained once for each new over-voltage. After all over-voltages are cycled the aperture is either added or removed from the setup and the

measurement cycle starts again. In between the measurements with and without aperture and for each over-voltage the measured value of $\mu_{\mathrm{SiPM}}^{\mathrm{Dark}}$ is stable on average within 2.5%, 3% and 6% for the Hamamatsu -100C, 50C and KETEK PM3350 SiPMs respectively.

The outcome of this approach is shown on the left hand side of figure 4.13 for the Hamamatsu S10362-050C SiPM type. A scan in $\mathrm{V_{LED}}$ at four selected values of $\mathrm{V_{OV}}$ is performed. The result of a fit to a constant parameter R (horizontal lines) is also shown. The χ^2/ndf values of the fits obtained with the Poissonian mean method show good compatibility with a constant. Some measurements show a slight trend towards a larger R value at very low-light levels which however quickly disappears as the light flux increases. This is likely due to the relatively larger effect the dark noise correction has, at the same light level, on measurements where the aperture is present and hence less cells fire. The low-light values are still within 5% around the fit average and measurements with and without this trend converge to compatible ratios. Additionally the results indicate a negligible dependence on the over-voltage. The measurements of R_{SiPM} and R_{PD} were carried out twice with several changes to the setup in between to evaluate the reproducibility of R_{Geo} due to mechanical accuracy. The final value of R_{Geo} is chosen as the mean between the maximum deviations observed with half the distance as uncertainty. The results for all SiPMs are shown in table 4.3. All SiPMs had an individual and dedicated custom-made aperture and mount, which results in the spread in R_{Geo} between the different models. We also investigated the possibility of using the mean of the charge instead of the Poissonian mean. However this technique provided a less satisfactory result showing higher dependence on $\mathrm{V_{OV}}$ and $\mathrm{V_{LED}}$.

We note that this technique may also be used to measure the PDE over the total active area of a SiPM (equation 4.4), avoiding the requirement that the SiPM has to be located behind an aperture during the whole measurement. An example of this is shown on the right hand side of figure 4.13. Shown is the Poissonian mean of the Hamamatsu S10362-100C SiPM type vs. the number of photons impinging on the SiPM (c.f. equation (4.4)) using R_{Geo}, without an additional aperture. The obtained PDE of 37 % at $\mathrm{V_{OV}}$ = 1.35 V matches well with previous results for the same type of SiPM and wavelength (35%, $\mathrm{V_{OV}}$=1.30 V [63]).

4.4.3. Conversion of SiPM Charge Spectra to Average Number of Fired Cells

The calculation of the *average* or *effective number of fired cells* n_{eff} is a straightforward process. From the obtained charge Gaussian peaks of unamplified SiPM signals (see for instance right-hand side of figure 4.12) we calculate the mean deposited charge corrected by dark noise ($\Delta Q = Q_{\mathrm{light}} - Q_{\mathrm{dark}}$) and its uncertainty, per setting of $\mathrm{V_{LED}}$ and t_{pulse}. From this we derive:

$$n_{\mathrm{eff}} = \frac{\Delta Q}{\Delta Q^{1\ \mathrm{cell}}(V_{\mathrm{OV}}) \cdot 1/G_{\mathrm{Amp}}} \tag{4.10}$$

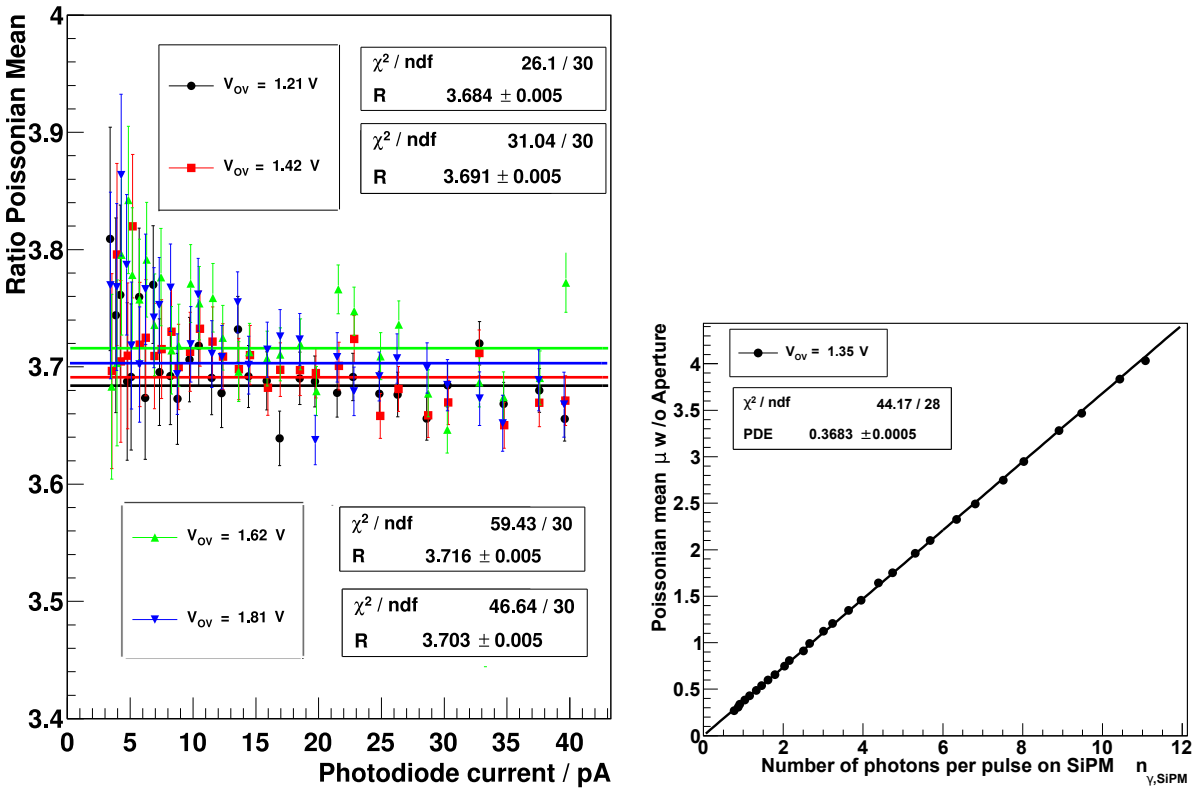

Figure 4.13.: Left: Ratio of the SiPM response R_{SiPM} from the Poissonian mean for Hamamatsu S10362-050C. Data points at each over-voltage (in Volts) are fit to a constant parameter R (horizontal lines). The used value of R_{SiPM} is the mean value between the two most extreme values observed. The largest observed value in this measurement was $R_{\mathrm{SiPM}} = 3.72$. During a measurement carried out a few days later, with other measurements with other apertures in between, the smallest observed value was $R_{\mathrm{SiPM}} = 3.52$, leading to a final value of $R_{\mathrm{SiPM}} = 3.62 \pm 0.10$ in table 4.3. **Right:** Poissonian mean vs. number of photons on the active surface of the Hamamatsu S10362-100C SiPM. The proportionality constant is the PDE.

where $\Delta Q^{1\ \mathrm{cell}}(V_{\mathrm{OV}})$ is the (amplified) charge produced by a single avalanche in a cell (see 4.3.1) and $G_{\mathrm{Amp}} = 100$ the nominal gain of the used amplifier provided by the manufacturer. This value was verified by comparing the SiPM response measured with the QDC, recorded with and without amplifier, for multiple widths of the integration gate and several illumination levels (see figure 5). This quantity is now independent of the used amplifier. Note that the expression *effective* is introduced since ΔQ also includes contributions from still recovering cells.

The values of the integrated charges by the SiPM are plotted against the number of photons impinging onto the photodiode (equation 4.1) in figure 4.14. The plot includes three values of $\mathrm{V_{OV}}$ and t_{pulse} (small, medium and large). The right hand side represents a zoom of the lower light levels of the corresponding left hand plot. Several conclusions can be drawn from this result. First, the correlation between $n_{\gamma,\mathrm{PD}}$ and ΔQ is very

Table 4.3.: Geometrical correction factor R_{Geo} for the different SiPM types, together with the photodiode R_{PD} and SiPM R_{SiPM} conversion factors (from equations 4.2 and 4.9, respectively). Absolute and relative uncertainties are given.

50 μm KETEK SiPM - PM3350	
R_{PD} :	63.2 ± 0.10 (0.2 %)
R_{SiPM}:	3.25 ± 0.10 (3.1 %)
$R_{\text{Geo}} = R_{\text{PD}}/R_{\text{SiPM}}$:	19.4 ± 0.7 (3.2 %)
100 μm Hamamatsu - S10362-33-100C	
R_{PD} :	43.3 ± 0.8 (2.0 %)
R_{SiPM} :	2.82 ± 0.12 (4.5 %)
$R_{\text{Geo}} = R_{\text{PD}}/R_{\text{SiPM}}$:	15.4 ± 0.8 (5.0 %)
50 μm Hamamatsu S10362-33-50C	
R_{PD} :	73.5 ± 0.2 (0.3 %)
R_{SiPM} :	3.62 ± 0.10 (2.8 %)
$R_{\text{Geo}} = R_{\text{PD}}/R_{\text{SiPM}}$:	20.3 ± 0.6 (2.9 %)

clean, the charge smoothly increases with the photon flux up to saturation. Moreover, the slope of the curves and the saturation value of the charge both rise with V_{OV} as a consequence of the increase of gain. Finally, enlarging the duration of the light pulse t_{pulse} also increases the probability to fire new cells (or the same cell more than once) and hence, the total integrated charge.

The geometrical correction factor R_{Geo} (from table 4.3) is used to convert the number of photons per pulse on the photodiode to the number of photons per pulse on the SiPM. This forms the abscissa of the plots in figure 4.15 where the results of all SiPMs are shown. The systematic uncertainties on this axis are dominated by the uncertainties of R_{Geo} (3-5%) and the calibration accuracy of the photodiode (3%).

4.5. The Dynamic Range: Results and Discussion

Given that, by construction, the devices have a finite number of cells N^{cell}, the maximal number of photons that can be detected in a given time frame (i.e. the dynamic range) is limited. The dynamic behaviour of the three tested SiPMs is shown in figure 4.15. The number of *effective fired cells* n_{eff} is plotted as a function of the number of photons per pulse impinging on the active SiPM surface. When the effective number of fired cells is small compared to the total number of cells of the SiPM (i.e. at low light fluxes) a smooth linear behaviour is observed. In the case of an ideal SiPM without correlated noise the slope of this linear behaviour would correspond the the photon detection efficiency (PDE)

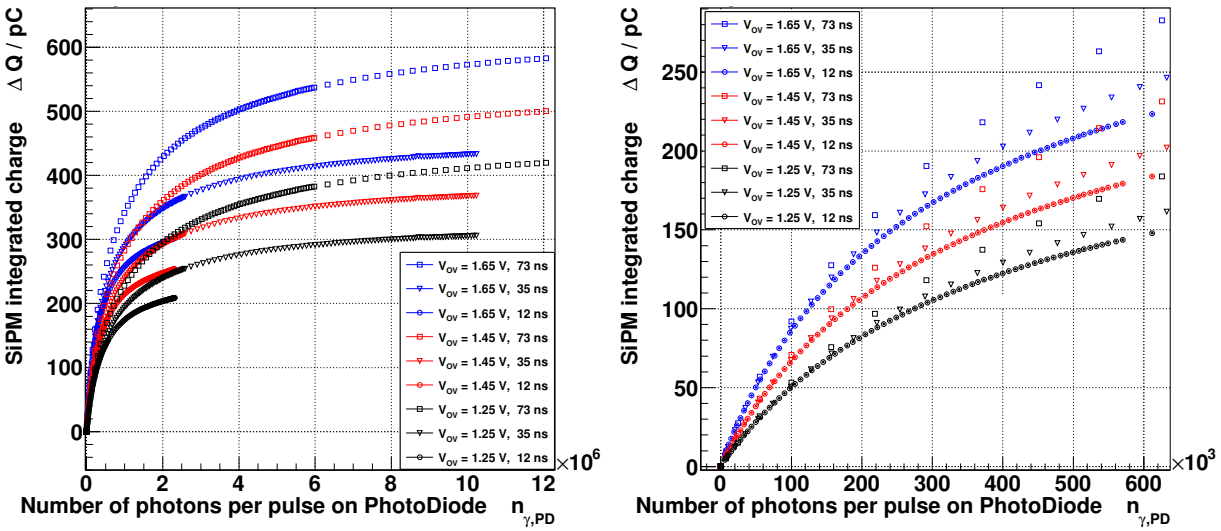

Figure 4.14.: Integrated charge of the SiPM as a function of the number of photons per pulse (left: full, right: zoom) on the photodiode (equation 4.1). The wider spacing of the data points at larger values of t_{pulse} is due to the same step size of V_{LED} for all pulse widths and hence more light is emitted from the LED (at the same V_{LED}) when the pulse width is larger. Data from Hamamatsu S10362-050C type. Integration gate length of 250 ns and various over-voltages V_{OV} and values of t_{pulse} are shown. A discussion of the individual features of the responses of the SiPMs can be found in section 4.5.2.

of the sensor. As correlated noise is present the slope represents an over-estimation of the PDE. On the other hand, increasing the light intensity eventually brings the SiPM to saturation due to the non zero recharge time of the cells. The reached maximum value of n_{eff} depends on the over-voltage and on the pulse width. The former may be caused by the increase of the SiPM detection efficiency at higher V_{OV} values, but also by the corresponding increase of the correlated noise. The latter is due to the fact that, for longer light pulses, some cells can trigger again at various states of recharge during the extended light pulse. This also leads to the fact that, at the longest pulse widths, the responses of the tested SiPMs do not seem to saturate but instead continue to increase, albeit at a much reduced rate compared to low light fluxes. Consequently, due to the non zero length of the light pulse and the presence of correlated noise (especially after-pulsing) the saturation value is not equal to the total number of cells N^{cell}.

Furthermore, the zoom on the non-saturated region (see for instance right-hand plots in figure 4.15) illustrates another outstanding result: the correlation between n_{eff} and $n_{\gamma,\mathrm{SiPM}}$ is measured to be *independent* of the light pulse width t_{pulse} up to a certain point and only dependent on the over-voltage. In other words, light pulses of different widths and intensities sending the same number of photons to the SiPM surface give the same number of equivalent fired cells. This is possible because we only use the integrated number of photons per pulse on the SiPM $n_{\gamma,\mathrm{SiPM}}$, estimated through R_{Geo} as described in section 4.4.2 instead of a quantity expressed in terms of a rate.

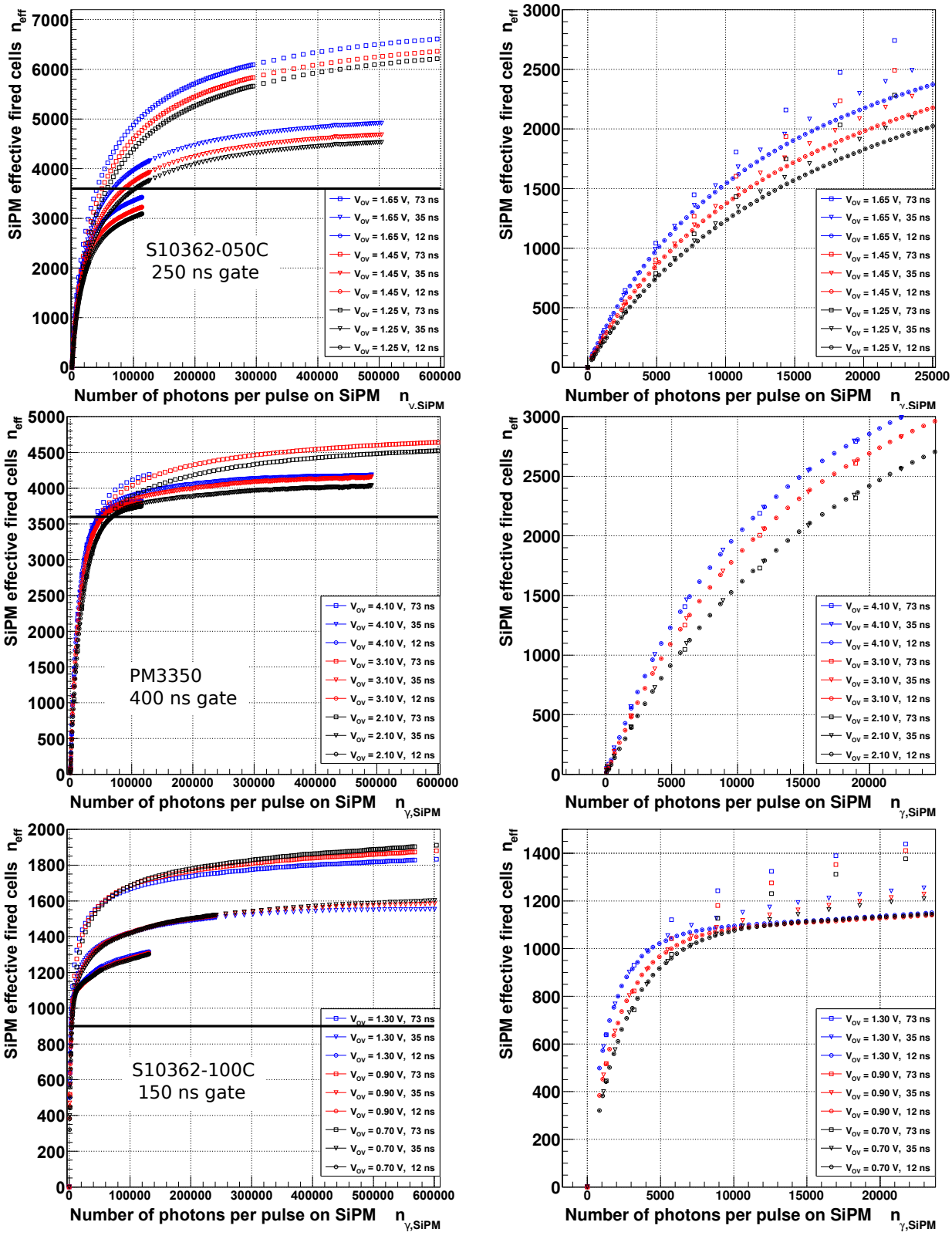

Figure 4.15.: *Effective fired cells* as a function of the number of photons per pulse on the active SiPM surface (full and zoom). Top: Hamamatsu S10362-050C type, 250 ns gate length. Middle: KETEK PM3350 type, 400 ns gate length (data points outside of QDC range not shown). Bottom: Hamamatsu S10362-0100C type, 150 ns gate length. The number of cells is indicated by the straight black line on the left hand side. All plots contain various over-voltages V_{OV} and values of t_{pulse}. The wider spacing of the data points at larger values of t_{pulse} is due to the constant step size of V_{LED}. A discussion of the observed features of all devices can be found in section 4.5.

4.5.1. The Calibration Method

The results obtained in the previous section provide already an experimental method to estimate the flux of incoming photons from the measured number of fired cells. That is, the parametrisation of the $n_{\gamma,\mathrm{PD}}$ *vs.* $n_{\gamma,\mathrm{SiPM}}$ dependence for a particular SiPM characterises the dynamic range and hence, the calorimetric performances of the device. We focus now on quantifying and parameterising the region of the data where the response of the SiPM in terms of n_{eff} is the same (within a chosen accuracy) regardless of t_{pulse}. Under this condition we approximate the number of fired cells and the number of photons impinging onto the detector by the following parametrisation:

$$n_{\mathrm{eff}}(n_{\gamma,\mathrm{SiPM}}) = n \cdot \left(1 - \exp\left(-\frac{n_{\gamma,\mathrm{SiPM}} \cdot k}{n}\right)\right) + C \tag{4.11}$$

Here, in the case of an ideal SiPM (without noise effects, zero cell recovery time, etc.) and an infinitely short light pulse, $n \equiv N^{\mathrm{cell}}$ would correspond to the total number of cells of the SiPM and k would correspond to the mean number of cells avalanching per photon impinging onto the SiPM [61, 58] and hence the PDE. Since a dark-noise correction has been performed (see section 4.4.3) the additional constant C should be compatible with zero.

Under real experimental conditions k (the PDE in the ideal case) will be overestimated due to the correlated noise effects and n will not match the expectations due to several reasons as discussed in section 4.5.2 and also depend on the range to which the fit of equation 4.11 is restricted, as described in the following. Additionally the proposed parametrisation can not represent the observed (see figure 4.15) non-saturation of the signal at the largest pulse widths, where recharging cells begin contributing again during the duration of the pulse. However the goal is to establish a common parametrisation for all pulse-widths including the shortest one. Equation 4.11 is expected to approximately (more on that later) describe the data from zero up to a maximum value of effective fired cells $n_{\mathrm{eff,cut}}$. The parametrisation becomes incompatible (i.e. the responses diverge by more than the chosen accuracy criterion, which is 5% in this work) with the experimental data if more points above this value are included in the fit.

How and which value of $n_{\mathrm{eff,cut}}$ is chosen as the end point for the fit depends on the specific purpose and accuracy for which the calibration is needed. Among others, a possible criterion is to require that the fit is only performed until the response at the largest pulse width does not diverge by more than a chosen degree of accuracy ϵ from the data points with the smallest pulse width. As an example we use the topmost plot in the left-hand side of figure 4.15. Here the curves with the smallest value of t_{pulse} end around 3000 fired cells. In contrast, at the same number of photons per pulse and at the largest value of t_{pulse} the number of fired cells reaches about 4700. To include data points up to this point the chosen degree of accuracy would need to be around 56%. As a more realistic example, we choose an accuracy of $\epsilon = 5\%$ and determine the value of $n_{\mathrm{eff,cut}}$ by linearly interpolating between the data points.

The black curves in figure 4.16 show the result of the fits to equation 4.11 for the three groups of $\mathrm{V_{OV}}$ as obtained for the Hamamatsu S10362-50C type. This result shows how,

for each over-voltage V_{OV}, data points for different settings of t_{pulse} overlap. For a single value of V_{OV} the fit is applied to all data points (including all measured t_{pulse} values) up to $n_{eff,cut} \approx 700 - 880$, where the 5% accuracy limit is exceeded. Increasing the range degrades the fit and hence, the quality of the $n_{eff} - n_{\gamma,SiPM}$ calibration.

The fits for the remaining Hamamatsu SiPM and the KETEK model are shown in figures 4.18 and 4.19, respectively. The values of $n_{eff,cut}$, together with the corresponding maximum number of hit cells $n_{\gamma,SiPM,cut}$, for all SiPM types and V_{OV} are summarised in table 4.4.

The value of $n_{eff,cut}$, which limits the fit range, actually depends not only on the accuracy criterion ϵ but also on the particular SiPM features (type, working conditions, etc.). This becomes evident when the fit is applied to the KETEK SiPM as shown in figure 4.19. While data points still satisfy the accuracy criterion, the parametrisation of equation (4.11) becomes increasingly worse as indicated by the large value of the constant C. The keep the parametrisation as simple as possible we use a different criterion and simply fix $n_{eff,cut}$ equal to a fraction of the nominal number of cells N^{cell}. Figure 4.20 shows the result for $n_{eff,cut} = 0.8 \times N^{cell}$.

We may interpret the fit results as "calibration curves" of the SiPM dynamic response despite the simple parametrisation proposed in equation 4.11. The method ensures an uncertainty better than a certain value fixed by the analysis (5% in this work) in the fitted range ($\leq n_{eff,cut}$). To better illustrate this idea, the inverse of equation 4.11 is plotted in figure 4.17 with the parameters n and k obtained from figure 4.16 at $V_{OV} = 1.65$ V for the Hamamatsu -50C SiPM. The solid line directly translates the measured number of n_{eff} to the actual number of photons impinging onto the SiPM. The dashed lines (blue) lines represent the uncertainty on the calibration curve arising from the quadratically combined relative uncertainties $\sigma_{rel} = \sqrt{\sigma_{rgeo}^2 + \sigma_{PIN}^2 + \sigma_\epsilon}^2 = 8\%$ on the geometrical correction factor ($\sigma_{rgeo} = 2.8\%$, see table 4.3), the calibration accuracy of the PIN-diode ($\sigma_{PIN} = 0.03/0.63 = 4.8\%$), the 5% criterion ($\sigma_\epsilon = 5\%$) and the non-zero constant C. Likewise, a "calibration curve" for the KETEK SiPM is shown in figure 4.21. For the KETEK SiPM the contributions are $\sigma_{rel} = \sqrt{(\sigma_{rgeo} = 3.1\%)^2 + \sigma_{PIN}^2 + \sigma_\epsilon}^2 = 8\%$ and for the Hamamatsu -100C SiPM $\sigma_{rel} = \sqrt{(\sigma_{rgeo} = 4.5\%)^2 + \sigma_{PIN}^2 + \sigma_\epsilon}^2 = 9\%$. We note that the only assumption made for these results is of a homogeneous spacing of the photons during the light pulse. The outcome of the fits for all over-voltages and the discussion of the results are reported in section 4.5.2.

4.5.2. Discussion

In general all three studied SiPMs show a similar behaviour. Initially, the number of *effective fired cells* rises with the number of photons impinging on the SiPM and the response of the sensor is homogeneous, regardless of the light pulse width (provided the same number of photons hit the SiPM). Equation 4.11, even though not exact, allows for a satisfactory parameterisation of $n_{\gamma,SiPM}$ as a function of n_{eff} as shown in figures 4.17, 4.18 and 4.20 and summarised in table 4.4. At higher light levels, the SiPMs responses deviate from each other, the output degrades and the SiPMs saturate.

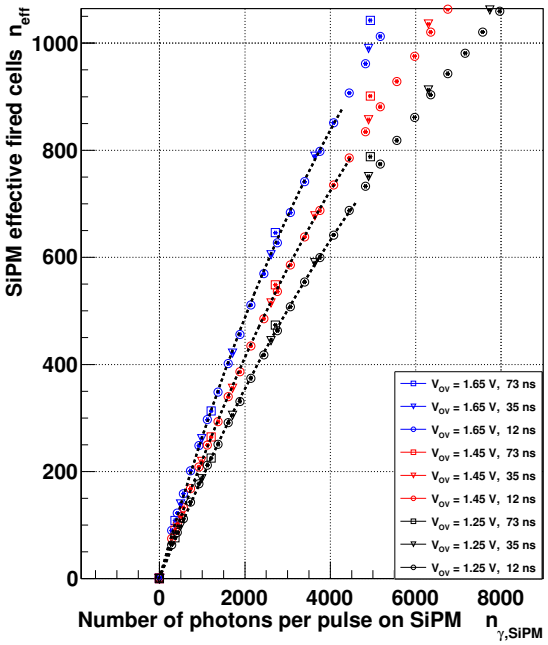

Figure 4.16.: *Effective fired cells* n_{eff} as a function of the number of photons per pulse on the active SiPM surface (**S10362-050C** type, 250 ns gate length). Equation 4.11 fitted to all values of t_{pulse} . Above $n_{\text{eff,cut}} \approx 800$ the results of the different settings of t_{pulse} start to deviate.

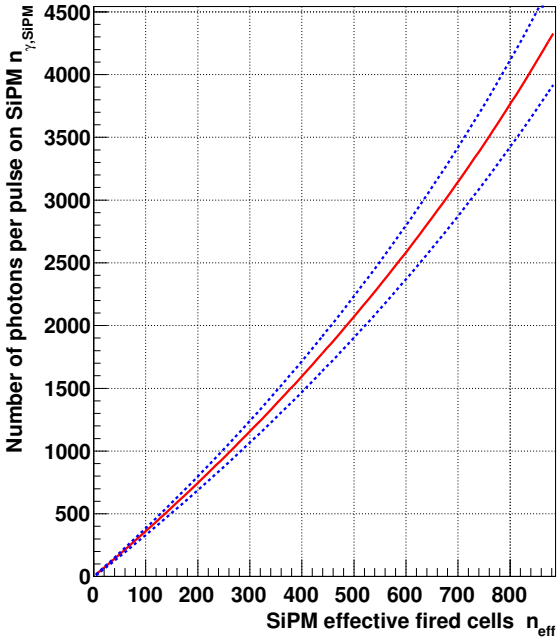

Figure 4.17.: Dynamic range calibration curve (**Hamamatsu S10362-050C** type, 250 ns gate length, $V_{OV} = 1.65$ V) The solid line corresponds to the inverse of equation 4.11 with the parameters from figure 4.16 (C is set to zero). The dashed (blue) lines represent the uncertainty on the calibration curve arising from the combined uncertainties on the geometrical correction factor, the calibration accuracy of the PIN-diode, the 5% criterion and the non-zero constant C. For a detailed breakdown of the contributions see section 4.5.1.

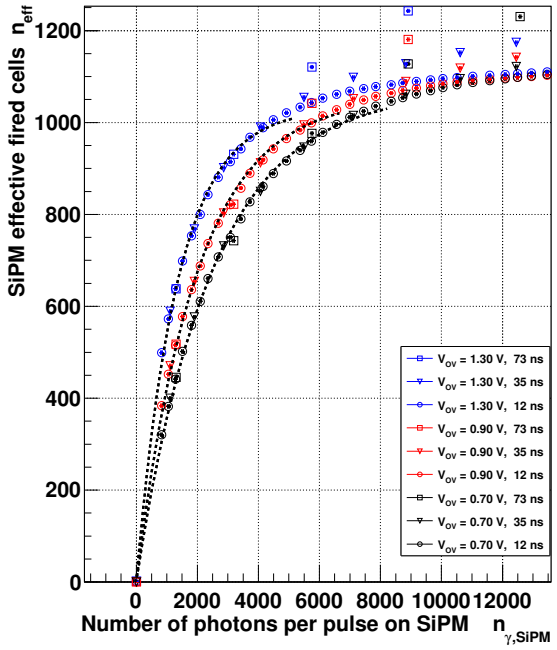

Figure 4.18.: *Effective fired cells* n_{eff} as a function of the number of photons per pulse on the active SiPM surface (**S10362-100C** type, 150 ns gate length).

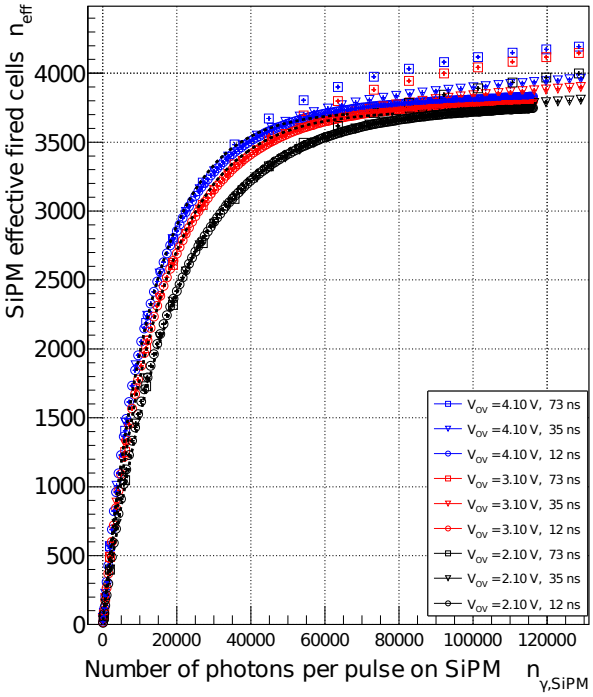

Figure 4.19.: *Effective fired cells* n_{eff} as a function of the number of photons per pulse on the active SiPM surface (**KETEK PM3350** type, 400 ns gate length).

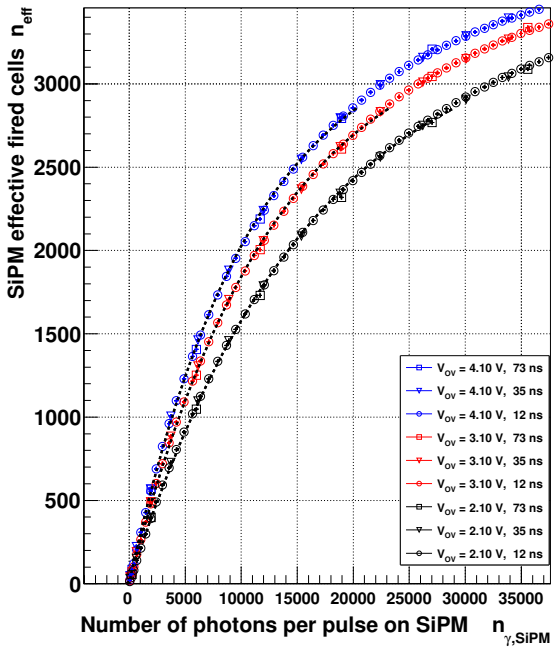

Figure 4.20.: Same as figure 4.19 with $n_{\text{eff,cut}} = 0.8 \times N^{\text{cell}}$ (**KETEK PM3350** type, 400 ns gate length).

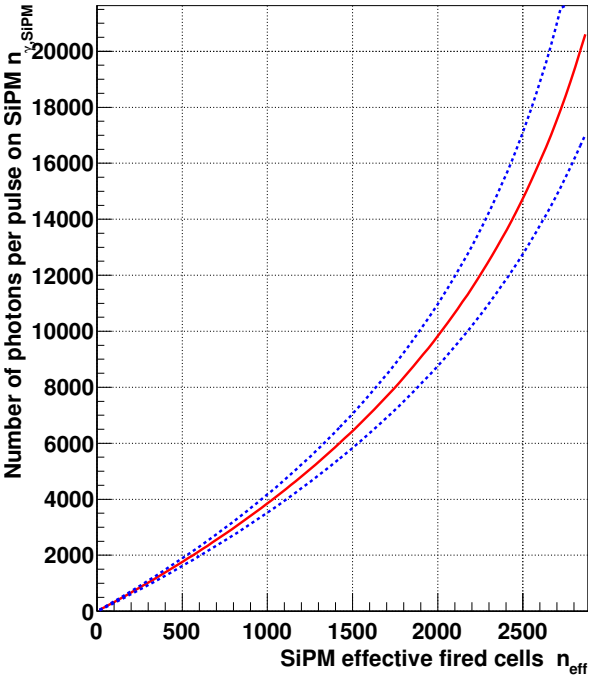

Figure 4.21.: Dynamic range calibration curve (**KETEK PM3350** type, 450 ns gate length, V_{OV} = 4.10 V) The solid line corresponds to the inverse of equation 4.11 with the parameters from figure 4.20 (C is set to zero). The dashed (blue) lines represent the uncertainty on the calibration curve arising from the combined uncertainties on the geometrical correction factor, the calibration accuracy of the PIN-diode, the 5% criterion and the non-zero constant C.

Table 4.4.: Summary of the parameters obtained from fitting equation 4.11 to the measured data up to $n_{\text{eff,cut}}$ and $t_{\text{pulse}} = 12$, 35 and 73 ns. The value of $n_{\text{eff,cut}}$ is chosen as the number of effective fired cells where the data points of the smallest and largest pulse widths start to deviate above a certain degree (5% here) for the same over-voltage.

V_{OV} (V)	$n_{\text{eff,cut}}$	$n_{\gamma,\text{SiPM,cut}}$	n	k	C
50 μm Hamamatsu - S10362-33-50C, $N^{\text{cell}} = 3600$					
1.25	710	4634	1640 ± 50	0.20 ± 0.01	1 ± 1
1.45	794	4510	1690 ± 50	0.24 ± 0.01	1 ± 2
1.65	887	4313	1740 ± 50	0.28 ± 0.01	2 ± 1
100 μm Hamamatsu - S10362-33-100C, $N^{\text{cell}} = 900$					
0.70	1044	8264	1066 ± 6	0.43 ± 0.01	2 ± 3
0.90	1031	6686	1054 ± 8	0.53 ± 0.02	2 ± 4
1.30	1029	5213	1030 ± 6	0.76 ± 0.02	2 ± 4
50 μm KETEK SiPM - PM3350, $N^{\text{cell}} = 3600$					
2.10	3739	109252	3707 ± 6	0.19 ± 0.01	21 ± 5
3.10	3734	79046	3710 ± 7	0.24 ± 0.01	18 ± 5
4.10	3738	66681	3710 ± 9	0.28 ± 0.01	20 ± 6
50 μm KETEK SiPM - PM3350, $n_{\text{eff,cut}} = 0.8 \times N^{\text{cell}}$, $N^{\text{cell}} = 3600$					
2.10	2880	29012	3425 ± 13	0.21 ± 0.01	2 ± 2
3.10	2880	23254	3422 ± 14	0.26 ± 0.01	3 ± 2
4.10	2880	20377	3386 ± 16	0.31 ± 0.01	4 ± 3

There is however, a difference in the response of the -050C Hamamatsu type in comparison to the -100C and KETEK types as shown in figure 4.15. The -050C Hamamatsu type shows a much earlier divergence of its response compared to the -100C and KETEK types. This is readily apparent from the small values of $n_{\text{eff,cut}}$ as compared to the total number of cells. Several reasons may explain this behaviour. On the one hand, with around 20 ns the recovery time of the -050C type is much smaller in comparison with the recovery time of 48 ns and 83 ns of the -100C and KETEK SiPMs, respectively [88] (c.f. table 4.2). On the other, the gain of the -100C and KETEK types is much higher [83, 84], which results in a higher voltage drop at the 10 kΩ series resistor (c.f. 4.5) in the readout circuit. In turn, this results in an effectively reduced over-voltage for the SiPM when many cells fire synchronously, slightly enlarging the dynamic range.

The effect of smaller recovery time of the Hamamatsu -050C in comparison to the KETEK SiPM with the same cell size is also visible in the regime of extreme saturation at the largest pulse width of 73 ns. Here, the output of the Hamamatsu SiPM keeps increasing even at a very high number of photons, in the end reaching nearly 6800 effective fired cells. The response of the KETEK SiPM also keeps increasing but at a much slower rate and in the end reaching a lower number of fired cells. This also leads to the larger spread in the responses to the 35 ns and 73 ns pulses.

Another difference in the response of the different types is visible at the shortest pulse length. Here the two 50 μm cell size SiPMs saturate roughly around their nominal

number of cells. The Hamamatsu -100C on the other hand saturates at around 1300 effective fired cells, well above the nominal value.

While the number of photons per cell is effectively four times larger due to the larger cell size this alone cannot explain the difference. A contributing factor can be the larger after-pulsing and crosstalk probability for this SiPM (c.f. table 4.2). This however is unlikely to be the complete answer as the saturation value is only slightly smaller at the lowest over-voltage where the correlated noise is also lower. This behaviour of *over-saturation* was also observed in [90]. In that publication a laser with a very short pulse width of 32 ps was used to saturate the smaller 1x1 mm^2 versions of the Hamamatsu SiPMs studied in this work. In contrast to the work described in this chapter, the pulse amplitude was used in that work to reconstruct the number of fired cells instead of the integrated charge, making the method less susceptible to the effects of after-pulsing and crosstalk [90]. A quantitatively similar over-saturation behaviour to the Hamamatsu -100C was observed in that work, finally resulting in an output twice as high as a naïve expectation would suggest. In that publication the authors speculate that under conditions of a high number of photons per cell impinging in a short time interval (relative to the recovery time) several avalanches may be triggered in the SiPM resulting in a higher *effective gain*. The authors also note that the behaviour of SiPMs under these extreme conditions is currently not completely understood. We note that, in contrast to [90], we did not observe a similar behaviour in the Hamamatsu -050C type. A possible explanation could be the larger minimum pulse width in this work of 12 ns, which comes close to the recovery time of the -050C type. A detailed exploration of this issue however is beyond the scope of this work.

Despite these issues the underlying idea of the presented calibration method only requires that the response of the SiPM is homogeneous in a range of *effective fired cells* which can be specified by each particular analysis according to the desired accuracy level. This is the case for all studied SiPMs.

4.6. Summary and Conclusions

Nowadays, many applications using silicon photomultipliers in several fields of research need the largest possible dynamic range and a precise measurement of the incident photon flux (calorimeters for high energy physics, PET and SPECT facilities, Cherenkov and fluorescence light detection in Astroparticle physics experiments, etc.). The dynamic range of an SiPM is largely determined by three factors: the cell pitch, the cell recovery time and the inherent SiPM noise. If the number of simultaneously arriving incident photons (times the photon detection efficiency) is much smaller than the number of cells, as in the case of experiments exposed to very low light intensities, the linear response of the SiPM can be easily measured and parametrised. If the incident light flux increases, however, two or more photons can hit the same cell at the same instant (i.e. synchronously) or within the cell recovery time, before the output pulse of the first photon is completely restored. In the first case the cell outputs only one pulse, regardless of whether one or more photons enter the cell. In the second, the output

pulse will have an amplitude and shape that varies according to the charge state of the cell. As a consequence, in both events the SiPM linearity degrades. The third limiting factor comes obviously from the noise triggers caused by any source (thermal, cross-talk or after-pulses) which a) increase the number of "busy" cells and b) create fake signals which worsen the photon counting resolution.

Therefore, SiPMs with high number of cells per unit area, short cell recovery time and small noise will exhibit, in general, extended dynamic ranges. Devices in a wide range of cell sizes from 10 μm up to 100 μm can be found on the market. The time needed for 50 μm pitch cells to restore the full gain is typically of the order of 10 ns, increasing with the pitch size.

In this chapter we have presented an experimental approach to characterise the full dynamic range of an SiPM, i.e. the measurement of the effective number of fired cells as a function of the absolute number of incident photons per pulse on the SiPM surface. The main procedure and conclusions can be summarised as follows:

- Three SiPM models from Hamamatsu and KETEK companies were tested (table 4.1). They have the same active area (3×3 mm^2) but different cell pitches (50 and 100 μm). A number of preparatory measurements, later required by the dynamic range studies, were carried out to characterise the basic features of the sensors (section 4.3). The dark count rate, the cross-talk probability and the gain were calculated at several over-voltages, enabling the estimation of the charge per cell, a basic quantity to compute the effective number of fired cells n_{eff} from the total deposited charge (section 4.4.3). A cooling chamber ensures a stable temperature of the sensors during data taking around 0°C.

- The other fundamental quantity is the number of photons per pulse impinging on the active SiPM surface $n_{\gamma,\text{SiPM}}$. The experimental setup (section 4.2) allows to illuminate a fraction (using dedicated apertures) or the total active surface of the SiPMs while measuring the pulsed light flux with a calibrated photodiode, as well as to physically interchange their positions on the experimental arrangement. Following the method described in section 4.4.2, the combined information provided by a calibrated photodiode and the SiPM allows the estimation of $n_{\gamma,\text{SiPM}}$ with a few percent precision.

- To perform a more complete characterisation of the dynamic range behaviour, the study is carried out through an automated scanning of the three following parameters: the SiPM over-voltage, the intensity of the light pulse and its time duration t_{pulse} (section 4.4.1). Data at different over-voltages provides information at different SiPM gains and noise levels. Increasing smoothly the intensity of the light flux allows a precise scan from the single photon detection up to saturation. Finally, exposing the SiPMs to short and long pulses, compared to the typical cell recovery times, gives knowledge on their response in case several photons overlap in time before cells have fully recovered.

- Several conclusions can be drawn from the final dynamic range data (see for instance figure 4.16). For a fixed over-voltage, the relation between the number of

impinging photons on the SiPM surface $n_{\gamma,\mathrm{SiPM}}$ and the effective number of fired cells n_{eff} is a smooth increase the higher the amount of impinging photons. Discarding data close to saturation, i.e. with a very high number of "busy" cells, the dynamic range trend can be well reproduced by a simple three parameter exponential formula (equation 4.11). As expected, in this regime data from short and long pulses give an equivalent number of fired cells provided the same number of photons is delivered from the light source. As a consequence, a satisfactory result is obtained even when including all t_{pulse} points in a common fit. Moreover, increasing the over-voltage for a fixed value of $n_{\gamma,\mathrm{SiPM}}$ has the effect of increasing n_{eff}, as expected. These results confirm that the technique proposed in this chapter allows for the reconstruction of the number of photons hitting the SiPM surface and hence a caloric measurement.

- The one-to-one correspondence between $n_{\gamma,\mathrm{SiPM}}$ and n_{eff} regardless of t_{pulse} is broken at high light fluxes. As expected, data obtained with large values of t_{pulse} tend to diverge from small t_{pulse} data points when the cell occupancy rate is high. The precise starting point and the trend of this divergence will depend on several factors like the cell recovery time, the pulse shape or the noise rate, therefore they should be evaluated for each particular SiPM model.

- We have shown that the knowledge of the dynamic behaviour of the devices through the characterisation in the laboratory of the parameters in equation 4.11 allows to deduce the number of photons arriving on the detector from the measurement of the effective number of fired cells. Besides the explicit results obtained with the three particular models tested in this work, it is worth remarking that the proposed technique can be easily applied to any other scenario requiring different specific light pulse forms (i.e. not homogeneously spaced in time as in this work) or another type of SiPMs.

In the context of the upgrade of the Pierre Auger Observatory, described in the previous chapter, this method can be easily used to study the dynamic range of any proposed SiPM type to be used in the upgrade. The results can than be evaluated to see whether the sensor meets the requirement for the physics goals outlined in [55]. In the rest of this work we focus on the analysis of data measured at the Pierre Auger Observatory in its current form. The used method is described in the next chapter.

5. The Needlet Wavelet Analysis Method

5.1. Introduction

As described in chapter 2 the current distribution of measured arrival directions of UHECRs at the Pierre Auger Observatory is largely isotropic. Due to the high degree of isotropic noise a sophisticated analysis is required to filter out any possible deviations from a purely isotropic distribution which could give a hint on the origin and propagation processes of UHECRs. In this work we use a Wavelet based analysis. We make use of a spherical Wavelet, the Needlet [91], allowing a spatially resolved analysis, across a wide range of angular scales on spherical data of measured arrival directions. The Needlet was originally introduced to study the data of the cosmic-microwave background (CMB) [92, 93]. The Needlet analysis may be viewed as a filter which enhances existing global and localised anisotropies of a given size. It is composed of multiple scales j, (i.e. filters) which are sensitive to angular structures of different sizes, ranging from large-scale to small-scale structures.
A detailed description of the derivation and properties of the Needlet can be found in [91]. We also point out previous publications which have proposed to use other kinds of Wavelets in the context of Auger data analysis [94, 95].

5.2. The Needlet Wavelet Analysis

In this work we continue the Needlet analysis method, originally developed in [96] in the context of analysing data measured at the Pierre Auger Observatory.

The general procedure of the analysis is to first represent the measured data on the sphere and then to expand the data into spherical harmonics. The expanded data is convoluted with the individual Needlet scales j and transformed back, resulting in a set of skymaps sensitive to structures of different angular extend. These skymaps are further processed to enhance possible deviations from isotropy across these angular scales. The result is an output skymap revealing features masked by noise in the original skymap. To illustrate this we show two Monte-Carlo (MC) input test skymaps on the top of figure 5.1. One skymap, on the left-hand side, contains an isotropic distribution as would be measured at the Auger Observatory with a maximum zenith angle of 60°. The other skymap contains a hidden dipole and a point source signature. These features and the generation of skymaps with such features are described the next chapter. The corresponding output skymaps, resulting from the Needlet analysis, are shown on the

bottom of figure 5.1. In the case of isotropy only a few insignificant random deviations from isotropy remain whereas the dipole signature and point source are clearly revealed. Based on these skymaps we define a global estimator of anisotropy to determine whether a given output skymap deviates from the isotropic expectation as illustrated in figure 5.11 as explained in later in this chapter.

In the following we describe the Needlet Wavelet and the analysis method, as developed in [96], in detail, using the two test skymaps shown on the top of figure 5.1 as an example.

5.2.1. Spherical Harmonics Expansion

In order to represent the data, i.e. the arrival directions in equatorial coordinates in declination δ and right ascension α, on the sphere and to expand it into spherical harmonics we use the the software package Healpix[1] [97] which was developed to analyse temperature fluctuations in the CMB. In the Healpix scheme the sphere is divided into k pixels or bins, each of equal area along constant latitudes allowing a fast transformation into spherical harmonics [97]. In all analyses in this work we use the Healpix parameter $N_{\text{side}} = 32$ which corresponds to a total of $N_{\text{pixels}} = 12,228$ pixels on the sphere. The choice of this and all further parameters is motivated in the following chapter. An example of two skymaps, binned in the Healpix representation, is shown on the top of figure 5.1.

The next step is the expansion of the data into spherical harmonics. In general any spherical function $f(\delta, \alpha)$ can be expanded in terms of spherical harmonics

$$f(\delta, \alpha) = \sum_{l \geq 0}^{\infty} \sum_{m=-l}^{m} a_{lm} Y_{lm}(\delta, \alpha), \tag{5.1}$$

representing the equivalent of Fourier transformation on the sphere. Here, a_{lm} are the multipole coefficients of the spherical harmonic functions $Y_{lm}(\delta, \alpha)$. A visualisation of the first three orders $l = 0, 1, 2$ of the spherical harmonic functions is shown in figure 5.2. The first order $l = 0$ corresponds to a monopole, i.e. a constant value over the whole sphere with its magnitude defined by the first spherical harmonic coefficient a_{00}. The next orders are the dipole ($l = 1$), the quadrupole ($l = 2$) and so on. The angular extend of structures described by a particular order in l are of extend $\propto 180°/l$ [52]. In general the index m goes from $-l$ to l. However in the case of real valued input functions coefficients with $m < 0$ are redundant and can be obtained via [99]:

$$a_{l-m} = (-1)^m a^*_{lm}. \tag{5.2}$$

In practice, the spherical harmonics expansion can only be performed up to a certain $l_{max} = 64$, in case of this work, which is motivated in the next chapter. The expansion of the Healpix representation of data into spherical harmonics is performed with the

[1] Hierarchical Equal Area isoLatitude Pixelization.

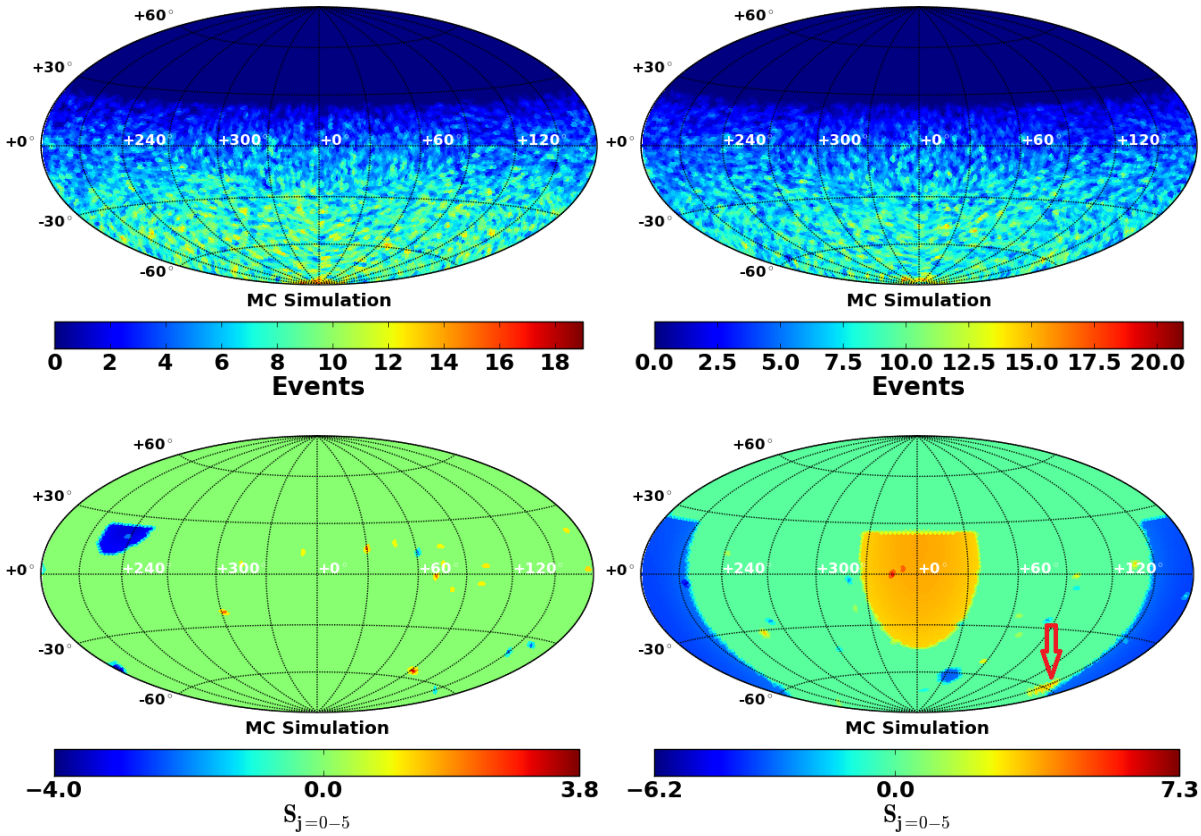

Figure 5.1.: All figures in this chapter are shown in equatorial coordinates (α, δ). **Top, Left:** Isotropic MC input test skymap with 50,000 events in total as seen by a detector with an Auger coverage and a maximum zenith angle of 60°.
Top, Right: Signal MC input test skymap with the same parameters as in the previous figure. Hidden in the skymap is a dipole signature with an amplitude of 3% centred around $(\alpha, \delta) = (0°, 0°)$ and a point source signature centred around $(\alpha, \delta) = (150°, -60°)$, which is marked via the red arrow.
Bottom, Left/Right: Resulting output skymaps after the Needlet analysis combining scales $j = 0 - 5$. In the case of an isotropic input skymap (left) only few fluctuations remain. In the case of a signal input skymap (right) the hidden dipole and the point source signature are revealed. To establish whether the resulting skymap deviates from isotropy the S-value (see equation 5.7) is used as illustrated in figure 5.11.

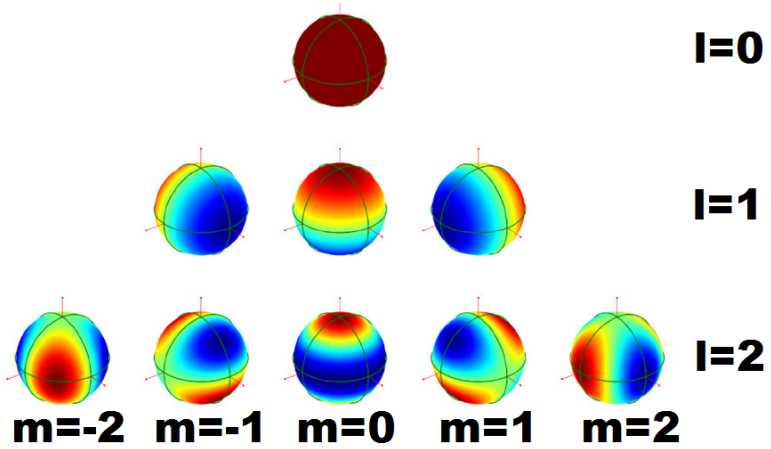

Figure 5.2.: Illustration of the spherical harmonics coefficients. From top to bottom $l = 0, 1, 2$ and from left to right $m = -2, -1, 0, 1, 2$ [98]. $l = 0$ represents the monopole scale, i.e. a constant value over the whole sphere. The dipole and quadrupole scale are given by $l = 1$ and $l = 2$, respectively.

program 'anafast' which is also part of Healpix.
Before the expansion, the skymap is weighted with the inverse of the relative exposure $1/\omega(\delta)$ (see equation 3.8). In contrast to the work in [96] we do not perform a monopole removing fit on the input skymap before expansion. In the performance studies, described in the next chapter, this step was observed to degrade the detection power and spatial reconstruction accuracy to large scale anisotropies.

5.2.2. The Needlet Wavelet

Wavelets were originally introduced within geophysics to decompose a time series into time-frequency space [100], unlike e.g. the Fourier decomposition which is only located in frequency space. There they are used to establish both the dominant modes, of e.g. weather patterns, of variability as well as their variation in time [100]. Such features are usually obscured by random noise requiring Wavelets analyses to be able to find patterns within the noise.

As described in the introduction, this analysis uses the Needlet Wavelet, a spherical Wavelet introduced by the CMB community to search for structures in the CMB background. It offers a variety of advantages generally not available in other spherical Wavelets. It is well defined in the spatial and in the harmonic domain and does not rely on the tangent plane approximation, i.e. the localised approximation of parts of the sphere as flat. We use the localisation in spatial space in section 8.3 of this work where we restrict the analysis to a portion of the sky. Likewise we use the localisation in harmonic space when we reconstruct the properties of the observed dipolar pattern in section 8.2. The Needlet is directly defined in harmonic space making it computationally

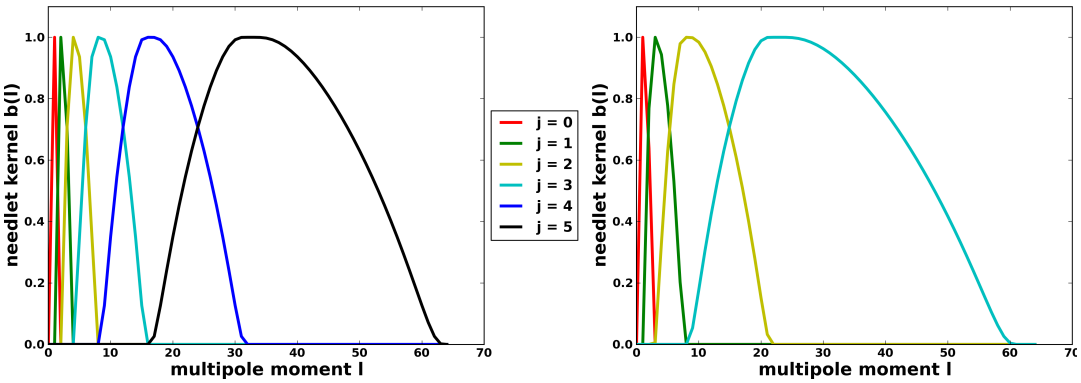

Figure 5.3.: Needlet kernel $b(l, B^{-j})$ as a function of the multipole moment l at different Needlet scales j. **Left:** Width parameter $B = 2.0$ (which is used in the following analyses), **Right:** $B = 2.8$. The range of multipole moments where $b(l)$ is non-zero ($j = 0 - 5$ for $B = 2.0$ and $j = 0 - 3$ for $B = 2.8$) is also summarised in table 5.1 and table 5.2. Needlet scales which are sensitive to $l > 64$ are not shown. The derivation of the Needlet kernel is described in [91].

very effective [91].

The Needlet analysis is based on two parameters: the Needlet scale j and the Needlet width parameter B. To illustrate this, we show the Needlet kernel $b(l, B^{-j})$, which essentially acts as a filter on the multipole moments l (see formula 5.3), in figure 5.3 at different j scales for two different width parameters B. The specific covered ranges in l are additionally given in tables 5.1 and 5.2. As one can see, the Needlet splits in different scales j, with only directly consecutive scales overlapping each other and the width of a given scale increasing with the width parameter. This introduces a small correlation between neighbouring Needlet scales. An additional correlation is introduced due to the incomplete sky coverage, however less so than for other Wavelet bases [91]. For a given B parameter, small Needlet scales are sensitive to large structures and vice versa. A one dimensional, spatial projection of the Needlet scales $j = 2$ and $j = 3$ is shown in figure 5.4 with a width of $B = 2.0$ on the left-hand and with $B = 2.8$ on the right-hand side. In this work a B parameter of 2.0 is used (as motivated in the next chapter) resulting in a total of 6 ($j = 0 - 5$) scales up to the used $l_{\max}$ as illustrated on the left-hand side of figure 5.3.

5.2.3. Convolution of Signal and Needlet

After the expansion into spherical harmonic coefficients a_{lm} the next step in the analysis is the convolution of the individual Needlet scales j with these coefficients.

To obtain these skymaps each of the Needlet scales j is convoluted with the a_{lm} coefficients. After a backwards transformation into pixel space the 'pixel power' β_{jk} of

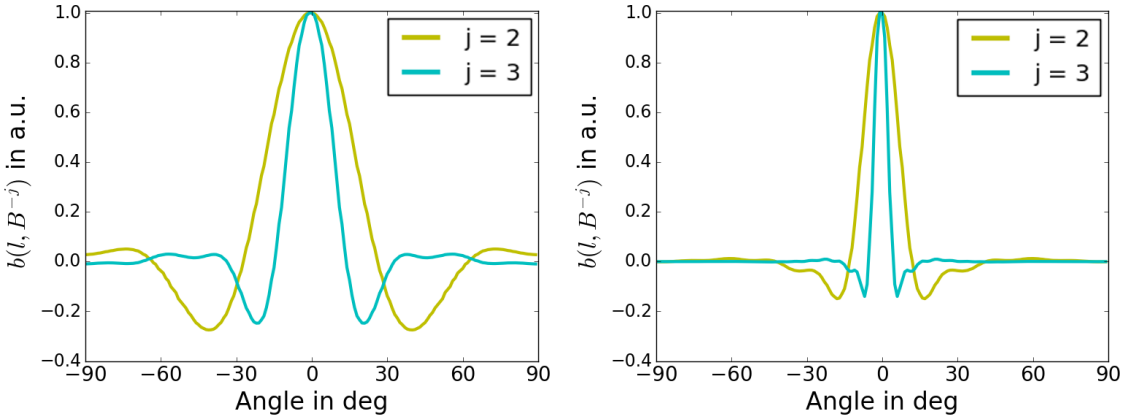

Figure 5.4.: Projection of the Needlet scale widths $j = 2$ and $j = 3$ with $B = 2.0$ on the left-hand side and with $B = 2.8$ on the right-hand side. For better visibility the individual Needlet scales have been scaled to share the same maximum $b(l, B^{-j})$ value.

Table 5.1.: Needlet range for Needlet width $B = 2.0$

Needlet scale j	Multipole moments l
0	1 (Dipole)
1	2-3
2	3-7
3	5-15
4	9-31
5	17-63

Table 5.2.: Needlet range for Needlet width $B = 2.8$

Needlet scale j	Multipole moments l
0	1-2
1	2-7
2	3-21
3	8-61

each pixel k in each Needlet scale j is given by [91]:

$$\beta_{jk}(\xi_k) = \sqrt{\lambda} \cdot \sum_{l=0}^{l_{\max}} b(l, B^{-j}) \sum_{m=-l}^{l} a_{lm} \cdot Y_{lm}(\xi_k). \tag{5.3}$$

Here, ξ_k denotes the coordinates of the pixel centre in the Healpix scheme and $\sqrt{\lambda}$ is a normalisation factor given by $\lambda = 1/N_{\text{pixels}}$. The resulting set of 'power' skymaps β_{jk} is shown in figure 5.5, in the case of the isotropic skymap as shown in figure 5.1 and in figure 5.6 in case of the signal skymap also shown in figure 5.1. As is expected from the properties of the Needlet, the structure sizes become smaller with larger j scales. Clear patterns however do not yet emerge, for these the power skymaps need to be processed further.

5.2.4. Normalisation and Threshold Cut

To reveal deviations from isotropy in the power skymap we proceed as described in the following. First, a large set of isotropic power skymaps with a given number of observed events is simulated as would be detected by an observatory with a given exposure. Second, from this set the mean pixel power $\langle\beta_{jk,iso}\rangle$ and the pixel power fluctuations $\sigma_{jk,iso}$ of each pixel k in each scale j are determined. In the case of a uniform sky exposure, the means and the variances would be identical for all pixels (in the limit of an infinite amount of events) within a given scale j. On the other hand, in the case of non uniform/incomplete exposure, they depend on the declination and/or right ascension. Third, each pixel power value is replaced by the (non-thresholded) pixel significance (as in [92])

$$S_{jk}^{NT} := \frac{|\beta_{jk} - \langle\beta_{jk,iso}\rangle|}{\sigma_{jk,iso}} \cdot \mathrm{sgn}(\beta_{jk}). \tag{5.4}$$

Additionally every pixel outside the exposure is assigned a value of zero. An example of this step is shown, again in case of an isotropic input skymap in figure 5.7 and in case of a signal input sky in figure 5.8. In comparison to the isotropic S_{jk}^{NT} skymaps the hidden dipole signature emerges in the $j = 0$ scale and the point source can be seen in the scale $j = 4$ (marked with a red arrow).

Fourth, to reduce the still remaining noise in the individual scales each pixel which satisfies

$$|S_{jk}| < T \tag{5.5}$$

is assigned a value of zero. The optimal value of the chosen threshold T depends on the statistics in the input skymap and also on the particular kind of anisotropic pattern the search is intended to observe. This is described in more detail in the next chapter. Unless otherwise noted, a threshold of $T = 3.0$ is used in this work. The resulting S_{jk} skymaps for both input skymaps are shown in figure 5.9 and in figure 5.10.

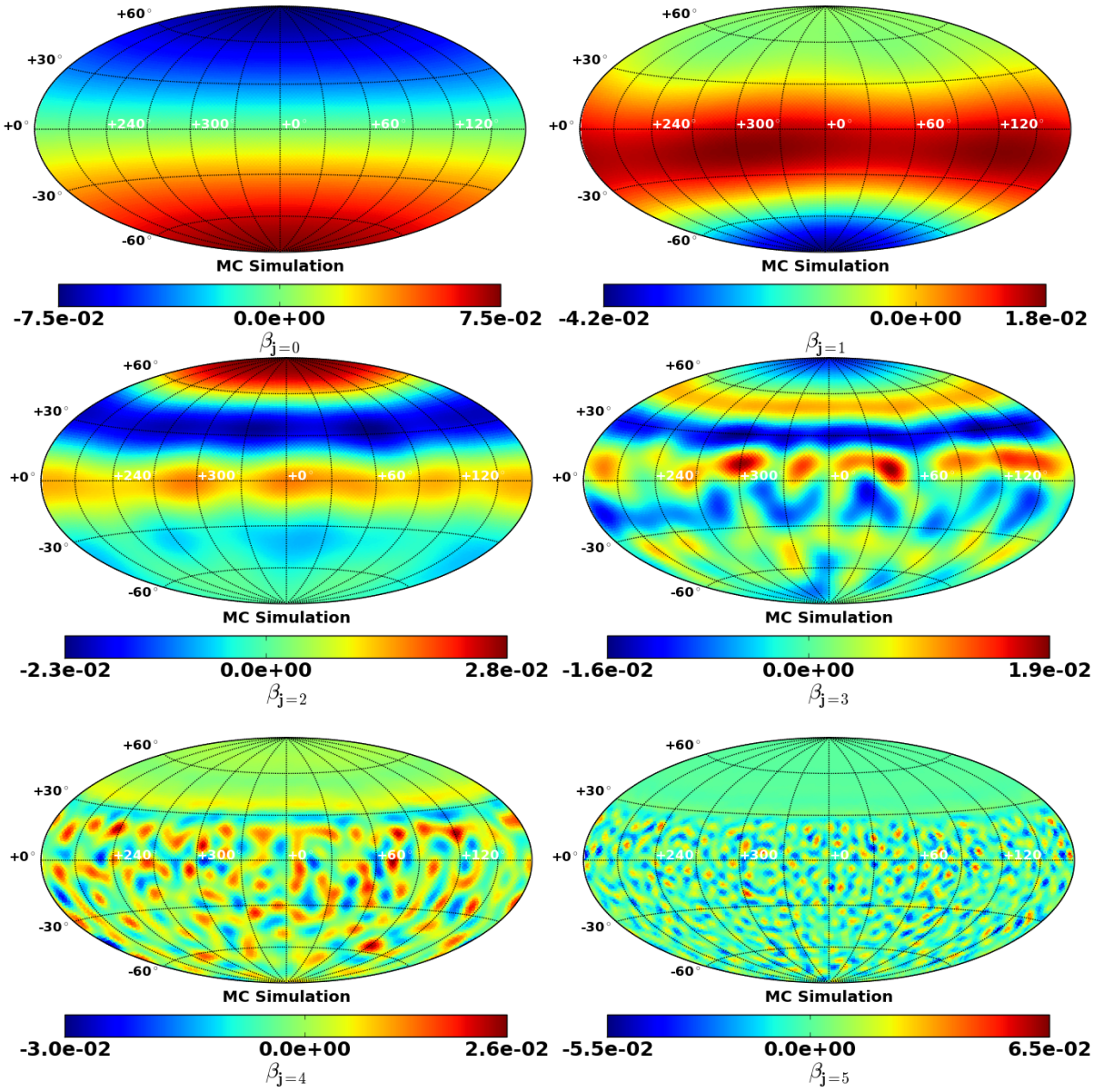

Figure 5.5.: Reconstructed pixel power skymaps β_{jk} in case of an isotropic input skymap with Auger coverage, as illustrated on the left-hand side of figure 5.1. From left to right and from top to bottom the Needlet scales are $j = 0, 1, 2, 3, 4, 5$. For better visibility of particular features all scales have their individual range.

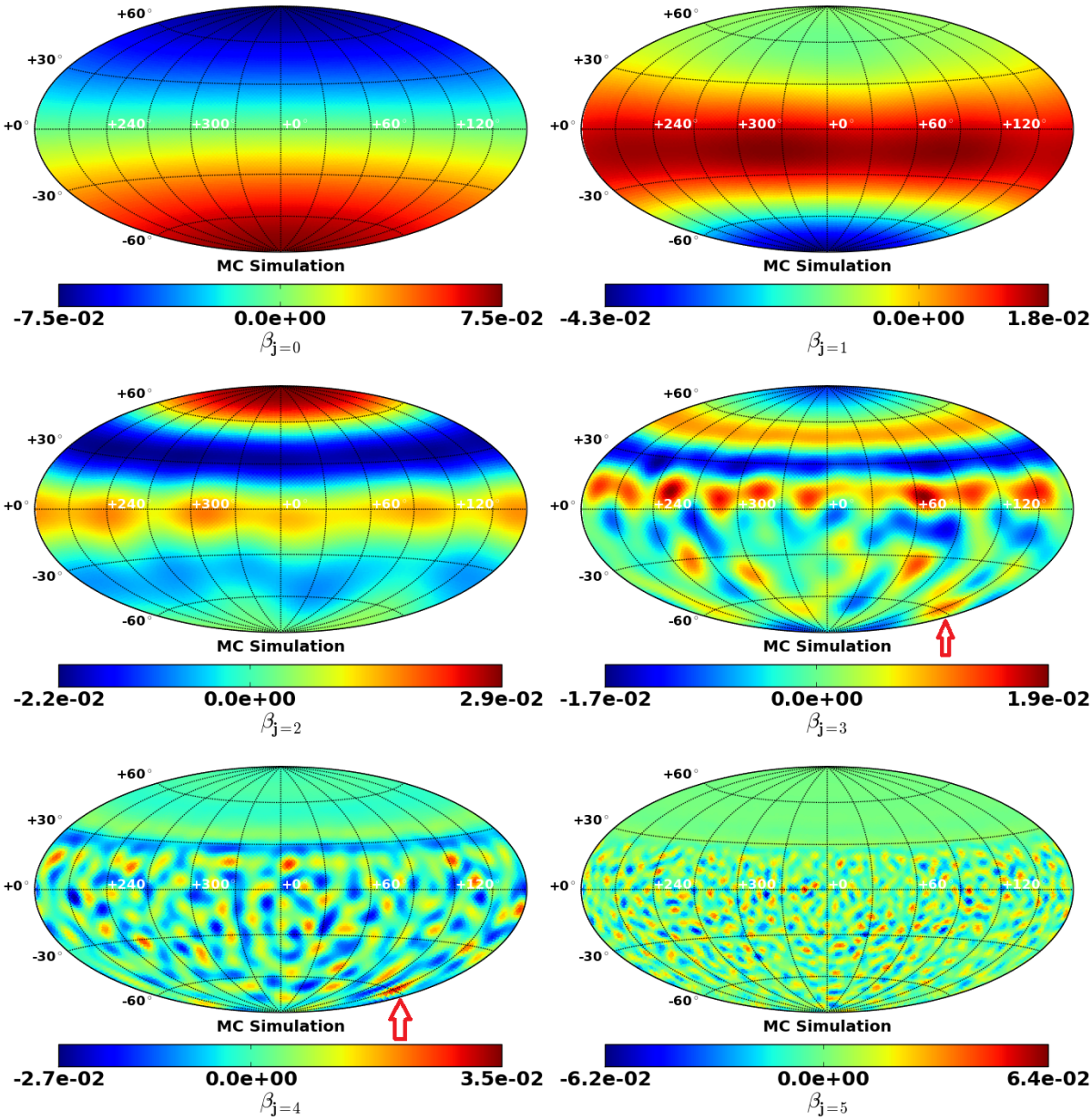

Figure 5.6.: Reconstructed pixel power skymaps β_{jk} in case of a signal input skymap with Auger coverage, as illustrated on the right-hand side of figure 5.1. In this step the hidden dipole signature does not appear yet, as it is obscured by the incomplete sky coverage. However the hidden point source can already be seen at the correct place $(\alpha, \delta) = (150°, -60°)$ in scales $j = 3, 4$ (marked with a red arrow) as these scales are less affected by the (large-scale) incomplete sky coverage. From left to right and from top to bottom the Needlet scales are $j = 0, 1, 2, 3, 4, 5$. For better visibility of particular features all scales have their individual range.

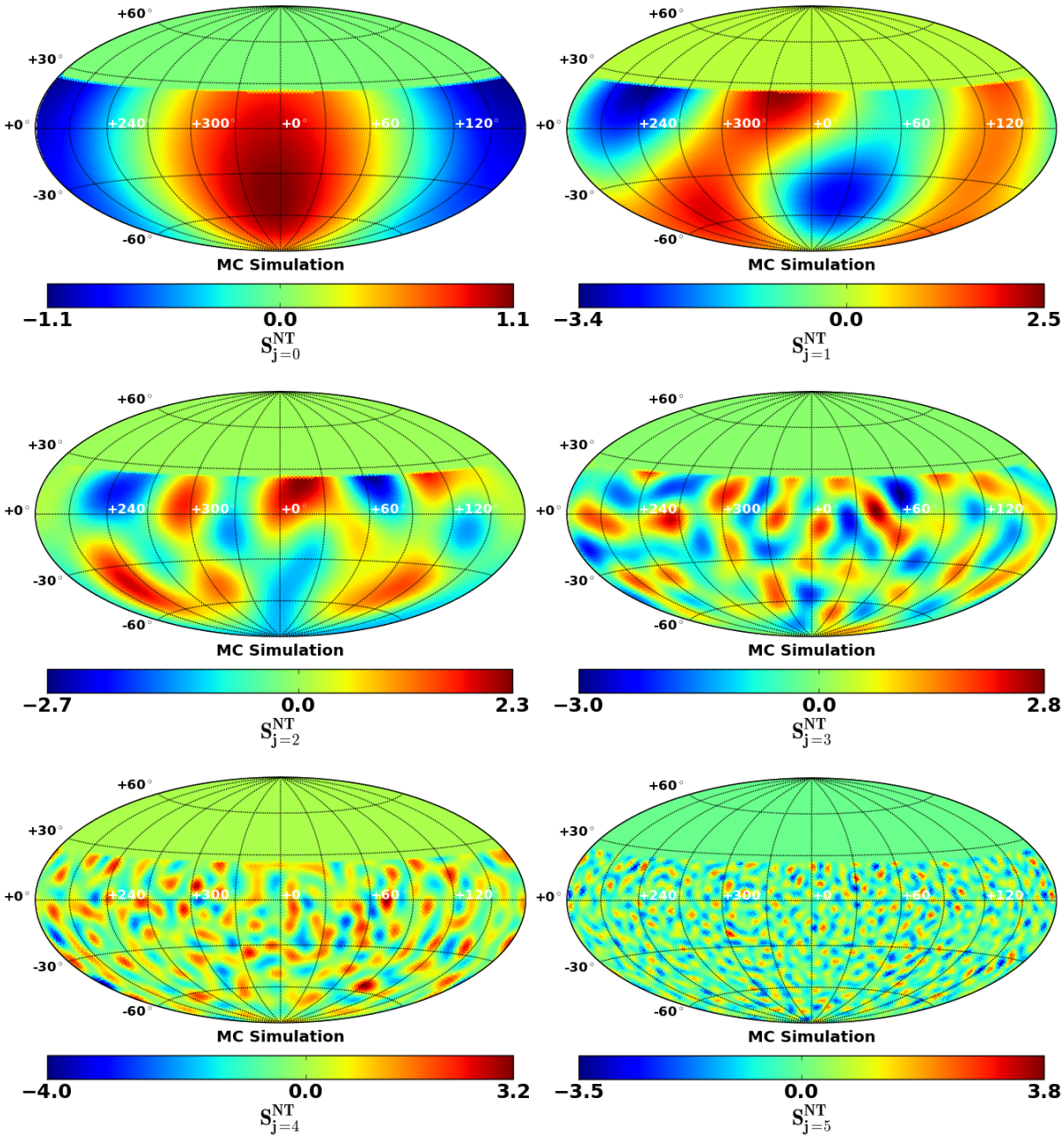

Figure 5.7.: Reconstructed but not thresholded skymaps S^{NT}_{jk} in case of an isotropic input skymap as illustrated in figure 5.1. From left to right and from top to bottom the Needlet scales are $j = 0, 1, 2, 3, 4, 5$. For better visibility of particular features all scales have their individual range (which differs between the isotropic and signal input skymaps).

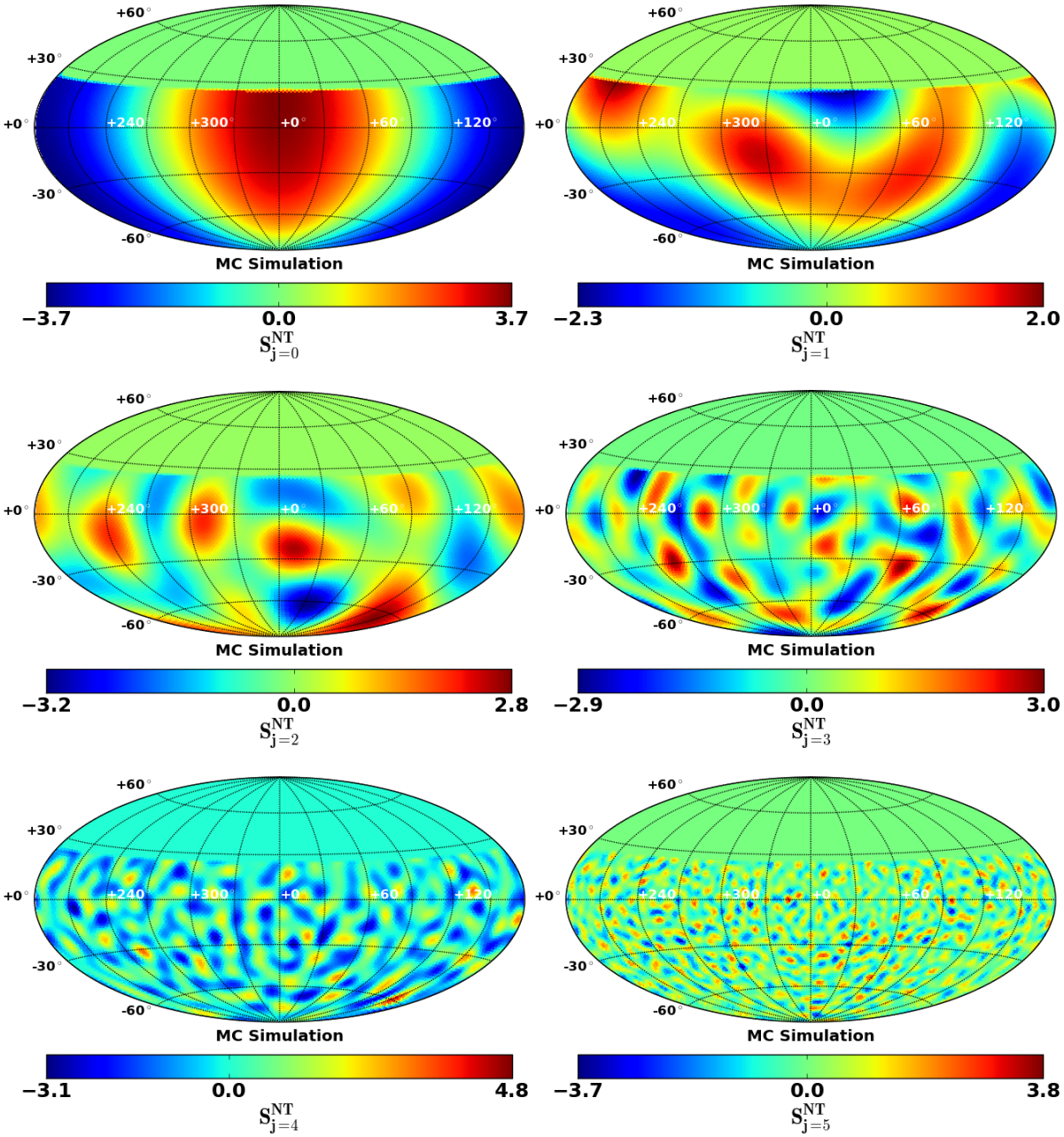

Figure 5.8.: Reconstructed but not thresholded skymaps S^{NT}_{jk} in case of a signal input skymap as illustrated in figure 5.1. In comparison to the isotropic case in the previous figure the appearance of the hidden dipole (in $j = 0$) and point source signature (in $j = 3, 4$) (see figure 5.1) can be seen. From left to right and from top to bottom the Needlet scales are $j = 0, 1, 2, 3, 4, 5$. For better visibility of particular features all scales have their individual range (which differs between the isotropic and signal input skymaps).

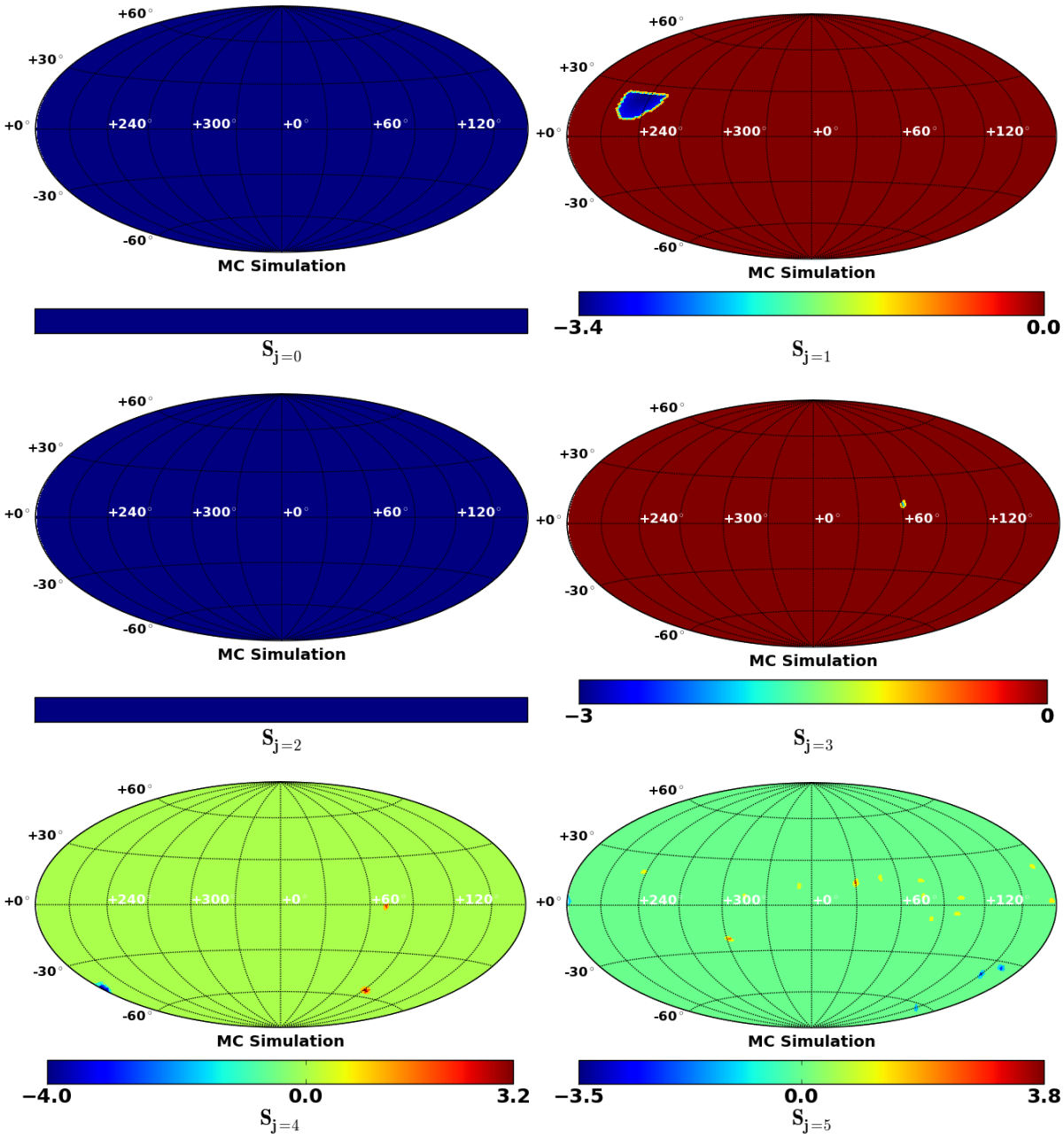

Figure 5.9.: Reconstructed and thresholded ($T = 3.0$) skymaps S_{jk} in case of an isotropic input skymap as illustrated in figure 5.1. In comparison to the signal case in the next figure only few fluctuations remain. From left to right and from top to bottom the Needlet scales are $j = 0, 1, 2, 3, 4, 5$. For better visibility of particular features all scales have their individual range.

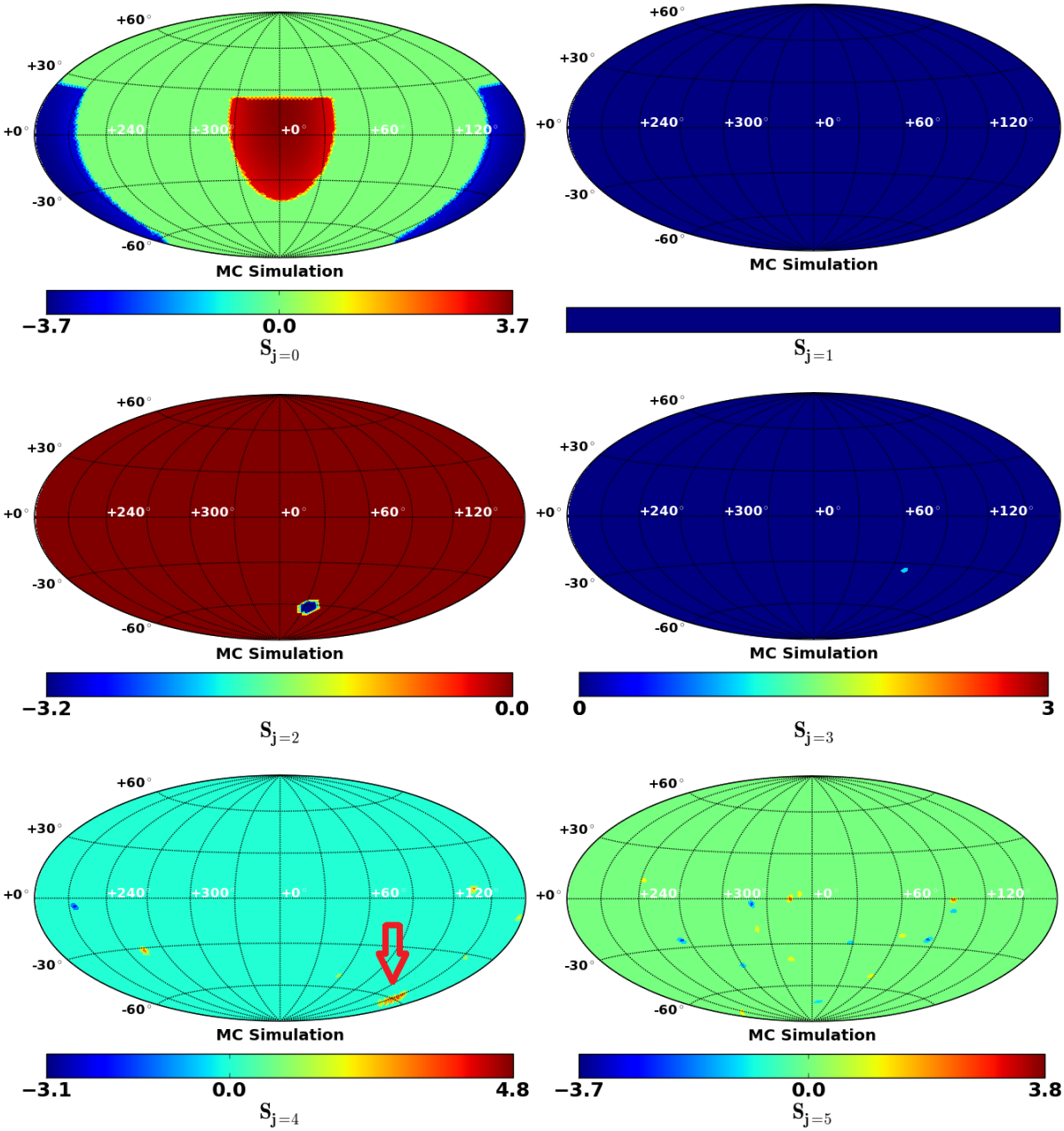

Figure 5.10.: Reconstructed and thresholded ($T = 3.0$) skymaps S_{jk} in case of a signal input skymap as illustrated in figure 5.1. In comparison to the isotropic case in the previous, not thresholded figure a clearer appearance of the hidden dipole (in $j = 0$) and point source signature (in $j = 4$, marked with a red arrow, see figure 5.1) can be seen. From left to right and from top to bottom the Needlet scales are $j = 0, 1, 2, 3, 4, 5$. For better visibility of particular features all scales have their individual range (which differs between the isotropic and signal input skymaps).

5.2.5. Combination of Skymaps and Anisotropy Search

Finally, a renormalised and thresholded combined skymap is created by summing up all scales j of interest

$$S_k = \sum_j S_{jk} \ . \tag{5.6}$$

Depending on the intended analysis one may only use one or two scales (e.g. $j = 0$ and $j = 1$ for large-scale structure search) or all scales which are sensitive up to a given multipole moment l for an undirected search for anisotropy, i.e. over all angular scales. If e.g. we sum up all scales from 0 to 5 we refer to this as considering the Needlet scales $j = 0 - 5$, if we analyse one or more scales by itself we specify this explicitly. Shown in the bottom of figure 5.1 are two examples of renormalised, thresholded and combined skymaps, with the corresponding input test skymaps shown at the top. The left skymap only contains isotropic noise and only a few fluctuations remain. In the case of the input skymap with the hidden dipole and point source signature both signatures are clearly reconstructed.

Finally, to determine the anisotropy level of a given combined, filtered and thresholded skymap S_k, we define the S-value anisotropy estimator (inspired from the contribution of Hülss in [101]):

$$S := \log \left(\frac{\sum_{k=1}^{N_{\text{pixels}}} |S_k|}{N_{\text{nonzero}}} \right), \quad N_{\text{nonzero}} > 0 \tag{5.7}$$

where N_{nonzero} is the number of pixels in the combined threshold skymap which are not zero.
The S-values of a large set of isotropic test skymaps are then combined to create a distribution of S-values as shown in figure 5.11. Now a given signal skymap which contains the same number of events and possesses the same exposure can be tested for anisotropy by evaluating its S-value in comparison to the isotropic reference $S-$value distribution at a given confidence level (C.L.) as illustrated in figure 5.11.

In case of this figure, 99% of 20,000 simulated isotropic skymaps have an S-value smaller or equal to 1.33 considering $j = 0-5$. In contrast the test input skymap shown at the right-hand side of figure 5.1 has an S-value of 1.58 making it incompatible with the expectation of an isotropic distribution at a C.L. of 99%.

In the case of analysing only one single j-scale, no pixel of a given skymap might pass the threshold introduced in equation (5.5). In this case a flat S-value distribution in skymaps not passing the cut is assumed.

In the next chapter we determine the optimal choice for the Needlet width B and the threshold T parameters, using MC simulations. We also compare the detection power of the Needlet method presented here with the performance of the also commonly used angular power spectrum.

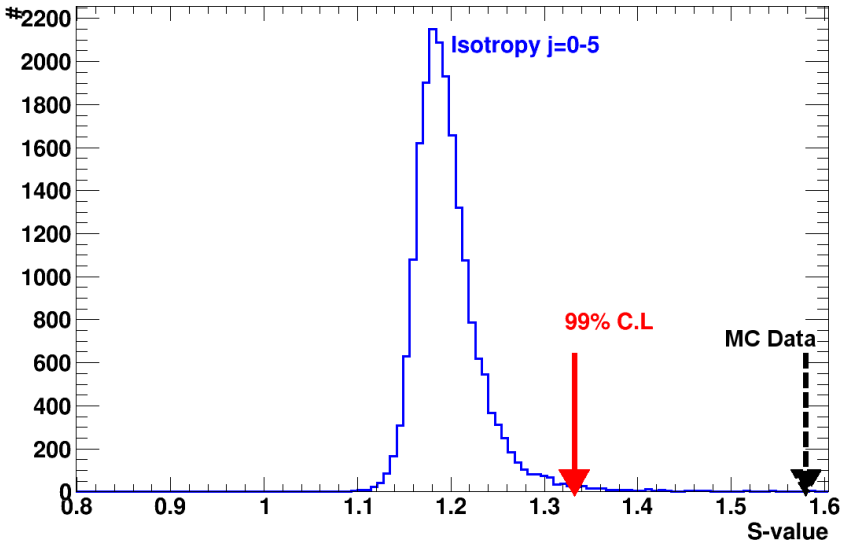

Figure 5.11.: S-value distribution of 20,000 simulated isotropic skymaps in blue (Auger coverage,$B = 2.0, T = 3.0$) and S-value of the MC signal test skymap (see right-hand side of figure 5.1 as indicated by the black, dotted arrow. The $S-$value at 99% of isotropic reference skymaps is indicated by the red, solid arrow.

6. Monte Carlo Benchmark Studies and Optimisations

6.1. Overview

The goal described in this chapter is to optimise the free parameters for the Needlet analysis introduced in the previous chapter. The parameters to be determined are the width B of the Needlet kernel, the applied threshold T, and the resolution of the binning in Healpix N_{side}. The chosen resolution determines the maximum multipole moment l_{max} up to which the spherical harmonics expansion is performed which also determines the maximum Needlet scale j_{max} included in the analysis. As the aim of the first analysis in this work is to perform an undirected search, i.e. a search for deviations from isotropy of any angular size, the goal is to find a set of parameters which provides a high sensitivity to various kinds of deviations from isotropy. To achieve this various Monte Carlo (MC) anisotropy scenarios, ranging from large to small scale anisotropies, are simulated and analysed with the Needlet analysis.

The description of the various scenarios can be found in section 6.3 as well as the corresponding results. A summary of the results as well as the choice for all parameters can be found in section 6.3.6. Finally the sensitivity of another method, the angular power spectrum (APS), also widely used to search for anisotropy in cosmic microwave background (CMB) and ultra-high energy cosmic rays (UHECR) experiments [102, 103, 104, 105, 106, 39, 37], is compared to the sensitivity of the Needlet analysis in section 6.4.

6.2. Resolution and Binning of the Data

In order to analyse the measured arrival directions of the Pierre Auger Observatory the data needs to be represented on the sphere. As described in the previous chapter, this work uses the widely used Healpix [97] distribution to bin the data on the sphere and expand the data into spherical harmonics. This extension can be performed up to an l_{max} corresponding to the angular resolution of the experiment. The analysis of Auger data, described in chapter 8, uses cosmic ray energies above the full efficiency of the surface detector, which is above 3 EeV for showers with a maximum zenith angle of 60° and above 4 EeV for showers with a zenith angle between 60° and 80°. In this range the angular resolution of the surface detector is in the order of $\sim 1.5°$ for events within an energy range of 3 EeV $<$ E $<$ 10 EeV and goes down to $\sim 1°$ for events E $>$ 10 EeV[54].

This corresponds roughly to an $l_{\max}$ of 128 and a corresponding Healpix parameter N_{side} of 64 resulting in 49,152 pixels on the sphere[1].

However, the expected deflection of even the highest energetic protons is around $\sim 3^o$ [107] through the galactic magnetic field (GMF) alone, according to the two most recent GMF models [108, 22], as described in section 2.4.1 (see also section 8.3).

Considering this minimum expected smearing of UHECRs and additionally aiming to increase the per-pixel statistics as well as to reduce the computing time, we choose the next lower N_{side} resolution of 32. This corresponds to 12,228 pixels on the sphere. The harmonic expansion is performed up to the corresponding $l_{max} = 64$ [109] $\sim 2.8^\circ$ pixel size.

With this choice of the resolution the remaining free parameters are the Needlet width B and the used threshold T. Their choice and the used MC scenarios are described in the following.

6.3. Benchmark Scenarios and Results

To find the optimal parameters for the Needlet width B and the threshold T we generate a variety of benchmark scenarios. We begin with the two most basic scenarios at both ends of the angular size, a dipolar and a quadrupolar anisotropy at the largest scales and a single point source at the smaller scales. Further scenarios include a catalogue based scenario, a skymap composed of a dipolar pattern combined with a single point source and a point source signature deflected through a model of the galactic magnetic field.

In the scenarios either the Needlet width B is fixed and the threshold T is varied or vice versa with their fixed values being identical to the previous work in [96] ($B = 2.0,\ T = 3.0$). The parameter B is varied between 1.6 and 3.0. Below these B values the Needlet is not defined and above the maximum number of available scales below $l_{\max} = 64$ is limited. The parameter T is varied from 0.1 to 3.5, both for signal and isotropic scenarios. A higher threshold significantly reduces the sensitivity to all anisotropic patters.

Different sets of events per skymap are simulated. Three different numbers of events are chosen, 7,000, 14,000 and 50,000, very roughly corresponding to the number of Auger events with a maximum zenith angle $\vartheta_{\max} = 60^\circ$ above an energy of 9, 6 and 3 EeV respectively. A summary of the parameters common to all benchmark scenarios is given in table 6.1. We choose a confidence level (C.L.) of 99.0% to classify whether a given test skymap differs from isotropy as illustrated in figure 5.11. Each isotropic reference distribution is composed of 20,000 skymaps and for each set of parameters in the scenarios 1,000 MC test skymaps are simulated. The detection efficiency is then given by the percentage of test skymaps that have a larger S-value (i.e. $S = 1.33$ for $B = 2.0$ and $T = 3.0$, see equation 5.7 and figure 5.11) than 99.0% of isotropic reference skymaps.

[1] $\text{N}_{\text{pixel}} = 12 * N_{\text{side}}^2$

Table 6.1.: Synoptic table containing the parameters common to all benchmark scenarios. The maximum Needlet scales $j_{\max}$ included in the analysis are listed in the same order as their corresponding B parameters.

Parameters	Values
Number of events per skymap	7000, 14,000, 50,000
Detector coverage	Auger (see eqn. 3.8), maximum zenith angle $\vartheta_{\max} = 60°$
Confidence level C.L. (%)	99.0
Isotropic reference skymaps	20,000
MC test skymaps	1,000
Fixed Needlet width B	$B = 2.0;\ T = 0.1;\ 0.5;\ 1.0;\ 0.1;\ 1.5;\ 2.0;\ 2.5;\ 3.0;\ 3.5$
Fixed threshold T	$T = 3.0;\ B = 1.6;\ 1.8;\ 2.0;\ 2.2;\ 2.4;\ 2.6;\ 2.8;\ 3.0$
Max. Needlet scale $j_{\max}$	7; 6; 5; 4; 3; 3; 3; 2
N_{side} used for MC generation	64
N_{side} used for MC analysis	32
$l_{\max}$ used for expansion	64

6.3.1. Dipole and Quadrupole Scenarios

Description

The first two possible large scale anisotropic patterns are the dipole and the quadrupole. A pure dipole contribution to an otherwise isotropic flux $\Phi(\mathbf{n})$ can be expressed as [33]:

$$\Phi(\mathbf{n}) = \frac{\Phi_0}{4\pi}\left(1 + r \cdot \mathbf{d} \cdot \mathbf{n}\right). \tag{6.1}$$

Here, $\Phi_0/(4\pi)$ is the average flux over the whole sphere, $\mathbf{n}$ is the unit direction, r is the amplitude of the dipole and $\mathbf{d}$ the unit vector in the direction of the dipole. The latter expressed in e. g. equatorial coordinates (α_d, δ_d) denotes the position of the maximum amplitude of the dipole. In the case of equation 6.1 the dipole amplitude r is given by the maximum anisotropy contrast:

$$r = \frac{\Phi_{\max} - \Phi_{\min}}{\Phi_{\max} + \Phi_{\min}}.$$

The dipole can also be expressed in spherical harmonics, in its corresponding multipole scale $l = 1$ [33]:

$$a_{10} = \frac{r}{\sqrt{3}} \cdot \sin(\delta_d) \cdot a_{00}\ ; \quad a_{11} = \sqrt{1/2 \cdot (r \cdot a_{00}^2/3.0 - a_{10}^2)} \cdot e^{i\alpha_d}\ ; \quad a_{1-1} = -1 \cdot a_{11}^* \tag{6.2}$$

The parameters used in this scenario are listed in table 6.2. An example of one resulting dipole probability distribution (PDF) over the whole sphere is shown on the left-hand side of figure 6.1. From this distribution events are drawn and either accepted or rejected according to the Auger coverage (see eqn. 3.8) until the desired number of

events is achieved. This procedure is common to all MC simulations and an example is shown on the right-hand side of figure 6.1.

The next large scale anisotropy is the quadrupole and can be viewed as an extension of eqn. 6.1 [33]:

$$\Phi(\mathbf{n}) = \frac{\Phi_0}{4\pi}\left(1 + r \cdot \mathbf{d} \cdot \mathbf{n} + \frac{1}{2}\sum Q_{ij} n_i n_j\right). \tag{6.3}$$

Here $\mathbf{Q}$ is a traceless and symmetric second order tensor. Its five independent components are determined from the $l = 2$ spherical harmonic moments $a_{2\mathrm{m}}$. A quadrupolar moment could be caused by an excess of cosmic rays along a plane [33]. In this scenario we set $a_{00} = 1$ and all other multipole moments, except a_{20}, to zero and vary the magnitude of a_{20} as summarized in table 6.3. These values expressed in galactic coordinates, as illustrated on the left hand side of figure 6.2, correspond to an excess along the galactic plane. The resulting PDF in equatorial coordinates is shown on the right-hand side of figure 6.2.

Table 6.2.: Synoptic table containing the parameters used in the simulations of the dipolar sky patterns.

Dipole Parameters	Values
Declination	$0°$, $-30°$ and $-60°$
Amplitude (%)	1.0; 3.0 and 5.0

Table 6.3.: Synoptic table containing the parameters used in the simulations of the quadrupolar sky patterns. The parameters (expressed in galactic coordinates) correspond to an excess along the galactic plane.

Quadrupole Parameters	Values
a_{00}	1
a_{20}	-0.010; -0.025; -0.050; -0.075; -0.100
a_{lm}	$0\ \forall\ (l,m)\ \notin\ [(0,0),(2,0)]$

Results and Discussion

The results of both, the dipole and the quadrupole scenarios are shown in figure 6.3. In the case of a fixed threshold T and a variable Needlet width B no clear trend emerges in the case of the dipole although a slight trend to a higher sensitivity can be seen for smaller values of B. This may be understood through the fact that for B values up to and including 2.0 the first Needlet scale $j = 0$ extends only over $l = 1$ and hence no additional noise overlaps the dipole signal in this scale. In the case of the quadrupole the two first B values, 1.6 and 1.8, give the highest sensitivity while the other B values cluster slightly below this sensitivity. Again, in this case, $j = 1$ consists only of $l = 2$

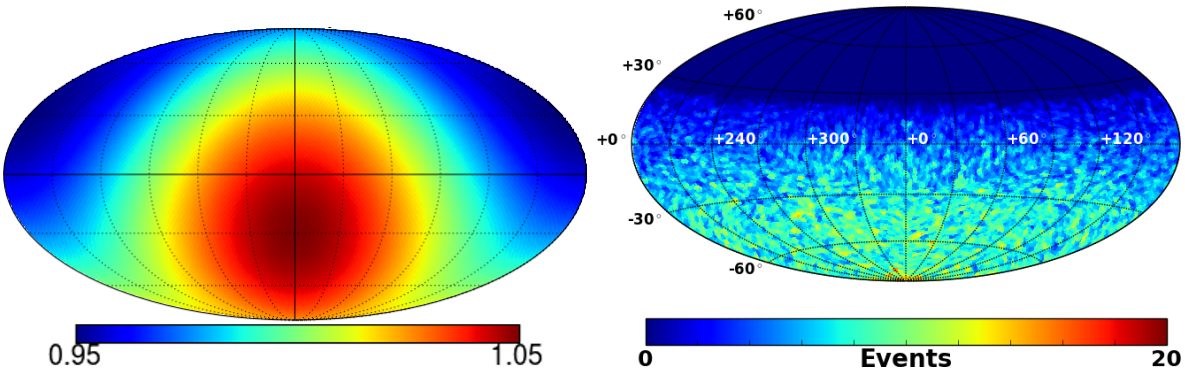

Figure 6.1.: Left: Dipole PDF with amplitude $r = 5.0\%$ at $(\alpha_d, \delta_d) = (0°, -30°)$ in equatorial coordinates. **Right:** Example of a test skymap with 50.000 input events and drawn from the figure on the left using the Auger coverage with a maximum zenith angle of 60°.

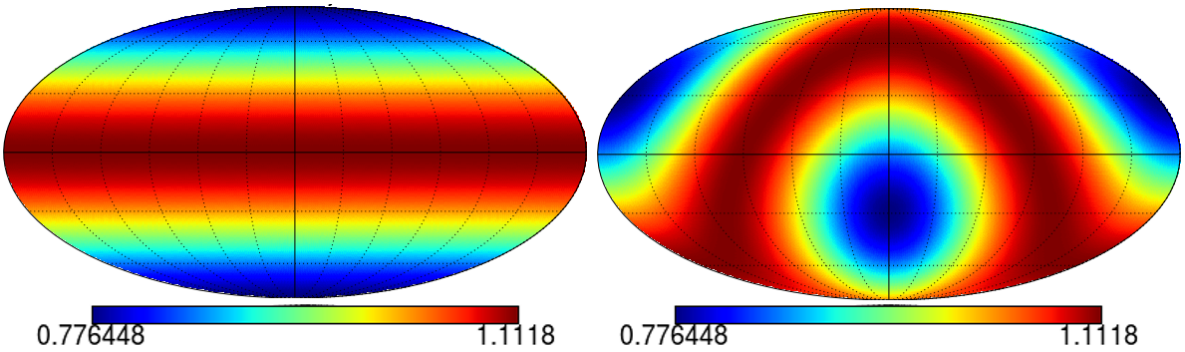

Figure 6.2.: Left: Quadrupole PDF in galactic coordinates with $a_{00} = 1$; $a_{20} = -0.01$ and $a_{lm} = 0$ for all other coefficients. A quadrupole with these parameters corresponds to an excess along the galactic plane. **Right:** The same quadrupole PDF transformed into equatorial coordinates.

for $B = 1.6$ and has only a minor contribution from $l = 3$ for $B = 1.8$.
At a fixed width B and a variable threshold T a clear trend emerges for both the, dipole and quadrupole scenarios. Above a minimum threshold around $T = 1.5$ to $T = 2.0$ an even higher threshold leads to a reduced sensitivity. How strongly the sensitivity is reduced depends on the number of events in the skymap. For 50,000 events only a threshold of $T = 3.5$ leads to a strong reduction. If only 7,000 events are present in the skymap even a threshold of $T = 2.5$ strongly reduces the sensitivity. Below this minimum threshold the results are comparable. This can be explained by the fact that, for these large scale anisotropies, the values of all pixels are highly correlated. Indeed, only the position of the dipole and its amplitude determine the properties of the dipole PDF. Hence when a significant dipole or quadrupole is present a large number of pixels will have a high significance in the corresponding j-scale. When the thresholded j-scales

are summed up a lower threshold will lead to more significant pixels in the resulting test skymap and hence will push the skymap above the chosen confidence level. This happens faster the lower the threshold is chosen as the noise from the other scales is suppressed relative to the many significant pixels from the dipolar or quadrupolar scale.

The sensitivity over the whole sphere to a 5.0% amplitude dipole anisotropy is shown in figure 6.4 with a total of 50,000 events and $B = 2.0$ and $T = 3.0$. As can be seen, the highest sensitivity is reached when only $j = 0$ is considered and the sensitivity is slightly reduced more and more for each additionally included Needlet scale. This is not surprising, as with $B = 2$ the Needlet scale $j = 0$ includes only the multipole scale $l = 1$, i.e. the dipole scale. The other Needlet scales contain only isotropic noise and hence add no further significance. The sensitivity is fairly symmetric in declination but a slightly higher sensitivity is achieved if the maximum of the dipole is located above $\approx 70^\circ$ in comparison to below $\approx -70^\circ$.

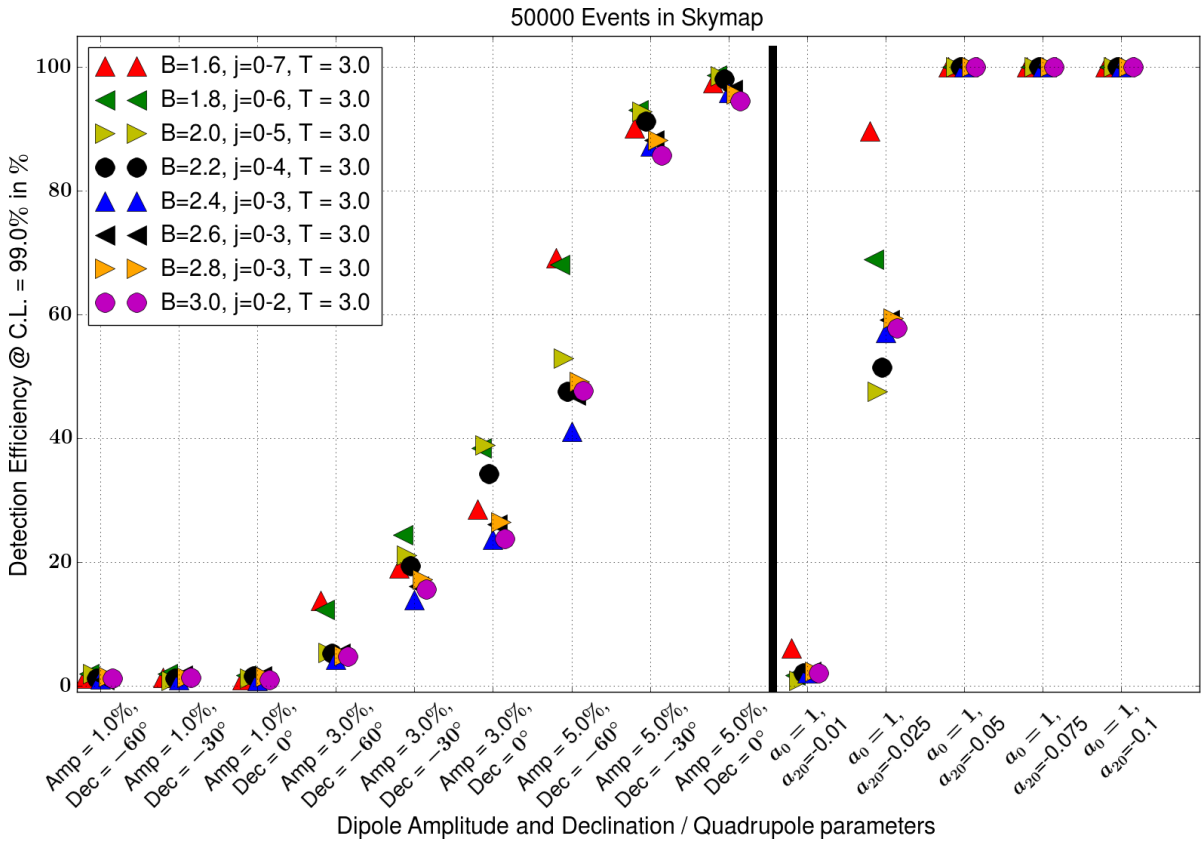
50000 Events in Skymap
B=1.6, j=0-7, T = 3.0
B=1.8, j=0-6, T = 3.0
B=2.0, j=0-5, T = 3.0
B=2.2, j=0-4, T = 3.0
B=2.4, j=0-3, T = 3.0
B=2.6, j=0-3, T = 3.0
B=2.8, j=0-3, T = 3.0
B=3.0, j=0-2, T = 3.0
Detection Efficiency @ C.L. = 99.0% in %
0
20
40
60
80
100
Amp = 1.0%, Dec = −60°
Amp = 1.0%, Dec = −30°
Amp = 1.0%, Dec = 0°
Amp = 3.0%, Dec = −60°
Amp = 3.0%, Dec = −30°
Amp = 3.0%, Dec = 0°
Amp = 5.0%, Dec = −60°
Amp = 5.0%, Dec = −30°
Amp = 5.0%, Dec = 0°
$a_0 = 1$, a_{20}=-0.01
$a_0 = 1$, a_{20}=-0.025
$a_0 = 1$, a_{20}=-0.05
$a_0 = 1$, a_{20}=-0.075
$a_0 = 1$, a_{20}=-0.1
Dipole Amplitude and Declination / Quadrupole parameters

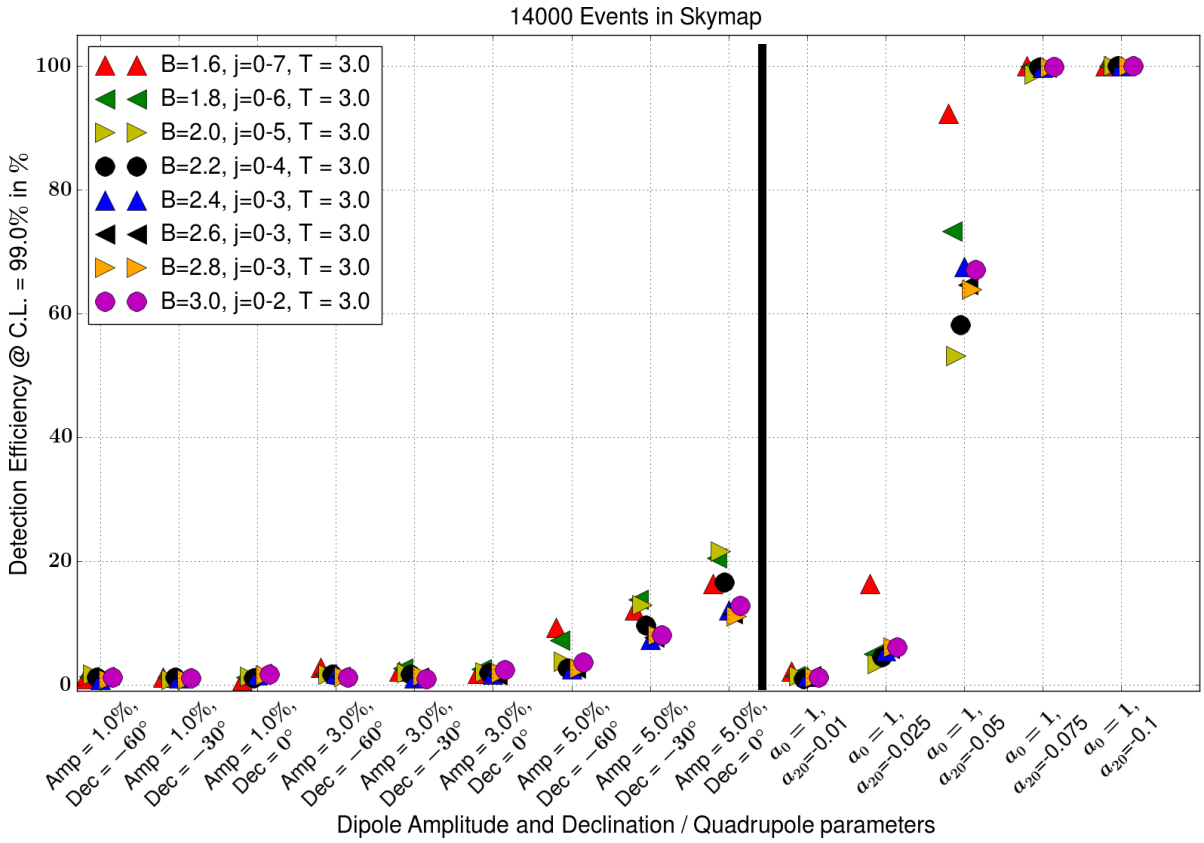
14000 Events in Skymap
B=1.6, j=0-7, T = 3.0
B=1.8, j=0-6, T = 3.0
B=2.0, j=0-5, T = 3.0
B=2.2, j=0-4, T = 3.0
B=2.4, j=0-3, T = 3.0
B=2.6, j=0-3, T = 3.0
B=2.8, j=0-3, T = 3.0
B=3.0, j=0-2, T = 3.0
Detection Efficiency @ C.L. = 99.0% in %
0
20
40
60
80
100
Amp = 1.0%, Dec = −60°
Amp = 1.0%, Dec = −30°
Amp = 1.0%, Dec = 0°
Amp = 3.0%, Dec = −60°
Amp = 3.0%, Dec = −30°
Amp = 3.0%, Dec = 0°
Amp = 5.0%, Dec = −60°
Amp = 5.0%, Dec = −30°
Amp = 5.0%, Dec = 0°
$a_0 = 1$, a_{20}=-0.01
$a_0 = 1$, a_{20}=-0.025
$a_0 = 1$, a_{20}=-0.05
$a_0 = 1$, a_{20}=-0.075
$a_0 = 1$, a_{20}=-0.1
Dipole Amplitude and Declination / Quadrupole parameters

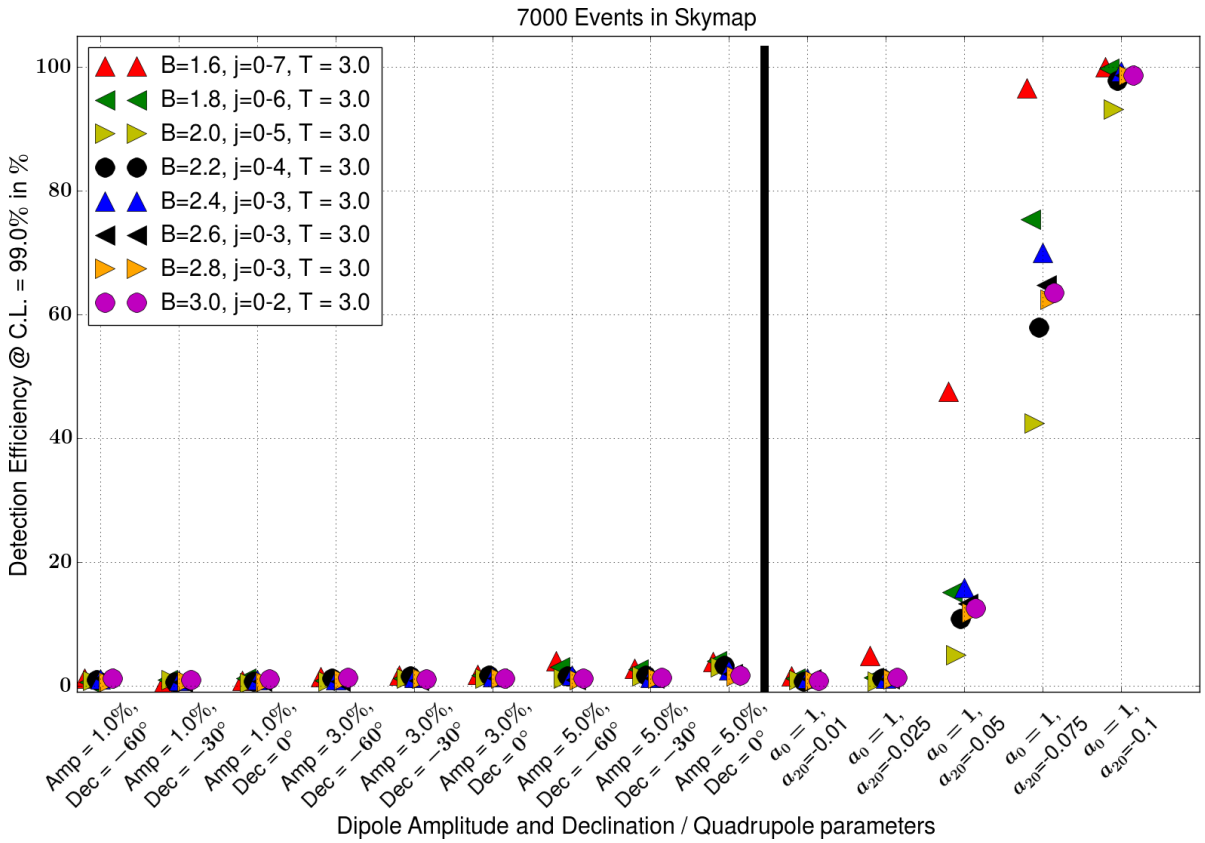
7000 Events in Skymap
B=1.6, j=0-7, T = 3.0
B=1.8, j=0-6, T = 3.0
B=2.0, j=0-5, T = 3.0
B=2.2, j=0-4, T = 3.0
B=2.4, j=0-3, T = 3.0
B=2.6, j=0-3, T = 3.0
B=2.8, j=0-3, T = 3.0
B=3.0, j=0-2, T = 3.0
Detection Efficiency @ C.L. = 99.0% in %
0
20
40
60
80
100
Amp = 1.0%, Dec = −60°
Amp = 1.0%, Dec = −30°
Amp = 1.0%, Dec = 0°
Amp = 3.0%, Dec = −60°
Amp = 3.0%, Dec = −30°
Amp = 3.0%, Dec = 0°
Amp = 5.0%, Dec = −60°
Amp = 5.0%, Dec = −30°
Amp = 5.0%, Dec = 0°
$a_0 = 1$, a_{20}=-0.01
$a_0 = 1$, a_{20}=-0.025
$a_0 = 1$, a_{20}=-0.05
$a_0 = 1$, a_{20}=-0.075
$a_0 = 1$, a_{20}=-0.1
Dipole Amplitude and Declination / Quadrupole parameters

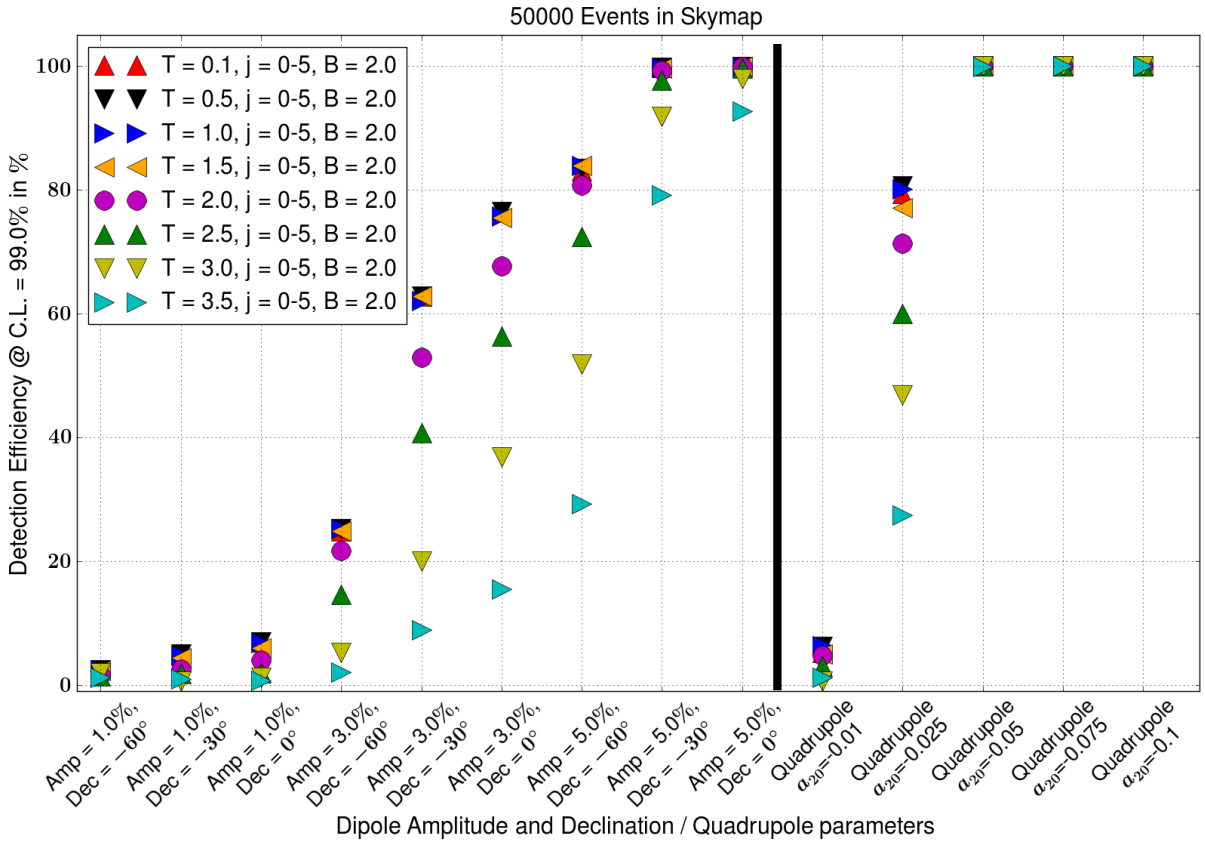
50000 Events in Skymap
T = 0.1, j = 0-5, B = 2.0
T = 0.5, j = 0-5, B = 2.0
T = 1.0, j = 0-5, B = 2.0
T = 1.5, j = 0-5, B = 2.0
T = 2.0, j = 0-5, B = 2.0
T = 2.5, j = 0-5, B = 2.0
T = 3.0, j = 0-5, B = 2.0
T = 3.5, j = 0-5, B = 2.0
Detection Efficiency @ C.L. = 99.0% in %
0
20
40
60
80
100
Amp = 1.0%, Dec = −60°
Amp = 1.0%, Dec = −30°
Amp = 1.0%, Dec = 0°
Amp = 3.0%, Dec = −60°
Amp = 3.0%, Dec = −30°
Amp = 3.0%, Dec = 0°
Amp = 5.0%, Dec = −60°
Amp = 5.0%, Dec = −30°
Amp = 5.0%, Dec = 0°
Quadrupole a_{20}=-0.01
Quadrupole a_{20}=-0.025
Quadrupole a_{20}=-0.05
Quadrupole a_{20}=-0.075
Quadrupole a_{20}=-0.1
Dipole Amplitude and Declination / Quadrupole parameters

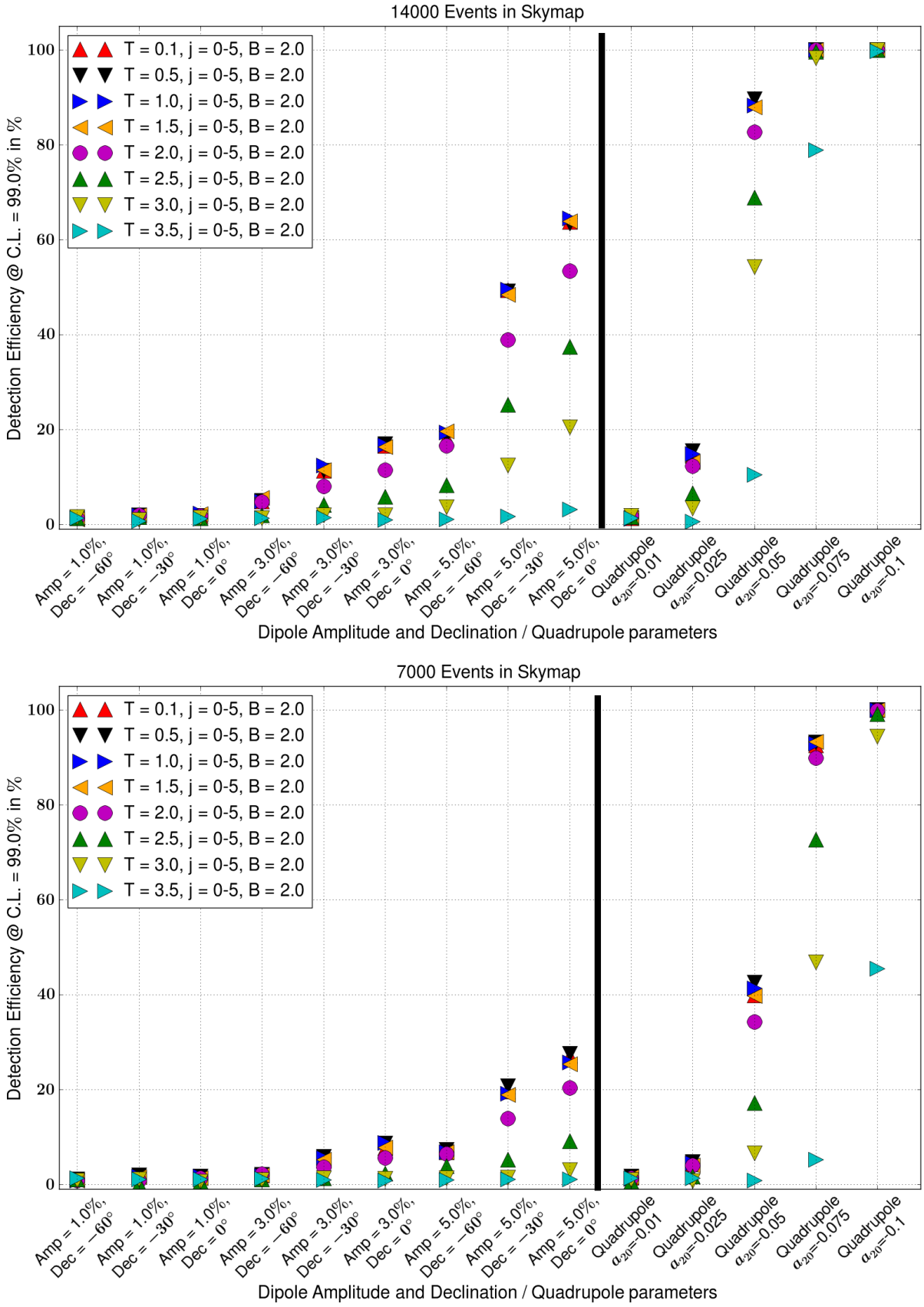

Figure 6.3.: Sensitivity to the dipole and quadrupole scenarios in section 6.3.1. **Top 3 figures:** Variable Needlet width B. **Bottom 3 figures:** Variable threshold T.

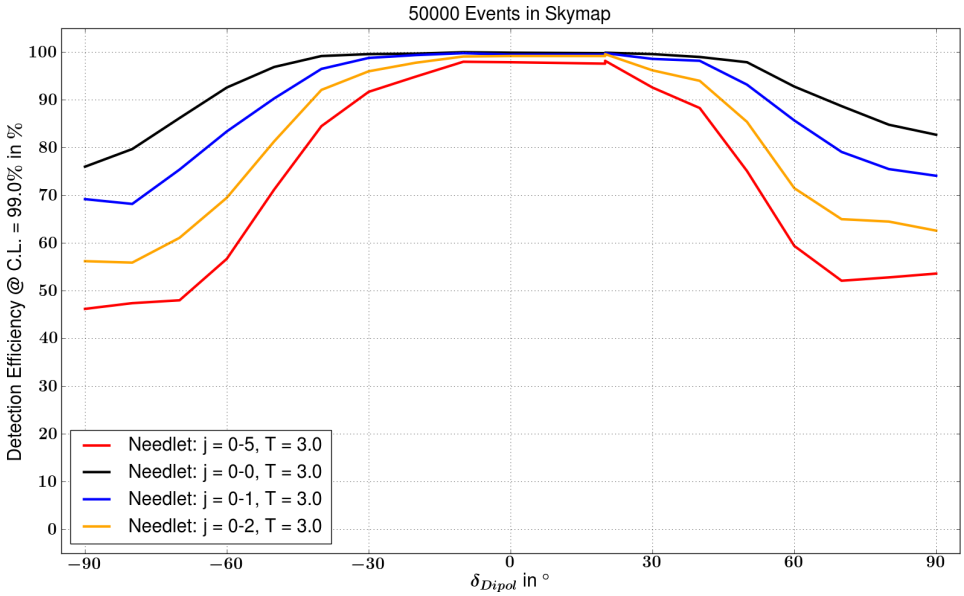

Figure 6.4.: Sensitivity to a dipole with 5% amplitude in a skymap with 50,000 events and $B = 2.0$. The different sensitivities, depending on the number of included Needlet scales $j_{\max}$, is also shown.

6.3.2. Single Point Source Scenario

Description

On the side of possible small scale anisotropies a single point source is the most basic one. Such an anisotropy could arise in the case of a single, strong cosmic ray source whose particles travel through a weak extra and intra galactic magnetic field ((E)GMF). Naturally the source itself is still a point source in the case of strong magnetic fields but through the deflections it would not necessarily appear that way at earth.

To generate the equivalent of a point source on the sphere we use the Mises-Fisher distribution [110]:

$$f(\mathbf{n}, \boldsymbol{\mu}, \kappa) = \frac{\kappa}{2(e^{\kappa} - e^{-\kappa})} \cdot \exp(\kappa \boldsymbol{\mu}^T \mathbf{n}). \tag{6.4}$$

Here $\mathbf{n}$ is the unit vector on the sphere, $\boldsymbol{\mu}$ the mean direction of the source and κ the concentration parameter which is a measure of how closely points are located on the sphere. In our case we use the approximation, of $\kappa = 1/\sigma^2$ where σ is the standard deviation of a 2D Gaussian. For a given source width σ we generate the PDF, overlay the PDF with the Auger exposure and draw the desired number of source events as is illustrated on the left-hand side of figure 6.5. The input skymap is generated by additionally adding isotropic noise (as seen by Auger) until the desired total number of events is reached, as can be seen on the right-hand side of figure 6.5.

Table 6.4 summarizes the set of parameters used, i.e, the point source direction, its angular width and the fraction of signal events of the total number of event in the skymap.

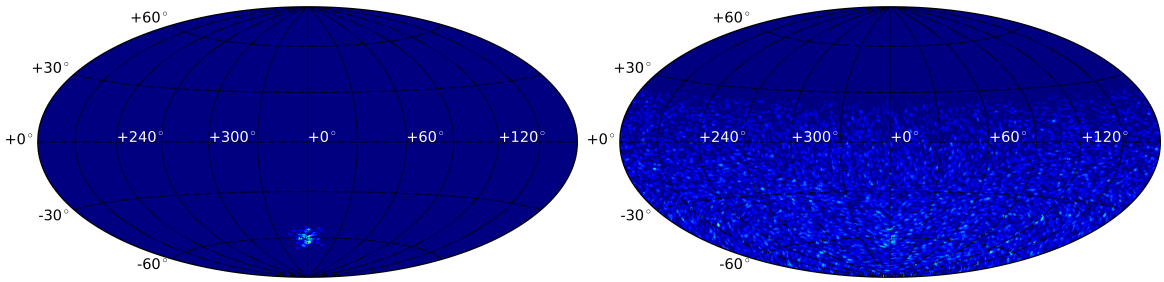

Figure 6.5.: Left: $14000 \cdot 0.5\% = 700$ source events drawn from a Mises-Fisher distribution with $\sigma = 3°$, located at $(\alpha, \delta) = (0°, -60°)$. **Right:** Test input skymap with the drawn source events plus isotropic noise (Auger coverage, 14,000 events in total).

Results and Discussion

The results of the single point source scenario are shown in figure 6.6. When the B value is varied no clear trend is visible but medium values between $B = 2.0$ and $B = 2.8$ generally achieve the highest sensitivity. If the threshold is varied a clear trend emerges. The higher the chosen threshold the higher the sensitivity. This is the opposite trend observed in the case of the dipolar and quadrupole scenarios making it clear that a

Table 6.4.: Parameters used in the point source scenario. The results from parameters marked with an $*$ can be found in appendix B

Point Source Parameters	Values
Point Source Directions	$(\alpha, \delta) = (0°, -60°)$ and $(\alpha, \delta) = (0°, 0°)^*$
FWHM $(2.35 \cdot \sigma)$	2°, 5°, 7°, 17°
Signal Fraction/%	0.02, 0.1, 0.5 and 1.0

trade-off between the sensitivity to large and small scale structures needs to be made in the search for anisotropies over all scales. The reason for this trend lies in the difference of how the chosen threshold affects small scale and large scale structures. As pointed out in the last discussion, large scale anisotropies affect the significance of all pixels in their respective j-scale and hence a lower threshold leads towards more significant pixels in the final sum of skymaps. The exact opposite is the case for small scale structures. Here a higher threshold filters out the remaining noise in the scale where the point source appears most prominent and amplifies the contribution of the significant pixels around the point source relative to the remaining noise.

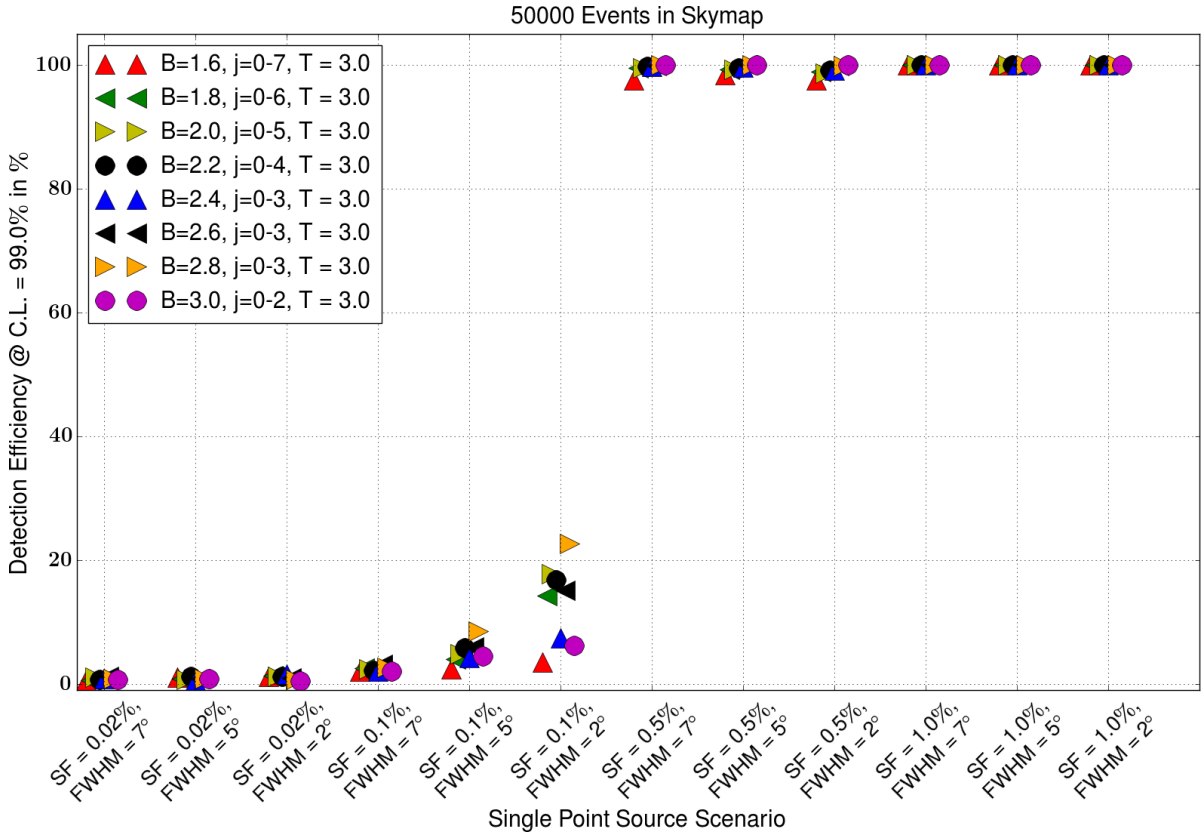
50000 Events in Skymap
B=1.6, j=0-7, T = 3.0
B=1.8, j=0-6, T = 3.0
B=2.0, j=0-5, T = 3.0
B=2.2, j=0-4, T = 3.0
B=2.4, j=0-3, T = 3.0
B=2.6, j=0-3, T = 3.0
B=2.8, j=0-3, T = 3.0
B=3.0, j=0-2, T = 3.0
Detection Efficiency @ C.L. = 99.0% in %
0
20
40
60
80
100
SF = 0.02%, FWHM = 7°
SF = 0.02%, FWHM = 5°
SF = 0.02%, FWHM = 2°
SF = 0.1%, FWHM = 7°
SF = 0.1%, FWHM = 5°
SF = 0.1%, FWHM = 2°
SF = 0.5%, FWHM = 7°
SF = 0.5%, FWHM = 5°
SF = 0.5%, FWHM = 2°
SF = 1.0%, FWHM = 7°
SF = 1.0%, FWHM = 5°
SF = 1.0%, FWHM = 2°
Single Point Source Scenario

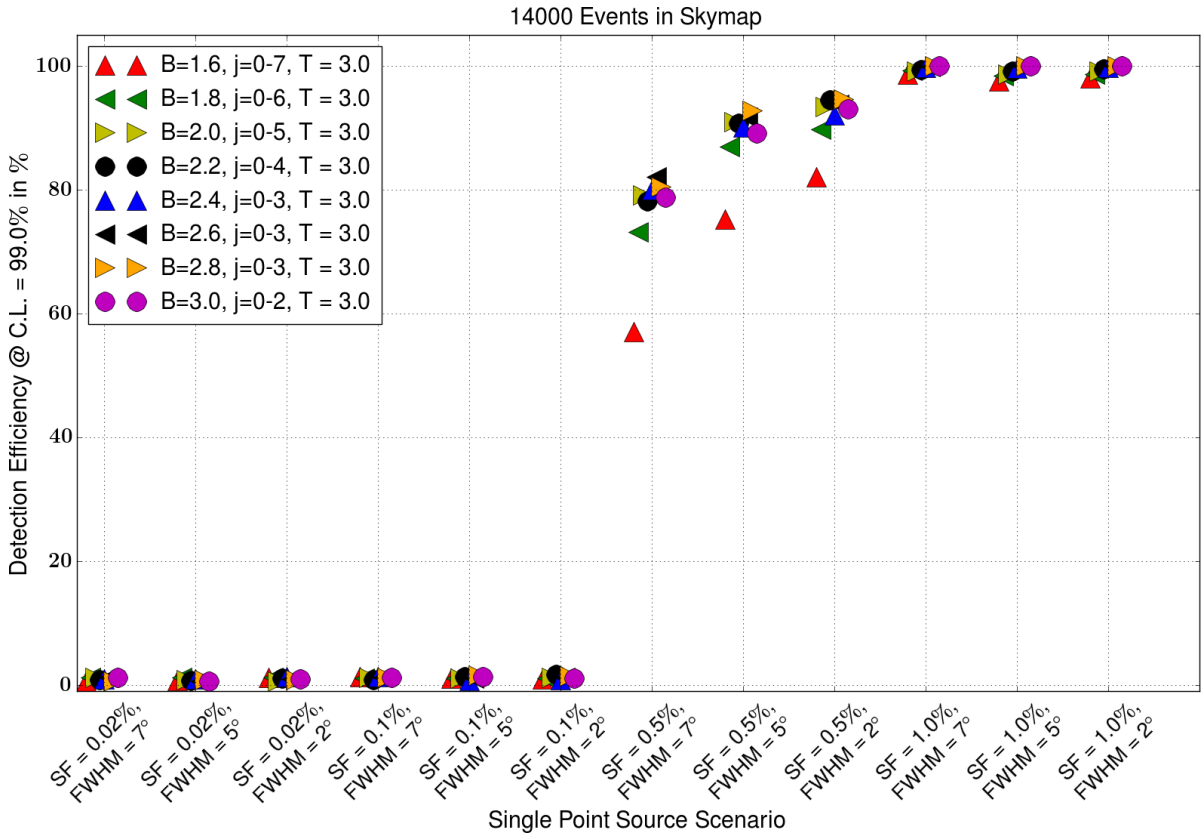
14000 Events in Skymap
B=1.6, j=0-7, T = 3.0
B=1.8, j=0-6, T = 3.0
B=2.0, j=0-5, T = 3.0
B=2.2, j=0-4, T = 3.0
B=2.4, j=0-3, T = 3.0
B=2.6, j=0-3, T = 3.0
B=2.8, j=0-3, T = 3.0
B=3.0, j=0-2, T = 3.0
Detection Efficiency @ C.L. = 99.0% in %
0
20
40
60
80
100
SF = 0.02%, FWHM = 7°
SF = 0.02%, FWHM = 5°
SF = 0.02%, FWHM = 2°
SF = 0.1%, FWHM = 7°
SF = 0.1%, FWHM = 5°
SF = 0.1%, FWHM = 2°
SF = 0.5%, FWHM = 7°
SF = 0.5%, FWHM = 5°
SF = 0.5%, FWHM = 2°
SF = 1.0%, FWHM = 7°
SF = 1.0%, FWHM = 5°
SF = 1.0%, FWHM = 2°
Single Point Source Scenario

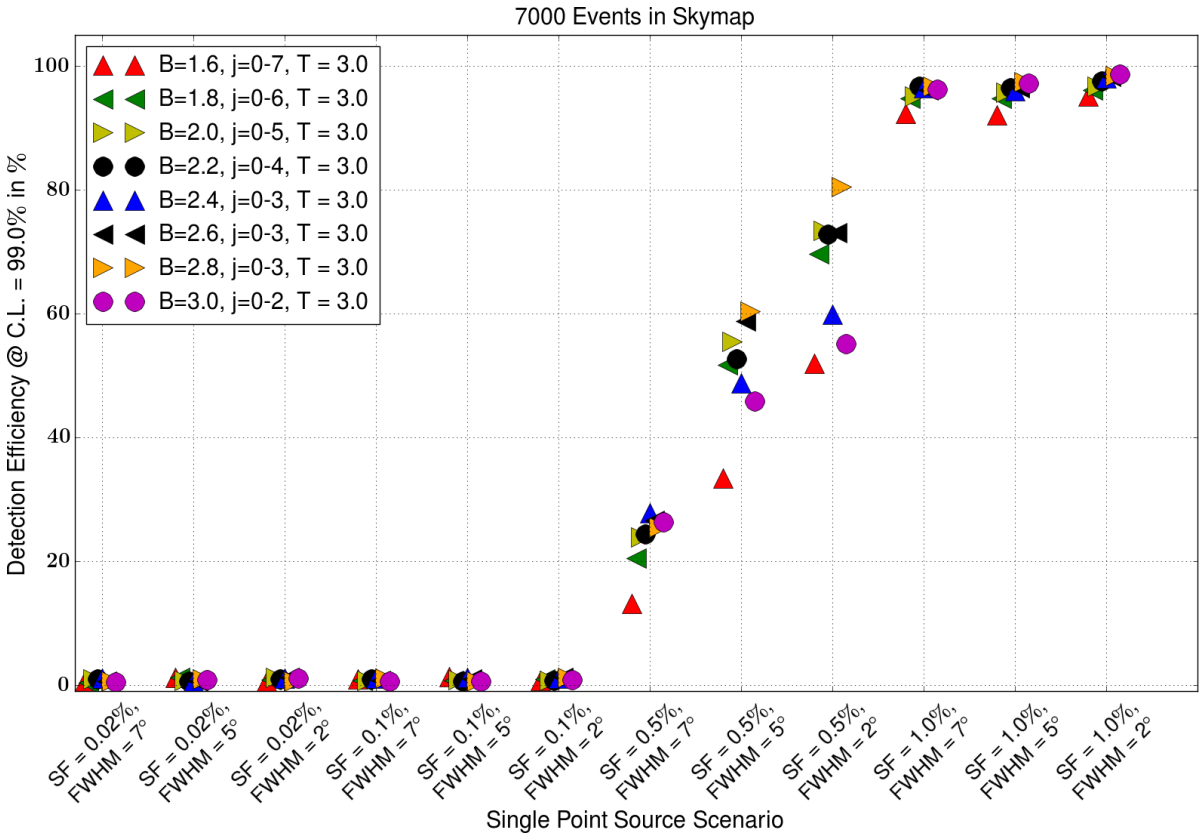
7000 Events in Skymap
B=1.6, j=0-7, T = 3.0
B=1.8, j=0-6, T = 3.0
B=2.0, j=0-5, T = 3.0
B=2.2, j=0-4, T = 3.0
B=2.4, j=0-3, T = 3.0
B=2.6, j=0-3, T = 3.0
B=2.8, j=0-3, T = 3.0
B=3.0, j=0-2, T = 3.0
Detection Efficiency @ C.L. = 99.0% in %
0
20
40
60
80
100
SF = 0.02%, FWHM = 7°
SF = 0.02%, FWHM = 5°
SF = 0.02%, FWHM = 2°
SF = 0.1%, FWHM = 7°
SF = 0.1%, FWHM = 5°
SF = 0.1%, FWHM = 2°
SF = 0.5%, FWHM = 7°
SF = 0.5%, FWHM = 5°
SF = 0.5%, FWHM = 2°
SF = 1.0%, FWHM = 7°
SF = 1.0%, FWHM = 5°
SF = 1.0%, FWHM = 2°
Single Point Source Scenario

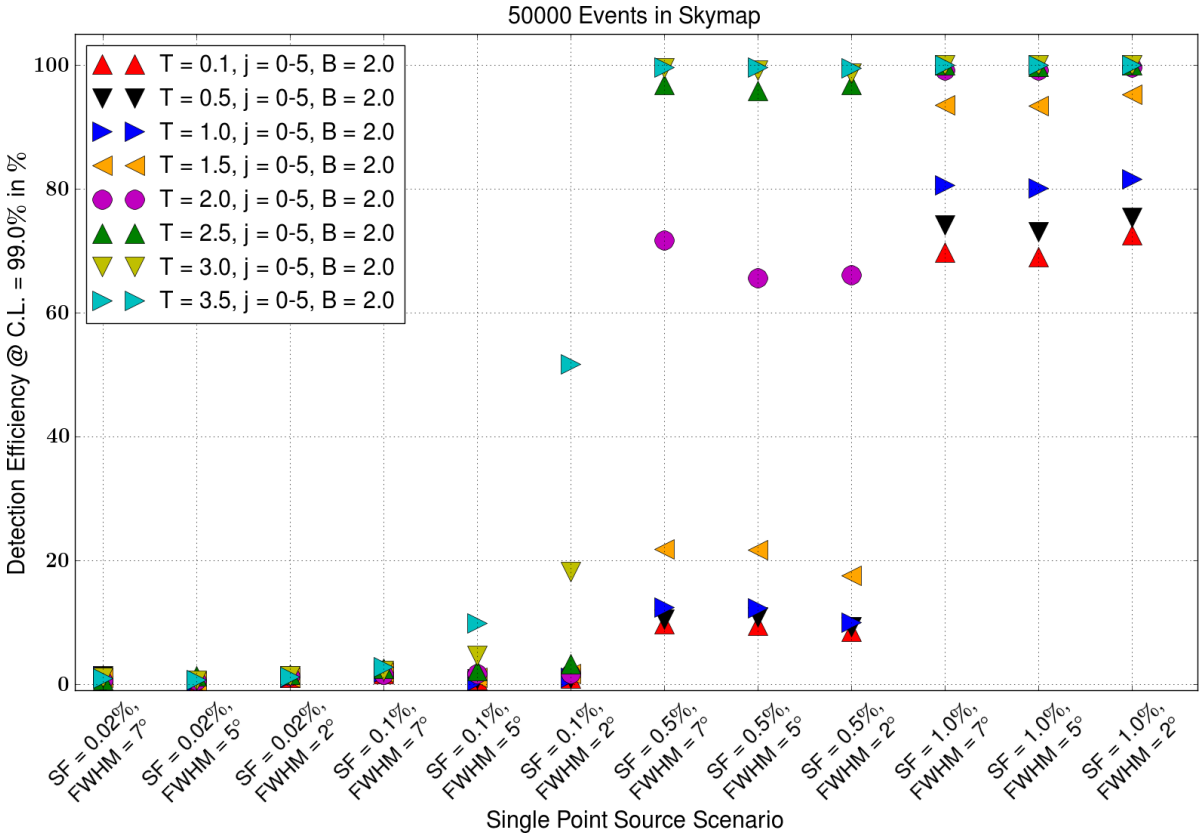
50000 Events in Skymap
T = 0.1, j = 0-5, B = 2.0
T = 0.5, j = 0-5, B = 2.0
T = 1.0, j = 0-5, B = 2.0
T = 1.5, j = 0-5, B = 2.0
T = 2.0, j = 0-5, B = 2.0
T = 2.5, j = 0-5, B = 2.0
T = 3.0, j = 0-5, B = 2.0
T = 3.5, j = 0-5, B = 2.0
Detection Efficiency @ C.L. = 99.0% in %
0
20
40
60
80
100
SF = 0.02%, FWHM = 7°
SF = 0.02%, FWHM = 5°
SF = 0.02%, FWHM = 2°
SF = 0.1%, FWHM = 7°
SF = 0.1%, FWHM = 5°
SF = 0.1%, FWHM = 2°
SF = 0.5%, FWHM = 7°
SF = 0.5%, FWHM = 5°
SF = 0.5%, FWHM = 2°
SF = 1.0%, FWHM = 7°
SF = 1.0%, FWHM = 5°
SF = 1.0%, FWHM = 2°
Single Point Source Scenario

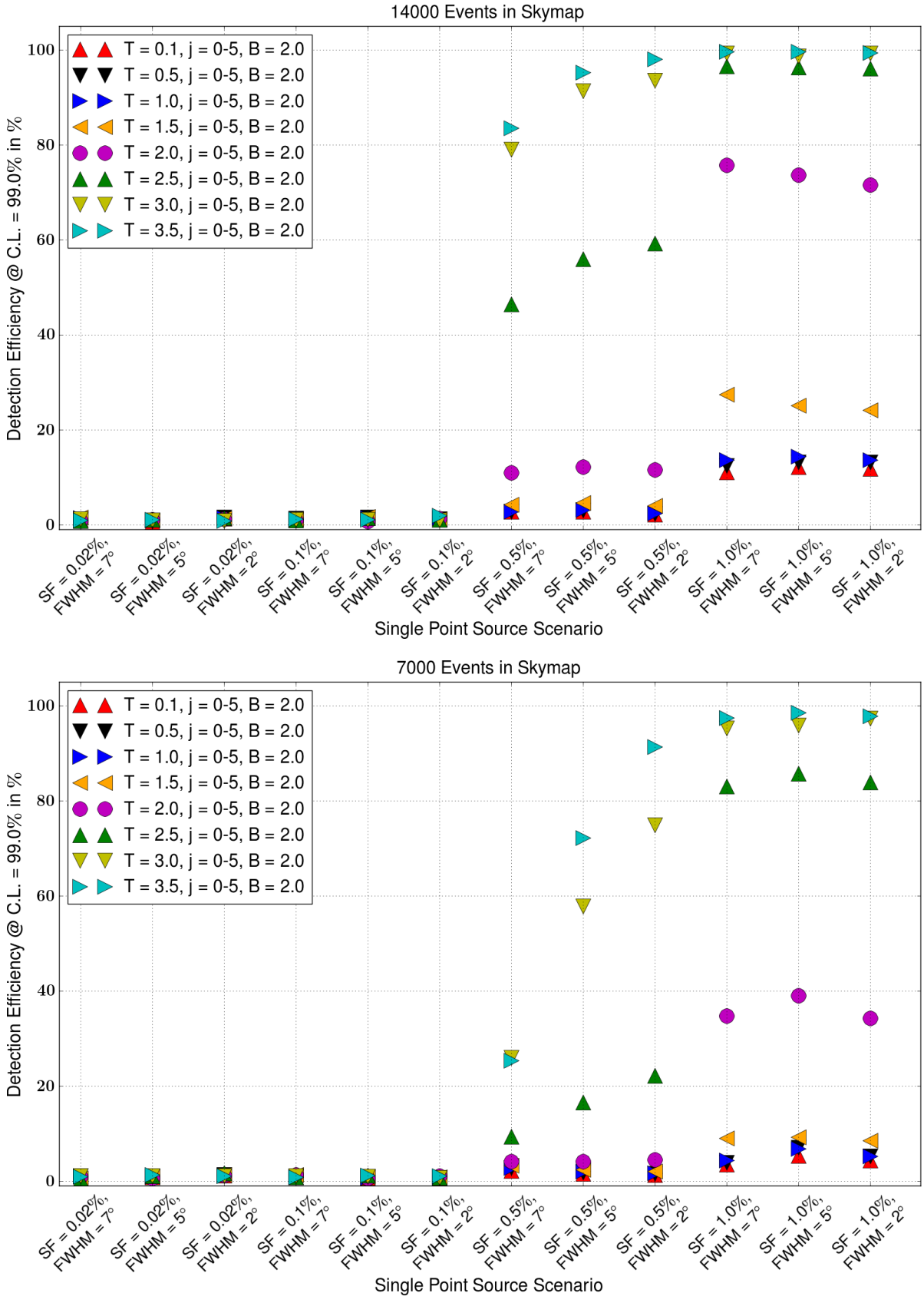

Figure 6.6.: Sensitivity to the single point source scenario in section 6.3.2. **Top 3 figures:** Variable Needlet width B. **Bottom 3 figures:** Variable threshold T.

6.3.3. Single Point Deflected through the GMF

Description

As mention in the previous scenario, a clear point source signature is only expected in the case of weak extra and intra galactic magnetic fields. This is a very idealistic scenario. Even though limits of the EGMF still allow for a weak EGMF, current models of the GMF do not suggest that the GMF is weak (see section 2.4.1).

In this scenario we use a GMF lens[2] derived from the JF12 model[22], as described in [111] (see 2.4.1 for details). The details on the construction of the lens can be found in [111] and details on the usage of the lens in section 8.3 of this work.

The lens consists of 175 lens bins each of which transform the PDF of arrival directions of a particular energy (or more specific rigidity) arriving at the edge of the galaxy to the PDF at earth. The lens bins cover a rigidity range equidistant in the logarithm of the rigidity, from 10^{17} eV to $3 \cdot 10^{20}$ eV.

The generation of the MC test skymaps in this scenario follows the work in [112, 25]. First, we generate a point source PDF at the edge of the galaxy. In this scenario we use the position and approximate size of Centaurus A (see table 6.5) as illustrated in the top, left-hand side of figure 6.7. This PDF is then folded through the lens bins resulting in 175 PDFs at earth which are convoluted with the Auger coverage. An example of this is shown on the top, right-hand side of figure 6.7 in the case of protons with an energy of 3 EeV.

Since the deflection in the GMF depends on the energy and charge of the particle, we need to make assumptions on the composition and energy spectrum. In this scenario we assume a power law spectrum with an index of $\gamma = -2.6$ (see section 2.1), a pure proton composition and neglect the EGMF[3]. Further we use a different starting energy for each given number of total events as shown in table 6.5.

Once the source PDFs at earth is derived, test input skymaps are generated. For this we dice an energy according to the specific starting energy and power law. From the corresponding PDF a random arrival direction is drawn. This is repeated until a skymap with a given signal fraction is achieved . To this we add isotropic noise (according to the Auger coverage) until the desired total number of events is reached. An example of these two steps is shown on the bottom of figure 6.7 for an energy threshold of 3 EeV.

Table 6.5 summarizes the set of parameters used in this scenario considering protons as the primary particle, the energy ranges of the simulated events, signal fractions, source size and source direction.

[2]Including the regular and a realisation of the turbulent field. Taken from http://web.physik.rwth-aachen.de/Auger_MagneticFields/PARSEC/downloads.php

[3]For an analysis additionally using a strong EGMF see section 8.3

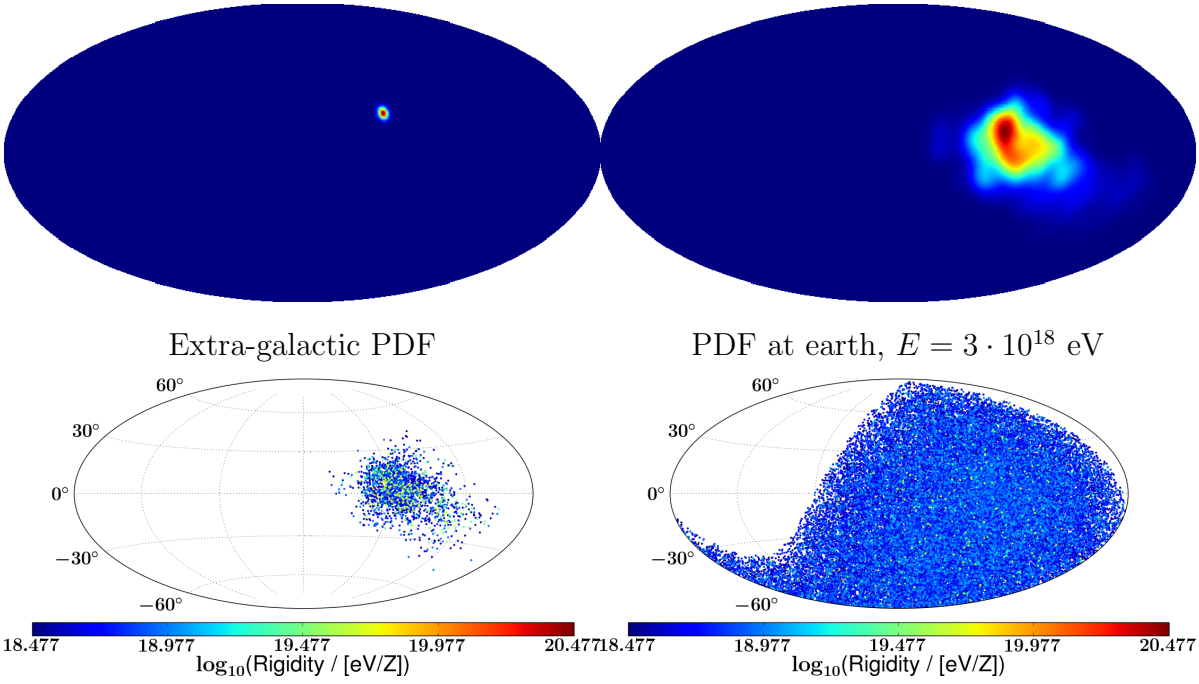

Figure 6.7.: All plots are shown in Galactic coordinates. **Top, Left:** Point source signature at the edge of the galaxy. **Top, Right:** Point source signature at earth transformed through the GMF lens ($E = 3$ EeV). **Bottom, Left (Right):** Draw of 1,000 (49,000) signal (isotropic) events, including the GMF lens, with energy $E \geq 3$ EeV. The energy is colour coded.

Table 6.5.: Parameters of the Centaurs A point source scenario using a GMF lens.

Energy/ Total Events	≥ 3 EeV / 50,000, ≥ 6 EeV / 14,000, ≥ 9 EeV / 7,000
Composition	Pure proton
Signal-Fraction (%)	0.00, 0.02, 0.05, 0.1, 0.5, 1.0, 2.0
Source σ	2°
Source Position / (α, δ)	(201°,−43°)

Results and Discussion

The results of the GMF scenario are shown in figure 6.8. Again no clear trend in the B values arises although, similar to the point source scenario without the GMF, B values between $B = 1.8$ and $B = 3.0$ achieve a slightly higher sensitivity. When the threshold is varied nearly the same trend as in the point source scenario without the GMF emerges: A higher threshold gives a higher sensitivity and vice versa. The reasons are the same as described in the previous discussion. The only deviation to the previous scenario appears at the highest chosen threshold of $T = 3.5$. Here the threshold is so high that the signal from the smeared point source starts to become suppressed.

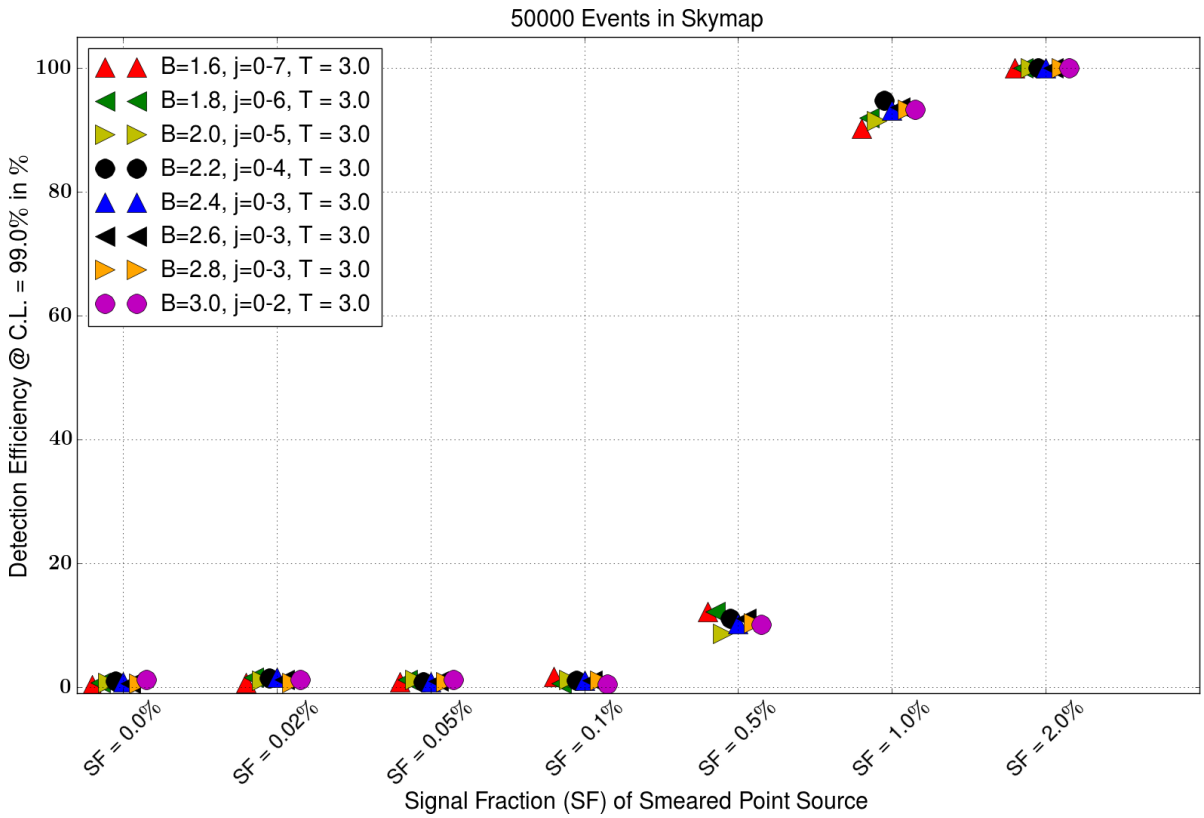
50000 Events in Skymap
B=1.6, j=0-7, T = 3.0
B=1.8, j=0-6, T = 3.0
B=2.0, j=0-5, T = 3.0
B=2.2, j=0-4, T = 3.0
B=2.4, j=0-3, T = 3.0
B=2.6, j=0-3, T = 3.0
B=2.8, j=0-3, T = 3.0
B=3.0, j=0-2, T = 3.0
Detection Efficiency @ C.L. = 99.0% in %
0
20
40
60
80
100
SF = 0.0%
SF = 0.02%
SF = 0.05%
SF = 0.1%
SF = 0.5%
SF = 1.0%
SF = 2.0%
Signal Fraction (SF) of Smeared Point Source

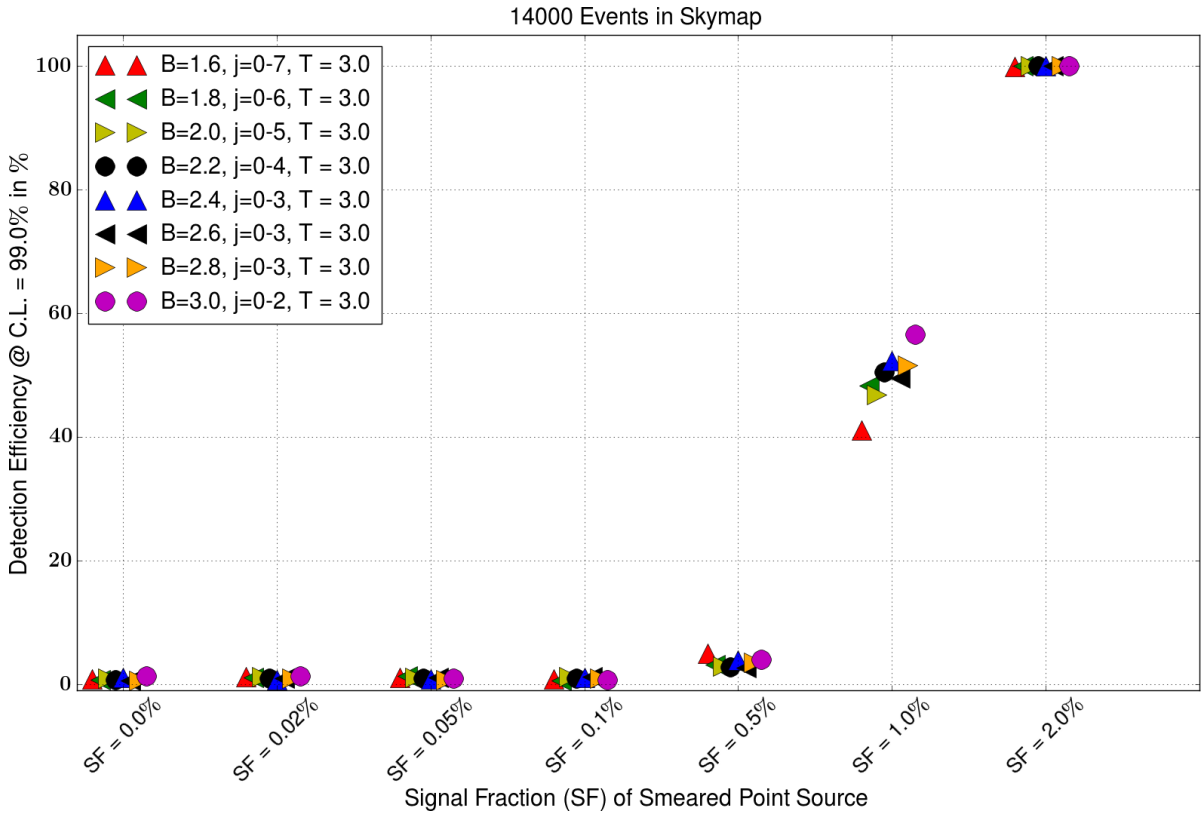
14000 Events in Skymap
B=1.6, j=0-7, T = 3.0
B=1.8, j=0-6, T = 3.0
B=2.0, j=0-5, T = 3.0
B=2.2, j=0-4, T = 3.0
B=2.4, j=0-3, T = 3.0
B=2.6, j=0-3, T = 3.0
B=2.8, j=0-3, T = 3.0
B=3.0, j=0-2, T = 3.0
Detection Efficiency @ C.L. = 99.0% in %
0
20
40
60
80
100
SF = 0.0%
SF = 0.02%
SF = 0.05%
SF = 0.1%
SF = 0.5%
SF = 1.0%
SF = 2.0%
Signal Fraction (SF) of Smeared Point Source

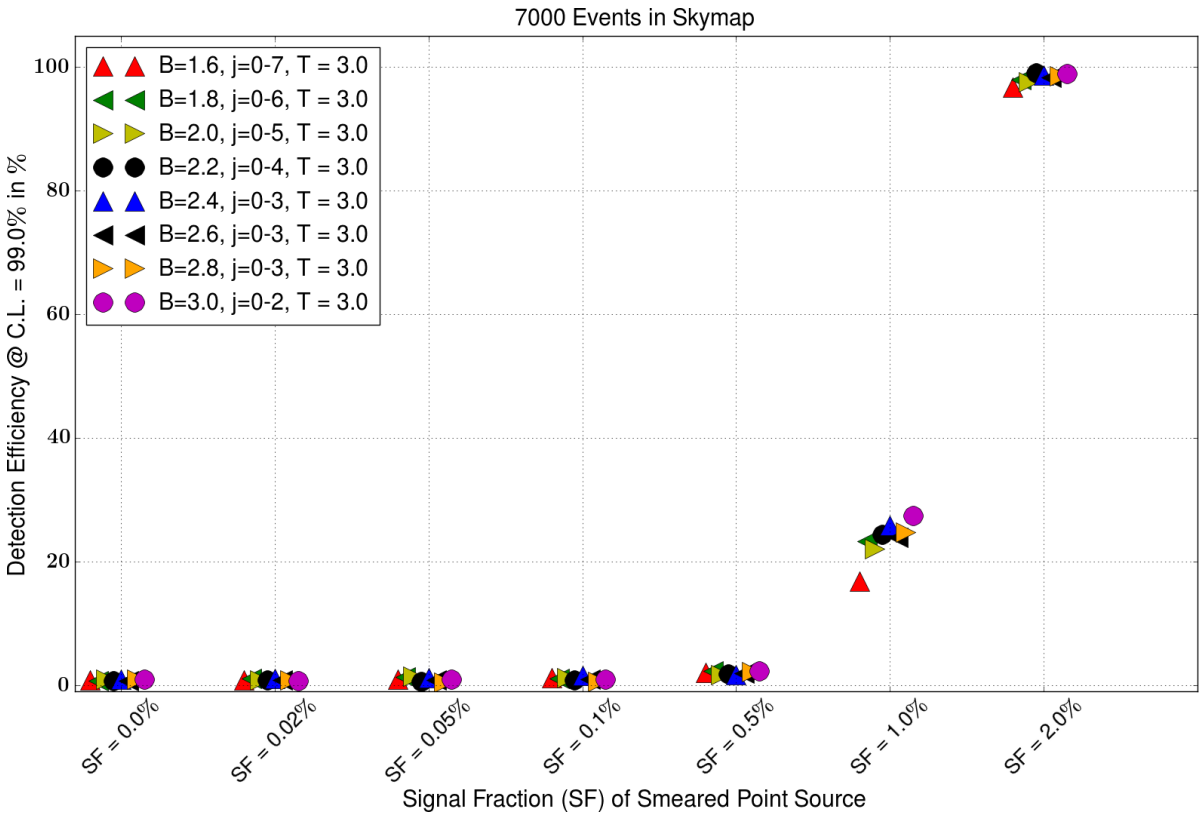
7000 Events in Skymap
B=1.6, j=0-7, T = 3.0
B=1.8, j=0-6, T = 3.0
B=2.0, j=0-5, T = 3.0
B=2.2, j=0-4, T = 3.0
B=2.4, j=0-3, T = 3.0
B=2.6, j=0-3, T = 3.0
B=2.8, j=0-3, T = 3.0
B=3.0, j=0-2, T = 3.0
Detection Efficiency @ C.L. = 99.0% in %
0
20
40
60
80
100
SF = 0.0%
SF = 0.02%
SF = 0.05%
SF = 0.1%
SF = 0.5%
SF = 1.0%
SF = 2.0%
Signal Fraction (SF) of Smeared Point Source

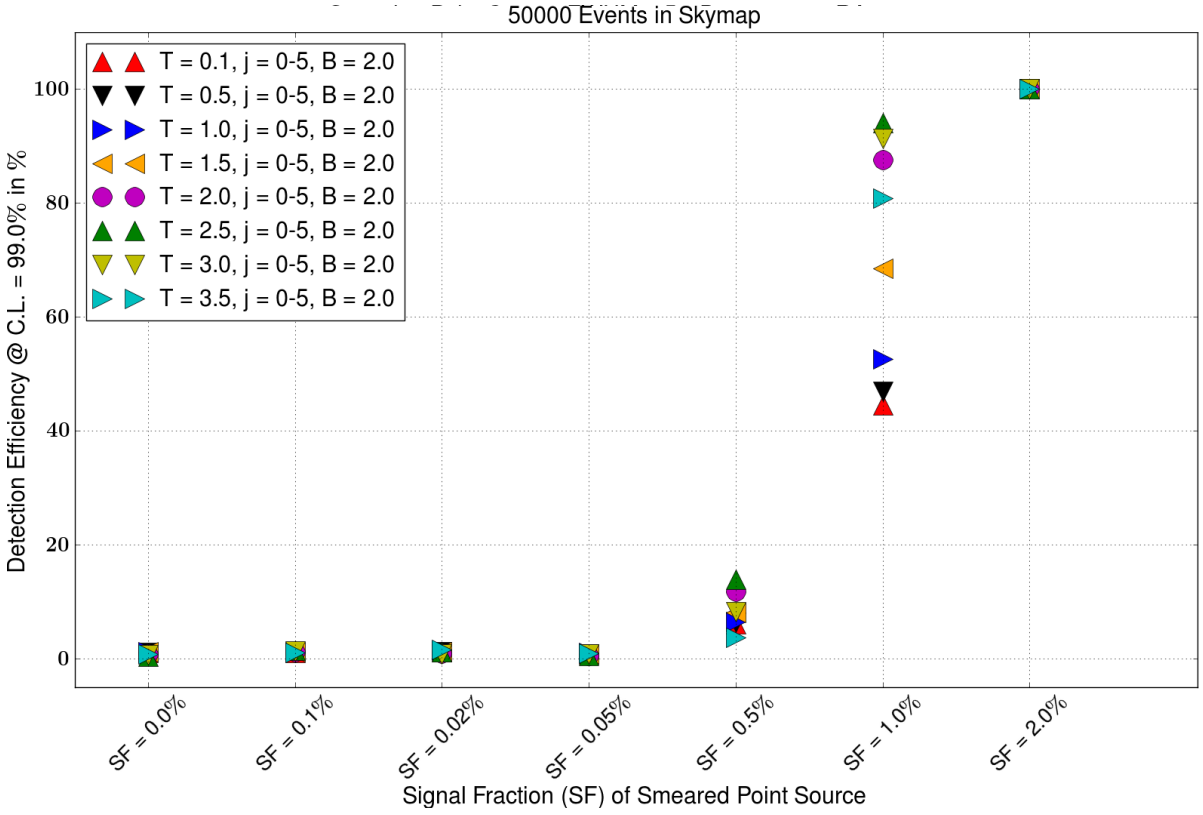
50000 Events in Skymap
T = 0.1, j = 0-5, B = 2.0
T = 0.5, j = 0-5, B = 2.0
T = 1.0, j = 0-5, B = 2.0
T = 1.5, j = 0-5, B = 2.0
T = 2.0, j = 0-5, B = 2.0
T = 2.5, j = 0-5, B = 2.0
T = 3.0, j = 0-5, B = 2.0
T = 3.5, j = 0-5, B = 2.0
Detection Efficiency @ C.L. = 99.0% in %
0
20
40
60
80
100
SF = 0.0%
SF = 0.1%
SF = 0.02%
SF = 0.05%
SF = 0.5%
SF = 1.0%
SF = 2.0%
Signal Fraction (SF) of Smeared Point Source

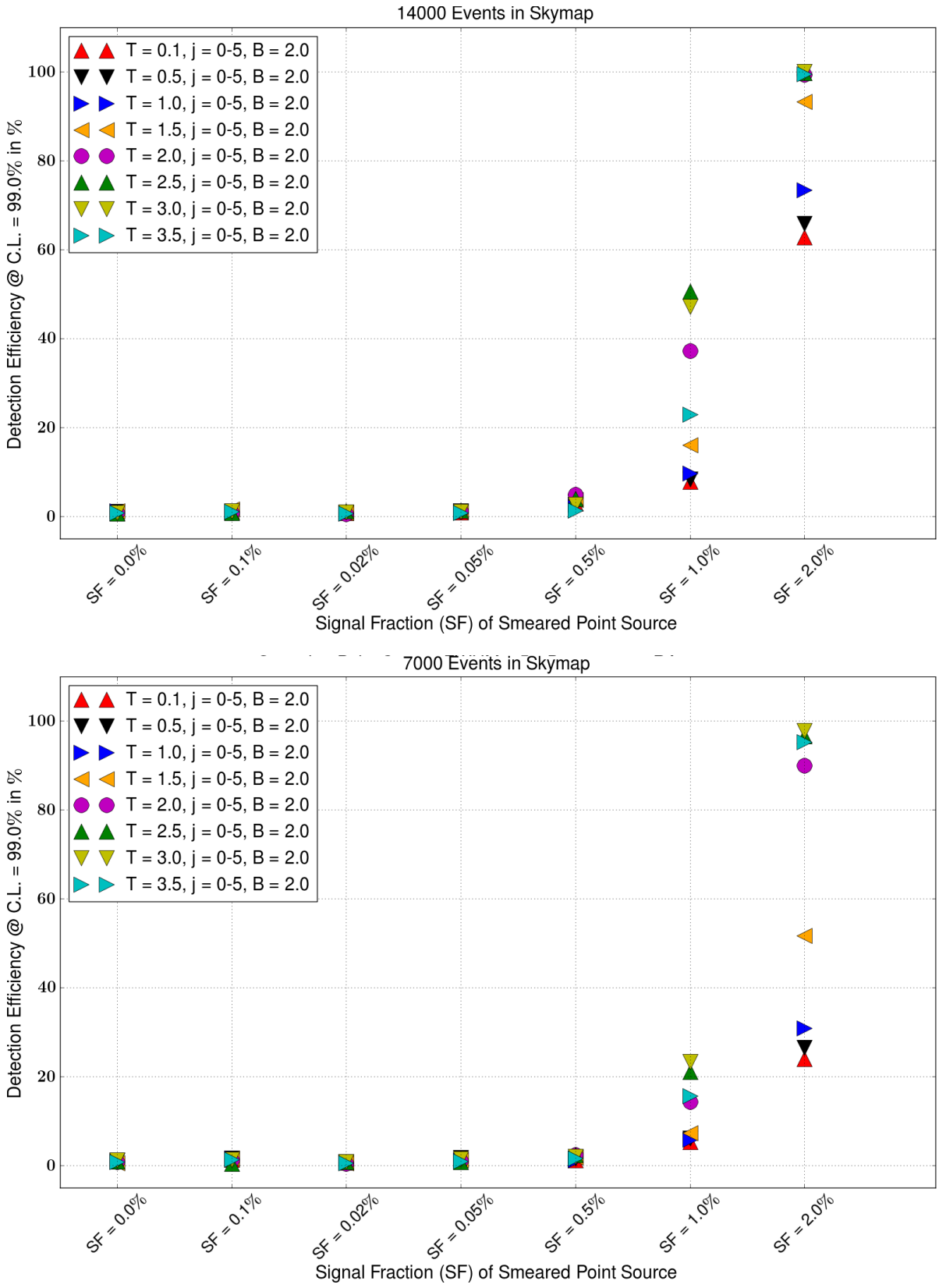

Figure 6.8.: Sensitivity to the single point GMF source scenario in section 6.3.3. **Top 3 figures:** Variable Needlet width B. **Bottom 3 figures:** Variable threshold T.

6.3.4. Combined Dipole and Point Source Scenario

Description

In this scenario we combine a dipole and a point source signature in a single skymap to demonstrate the ability of the method to simultaneously detect patterns in a wide range of angular scales.
We reuse the input skymaps with a hidden dipole signature already used in the dipole scenario and the point source events (see figure 6.5) generated previously. For a given parameter set of dipole amplitude and point source signal fraction we randomly discard events from the dipole skymap to fill it up with point source events. An example of a reconstructed, mixed skymap is shown in figure 6.9. Table 6.6 summarizes the set of parameters used in this scenario, i.e, the point source direction, its angular width, fraction of point source signal used in the simulations, dipole amplitude and dipole direction.

Table 6.6.: Parameters used in the point source plus dipole simulated scenario. The results from parameters marked with an $*$ can be found in appendix B.

Mixed Scenario Parameters	Values
Dipole Amplitude	3%
Dipole Position	$(\alpha_d, \delta_d) = (0°, 0°)$
Point Source Signal-Fraction (%)	0.1, 0.5, 1.0
Point Source σ	2°, 3°
Point Source Directions	$(\alpha, \delta) = (0°, -60°), (150°, -60°)^*$

Results and Discussion

The results are shown in figure 6.10. Again no clear trend in the B values emerges but a slightly higher sensitivity is seen for B values between $B = 1.8$ and $B = 2.2$. As expected, in this scenario composed of a dipole and a point source, the trend in the threshold is a mix of the individual trends for both signatures. If the point sources is weak, i.e. has a low signal fraction, a higher threshold provides a higher sensitivity. The trend reverses once the signal fractions of the point source becomes larger.

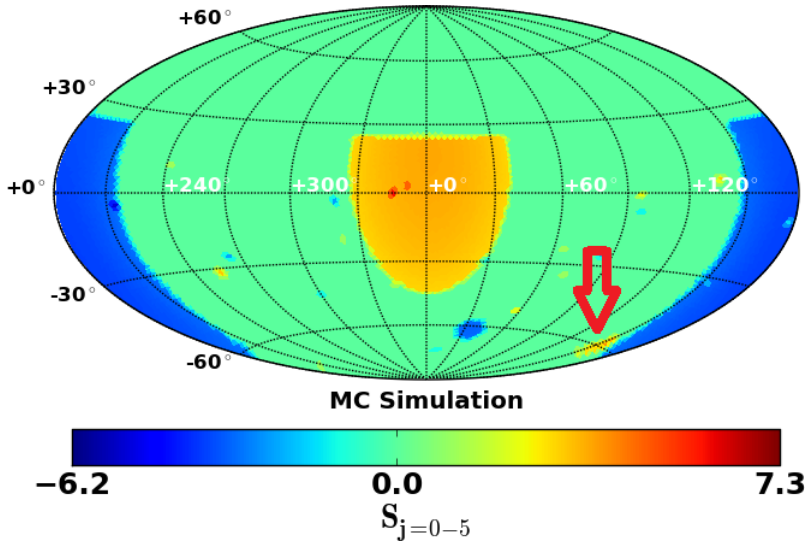

Figure 6.9.: A skymap in equatorial coordinates, with 50,000 input events, reconstructed with the Needlet analysis ($j = 0 - 5$). The input skymap contains a dipole signature at $(0°, 0°)$ with an amplitude of 3% and a point source (marked with a red arrow) at a declination and right-ascension at $-60°$ and $150°$ respectively. Both, the dipole and point source signatures are visible.

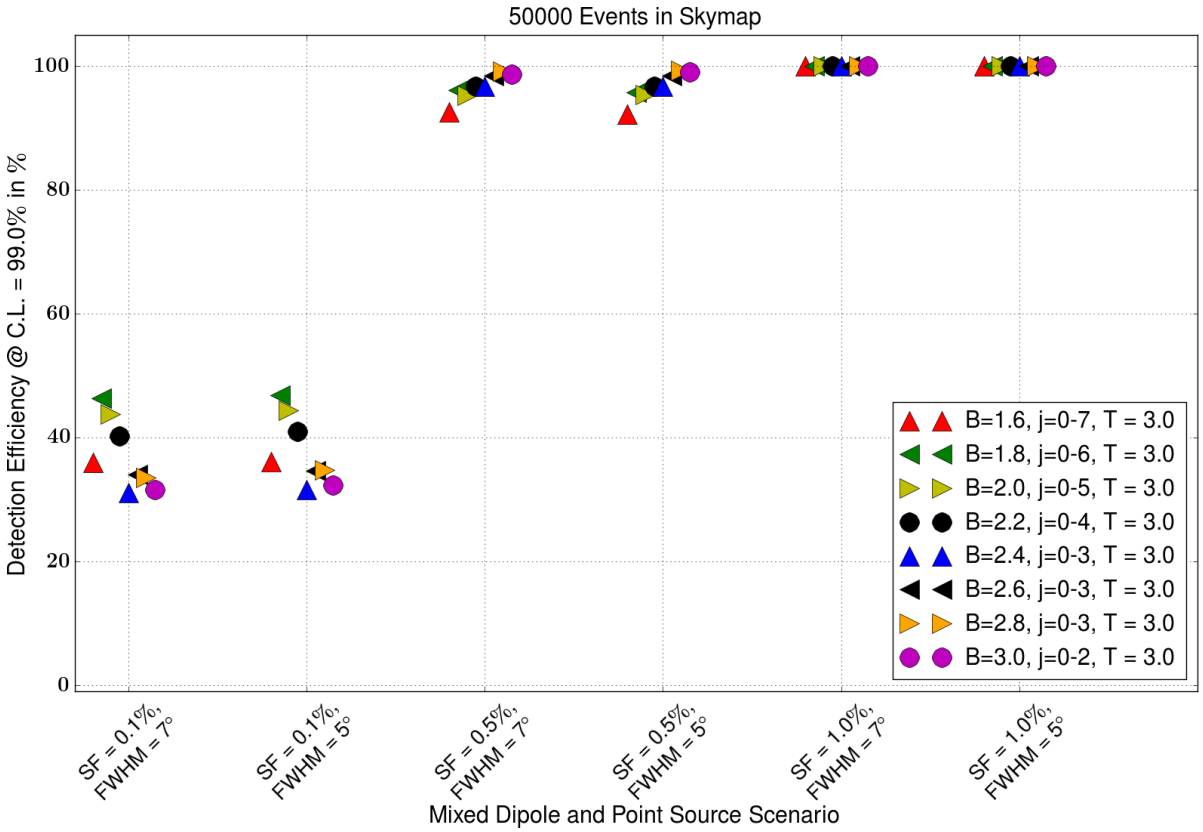
50000 Events in Skymap
Detection Efficiency @ C.L. = 99.0% in %
0
20
40
60
80
100
B=1.6, j=0-7, T = 3.0
B=1.8, j=0-6, T = 3.0
B=2.0, j=0-5, T = 3.0
B=2.2, j=0-4, T = 3.0
B=2.4, j=0-3, T = 3.0
B=2.6, j=0-3, T = 3.0
B=2.8, j=0-3, T = 3.0
B=3.0, j=0-2, T = 3.0
SF = 0.1%, FWHM = 7°
SF = 0.1%, FWHM = 5°
SF = 0.5%, FWHM = 7°
SF = 0.5%, FWHM = 5°
SF = 1.0%, FWHM = 7°
SF = 1.0%, FWHM = 5°
Mixed Dipole and Point Source Scenario

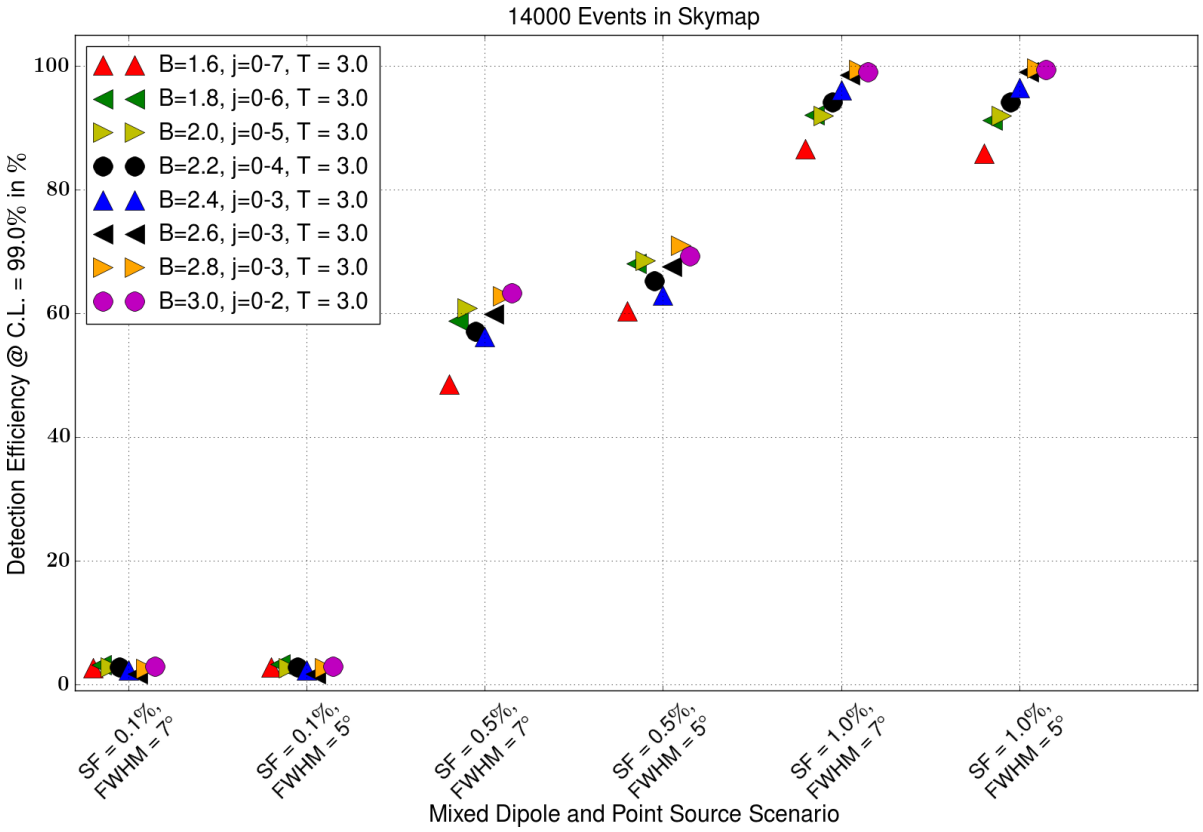
14000 Events in Skymap
Detection Efficiency @ C.L. = 99.0% in %
0
20
40
60
80
100
B=1.6, j=0-7, T = 3.0
B=1.8, j=0-6, T = 3.0
B=2.0, j=0-5, T = 3.0
B=2.2, j=0-4, T = 3.0
B=2.4, j=0-3, T = 3.0
B=2.6, j=0-3, T = 3.0
B=2.8, j=0-3, T = 3.0
B=3.0, j=0-2, T = 3.0
SF = 0.1%, FWHM = 7°
SF = 0.1%, FWHM = 5°
SF = 0.5%, FWHM = 7°
SF = 0.5%, FWHM = 5°
SF = 1.0%, FWHM = 7°
SF = 1.0%, FWHM = 5°
Mixed Dipole and Point Source Scenario

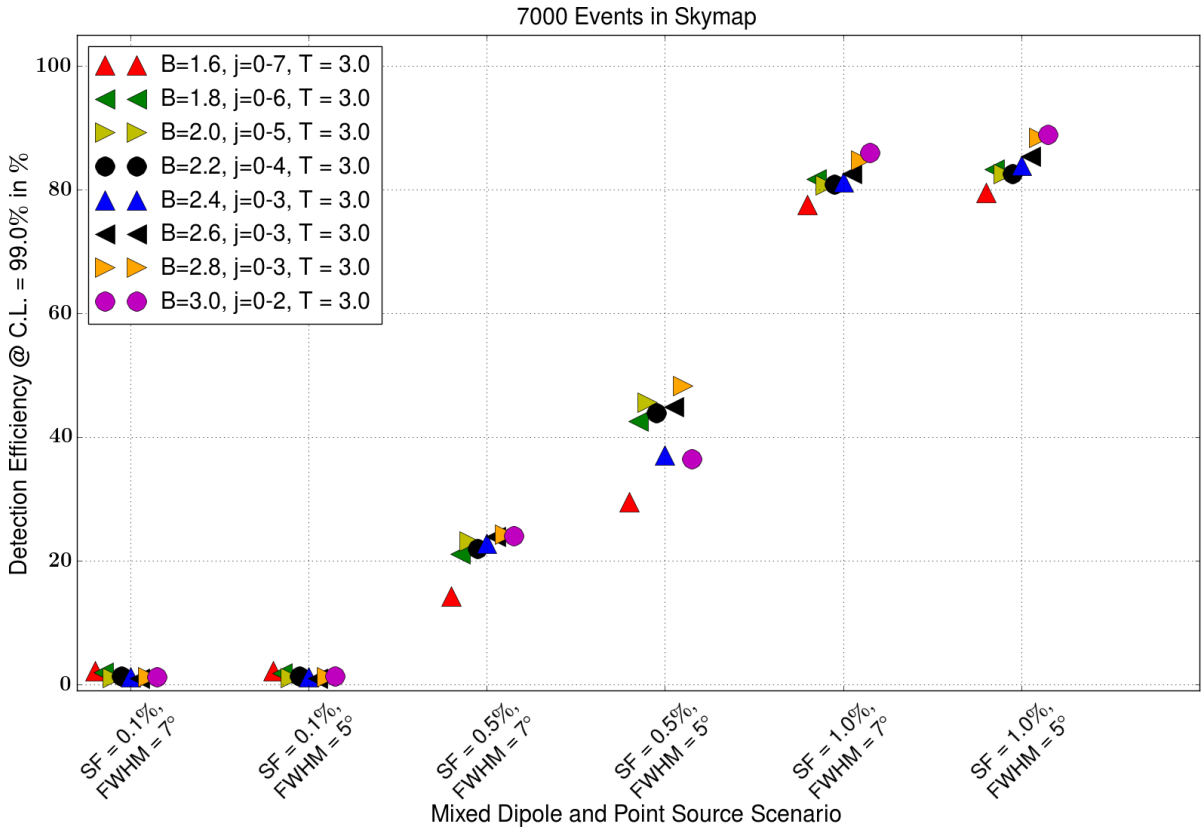
7000 Events in Skymap
B=1.6, j=0-7, T = 3.0
B=1.8, j=0-6, T = 3.0
B=2.0, j=0-5, T = 3.0
B=2.2, j=0-4, T = 3.0
B=2.4, j=0-3, T = 3.0
B=2.6, j=0-3, T = 3.0
B=2.8, j=0-3, T = 3.0
B=3.0, j=0-2, T = 3.0
Detection Efficiency @ C.L. = 99.0% in %
0
20
40
60
80
100
SF = 0.1%, FWHM = 7°
SF = 0.1%, FWHM = 5°
SF = 0.5%, FWHM = 7°
SF = 0.5%, FWHM = 5°
SF = 1.0%, FWHM = 7°
SF = 1.0%, FWHM = 5°
Mixed Dipole and Point Source Scenario

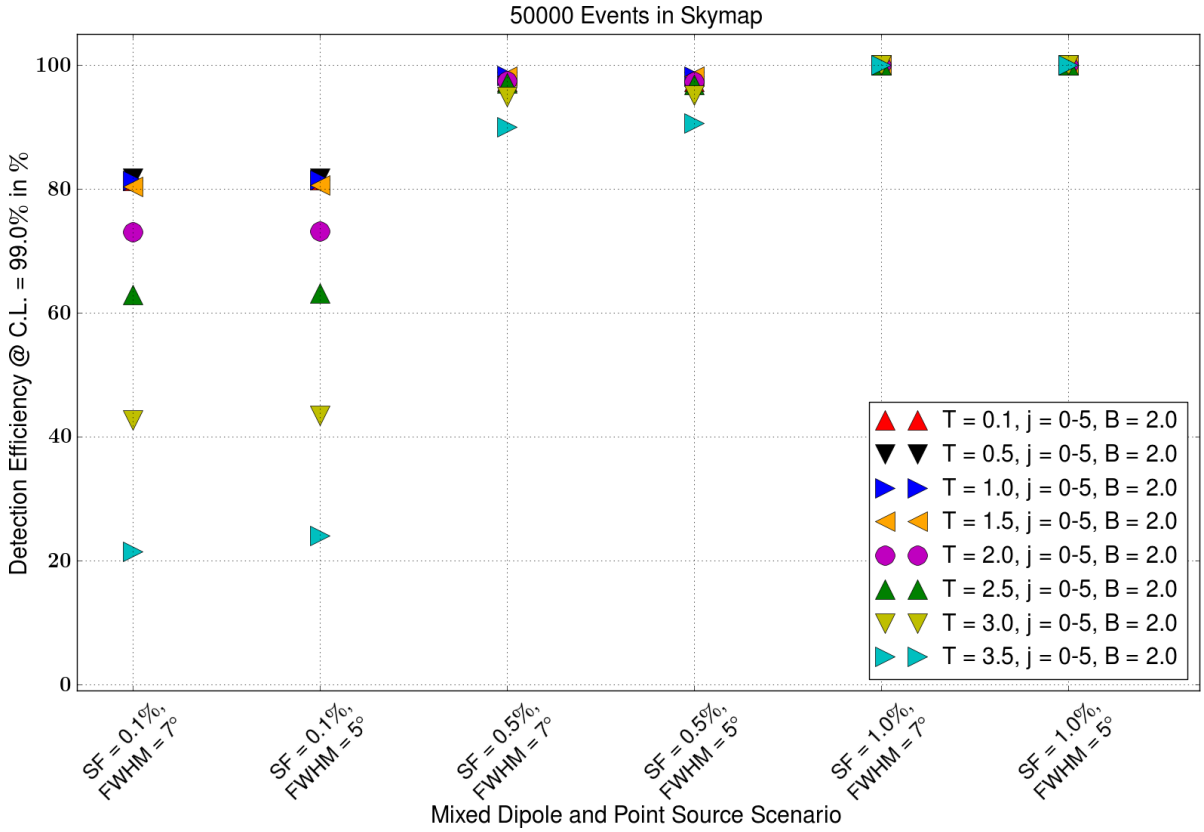
50000 Events in Skymap
T = 0.1, j = 0-5, B = 2.0
T = 0.5, j = 0-5, B = 2.0
T = 1.0, j = 0-5, B = 2.0
T = 1.5, j = 0-5, B = 2.0
T = 2.0, j = 0-5, B = 2.0
T = 2.5, j = 0-5, B = 2.0
T = 3.0, j = 0-5, B = 2.0
T = 3.5, j = 0-5, B = 2.0
Detection Efficiency @ C.L. = 99.0% in %
0
20
40
60
80
100
SF = 0.1%, FWHM = 7°
SF = 0.1%, FWHM = 5°
SF = 0.5%, FWHM = 7°
SF = 0.5%, FWHM = 5°
SF = 1.0%, FWHM = 7°
SF = 1.0%, FWHM = 5°
Mixed Dipole and Point Source Scenario

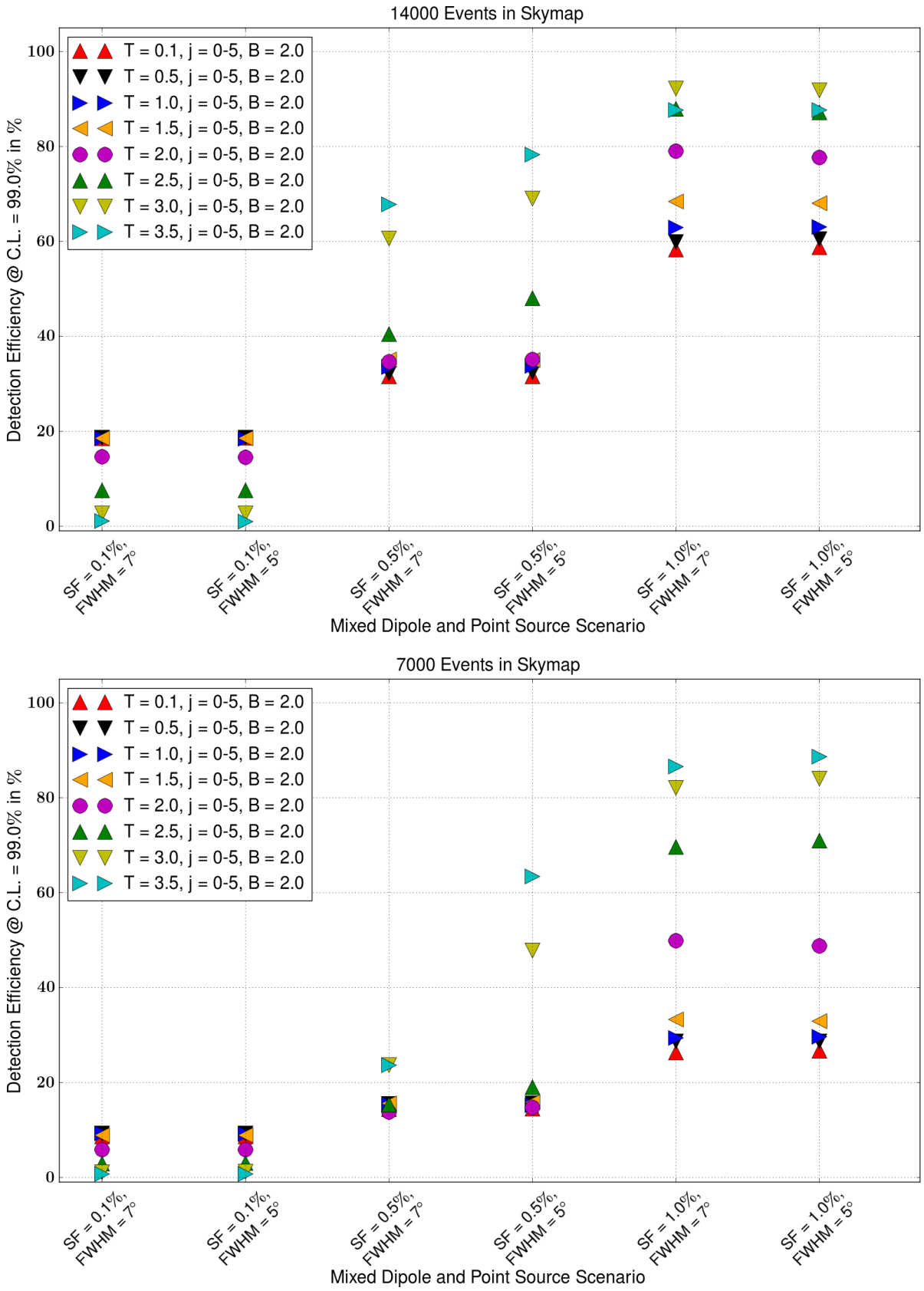

Figure 6.10.: Sensitivity to the mixed dipole and point source scenario in section 6.3.4. **Top 3 figures:** Variable Needlet width B. **Bottom 3 figures:** Variable threshold T.

6.3.5. Catalogue Based Scenario

Description

In contrast to the previous scenarios which used one particular (or combinations thereof) kind of anisotropy, this scenario uses the measured distribution of structures around our galaxy. To generate the catalogue scenario we use the 2MASS Red-shift Survey (2MRS) catalogue. The 2MRS aims to map the distribution of galaxies and dark matter in the local universe out to a mean red-shift of $z = 0.03$ [113].

From this catalogue we randomly choose a set of 1,000 entries up to a $z_{\max} = 0.018 \equiv 76$ MPC[4]. We note that this excludes the region around the galactic centre/bulge where the catalogue is empty. To not introduce a spurious anisotropy due the lack of information in the catalogue, we add an isotropic distribution of arrival directions in this region. We describe the process to get from these components to a set of test skymaps in the following:

- **Generation of the catalogue probability density distribution (PDF):**
  The signal fraction determines the number of source events in the final skymap N_S. To generate N_S events we randomly draw N_D events from the previously mentioned set of 1,000 entries and additionally smear the drawn events with a Mises-Fisher distribution (see the single point source scenario) with $\sigma = 2^\circ$ to give an angular extend to the selected sources. Each draw is either accepted or rejected randomly according to the Auger coverage until N_S events are generated. An example is shown in the top left of figure 6.11.

- **Generation of the filler:**
  Since the region of the galactic plane and bulge are empty we additionally generate an isotropic filler in this region to avoid an artificial anisotropy. If p_{empty} percent of the sky are empty, we draw $p_{\text{empty}} \cdot \frac{N_D}{1-p_{\text{empty}}}$ events uniformly distributed in the empty region. These events are then accepted or rejected by the Auger exposure. An example of one filler is shown in the top right of figure 6.11.

Both filler and the source events are combined into an input skymap which is filled with additional isotropic noise (as seen by Auger) until the desired number of total events is reached. An example of such an input skymap is shown in the middle part of figure 6.11 with the resulting reconstructed skymap being shown on the bottom of the figure. The parameters used in this catalogue scenario are shown in table 6.7.

Catalogue Parameters	Values
Signal-Fraction (excluding the galactic plane) (%)	0.0, 0.5, 2.0, 5.0, 10.0, 15.0

Table 6.7.: Parameters used in the catalogue scenario.

[4]For brevity, we use $z_{\max} = 0.018$ as used in [114].

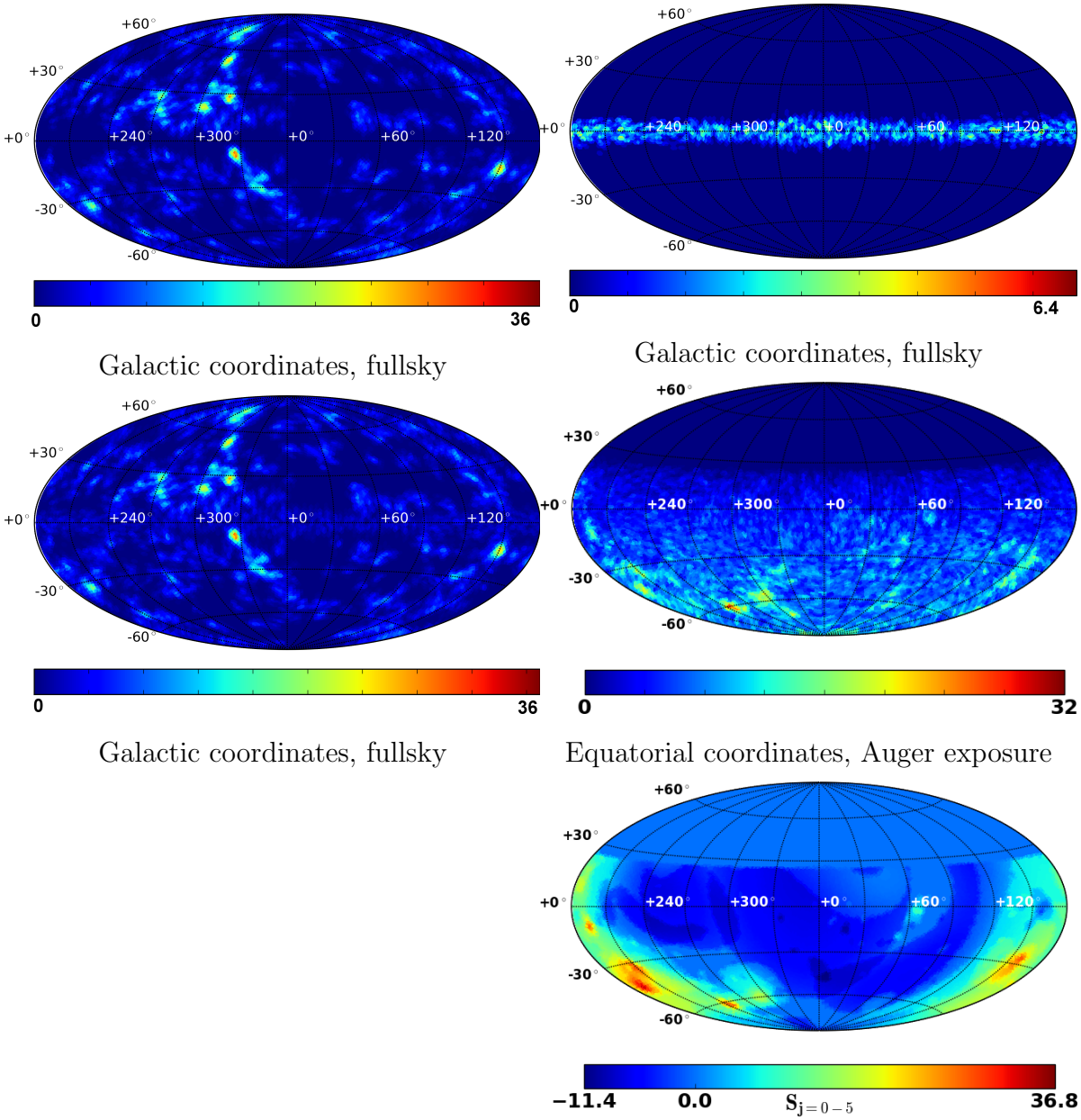

Figure 6.11.: Top, Left: Smeared signal events drawn from a set of 1,000 entries of the 2MRS catalogue. **Top, Right:** Isotropic filler for the galactic plane and bulge. **Middle, Left:** Sum of signal and filler events. **Middle, Right:** Test input skymap with additional isotropic noise (as seen by Auger). (Parameters: 50,000 total events, 10% signal fraction). **Bottom, Right:** Reconstructed,thresholded and combined significance skymap $S_{j=0-5}$ of the MC input skymap, shown in the middle, right-hand side of this figure.

Results and Discussion

The results of the catalogue scenario are shown in figure 6.12. No clear B value provides a larger sensitivity. The values cluster around each other. If the threshold is varied, the results are comparable provided the threshold is not too large. The point at which the threshold starts to suppress the sensitivity depends on the number of events in the skymap. At 50,000 events only the highest threshold of $T = 3.5$ leads to a large reduction of the sensitivity followed by a small reduction for $T = 3.0$. This mainly holds also true for 14,000 events although at a small signal fraction also $T = 3.0$ suppresses the sensitivity. At 7,000 events even a threshold of $T = 2.5$ leads to a reduced sensitivity.

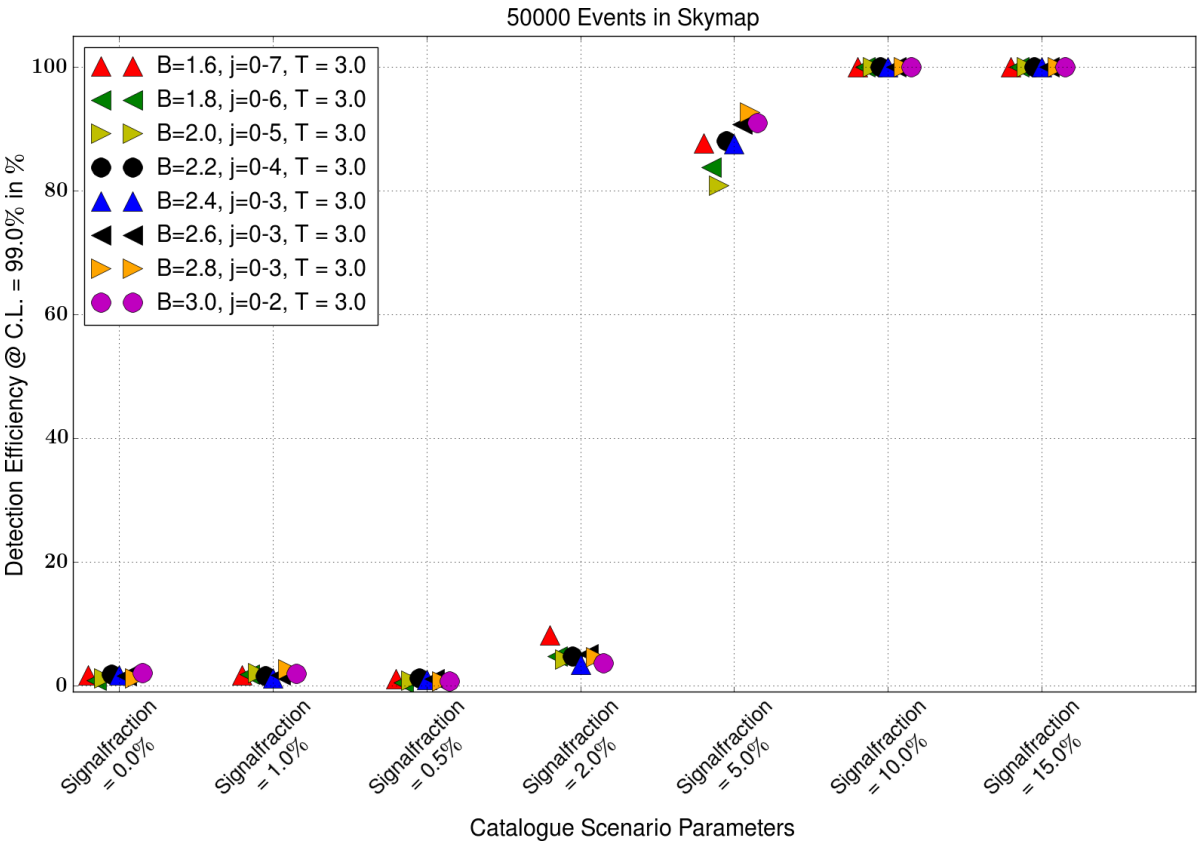
50000 Events in Skymap
B=1.6, j=0-7, T = 3.0
B=1.8, j=0-6, T = 3.0
B=2.0, j=0-5, T = 3.0
B=2.2, j=0-4, T = 3.0
B=2.4, j=0-3, T = 3.0
B=2.6, j=0-3, T = 3.0
B=2.8, j=0-3, T = 3.0
B=3.0, j=0-2, T = 3.0
Detection Efficiency @ C.L. = 99.0% in %
0
20
40
60
80
100
Signalfraction = 0.0%
Signalfraction = 1.0%
Signalfraction = 0.5%
Signalfraction = 2.0%
Signalfraction = 5.0%
Signalfraction = 10.0%
Signalfraction = 15.0%
Catalogue Scenario Parameters

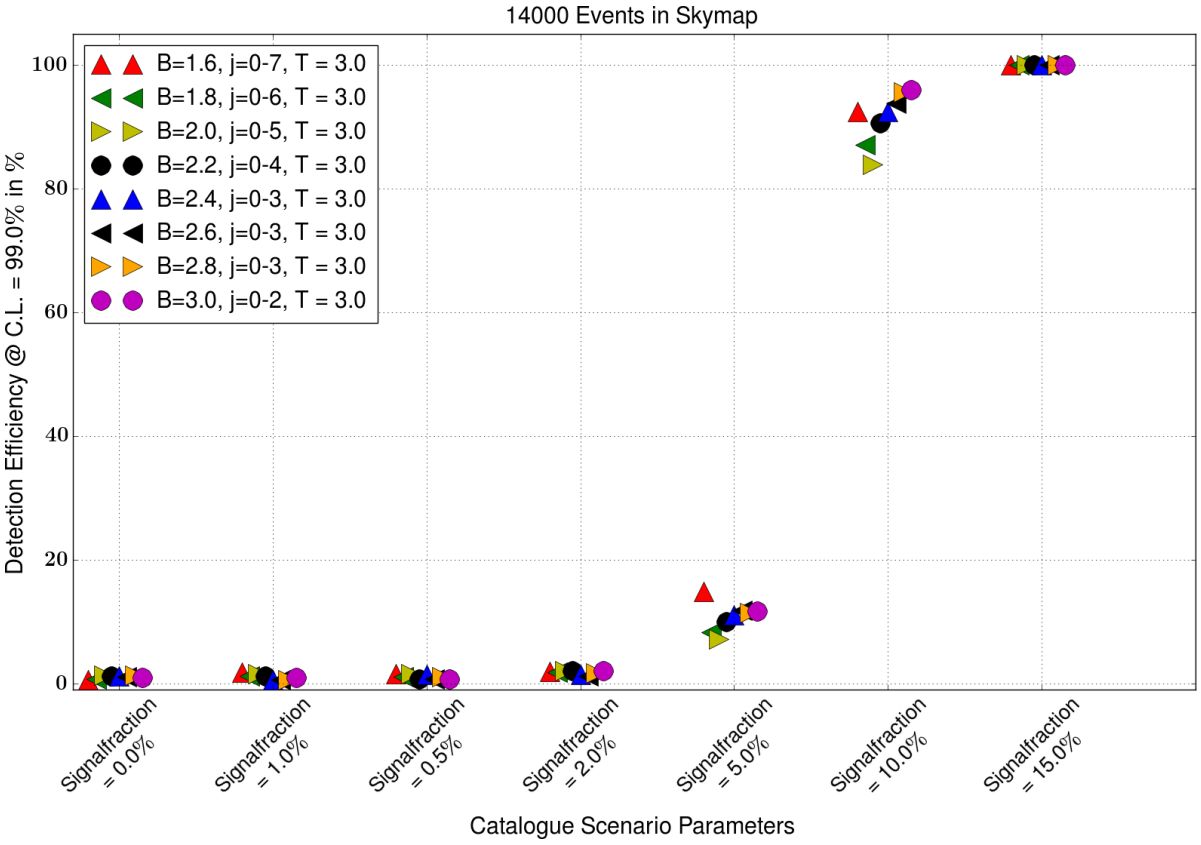
14000 Events in Skymap
B=1.6, j=0-7, T = 3.0
B=1.8, j=0-6, T = 3.0
B=2.0, j=0-5, T = 3.0
B=2.2, j=0-4, T = 3.0
B=2.4, j=0-3, T = 3.0
B=2.6, j=0-3, T = 3.0
B=2.8, j=0-3, T = 3.0
B=3.0, j=0-2, T = 3.0
Detection Efficiency @ C.L. = 99.0% in %
0
20
40
60
80
100
Signalfraction = 0.0%
Signalfraction = 1.0%
Signalfraction = 0.5%
Signalfraction = 2.0%
Signalfraction = 5.0%
Signalfraction = 10.0%
Signalfraction = 15.0%
Catalogue Scenario Parameters

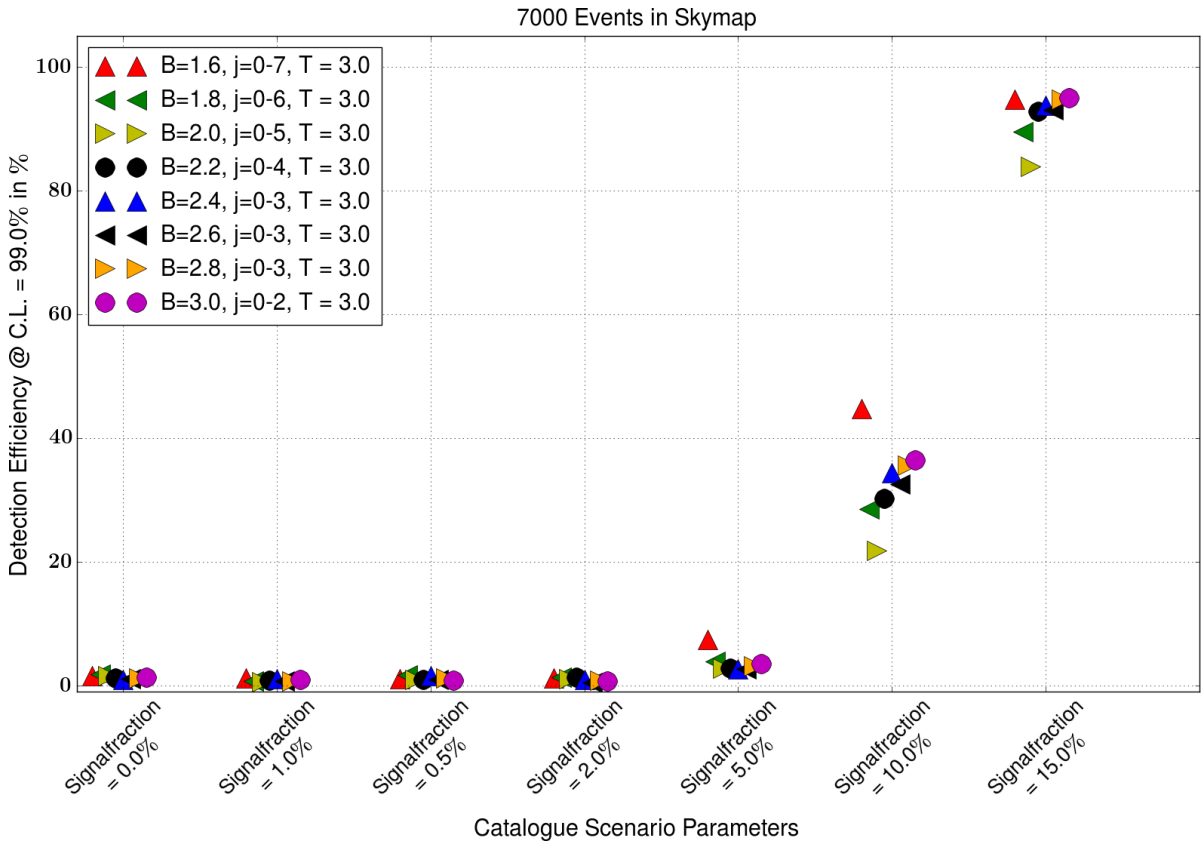
7000 Events in Skymap
B=1.6, j=0-7, T = 3.0
B=1.8, j=0-6, T = 3.0
B=2.0, j=0-5, T = 3.0
B=2.2, j=0-4, T = 3.0
B=2.4, j=0-3, T = 3.0
B=2.6, j=0-3, T = 3.0
B=2.8, j=0-3, T = 3.0
B=3.0, j=0-2, T = 3.0
Detection Efficiency @ C.L. = 99.0% in %
0
20
40
60
80
100
Signalfraction = 0.0%
Signalfraction = 1.0%
Signalfraction = 0.5%
Signalfraction = 2.0%
Signalfraction = 5.0%
Signalfraction = 10.0%
Signalfraction = 15.0%
Catalogue Scenario Parameters

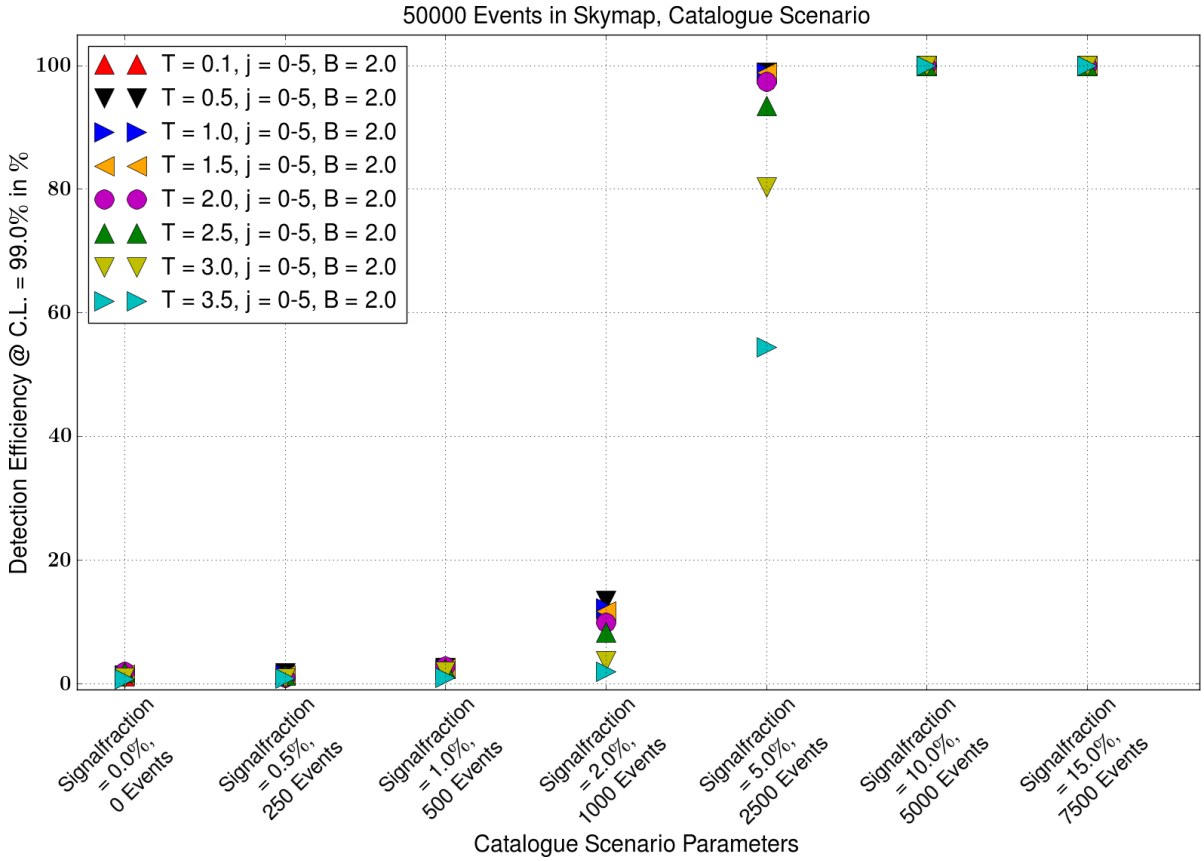
50000 Events in Skymap, Catalogue Scenario
T = 0.1, j = 0-5, B = 2.0
T = 0.5, j = 0-5, B = 2.0
T = 1.0, j = 0-5, B = 2.0
T = 1.5, j = 0-5, B = 2.0
T = 2.0, j = 0-5, B = 2.0
T = 2.5, j = 0-5, B = 2.0
T = 3.0, j = 0-5, B = 2.0
T = 3.5, j = 0-5, B = 2.0
Detection Efficiency @ C.L. = 99.0% in %
0
20
40
60
80
100
Signalfraction = 0.0%, 0 Events
Signalfraction = 0.5%, 250 Events
Signalfraction = 1.0%, 500 Events
Signalfraction = 2.0%, 1000 Events
Signalfraction = 5.0%, 2500 Events
Signalfraction = 10.0%, 5000 Events
Signalfraction = 15.0%, 7500 Events
Catalogue Scenario Parameters

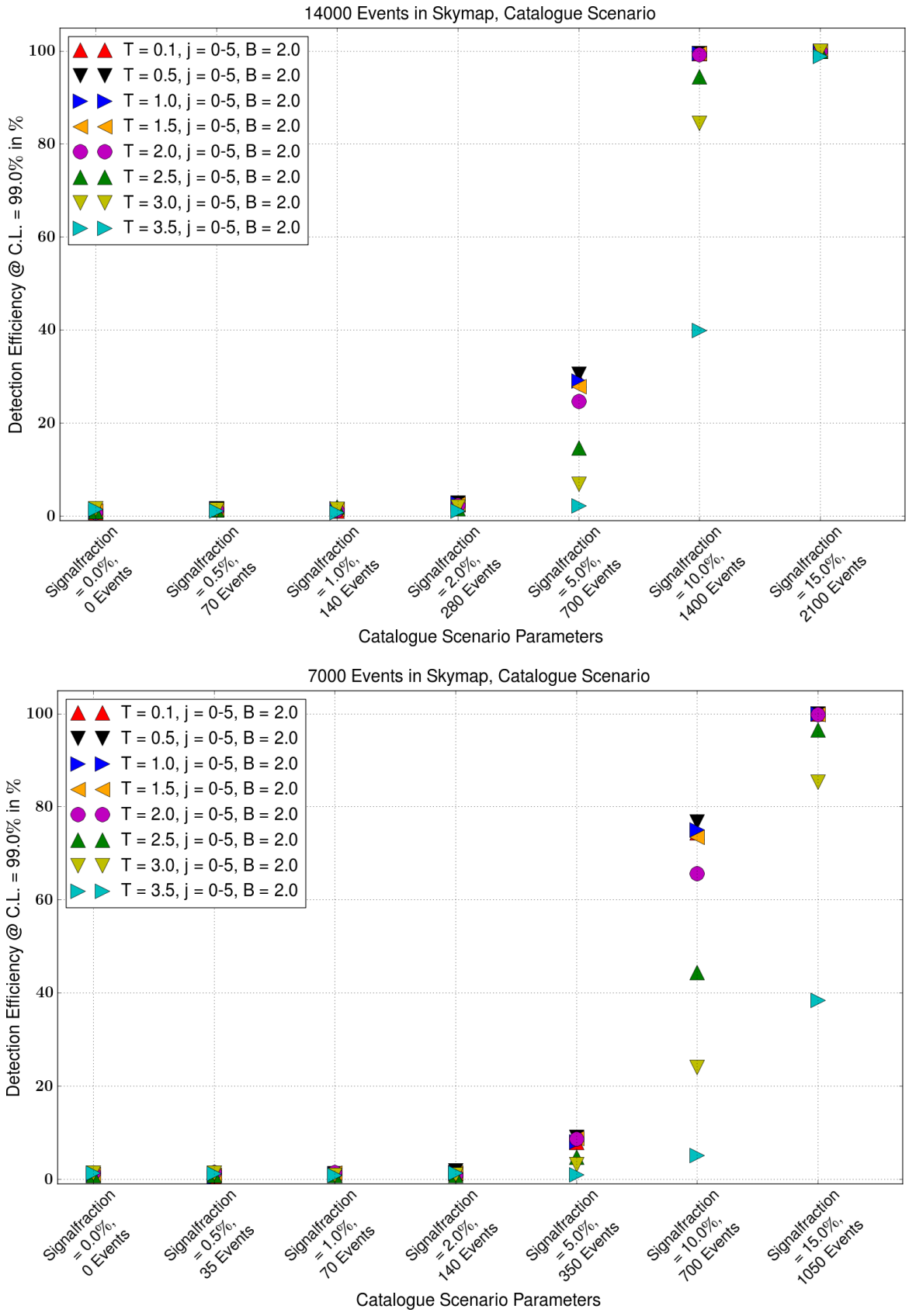

Figure 6.12.: Sensitivity to the catalogue scenario in section 6.3.5. **Top 3 figures:** Variable Needlet width B. **Bottom 3 figures:** Variable threshold T.

6.3.6. Analysis Parameters

Based on the results from the previous scenarios, one value for the Needlet width B and one value for the threshold needs to be chosen for the following analyses. In most scenarios there was no strong influence of the B parameter with a slightly higher overall sensitivity for B value between $B = 1.8$ and B=2.8 and preference for $B = 1.8$ to $B = 2.2$ in the case of the point source smeared with the GMF lens. For the following analyses we chose a value of $B = 2.0$ providing 6 Needlet scales ($j = 0 - 5$) to analyse the data. The choice of the threshold T is more difficult. There is an opposite preference for large and small scale scenarios and also a dependence on the total number of events in the skymap. Based on the results it would appear that it is beneficial to choose a different threshold for each of the Neetlet scales j. For example a low threshold for the dipole scale and a high threshold for smaller scales. However a low threshold on the dipole scale will still decrease the sensitivity to point sources as it still introduces additional noise in the combined skymap. Hence we continue to choose one threshold T for all scales to achieve an overall good sensitivity. We focus on the results from skymaps with 14,000 and 50,000 events as these numbers are close to the total number of events in the two energy bins used in the Auger data analysis in chapter 8. In the case of 50,000 events a value of $T = 3.0$ gives a high sensitivity to small scale structures without a large reduction in the sensitivity to large scale structures and the catalogue scenario. When $14,000$ events are present arguably $T = 2.5$ and $T = 3.0$ are reasonable choices to achieve an overall high sensitivity to various kinds of anisotropy. To keep the numbers of free parameters to a minimum and also in the expectation of an even higher event statistic in the future we choose a value of $T = 3.0$ for the following analyses. In the case of skymaps with a total number of events around 7,000 $T = 2.0$ would be a better overall choice.

Unless otherwise noted all following analyses will use the parameters summarised in table 6.8.

Table 6.8.: Analysis parameters

Healpix		
Resolution	N_{side}	32
Pixels	N_{Pixels}	12228
Needlet		
Needlet width	B	2.0
Threshold	T	3.0
Considered scales	j	0 to 5
$\leftrightarrow$ Max. multipole moment	l_{max}	64

6.4. Performance of the Angular Power Spectrum compared to the Needlet Wavelet Analysis

In this section we use the previously generated MC scenarios to compare the sensitivity of the Needlet analysis to that of the angular power spectrum (APS). Both methods are currently used to analyse the arrival directions detected at the Pierre Auger Observatory. We first give a short introduction to the angular power spectrum and its evaluation in the case of data which does not cover the whole sphere. After that we compare the sensitivities of both methods using the parameters from table 6.8. In the discussion we focus on the results of the skymaps with 14,000 and 50,000 events. The results from skymaps with 7,000 events can be found in the appendix B. We note that the analysis was not performed nor developed by the author of this work; instead the analysis and the results were kindly provided by Jaime Souza and Rogerio Menezes de Almeida of Universidade Federal Fluminense of Brazil which are also members of the Pierre Auger Collaboration. Both methods and their results are currently being prepared as publication from the Pierre Auger Collaboration (see Declaration of pre-released extracts at the end of this thesis).

6.4.1. The Angular Power Spectrum in Case of an Incomplete Sky Coverage

In its most basic form the APS is given by [115]:

$$C_\ell = \frac{1}{2\ell+1} \sum_{m=-\ell}^{\ell} |a_{\ell m}|^2. \tag{6.5}$$

The C_l coefficient is a measure of the averaged amplitude of the $a_{\ell m}$ in a particular scale l. It can be thought of as the standard deviation of a Gaussian on the sphere at a particular angular size. If the APS is plotted as a function of the multipole moment, it visualises how much correlation exists at a given angular scale. More specifically the APS can be viewed as a two point correlation function on the sphere encoding the correlation between two directions separated by an angular size of $\approx 180^\circ/l$ [52]. In the case of a full sky observatory a deviation from the isotropic expectation in a given C_l can be directly related to the presence of an anisotropy in the corresponding l scale. E.g. a significant C_1 or C_2 would indicate the presence of a dipole or quadrupole. Due to the non uniform and incomplete sky coverage of the Auger observatory a mixing between the multipole scales is introduced [103] and this inference is no longer valid. However, it has been shown in [115] that with the knowledge of the relative coverage of the experiment $W(\mathbf{n})$ (see equation 3.8) it is, on average, possible to decouple the different C_l coefficients. The basic idea behind the decoupling is that the harmonic expansion of the measured flux $\tilde{\Phi}(\mathbf{n}) = \Phi(\mathbf{n}) * W(\mathbf{n})$ which is the convolution of the actual flux and the relative exposure, is itself the convolution of the harmonic transforms of $\Phi(\mathbf{n})$ and $W(\mathbf{n})$ separately[115]. Based on this, it is possible to, on average, relate the mode-coupled APS $\left\langle \tilde{C}_\ell \right\rangle$ of $\tilde{\Phi}(\mathbf{n})$

to the true underlying APS $\langle C_\ell \rangle$ via

$$\left\langle \tilde{C}_{\ell_1} \right\rangle = \sum_{\ell_2} M_{\ell_1 \ell_2} \langle C_{\ell_2} \rangle \,. \tag{6.6}$$

The matrix $M_{\ell_1 \ell_2}$ is given by

$$M_{\ell_1 \ell_2} = \frac{2\ell_2 + 1}{4\pi} \sum_{\ell_3} (2\ell_3 + 1)\, W_{\ell_3} \begin{pmatrix} \ell_1 & \ell_2 & \ell_3 \\ 0 & 0 & 0 \end{pmatrix}^2 . \tag{6.7}$$

Here $W_{\ell_3} = \frac{1}{2\ell_3+1} \sum_m |\omega_{\ell_3 m}|^2$ is the APS of the relative coverage $W(\mathbf{n})$.

The true underlying C_ℓ can be recovered (on average) via inversion of the matrix $M_{\ell_1 \ell_2}$:

$$\left\langle C^{exp}_{\ell_2} \right\rangle = \sum_{\ell_1} M^{-1}_{\ell_1 \ell_2} \left\langle \tilde{C}_{\ell_1} \right\rangle . \tag{6.8}$$

Based on the recovered APS a global anisotropy estimator is defined (see also 5.7, inspired from Hülss in [101]):

$$D^2 := \frac{1}{\ell_{max}} \sum_{\ell=1}^{\ell_{max}} \left(\frac{C_{\ell,data} - \langle C_{\ell,iso} \rangle}{\sigma_{\ell,iso}} \right)^2 . \tag{6.9}$$

Here, $C_{\ell,data}$ is obtained from a given data or test skymap. $C_{\ell,iso}$ and $\sigma_{\ell,iso}$ are the average and standard deviation of the C_l coefficients, obtained from isotropic MC simulations with the same number of events in the data/test skymap. As in the case of the Needlet analysis, the evaluation of the APS and the global anisotropy estimator can be restricted up to an $l_{\max}$ appropriate to the intended search. In the following, we show the sensitivity of both methods to the previously described benchmark scenarios[5] at a C.L. of 99%. The Needlet parameters are given by table 6.8. The chosen $l_{\max}$ for the APS is 64 equivalent to the considered Needlet scale $j = 0 - 5$. The commonly analysed scenarios include the Auger coverage with a maximum zenith angle of 60°.

Dipole and Quadrupole Scenarios

The comparison of the sensitivity of both methods is shown in figure 6.13. The corresponding scenario is described in section 6.3.1. In the case of 50,000 events in the skymap the APS has a slightly higher dipole sensitivity compared to the Needlet analysis. This is further increased when the number of total events drops down to 14,000. As pointed out previously, the sensitivity of the Needlet analysis can be increased by lowering the threshold at the expense of sensitivity to small scale structures. No conclusion can be drawn in the case of the quadrupole as only one data point is available for the APS and both methods have a negligible sensitivity to the weak quadrupole in this case. The

[5] In some cases no information on the sensitivity of the APS is available for a given set of parameters. These are omitted from the figures.

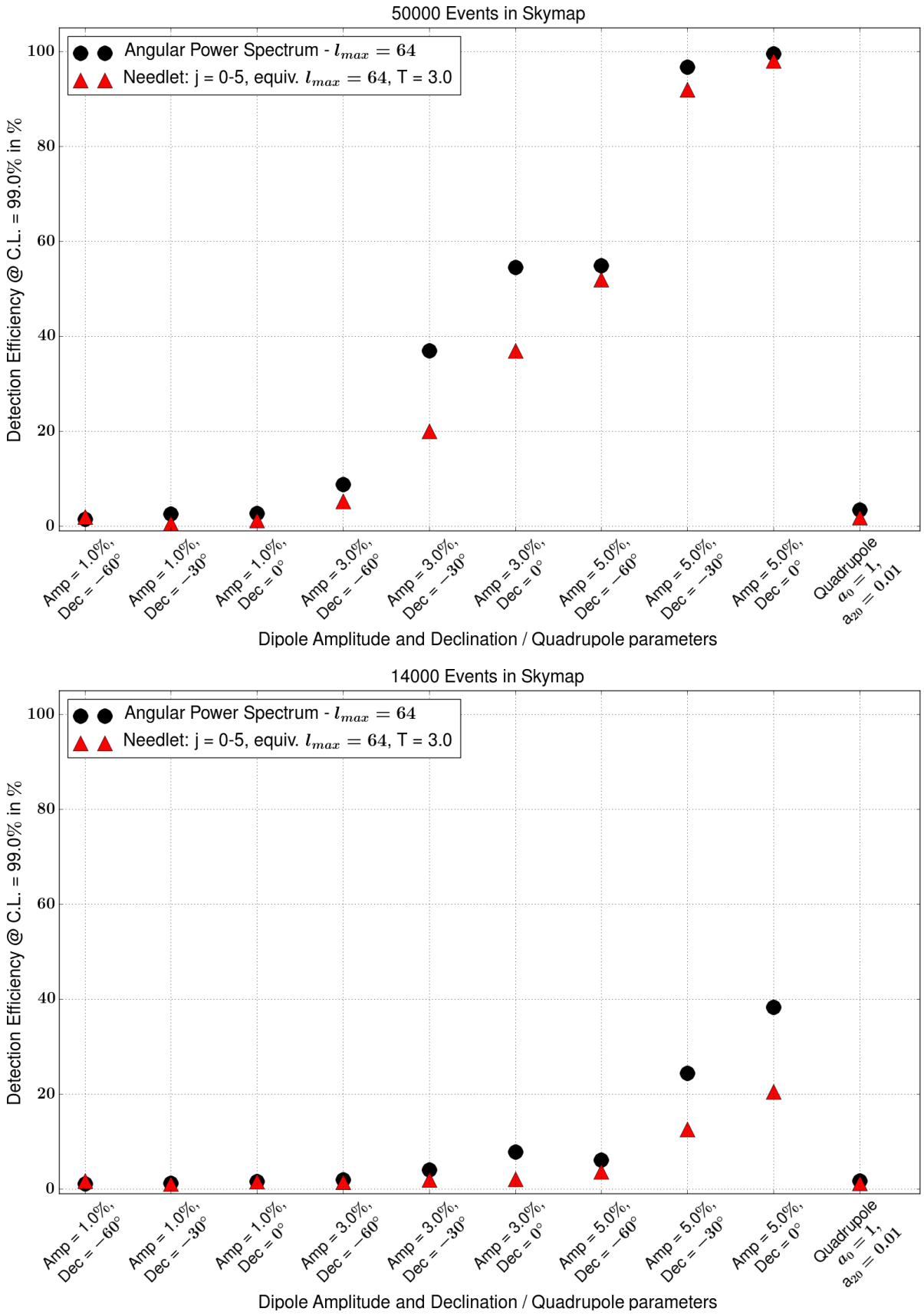

Figure 6.13.: Sensitivity of the APS (black circles) and Needlet analysis (red triangles) to the dipole and quadrupole scenario described in section 6.3.1.

sensitivity of both analyses restricted to be most sensitive to dipolar and quadrupolar anisotropy are shown in figure 6.14. The APS was restricted to an $l_{\max} = 1$ and $l_{\max} = 2$ for the dipolar and quadrupole analysis respectively. The Needlet analyses either to $j = 0$ or $j = 0 - 1$. Here the situation is different from the unrestricted analysis. In most cases the APS and Needlet analyses provide a similar sensitivity. An exception is present when the declination of the dipole is at $\delta_d = -60°$. Here the Needlet analysis achieves a higher sensitivity suggesting a faster drop in dipole sensitivity of the APS towards the poles.

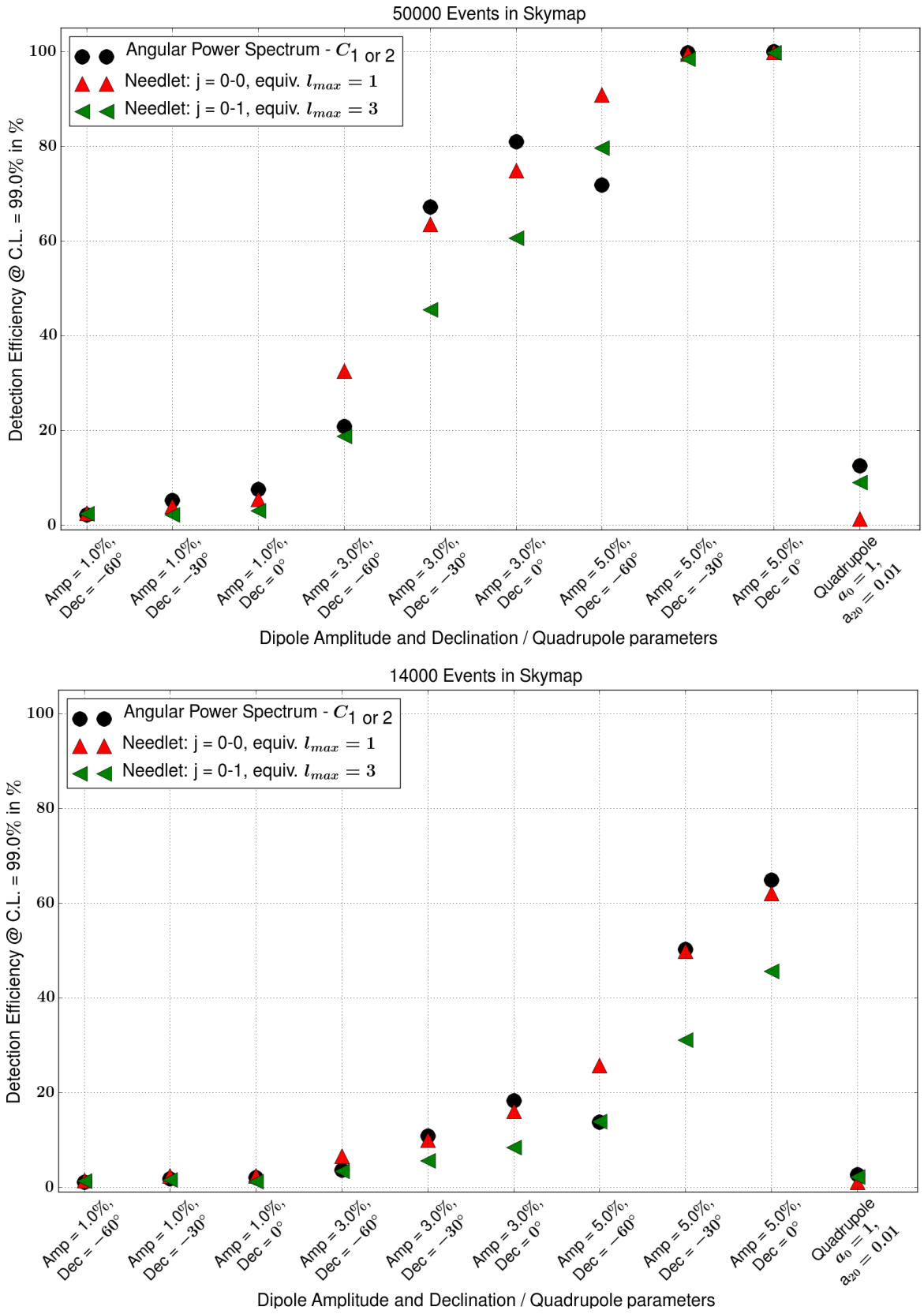

Figure 6.14.: Sensitivity of the APS (black circles) and Needlet analysis (red triangles) to the dipole and quadrupole scenario described in section 6.3.1. The analysis ranges are restricted to be most sensitive to a dipolar and quadrupolar anisotropy.

Single Point Source Scenario

The comparison of the sensitivity of both methods is shown in figure 6.15. The corresponding scenario is described in section 6.3.2. In this scenario the Needlet analysis clearly possesses a higher sensitivity in comparison to the APS. The reason is the ability of the Needlet analysis to filter out localised noise in the corresponding Needlet scale where the point source is present. In contrast the averaging over all a_{lm} coefficients and hence over the whole (visible) sky of the APS reduces its sensitivity to localized excesses.

Single Point Deflected through the GMF

The comparison of the sensitivity of both methods is shown in figure 6.16 with and without the application of the GMF lens. The corresponding scenario is described in section 6.3.3. As in the previous scenario the Needlet analysis achieves a higher sensitivity in comparison to the APS and for the same reason as outlined before.

Combined Dipole and Point Source Scenario

The comparison of the sensitivity of both methods is shown in figure 6.17. The corresponding scenario is described in section 6.3.4. As expected from the previous results the APS has a slightly higher sensitivity when the signal fraction of the point source is small and hence the contribution of the dipole is relatively strong. When the point source signal fraction becomes larger the Needlet analysis achieves a higher sensitivity.

Catalogue Based Scenario

The comparison of the sensitivity of both methods is shown in figure 6.18. The corresponding scenario is described in section 6.3.5. In this case both methods achieve a comparable performance with a slightly higher sensitivity of the APS.

6.4.2. Discussion

The sensitivity to various kinds of anisotropy of the APS and the Needlet analysis were compared. In general the APS provides a slightly higher sensitivity towards large scale structures in comparison to the Needlet analysis. In contrast, the localized filtering of the Needlet analysis allows for a higher sensitivity towards small scale structure. An advantage of the APS as described here is that it corrects for the correlation between the C_ls whereas this is not the case in the Needlet analysis. On the other hand the Needlet analysis gives a reconstructed skymap of the observed anisotropies allowing both to obtain the position of the anisotropy, as described in section 8.2, and also to restrict the analysis to parts of the sky, as described in section 8.3.

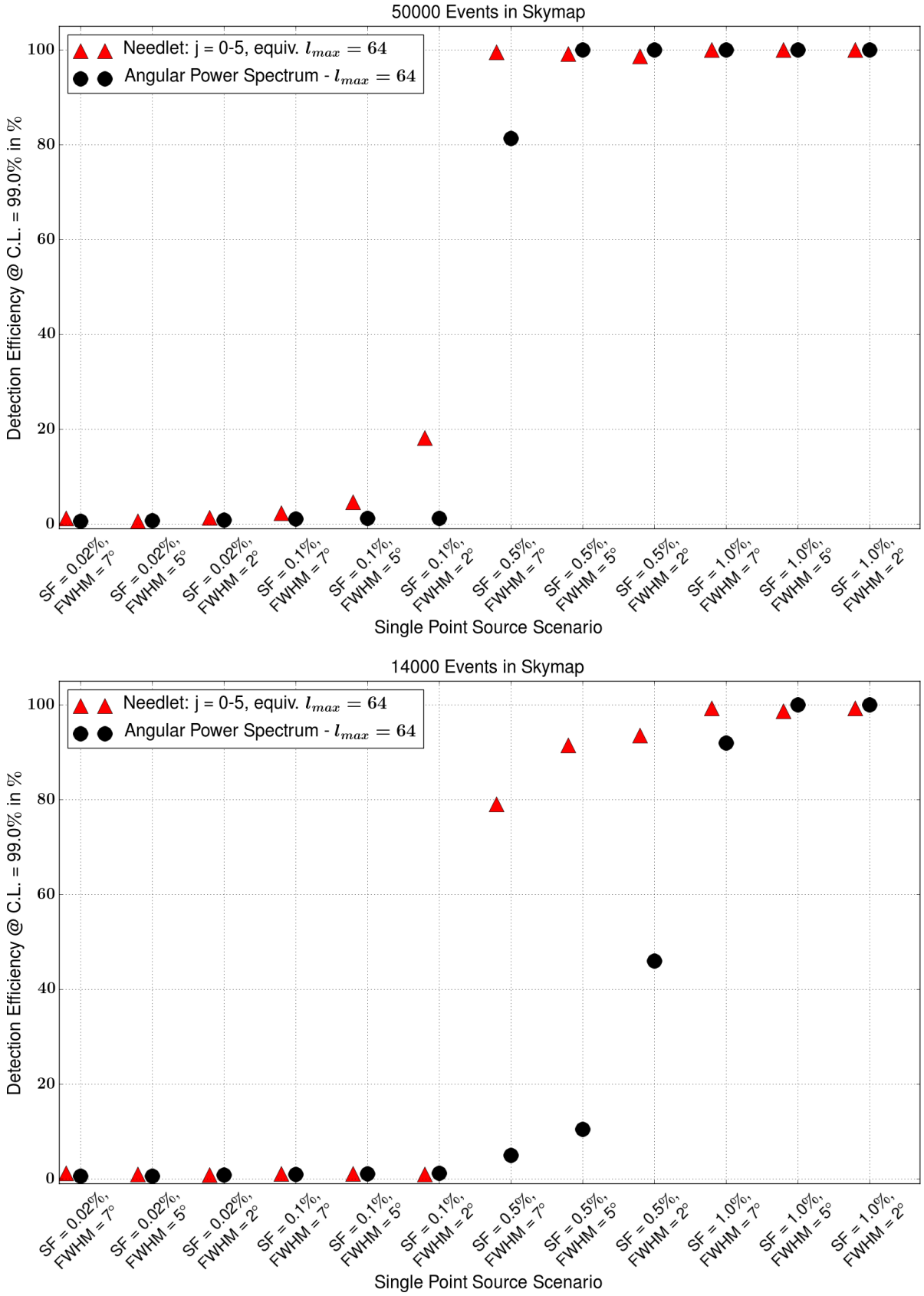

Figure 6.15.: Sensitivity of the APS (black circles) and Needlet analysis (red triangles) to the single point source scenario described in section 6.3.2.

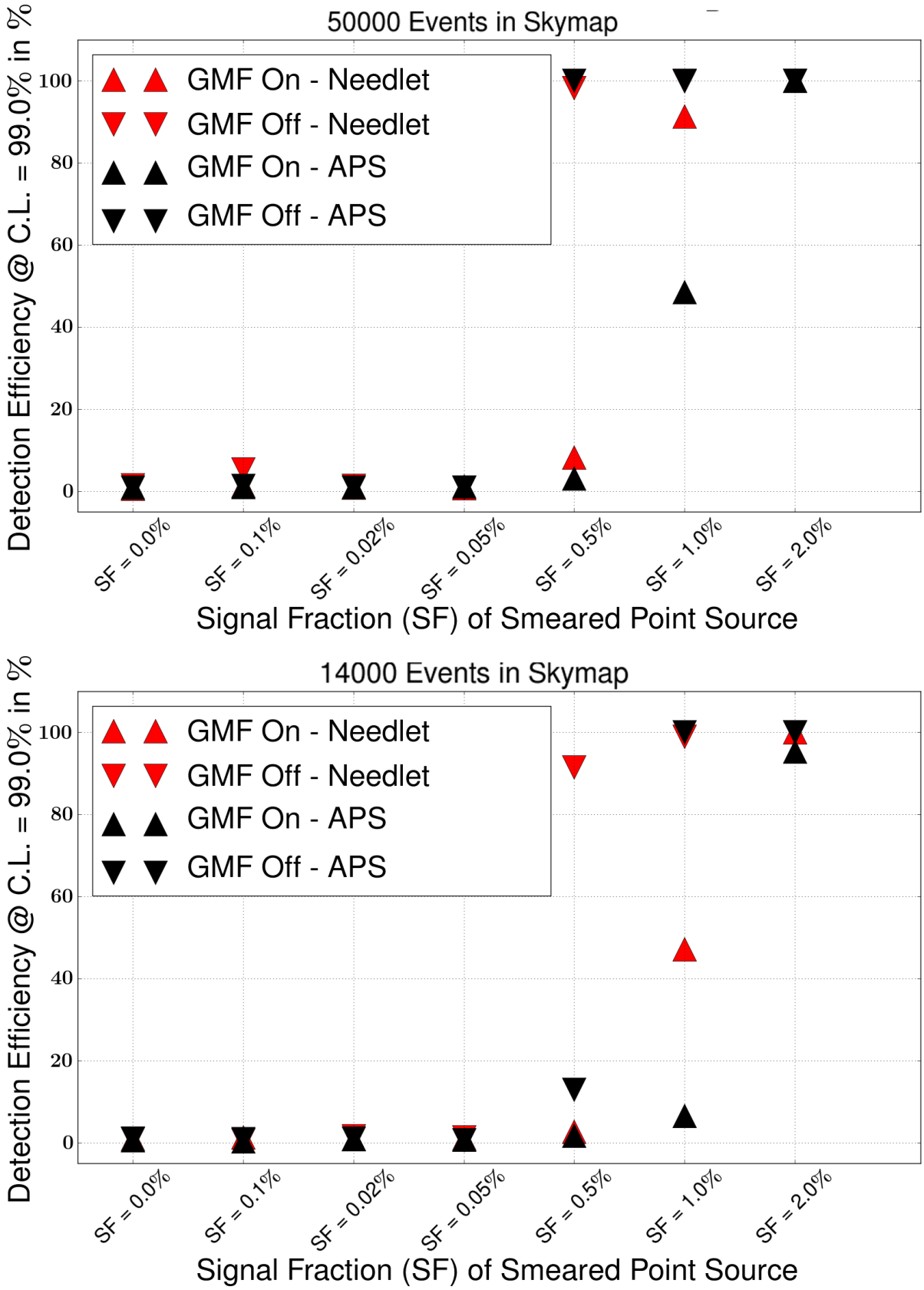

Figure 6.16.: Sensitivity of the APS (black triangles) and Needlet analysis (red triangles) to the single point source smeared through the GMF scenario described in section 6.3.3.

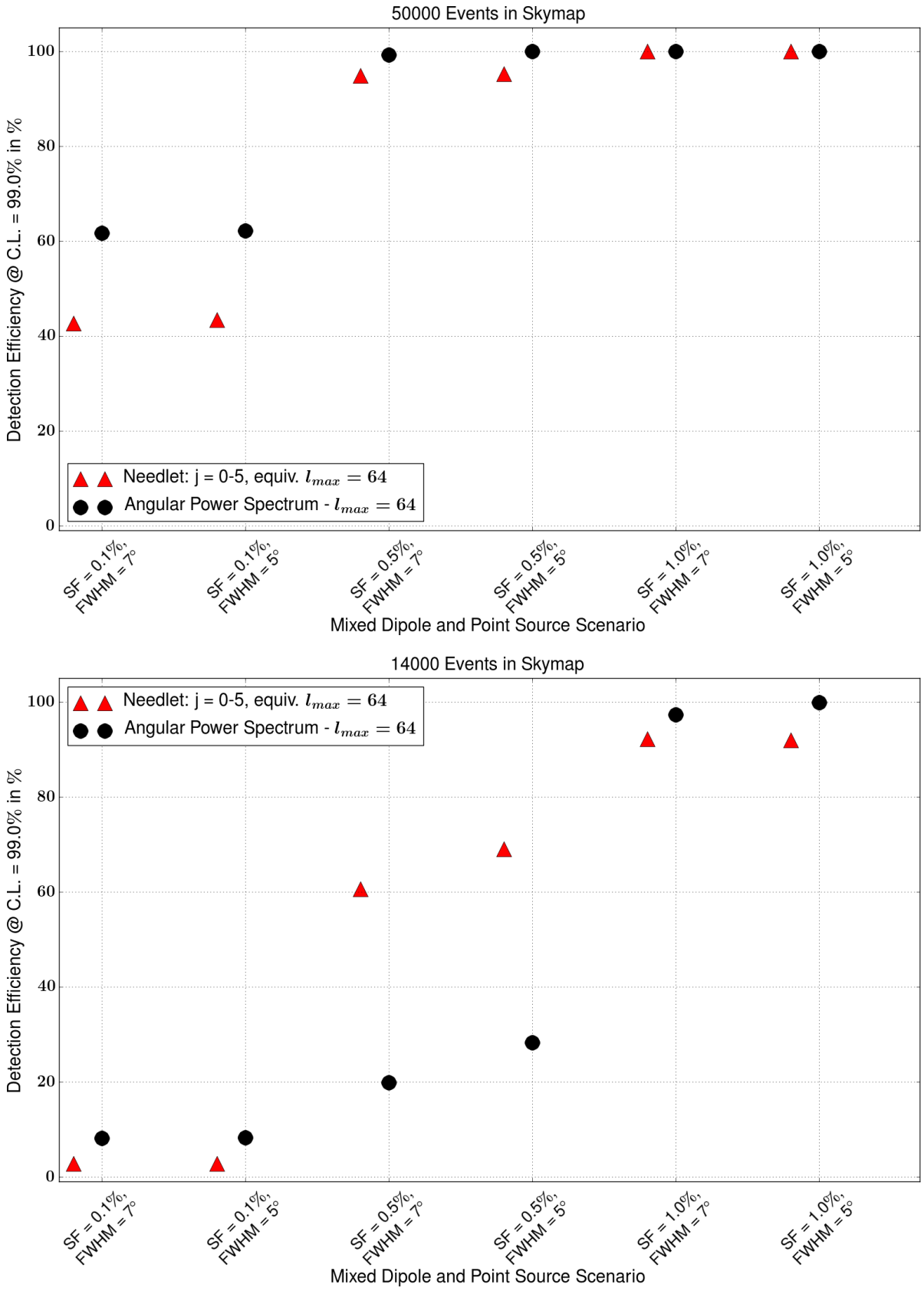

Figure 6.17.: Sensitivity of the APS (black circles) and Needlet analysis (red triangles) to the mixed dipole and point source scenario described in section 6.3.4.

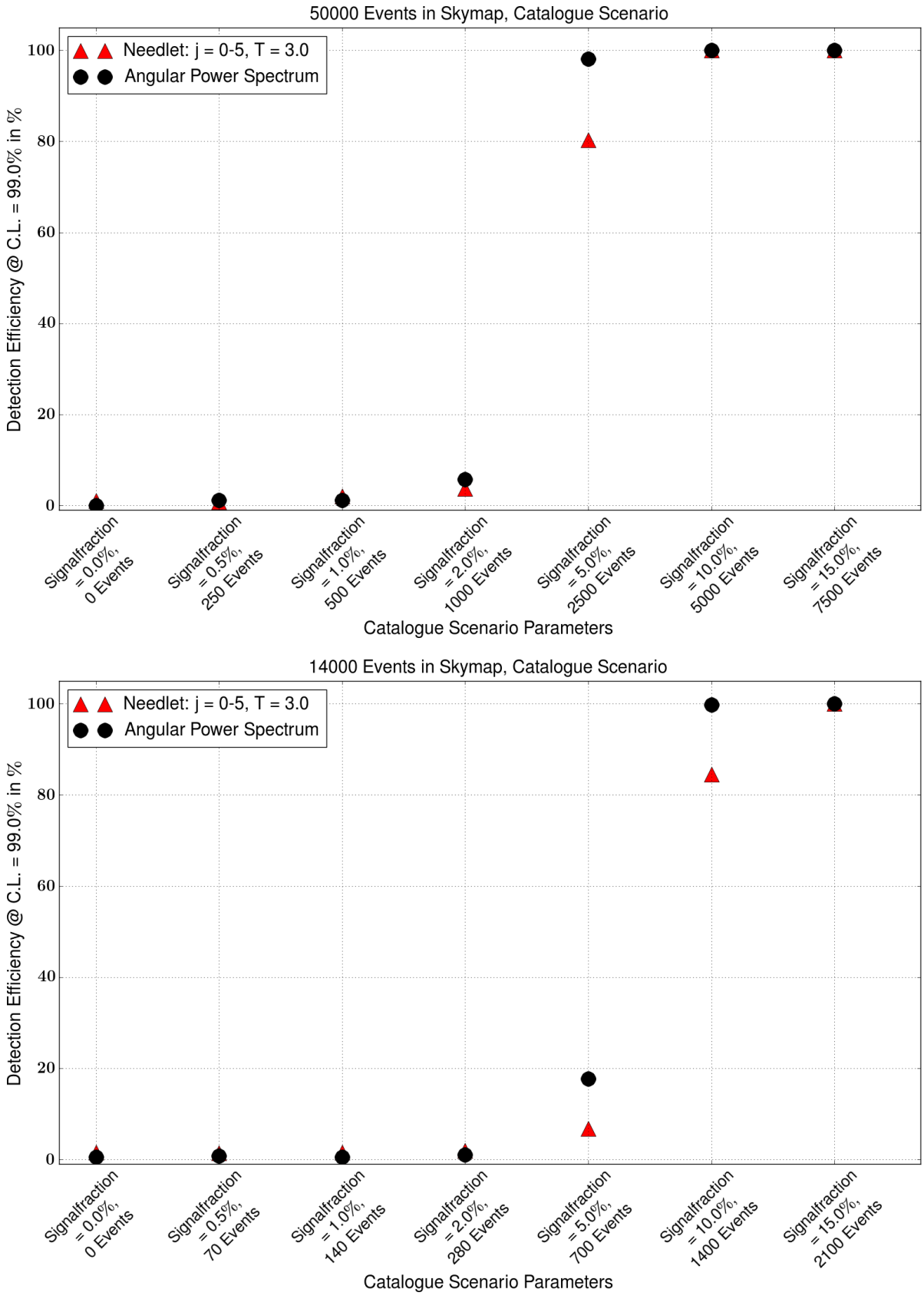

Figure 6.18.: Sensitivity of the APS (black circles) and Needlet analysis (red triangles) to the catalogue scenario described in section 6.3.5.

6.5. Summary

In this chapter the sensitivity of the Needlet analysis to various kinds of anisotropies was evaluated and compared to the sensitivity of the APS. Based on the results the parameters for the following analyses have been chosen as summarized in table 6.8 on page 115. The next chapter will present the used data set to which the analysis is applied in chapter 8 using the parameters determined here.

7. Data Set

The data set and reconstruction used in this analysis is the same used in [34], consisting of events detected with the surface detector (SD) of the Pierre Auger Observatory starting at 1/1/2004 up to 31/12/2013. It consists of both events with a zenith angle smaller than 60° (vertical events) and of events with a zenith angle from 60° up to 80° (inclined events). The data set is divided in two energy bins: 4 EeV $\leq$ E $<$ 8 EeV and E $\geq$ 8 EeV. Above 4 EeV the SD becomes fully efficient for both vertical and horizontal events. This allows to determine the exposure (see figure 7.1) using equation 3.8, as systematic uncertainties on trigger and other effects become negligible. The corresponding total exposures are 37,142 km^2 sr yr for the vertical events and 10,887 km^2 sr yr for the inclined events. Shown in figure 7.1 is the exposure of both vertical and horizontal events as well as the combined exposure as a function of the declination. Table 7.1 summarises the total number of events used in this work for both energy ranges.

Energy range (EeV)	$\theta < 60°$	$60° \leq \theta \leq 80°$
4 - 8	39,049	11,368
≥ 8	15,418	4,379

Table 7.1.: Number of events for vertical and inclined data sets of the two energy bins used in this analysis. A skymap of both energy bins is shown in figure 8.1.

For vertical events we require that all six water-Cherenkov detectors (WCD) surrounding the station with the largest signal are operational at the time the event was recorded (6T5-trigger). An illustration of this configuration is shown on the right-hand side of figure 3.6. For inclined events we require that six stations around the station closest to the core position to be active at the time of detection. These requirements assure an accurate reconstruction of the shower geometry [42].

7.1. Correction for Detector Effects

In order to avoid spurious effects due to array growth[1] as well as the dead periods of each detector, we correct the exposures considering the variations in the number of active elemental cells. The small tilt of the array of about 0.2° towards a direction 30° from the

[1]The deployment of the SD detector stations started in 2004 and was completed in 2007. During that time the deployed detector stations recorded data leading to a steadily increasing detector area.

East to the South ($\phi_{tilt} = -30°$) modulates the effective elemental cell area. To correct for these two effects, every event is weighted by a factor given by

$$[\Delta N_{cell}(\alpha_0)]^{-1} \times [1 + 0.003 \tan\theta \cos(\phi - \phi_{tilt})]^{-1} . \quad (7.1)$$

Here $\Delta N_{cell}(\alpha_0)$ is the relative variation of the total number of active cells as a function of the sidereal time, α_0, and θ and ϕ are the local arrival direction coordinates (zenith and azimuth respectively) of the air shower [32]. The correction for the number of active elemental cells includes the exclusion of 'bad-periods' from the data. Causes for bad-periods include maintenance, software updates and instabilities in communications.

Moreover, the energy estimator $S(1000)$ (see section 3.2) is affected by the geomagnetic field as described in [116] and by current atmospheric conditions such as pressure as described in [117]. In a fixed energy threshold analysis, such as this one, these effects could introduce spurious anisotropies into the analysis. To avoid this, the energy estimator is corrected for these weather and geomagnetic effects as described in [116, 117]. A correction of the energy estimator of inclined events N_{19} (see section 3.2) is not necessary as the geomagnetic field is already included in the reconstructions and the weather effects do not influence the muonic component which dominates horizontal events [34].

An overview over the individual corrections can be found in [32].

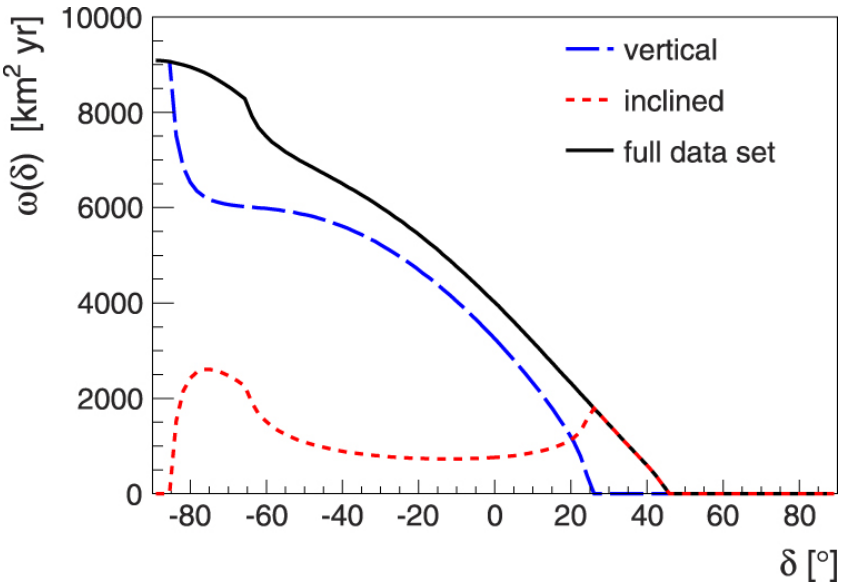

Figure 7.1.: Exposure of vertical, horizontal and combined data set as a function of the declination [34].

8. Data Analysis

The Needlet analysis described in chapter 5 with the analysis parameters summarised in table 6.8 is now applied to the data set described in the previous chapter. In section 8.1 both energy bins ($E = 4 - 8$ EeV, $E \geq 8$ EeV) are analysed using all available Needlet scales $j = 0 - 5$ to search for anisotropy of various kinds in the measured arrival directions of UHECRs at the Pierre Auger Observatory. As the only observed significant deviation from isotropy is a dipolar signal in the $E \geq 8$ EeV bin, we further analyse and characterise this signal in section 8.2. This includes data based cross-checks to establish the stability of the observed signal; this is described in section 8.2.3. Finally, in section 8.3, we exploit the localized nature of the higher Needlet scales to restrict the search to a region of the sky to look for a signal from the AGN closest to earth, Centaurus A.

8.1. Global Anisotropy Search

As described in the previous chapter, we divide the data into two separate energy bins: 4 EeV $\leq$ E $<$ 8 EeV with a total number of events of 50,417 and E $\geq$ 8 EeV with a total number of events of 19,797. The binned input data of both energy bins is shown in figure 8.1. Using the analysis parameters outlined in table 6.8, on page 115 we apply the Needlet analysis to both energy bins.

First we analyse, the 4 EeV $\leq$ E $<$ 8 EeV bin. The individual reconstructed S_{jk} skymaps are shown in figure 8.4. On the left-hand side of figure 8.2 the global anisotropy estimator as well as the reference S-value distribution ($j = 0 - 5$) of 500,000 isotropic Monte Carlo skymaps are shown. The black (dashed) line shows the S-value of the Auger data set and the red (straight) line represents the 99% C.L. limit. Of all isotropic skymaps 27% have either the same or a higher significance (p-value) and hence no deviation from isotropy is detected. The p-values of the individual reconstructed S_{jk} skymaps are shown on the right-hand side of figure 8.2 as a function of the Needlet scale j. Again no deviation from isotropy is observed in any j-scale. The filtered sum skymap of all scales $j = 0 - 5$ is shown on the top of figure 8.6, sharing the same range with the $E \geq 8$ EeV skymap below. A version with the range limited to the maximum and minimum of the 4 EeV $\leq$ E $<$ 8 EeV skymap can be found in appendix B (B.8). As can be seen, no large scale structure is visible in the skymap. Only small scale excesses remain. The largest excess is located around $(\alpha, \delta) = (280°, -35°)$. The maximum corresponding $S_{k,j=1-5}$ value is around 7.1, however the global significance is low as seen in figure 8.2. The high local excess arises due to the addition of a small scale excess in j=5 (see figure 8.4) of around $S_{k,j=5} = 3.5$ and additional contributions from $j = 1$ and $j = 2$ (also see figure 8.4).

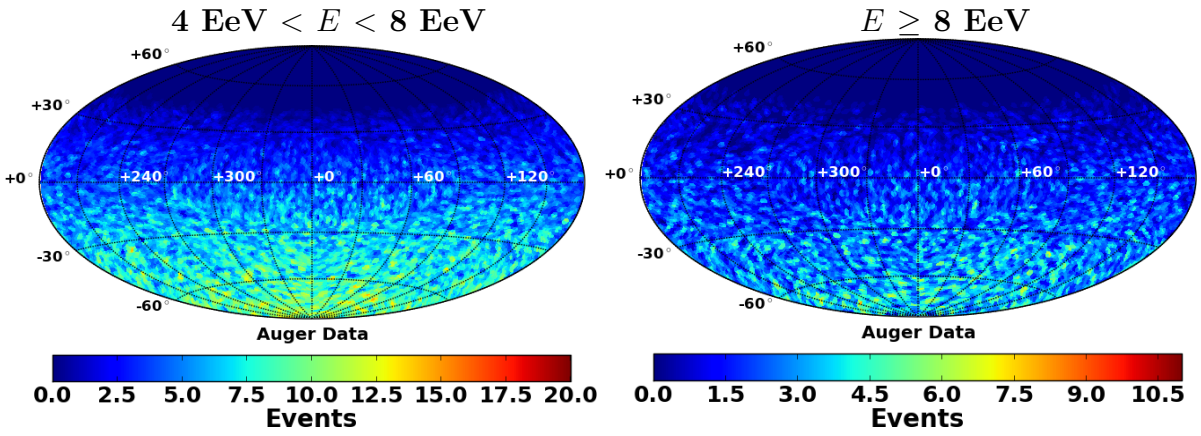

Figure 8.1.: Measured arrival directions by the SD of the Pierre Auger Observatory from 01/01/2004 to 12/31/2013 with a maximum zenith angle of 80° and an energy E of 4 EeV $\leq$ E $<$ 8 EeV (left) and E $\geq$ 8 EeV (right).

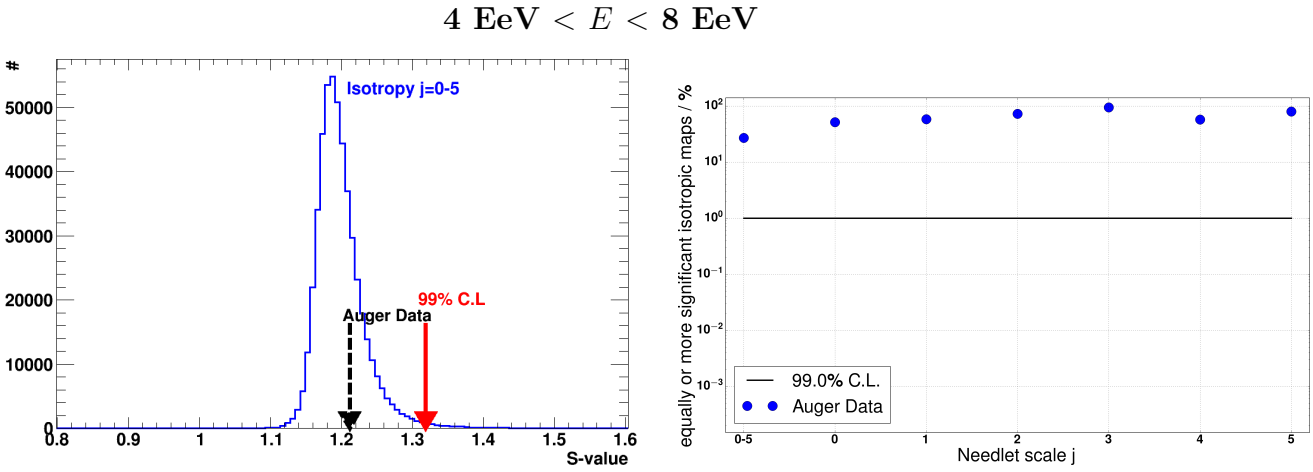

Figure 8.2.: The results from the Needlet analysis for 4 EeV $<$ E $<$ 8 EeV and $j = 0-5$. In the left image the S-value distribution from 500,000 isotropic simulations for $j = 0-5$ is shown. The red (straight) arrow represents the S-value threshold to accept/reject the isotropy hypothesis with 99% C.L.. The S-value from data, represented by the black (dashed) arrow, is smaller than that threshold supporting the isotropy hypothesis. In the right image the p-value of the individual reconstructed S_{jk} skymaps, as a function of the Needlet scale j, as well as of $j = 0-5$ is shown. The large p-values are due to the fact that the individual S_{jk} skymaps do not pass the applied threshold (see eqn. (5.5)).

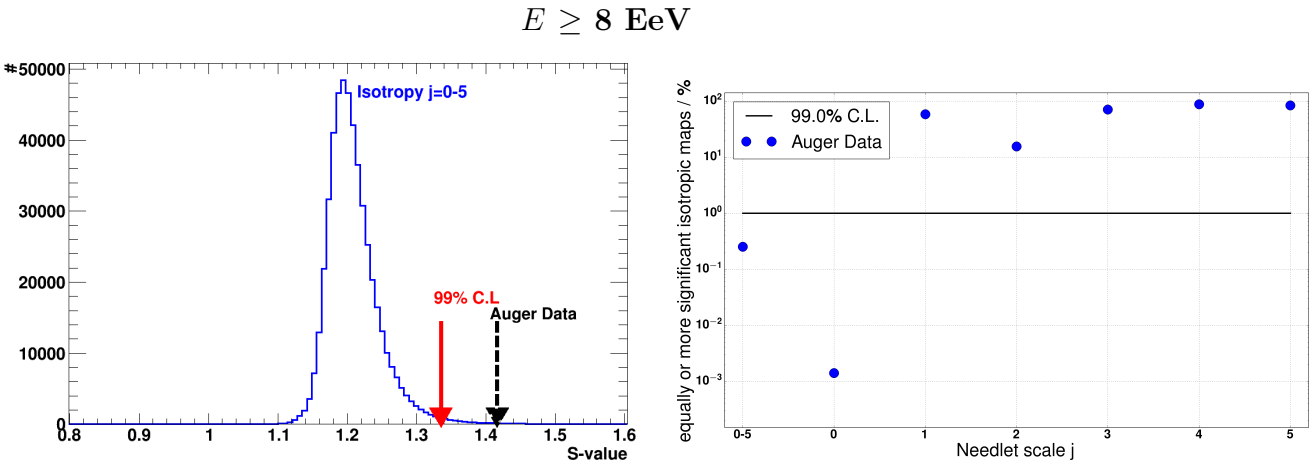

Figure 8.3.: The results from the Needlet analysis for E $\geq$ 8 EeV and $j = 0 - 5$. In the left image the S-value distribution from 500,000 isotropic simulations for $j = 0 - 5$ is shown. The red (straight) arrow represents the S-value threshold to accept/reject the isotropy hypothesis with 99% C.L.. The S-value from data, represented by the black (dashed) arrow, is larger than that threshold which gives a hint of deviation from the isotropy hypothesis. A detailed look into the individual Needlet scales shows that only the Needlet scale $j = 0$ deviates from isotropy pointing towards an anisotropy compatible with a dipolar anisotropy. In the right image the p-value of the individual reconstructed S_{jk} skymaps, as a function of the Needlet scale j, as well as of $j = 0 - 5$ is shown.

Next, we analyse the E $\geq$ 8 EeV bin. The individual reconstructed S_{jk} skymaps are shown in figure 8.5. The global anisotropy estimator of the E $\geq$ 8 EeV energy bin is shown on the left-hand side of figure 8.3. In the case of this bin, a hint of deviation from isotropy of the global anisotropy estimator from $j = 0 - 5$ is observable. The probability of this global estimator to arise by chance from an isotropic distribution is $p = 2.5 \times 10^{-3}$ (not accounting for the search in two energy bins). A look into the individual reconstructed S_{jk} skymaps, as a function of the Needlet scale j, on the right hand side of figure 8.3 shows that the only significant deviation from isotropy is detected in the $j = 0$ (i.e. dipolar) scale. Indeed only 0.0014% of the 500,000 simulated isotropy skymaps possesses an equal or higher significance if the search is explicitly restricted to $j = 0$ a posteriori. If the search includes all (i.e. $j = 0 - 5$) Needlet scales the p-value increases to the above mentioned value. The dipole also appears as the most dominant structure in the filtered, sum skymap of all scales $j = 0 - 5$ at the bottom of 8.6.

In summary, a hint of deviation from isotropy was observed from the global anisotropy estimator of the $E \geq 8$ EeV bin with a probability of the global anisotropy estimator arising by chance of $p = 2.5 \times 10^{-3}$. A look into the individual Needlet scales shows only the $j = 0$, i.e. dipolar, scale deviates from isotropy. No other deviations from isotropy were observed for any other Needlet scale or energy. This observation is compatible with and extends the results reported by the Pierre Auger Collaboration in [34] which also observed a dipolar deviation from isotropy in the same data set and energy bins, but was

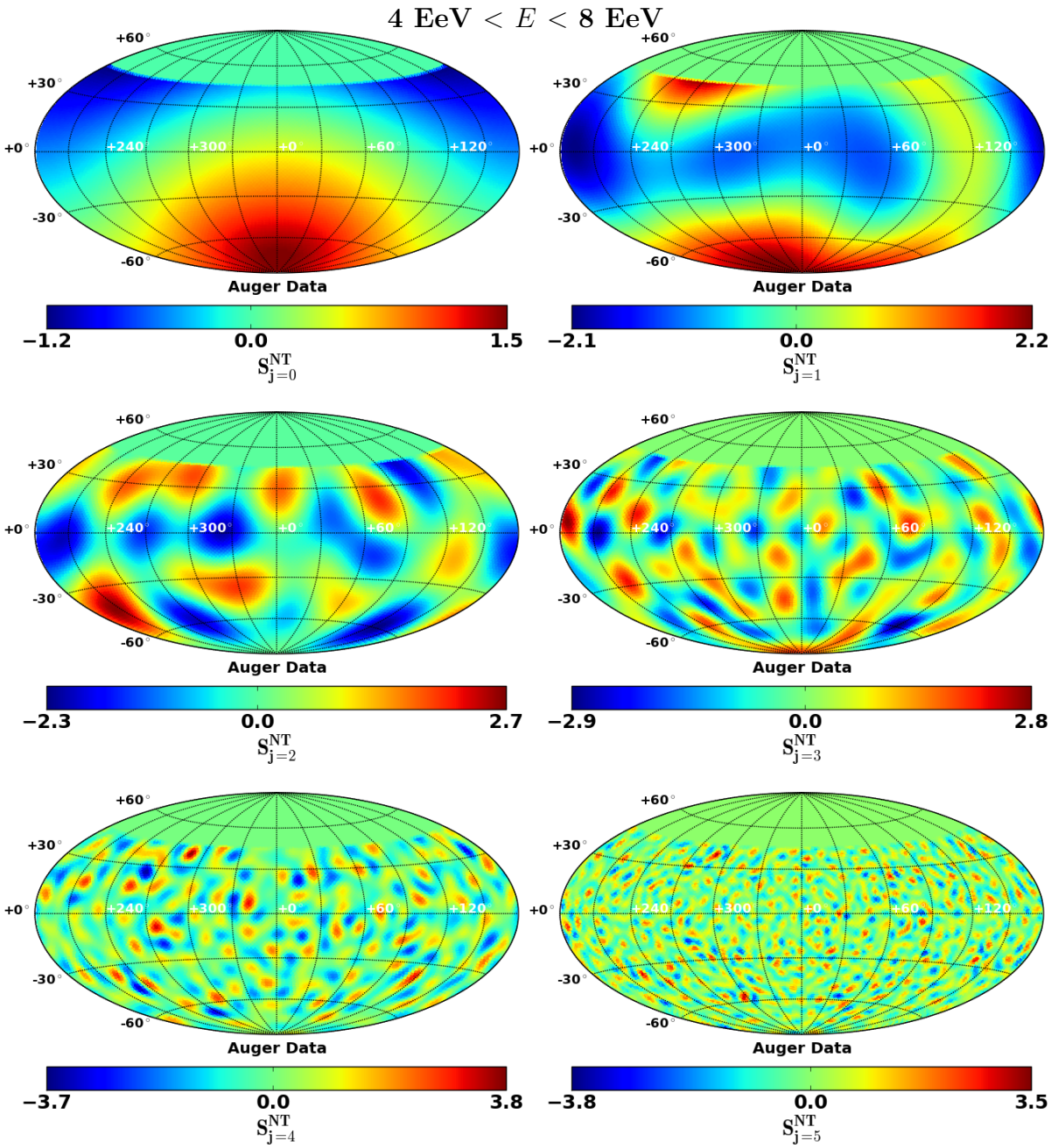

Figure 8.4.: Reconstructed but not thresholded skymaps S_{jk}^{NT} for 4 EeV $< E <$ 8 EeV. From left to right and from top to bottom the Needlet scales are $j = 0, 1, 2, 3, 4, 5$. For better visibility of particular features all scales have their individual range.

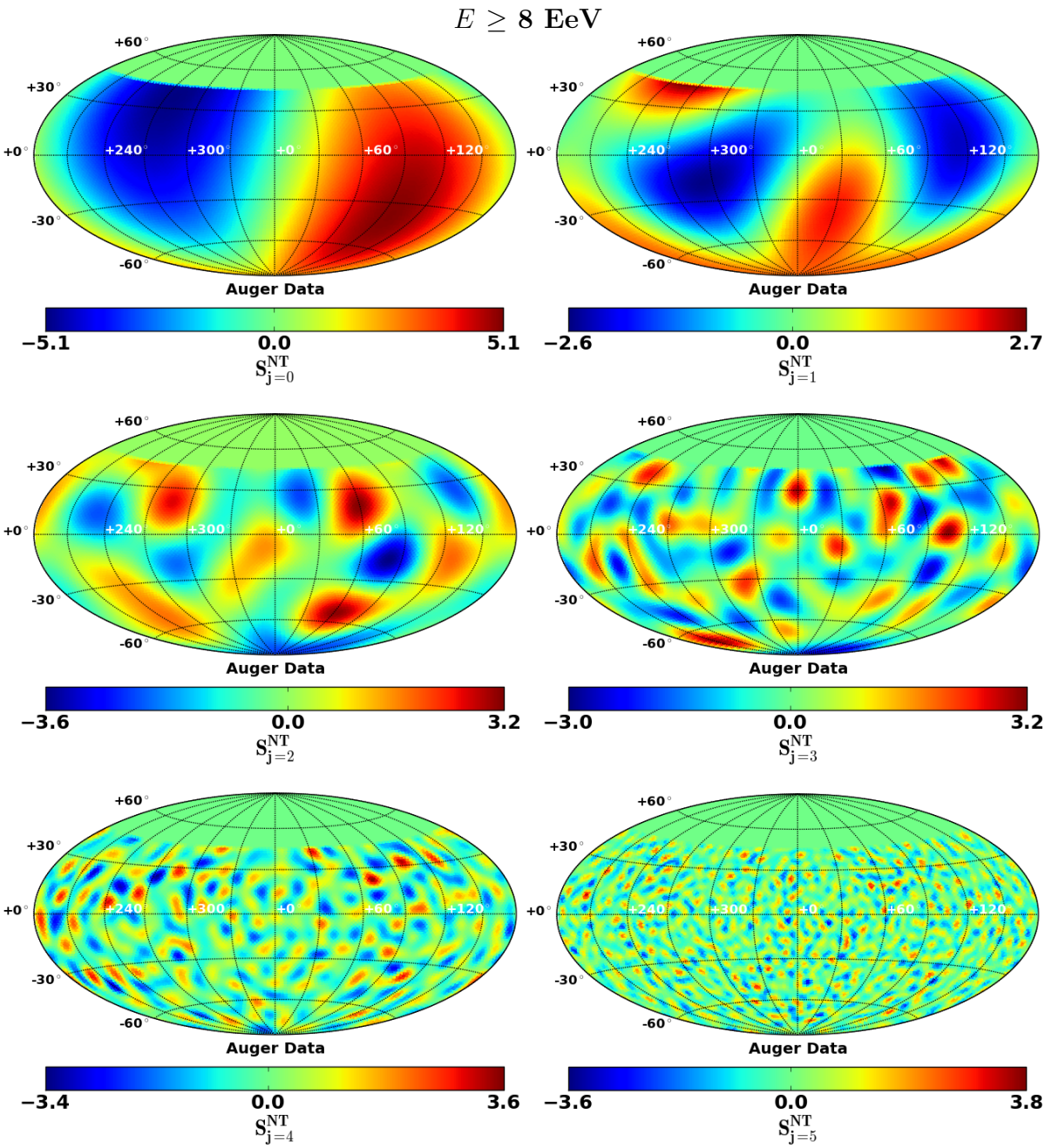

Figure 8.5.: Reconstructed but not thresholded skymaps S^{NT}_{jk} for $E \geq 8$ EeV. From left to right and from top to bottom the Needlet scales are $j = 0, 1, 2, 3, 4, 5$. For better visibility of particular features all scales have their individual range.

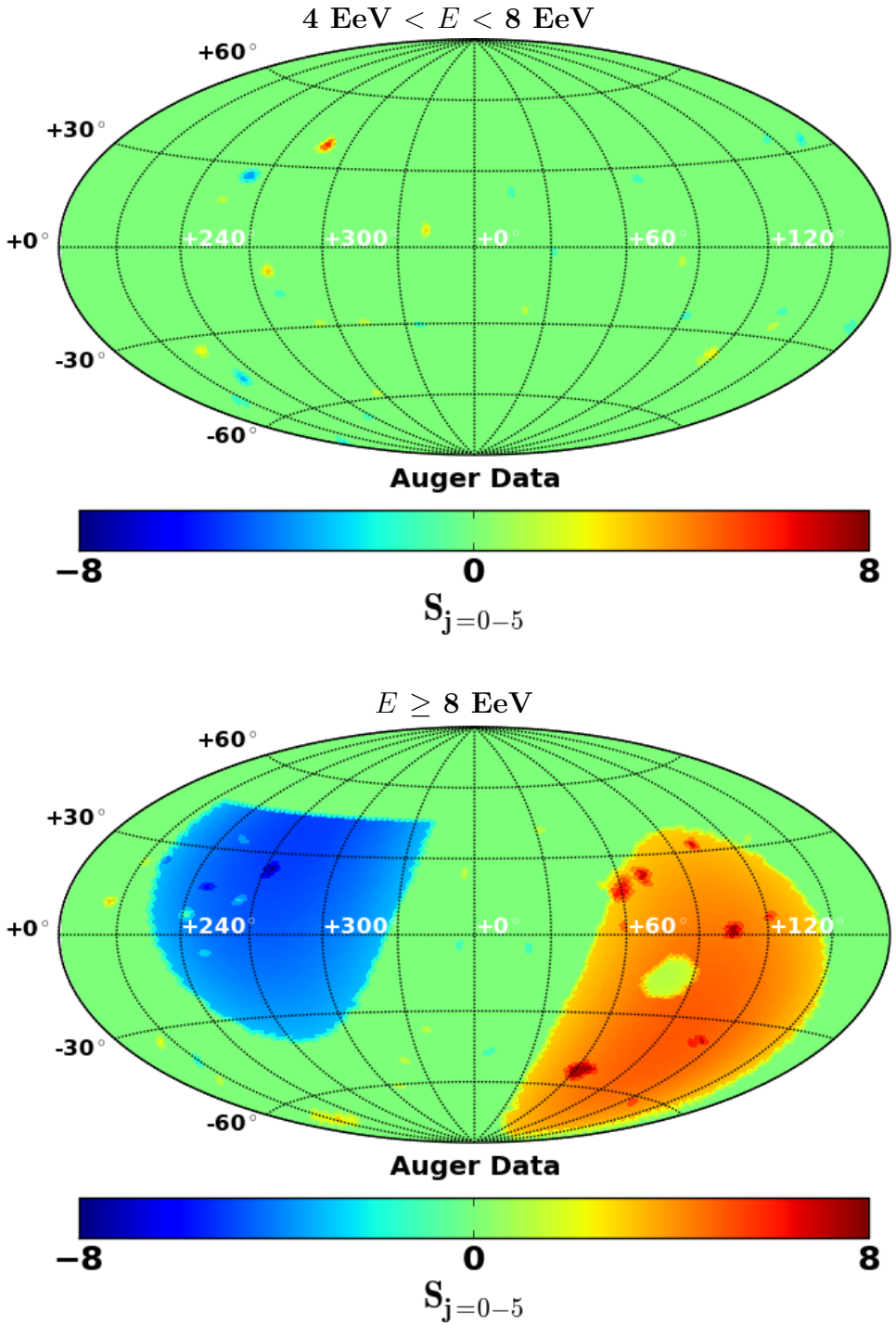

Figure 8.6.: Reconstructed,thresholded and combined significance skymap $S_{j=0-5}$ for 4 EeV $< E <$ 8 EeV **(top)** and $E \geq 8$ EeV **(bottom)**. The most prominent visible features are the dipole signature for $E \geq 8$ EeV and a localised excess around $(\alpha, \delta) = (280°, -35°)$ for 4 EeV $< E <$ 8 EeV. However, the global significance of this local excess is low as shown in figure 8.2. The high local excess arises due to the addition of a small scale excess in j=5 (see figure 8.4) of around $S_{k,j=5} = 3.5$ and additional contributions from $j = 1$ and $j = 2$ (also see figure 8.4). On the other hand the global anisotropy estimator of $E \geq 8$ EeV shows a hint of deviation from isotropy (see figure 8.3). The dipole-signature is further analysed and characterised in section 8.2. To compare both energy bins the two figures share the same colour range, versions of the plot with individual ranges can be found in appendix B (B.8).

restricted to searches to dipolar and quadrupolar patterns. In the following, we study the observed dipolar pattern in more detail and compare the results with published data from the Pierre Auger Collaboration [34] and a joint publication by the Pierre Auger Collaboration and the Telescope Array [37, 39].

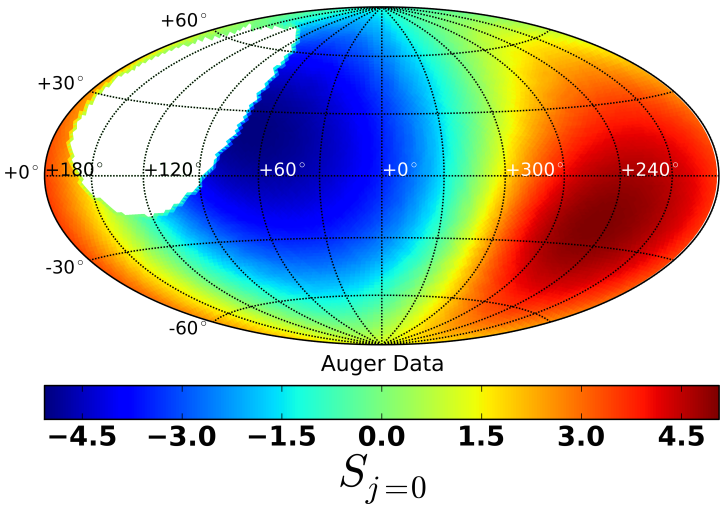

Figure 8.7.: Reconstructed (non-thresholded) significance skymap $S^{NT}_{j=0}$ in Galactic coordinates, E $\geq$ 8 EeV. Areas outside the Auger coverage are coloured in white.

8.2. A Detailed Look at the Dipole Scale

As the only observed significant Needlet scale was $j = 0$ for $E \geq 8$ EeV, we have a closer look at this scale and this energy bin. The flux is still expanded to $l_{\max} = 64$ but only $j = 0$ is analysed. The (non-thresholded) $j = 0$ significance skymap S^{NT}_{jk} is again shown in figure 8.7, in Galactic coordinates. The maximum is located at $(l_d, b_d) = (247°, -21°)$.

8.2.1. Dipole Position

Under the assumption that the observed pattern is indeed due to a dipole dominated flux[1] we continue to reconstruct its parameters. We use the position of the bin with the maximum significance to reconstruct the position of the dipole. In the case of the $E \geq 8$ EeV data bin this position is at $(\alpha_d, \delta_d) = (97°, -33°)$. To give an estimate of the systematic and statistical uncertainties of this method of reconstruction we simulate a set of Monte Carlo (MC) dipoles over a wide range of amplitudes and declinations. The parameters of this simulation are summarised in table 8.1.

Using the same method of reconstruction we show the average reconstructed dipole declination vs. the Monte Carlo truth in figure 8.8 for various amplitudes. As one can see the systematic offset in the reconstructed declination is below $3-4°$ if the true declination is between $-70°$ to $70°$. The offset increases only around the poles. The right ascension is reconstructed without a significant bias as well. Using the MC dipoles we also estimate the statistical uncertainties, resulting in a position of the reconstructed, significant dipole of $(\alpha_d, \delta_d) = (97° \pm 16°, -39° \pm 17°)$ in equatorial and $(l_d, b_d) = (247° \pm 16°, -21° \pm 17°)$ in Galactic coordinates.

[1] We relax the assumption later in this chapter.

Table 8.1.: Table containing the parameters used in the simulations of the dipolar sky patterns. For each combination of parameters 1,000 MC skymaps with the same number of events as in the $E \geq 8$ EeV data set were simulated assuming a sky coverage up to a maximum zenith angle of 80°.

Dipole Parameters	Range	Step-size
Declination δ	$-90°$ to $90°$	$10°$ (plus additionally $-35°$)
Amplitude r	0.0% to 10.0%	1.0%

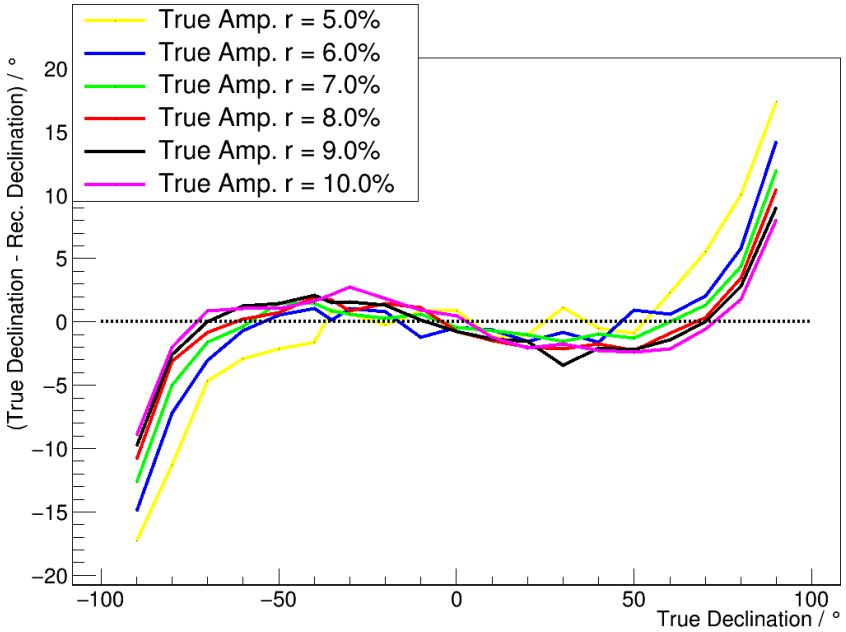

Figure 8.8.: Reconstructed average dipole declination vs. the MC truth for various MC dipole amplitudes r (with the Needlet analysis in $j = 0$). The number of simulated events in each MC skymap is equal to the number of events in the $E \geq 8$ EeV data set with 1,000 MC dipoles per parameter set. The dashed black line represents a perfect reconstruction. With the exception of the poles the declination is reconstructed with only a minor systematic shift, depending on the true declination of the input MC dipole.

8.2.2. Dipole Amplitude

The reconstructed S_{0k} skymap does not give a direct access to the amplitude of the dipole, but only to the position of the maximum significance and its value. To obtain the amplitude using the Needlet analysis we instead choose to use the simulated Monte Carlo dipoles to obtain a 'calibration' which relates the information in the significance skymaps to the amplitude. Empirically we find that the quantity

$$\frac{(S_{\max} - \langle S_{\max,\mathrm{iso}} \rangle)}{\sqrt{\cos(\delta_d)}} \tag{8.1}$$

is suited to relate the reconstructed information to the true amplitude. Here $S_{\max}$ is the maximum significance in the reconstructed skymap, $\langle S_{\max,\mathrm{iso}} \rangle$ the average maximum significance in the case of isotropy and $\cos(\delta_d)$ is the cosine of the reconstructed declination. A plot of the average of this quantity vs. the true MC dipole amplitude is shown in figure 8.9 for all simulated MC dipole skymaps. The red (dashed) line shows the value of the quantity of the $E \geq 8$ EeV data set and the blue (dot-dashed) lines its statistical uncertainties estimated from a MC dipole with the best-fit parameters as input.

By projecting the y-axis values and uncertainties onto the x-axis a dipole amplitude $r = (6.8 \pm 1.6)\%$ is reconstructed. As the declination is not known exactly ($-39^\circ \pm 17^\circ$) the calibration curves used to reconstruct the uncertainty are chosen to provide a conservative estimate of the uncertainty within the allowed declinations.

8.2.3. Cross-checks of the Observed Dipolar Pattern

Cross-checks Based on Data Subsets

To establish the stability of the observed dipolar signal in the $E \geq 8$ EeV bin we analyse various subsets of the data. These sub-sets consist of random sub-sets, date or day and night ordered sub-sets, and sets using different maximum zenith angels or energy cuts. The uncertainties on the direction and amplitude of the dipolar pattern are calculated the same way as previously described. In the case of the day and night time sub-set the correction for the number of active hexagons (see equation 7.1) is calculated again as described in section 7.1. In accordance with the results from section 6.3 the threshold for all skymaps with 12,000 or less events is lowered from $T = 3.0$ to $T = 2.0$. Most sub-sets contain 9,501 events which is slightly lower than half of the total events (9898) in the 8 EeV energy bin to allow for fluctuations in the number of events measured e.g. only during day and night time where a split would not necessarily result in the same number of events[2]. Thus only one set of MC dipoles is required to reconstruct the amplitude of these sub-sets. In the case that more events are available these are discarded randomly.

In the following we describe the various sub-sets used and discuss the results from each sub-set. All results are listed in table 8.2, including the position of the reconstructed dipolar signal, its amplitude and whether the sub-set is significant at a C.L. of 99% either using only $j = 0$ or all Needlet scales $j = 0 - 5$.

[2]I.e. 9798 events measured during the day and 9998 events during the night.

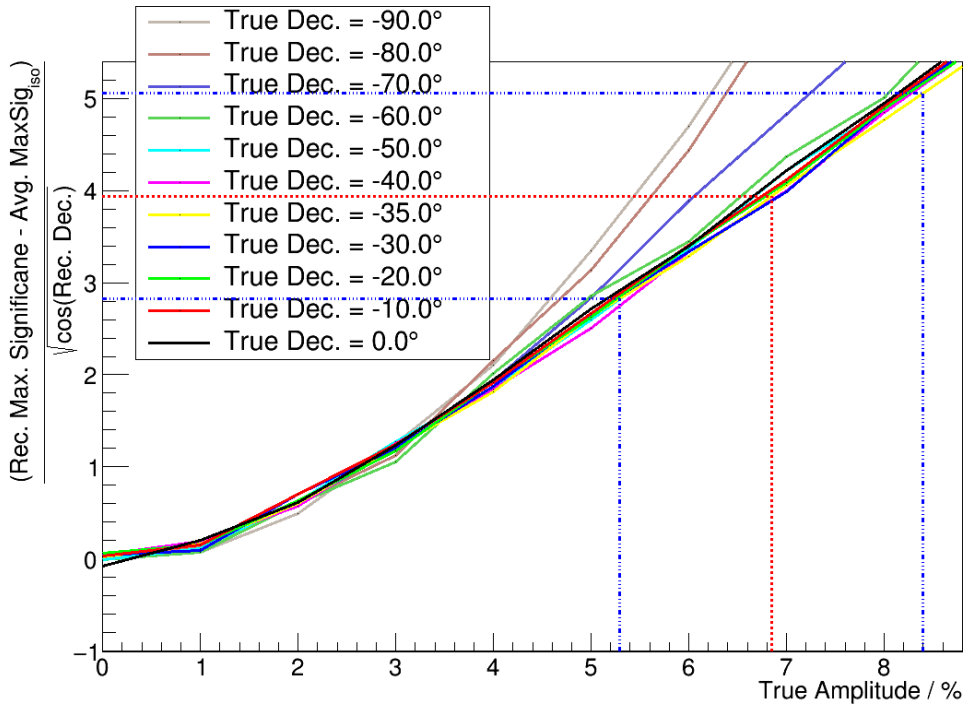

Figure 8.9.: MC calibration curves to reconstruct the dipole amplitude with the Needlet analysis restricted to $j = 0$ for various MC dipole declinations. The dashed (red) line represents the reconstructed dipole amplitude for the $E \geq 8$ EeV data set. The statistical uncertainties are represented by the dot-dashed (blue) lines. The number of simulated events in each MC skymap is equal to the number of events in the $E \geq 8$ EeV data set.

1. Random sub-sets: We select 5 random subsets from the otherwise unmodified $E \geq 8$ EeV energy bin. Each sub-set consists of 9501 events. The reconstructed dipole parameters vary around the best-fit parameters in a non-systematic way and are compatible within the uncertainties. Out of the 5 subsets 3 skymaps contain a significant dipole scale $j = 0$.

2. Chronological order of events: We order the events chronologically and use the first and last 9501 observed events. Again the reconstructed dipole parameters are compatible with the results using the whole data set and all $j = 0$ scales are significant at a 99% C.L..

3. Local detection time: We separate the events by their local detection time at the Pierre Auger Observatory. We roughly define day-time detections as between 6 AM up to 6 PM and night-time between 6 PM up to 6 AM. Again both sets are significant in the $j = 0$ scale and the dipole parameters are compatible with the complete data set.

4. Vertical events only: Here we only use the events from the vertical data set (see chapter 7). This is important to establish that the addition of the horizontal data

set does not introduce spurious anisotropies into the result. We use two maximum zenith angles $\theta_{max} = 50°$ and $\theta_{max} = 60°$. Again the results are compatible with the whole data set and remain significant at the $j = 0$ scale.

5. Different energy cuts: While the ≥ 8 EeV cut was chosen a priori before analysing the data with the Needlet analysis we now vary the minimum energy cut in both directions to investigate whether the dipolar signature remains or is only present for the 8 EeV cut. In one sub-set we lower the energy to 7 EeV and in the other we raise it to 10 EeV. In both cases the reconstructed parameters are compatible with the 8 EeV energy cut and both $j = 0$ scales are significant at the 99% C.L.. At the higher energy cut the reconstructed declination trends towards a smaller value of -50° ± 18°. Similarly the dipole amplitude shows a trend to rise with the lower energy cut from (5.5 ± 1.5)% to (6.8 ± 1.6)% and to (7.5 ± 2.4)% for a lower energy cut of 7, 8 and 10 EeV, respectively.

In summary all cross-checks provide dipole parameters which are compatible with the whole data set indicating that the observed dipolar signal is indeed present in the data set and not the result of the exact chosen energy cut or an artificially introduced anisotropy due to the combination of vertical and horizontal events.

Dipole Amplitude: Relaxing the Dominant Dipole Flux Assumption

By taking advantage of the full sky coverage when using data from both the Telescope Array and the Pierre Auger Observatory, the results reported in [39] also include an unbiased measurement of the angular power spectrum up to multipoles of $l = 20$ above an energy of 8.8 EeV in terms of the Auger energy scale. While all C_ls with the exception of $l = 1$ are compatible with fluctuations from isotropy they represent hitherto the most accurate measurement of the angular power spectrum (APS) at these energies. As explained previously the reconstruction of the amplitude of the observed dipolar anisotropy assumes that the observed flux is indeed dominated by a dipole. However, due to the incomplete coverage of the sky it is possible that higher order anisotropies artificially increase the reconstructed properties of the dipole. In the following we use the measured C_ls to evaluate what influence the additional contributions to the flux have on the reconstruction of the dipole amplitude.

To achieve this we follow the same reconstruction procedure as outlined previously. However, instead of using the data skymap based on the observed arrival directions we use a set of 1,000 MC skymaps with the reconstructed parameters of the dipolar anisotropy (see table 8.4) as input. If no additional anisotropies are included in the skymaps, the reconstructed amplitude naturally fluctuates around the input value as shown in table 8.3. Now we add to the already present dipole an additional anisotropy based on the measured APS in [39] up to $l = 6$. The values of the individual C_ls are also listed in table 8.3. As only the APS and not the individual multipole moments are reported in [39] we have no information on the direction of the specific anisotropies. Instead we randomly generate the absolute value of the multipole moments a_{lm} to produce the observed C_l (see equation 6.5). This is sufficient for the real-valued a_{l0} coefficient.

Table 8.2.: Summary of cross-checks on different samples from the data set with energy $E \geq 8$ EeV unless otherwise mentioned. Reconstructed dipole right-ascension α_d, declination δ_d and amplitude r are listed. The information whether the given data set is significant at a C.L. of 99% using the first Needlet scale $j = 0$ or all scales $j = 0 - 5$ is also given. The uncertainties on the direction and amplitude of the dipolar pattern are calculated the same way as for the full data set as previously described.

Selection	Events	$\alpha_d/(^\circ)$	$\delta_d/(^\circ)$	Amp. $r/(\%)$	Sig. @ 99% C.L.	
					$j = 0$	$j = 0 - 5$
Original Events						
All Events	19797	97 ± 16	-39 ± 17	6.8 ± 1.6	Yes	Yes
Random Subset						
Random #1	9501	97 ± 26	-39 ± 25	6.9 ± 2.5	Yes	No
Random #2	9501	103 ± 42	-42 ± 28	5.6 ± 2.6	No	No
Random #3	9501	86 ± 25	-36 ± 24	7.2 ± 2.4	Yes	Yes
Random #4	9501	116 ± 40	-51 ± 31	4.8 ± 3.3	No	No
Random #5	9501	89 ± 30	-20 ± 28	6.0 ± 2.1	Yes	No
Chronological order of events						
Earliest	9501	96 ± 20	-23 ± 24	6.2 ± 2.2	Yes	Yes
Latest	9501	95 ± 30	-53 ± 19	7.9 ± 3.0	Yes	Yes
Day or Night measurements (6 PM < night-time < 6 AM)						
Day	9501	127 ± 23	-42 ± 20	7.2 ± 2.5	Yes	Yes
Night	9501	69 ± 19	-30 ± 21	7.7 ± 2.3	Yes	Yes
Vertical events only, Different max. zenith angle ϑ_{max}						
$\theta_{max} = 50^\circ$	12000	104 ± 21	-40 ± 33	6.0 ± 2.6	Yes	Yes
$\theta_{max} = 60^\circ$	15418	94 ± 17	-28 ± 23	6.3 ± 2.0	Yes	No
Different energy cut						
$E \geq 7$ EeV	25106	91 ± 16	-43 ± 16	5.5 ± 1.5	Yes	Yes
$E \geq 10$ EeV	13195	79 ± 25	-50 ± 18	7.5 ± 2.4	Yes	No

For the other, complex-valued, coefficients we randomly align the complex angle in a uniform manner. A summary of the reconstructed amplitudes is listed in table 8.3 for energies greater than 8 EeV. As can be seen, with the exception of C_2, no additional C_l introduced a significant shift in the reconstructed amplitude. However, in the case of using C_2 the reconstructed amplitude is 0.5% percentage points larger than in the case of a pure dipolar input. Consequently we simulate a set of MC skymaps with this C_2 and a lower amplitude of 6.3% as input values. In this case an amplitude equal to 6.8% is reconstructed, which is equal to the previously discussed results for energies greater than 8 EeV.

In summary, with one exception, including additional anisotropies based on the measured APS up to $l = 6$ in [39] do not significantly alter the reconstruction of the amplitude of the observed dipolar pattern. The exception is the presence of a possible quadrupolar moment C_2. In this case the reconstructed amplitude of 6.8% ± 1.6% could be overestimated by 0.5% percentage points.

For comparison the table also shows the results if an energy cut of 10 EeV is used.

Table 8.3.: Influence on the reconstructed amplitude by an additional C_l component in the simulated flux. The measured C_ls are taken from figure 4 on page 24 in [39]. Shown is the input amplitude of the 1,000 MC dipoles and the included additional C_l and compared to the average of the reconstructed output amplitude. Only am additional C_2 changes the reconstructed amplitude for both $E \geq 8$ EeV and $E \geq 10$ EeV. A presence of the maximum allowed C_2 could lead to an over-estimation of the dipole amplitude of about 0.5%. This is shown when the same C_2 is included in a MC dipole with an amplitude of 6.3% for $E \geq$8 EeV.

Input Amp. r / (%)	Additional C_l	Output Amp. r / (%)
Energy ≥ 8 EeV		
6.8	none	6.8 ± 1.6
6.8	$C_2 = 0.0020$	7.3 ± 1.6
6.8	$C_3 = 0.0010$	6.8 ± 1.6
6.8	$C_4 = 0.0010$	6.8 ± 1.6
6.8	$C_5 = 0.0010$	6.8 ± 1.6
6.8	$C_6 = 0.0018$	6.8 ± 1.6
6.3	$C_2 = 0.0020$	6.8 ± 1.6
Energy ≥ 10 EeV		
7.5	none	7.5 ± 2.4
7.5	$C_2 = 0.0020$	7.7 ± 2.4
7.5	$C_3 = 0.0010$	7.5 ± 2.4
7.5	$C_4 = 0.0010$	7.5 ± 2.4
7.5	$C_5 = 0.0010$	7.5 ± 2.4
7.5	$C_6 = 0.0018$	7.5 ± 2.4

8.2.4. Summary and Discussion of the Results of the Dipole Scale

A summary of all results is contained in table 8.4 including the results which occur when the correction for the active number of hexagons or the correction for the tilt of the array are not included (see section 7). As discussed in section 2.5 the same

Table 8.4.: Reconstructed dipole amplitude and direction with the Needlet analysis in the $\geq$ 8 EeV bin. The last column indicates whether the corrections for the active number of hexagons (Hexa.) and tilt of the array (Tilt) have been applied to the data.

E / EeV	Amplitude r/%	δ_d	α_d	Corrections
$E \geq 8$	6.8 ± 1.6	-39° ± 17°	97° ± 16°	Hexa. + Tilt
$E \geq 8$	7.2 ± 1.6	-42° ± 17°	97° ± 16°	Hexa.
$E \geq 8$	7.2 ± 1.6	-40° ± 17°	96° ± 16°	-

data set and bins were also analysed in [34]. There two Rayleigh analyses (see [30] for an overview on the method), one in the right ascension and one in the azimuth angle distributions, were performed. As in this work, a departure from isotropy appears in the E $\geq$ 8 EeV energy bin, with an amplitude for the first harmonic in right ascension of $(4.4 \pm 1.0) \cdot 10^{-2}$, and a chance probability of $6.4 \cdot 10^{-5}$. This corresponds to a dipole amplitude of $r = (7.3 \pm 1.5)\%$ in the direction of $(\alpha, \delta) = (95° \pm 13°, -39° \pm 13°)$. These results are compatible with the results obtained in this analysis.

Similarly (also discussed in section 2.5) a joint, full-sky, analysis of the arrival directions measured at the Telescope Array (TA, data from May 2008 to May 2014) and the Pierre Auger Observatory (data from 2004-2013, max. zenith of 80°) also observed, by measuring the spherical harmonic coefficients with a multipole analysis, a dipolar flux [39] with an amplitude $r = (6.5 \pm 1.9)\,\%$ and a chance probability of 5×10^{-3} pointing to $(\alpha, \delta) = (93° \pm 24°, -46° \pm 18°)$. This flux was observed above 10 EeV in terms of the TA energy scale and above 8.8 EeV in terms of the Auger energy scale. While this does not exactly match the $E \geq 8$ EeV data analysed here, the results are still compatible. The performed cross-checks show that the obtained dipolar anisotropy is robust and is also present if the energy threshold is varied to 7 and 10 EeV. The obtained dipole amplitude is also stable. However, a possible quadrupolar contribution to the flux could lead to a slight over-estimation of the amplitude.

Naturally the question on the origin of the dipolar pattern arises.

As discussed in chapter 2.5 a dipolar pattern can arise if an observer moves relative to a cosmic ray rest frame, referred to as the Compton–Getting effect [40]. For example, if the rest frame of UHECRs coincides with the CMB rest frame, an observer in the solar system would move with a velocity around 368 km/s with respect to that frame [40]. However, the expected dipole amplitude from this motion would be around 0.6% [40] - far too low to explain the observed amplitude.

Another possible source of a dipole anisotropy could be an inhomogeneous distribution of nearby sources of UHECRs. In this case the direction of the maximum of the dipole

distribution would point towards the highest concentration of nearby sources [34]. The diffusion of particles from sources through turbulent (i.e. non-regular) extra-galactic magnetic fields (EGMFs) can also create a dipolar anisotropy [41] whereby the amplitude depends on the density of sources and the direction depends on the positioning of the sources. In [41] an attempt was made to combine the last two effects, i.e. the inhomogeneous distribution of nearby sources and the propagation of particles from these sources through a turbulent EGMF. In case of sources with a density around $10^{-5} - 10^{-4}$ per Mpc^{-3} modelled around the measured local matter distribution of the 2MRS catalogue [113] (see section 6.3.5) within 100 Mpc around the galaxy, a dipole anisotropy with an amplitude around 3%-10% and pointing towards the Local Group (coordinates $(\alpha, \delta) = (163°, -27°)$) was simulated. The results suggest that a combination of the two described effects could at least be a plausible explanation of the observed dipolar pattern. Naturally the modelling of the propagation of UHECRs depends on the strength and coherence length of the EGMF and the mass composition.

Further uncertainties are introduced due to the galactic magnetic field (GMF), which can modify the amplitude and direction of a dipolar anisotropic pattern arriving at the galaxy [41].

In summary, while possible mechanisms exist which can give rise to the observed pattern a clear identification of the cause depends on better understanding of the composition of UHECRs and the properties of the EGMF and GMF.

8.3. Search for a Point Source Deflected through the (Extra) Galactic Magnetic Field

In the previous, full-sky analysis only one, large-scale, deviation from isotropy was observed, at the Needlet scale $j = 0$ for energies greater than 8 EeV. We now use the localized properties of the larger Needlet scales to restrict the search to a portion of the sky. More specifically we try to identify a possible signal from the AGN closest to earth: Centaurus A. In contrast to previous analyses using Auger data [35] we do not scan the region around Centaurus A as a function of the angular distance. Instead we use a model of the GMF [22, 111] and assumptions on the EGMF to identify an a priori region of interest (ROI) where a possible signal from Centaurus A would be most prominent. As the deflection of UHECR depends on their charge and energy, each is assigned an individual ROI. We use three different energy thresholds 8, 10 and 12 EeV and consider only a proton composition. The larger charge of heavier elements, such as iron, increases the deflection to such a degree that a discrimination from isotropy is not possible with the approach outlined in the following.

8.3.1. Simulation and Analysis

To derive the expected contribution of Centaurus A to an otherwise assumed isotropic sky (in the scales analysed) the following steps are required. First, the propagation of the particles from Centaurus A to the Milky Way needs to be modelled. Then, they need to be propagated through the GMF to earth. Finally, the detector response needs to be included and the data analysed. In the following we describe this process. First the propagation through the EGMF and GMF, then the definition of the ROIs and finally the analysis.

8.3.2. Extra-galactic Magnetic Field

As described in section 2.4.2 the propagation of cosmic rays through the EGMF can, under certain circumstances and under the neglect of energy loss, be modelled as a smearing of the original source via an average deflection [21]. Using more appropriate units in formula 2.9 on page 13 yields for the average deflection:

$$\sigma_{\mathbf{EGMF}} \approx 21.6^\circ \cdot \left(\frac{E/Z}{\mathrm{EeV}}\right)^{-1} \cdot \left(\frac{B_{\mathrm{rms}}}{\mathrm{nG}}\right) \cdot \sqrt{\left(\frac{d \cdot l_c}{\mathrm{Mpc}^2}\right)}. \tag{8.2}$$

Here, E is the energy and Z the charge of the particle, B_{rms} the average strength of the turbulent EGMF, d the distance of the source to the observer and l_c the coherence length of the EGMF. In this analysis we approximate Centaurus A as an extended point source, modelled by a Fisher-distribution (see equation 6.4 on page 93), located at $(l, b) = (309.5^\circ, 19.4^\circ)$ with an intrinsic width (including the lobes) of 2° and a distance of $d = 3.8$ Mpc [118]. We consider two possible values for the strength of the EGMF. First, a 'strong' EGMF with a value of $B = 0.65$ nG and a coherence length of $l_c = 1$

Mpc. This corresponds to the current upper limit [28]. Second, a 'weak' EGMF with a value of $B = 0.001$ nG. This is still far above the lower limit [29], however, at this value the average deflection becomes negligible in comparison to the intrinsic source size. Both the intrinsic size and average deflection are added quadratically and inserted into a Fisher-distribution (see equation 6.4) with $\kappa = \sigma^{-2}$. An example of the resulting distribution for low and high energies can be found at the top of figures 8.10. Here, the lower energy proton signature at 8 EeV is only slightly enlarged compared to the highest energies where the effect of the EGMF is negligible.
While it would be of interest to compare a pure proton composition to a pure iron composition in this scenario, this is not possible at the studied energies. Due to the 26 times larger deflection of iron the propagation through a strong EGMF can not be modelled via an average deflection, here the particles enter a diffusive propagations regime and loose the information on their source direction [21]. In the case of a weak EGMF this also holds true for the GMF (see the left-hand side of figure 2.6) with the additional difficulty that particles can become trapped in the galaxy making the derivation of a GMF lens, as described in the following, unreliable [119].

8.3.3. Galactic Magnetic Field

To model the propagation of the UHECRs through the galaxy we use the forward lensing technique from [111] in combination with the JF-12 model [22] used e.g. in [25, 112]. As discussed in section 2.4.1, the JF-12 model is a model of the GMF based on various measurements [22, 23]. Using this model and the technique described in the following, it is possible to trace forward particles arriving at the edge of the galaxy, through the GMF to earth. The forward lensing is performed using a galactic magnetic field lens $\mathcal{L}$ which is derived as described in the following.

While the goal in this chapter is the forward tracing of particles, the lens itself is derived by back tacking anti-particles of energy E_i emerging isotropically at earth, through the JF-12 model to their exit location at the edge of the galaxy. This way one can derive the probability of observing a particle at earth with direction m^i, which arrived at the galaxy with direction n^i. The set of all $l^i_{m,n}$ then represents a matrix or lens bin $\mathcal{L}_i$ for particles of energy E_i [111].

This way an extra galactic probability vector of arrival directions P_i^{eq} can be transformed to the expected probability vector at earth P_i^{obs} using lens bin i:

$$\mathcal{L}_i \cdot P_i^{eq} = P_i^{obs} \tag{8.3}$$

[111]. The combination of all lens bins $\mathcal{L}_i$ then forms the GMF lens $\mathcal{L}$. In this work we use the lens published under [120] and derived as described previously. The lens consists of 175 lens bins which cover a rigidity range equidistant in the logarithm of the rigidity, from 10^{17} eV to $3 \cdot 10^{20}$ eV.

In the case of this analysis the extra galactic probability vectors P_i^{eq} correspond to the previously generated, energy and composition dependent, Centaurus A signature. Each available lens bin i is combined with the corresponding extra galactic signature, resulting

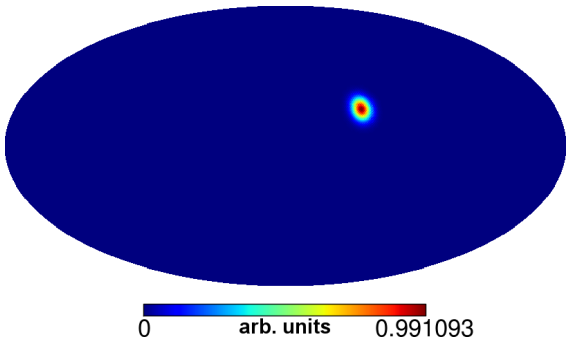

(a) Extra-galactic PDF, $E = 8 \cdot 10^{18}$ eV, proton

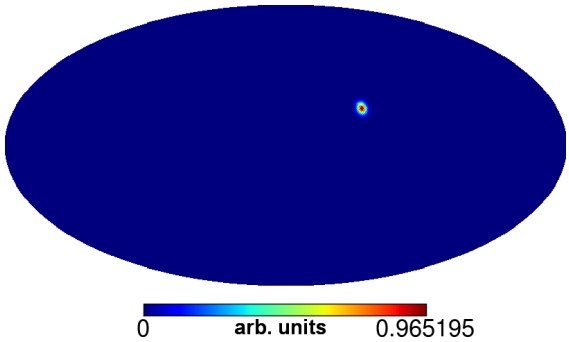

(b) Extra-galactic PDF, $E = 3 \cdot 10^{21}$ eV, proton

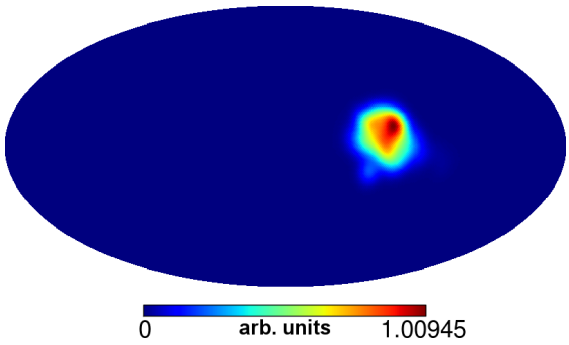

(c) PDF at earth, $E = 8 \cdot 10^{18}$ eV, proton

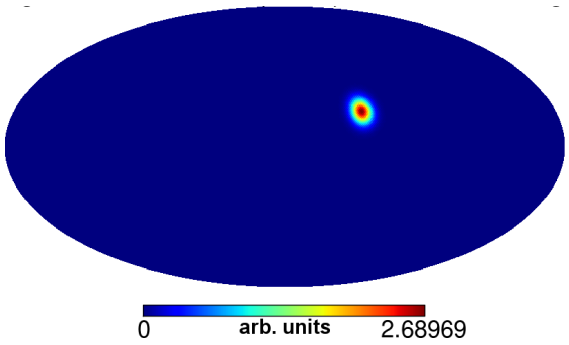

(d) PDF at earth, $E = 3 \cdot 10^{21}$ eV, proton

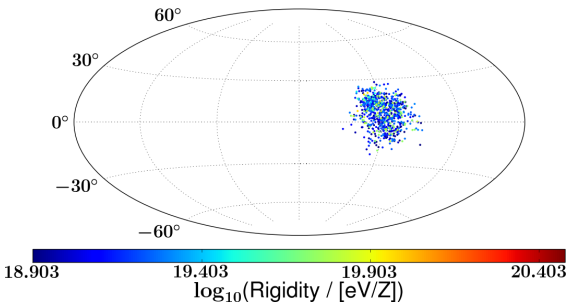

(e) Drawn signal (2%), $E \geq 8 \cdot 10^{18}$ eV, Auger coverage

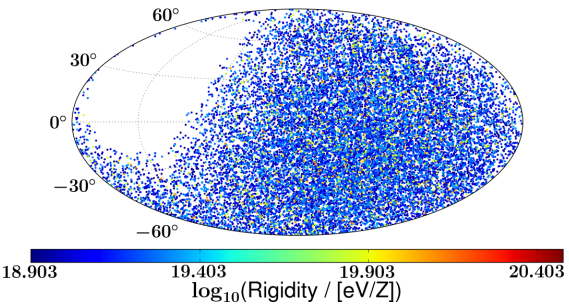

(f) Drawn isotropy, $E \geq 8 \cdot 10^{18}$ eV, Auger coverage

Figure 8.10.: Illustration of the simulation method to obtain the expected flux from Centaurus A. Centaurus A is assumed to be an extended point source of 2° size. The intrinsic width is widened by the expected average deflection through the EGMF as described in formula 8.2. In **(a)** the widening of the probability density function (PDF) in case of a proton composition through a EGMF of 0.65 nG with 8 EeV is shown. In contrast the widening becomes negligible at the highest energies **(b)**. The PDFs at the edge of the galaxy are folded through the corresponding GMF-lens bins. The PDF at earth for protons with 8 EeV is shown in **(c)** and at the highest energies in **(d).** An energy is then drawn according to the energy spectrum ($E \geq 8 \cdot 10^{18}$ eV here) and an arrival direction from the corresponding PDF is diced and either rejected or accepted according to the Auger coverage. This is repeated until the number of draws corresponds to the signal-fraction (s.f.) as indicated in the scatter plot **(e)**. The rest of the input skymap is filled with isotropy as indicated in the scatter plot **(f)**. This is different from the benchmark scenario in section 6.3.3 where the s.f. gave the number of source events in a simulated Auger skymap. In this scenario the s.f. corresponds to the s.f. at earth. All figures are shown in Galactic coordinates.

in, at most, 175 PDFs at earth. An example of the lens applied to the extra-galactic distribution of low and high energy protons in the case of a strong EGMF can be found in the middle of figure 8.10.

In the case of an energy of 8 EeV a clear smearing out of the extra-galactic signature can be observed. At the highest energies the source is only marginally widened.

A caveat in using the lensing technique is that, during the generation of the lens via back tracking, anti-particles emerging isotropically from earth do not leave the galaxy uniformly. Due to the GMF particular regions of exit from the galaxy are preferred over others [25]. In regions where fewer particles leave the galaxy the relative fluctuations between individual realizations are stronger than in other regions [25]. This introduces an uncertainty on the observed probability distribution, especially at lower rigidities where the particles are strongly affected by the GMF. In [25] a spherical Gaussian $\mathcal{G}$ smoothing with a width of 4° was shown to reduce this effect drastically for energies $\gtrsim$ 4 EeV via

$$\mathcal{L}_i \cdot \mathcal{G} \cdot P_i^{eq} = P_i^{obs}. \tag{8.4}$$

(see figure 3.5 and equation 3.18 in [25]). As this approach is very computationally expensive we apply the smoothing to the resulting PDF instead ($\mathcal{G} \cdot P_i^{obs}$).

Because this effect is of a statistical nature, future realisations of the lens with a larger number of backtracked particles will reduce this effect. With the current lens the method above is used. As this further smears the observed probability distribution this may worsen any derived limits on the flux (see below) but is necessary to avoid too stringed limits.

8.3.4. Detection of the Particles at Earth

To obtain test skymaps including the detector from the previously obtained PDFs we proceed the following way:

- We draw a random energy E_i according to an energy spectrum with a power law index of $\gamma = -2.6$ (see section 2.1) beginning at the starting energy of either 8, 10 or 12 EeV.
- According to the chosen signal fraction (see table 8.5), we randomly dice whether the event with energy E_i is a signal or isotropic event. If the event is isotropic, we dice a randomly distributed direction on the sphere. If it is a signal event, we dice a direction according to the PDF with the corresponding rigidity.
- The event is either accepted or rejected according to the Auger coverage (see equation 3.8) with a maximum zenith angle of 80°.

This is repeated until the desired number of total events is generated and signal and isotropic events are added to a complete skymap. An example scatter-plot of thus generated isotropy and signal skymaps is shown in the bottom of figure 8.10 as a function of rigidity and in the case of a strong EGMF. Here a clustering of the signal events around the same region can be seen, which grows stronger as the rigidity increases. A summary

of parameters used to generate the skymaps is shown in table 8.5. For each combination of parameters 1,000 skymaps are simulated. Finally, we generate a large number ($\approx 10^7$) of pure signal and pure isotropic events to find a region of interest as described in the following.

Table 8.5.: Parameters chosen to simulate the expected flux from Centaurus A as described in section 8.3.1. For each parameter set 1000 skymaps are simulated.

Composition	EGMF strength / nG	signal-fraction / %
Pure proton	0.001; 0.65	0.0; 0.02; 0.05; 0.1; 0.2; 0.3; 0.4; 0.5; 0.6; 0.7; 0.8; 0.9; 2.0

8.3.5. Defining the Region of Interest

In the previous analyses, a search over the whole sky did not yield a significant deviation from isotropy for $E \geq 8$ EeV in the Needlet scales $j = 1 - 5$. Hence, the idea behind this analysis is to restrict the analysis to a part of the sky based on the previous results. We use the previously generated skymaps consisting of a large number of either only isotropic or signal results as seen through the Auger coverage. In order to find the region of the sky where a possible signal from Centaurus A is strongest, we first use the pure signal skymap to find the mean direction:

$$\langle \mathbf{n} \rangle \propto \sum \mathbf{n}^{\mathbf{i}}_{\mathrm{sig}} \tag{8.5}$$

of all unit vectors of the signal event directions $\mathbf{n}^{\mathbf{i}}_{\mathrm{sig}}$. An example of a pure signal skymap is shown in the bottom of figure 8.11 in the case of a strong EGMF. This is performed for all possible combinations of EGMFs strength and energy thresholds. All mean directions are listed in table 8.6. To find the optimal search location in the skymap we maximise the following SNR ratio:

$$SNR(n_{\mathrm{br}}) = \frac{N_{\mathrm{sig}}(n_{\mathrm{nbr}})}{\sqrt{N_{\mathrm{iso}}(n_{\mathrm{nbr}})}}, \tag{8.6}$$

as a function of the distance in terms of included nearest neighbours of n_{nbr} as explained in the following. Here N_{sig} and N_{iso} is the sum of all events within the current ROI in the previously generated signal and isotropic skymaps, respectively. The ROI is constructed as follows: Starting from the Healpix pixel located at the mean direction we add its 4 nearest neighbouring pixels as illustrated in the top of figure 8.11 and calculate the SNR. This corresponds to a distance in term of nearest neighbours of $n_{\mathrm{nbr}} = 1$. This process is continued, again as illustrated in the top of figure 8.11. At each turn the SNR is calculated as a function of n_{nbr}. This process is repeated until the next distance in terms of nearest neighbours would include pixels which would be further than 45° apart from the starting pixel. This is the point where the smallest Needlet scale $j = 1$ and

hence the one sensitive to larger structures starts to become less sensitive of even larger structures. The scale $j = 1$ includes the spherical harmonic moments with $l = 2$ and $l = 3$ and hence is sensitive to angular distances up to $\propto 180°/2 = 90°$, or in terms of the half angle of 45°.
Finally the distance of $n_{\mathrm{nbr,max}}$ which provides the maximum SNR ratio is defined as the used ROI. In the case of a threshold of 8 EeV and a strong EGMF the determined ROI is shown in the bottom of figure 8.11 and includes all pixels up to a distance of $n_{\mathrm{nbr,max}} = 10$. The position of Centaurs A is marked with a black star. As can be seen the highest concentration of events lies slightly more towards the galactic plane and slightly more towards higher longitudes in comparison to the actual position of Centaurus A. This can be explained due to pull of the flux towards the galactic plane by the GMF as can be seen in the middle, left-hand side panel in figure 8.10. This has also been observed in other works using the same GMF model [119]. The found ROIs and the distances which maximise the SNR in terms of nearest neighbours $n_{\mathrm{nbr,max}}$ are shown in table 8.6. Also shown are the used Needlet scales which are selected to be most sensitive to the size of the ROI and even smaller scales as well as the angular distance of the end of the ROI to the centre of the ROI.
As can be seen from the results the relatively low influence of the strength of the EGMF on a pure proton composition leads to the same ROI for protons regardless of the EGMF strength. Also the ROI shrinks as the energy threshold rises as is expected since higher energy particles are less deflected.

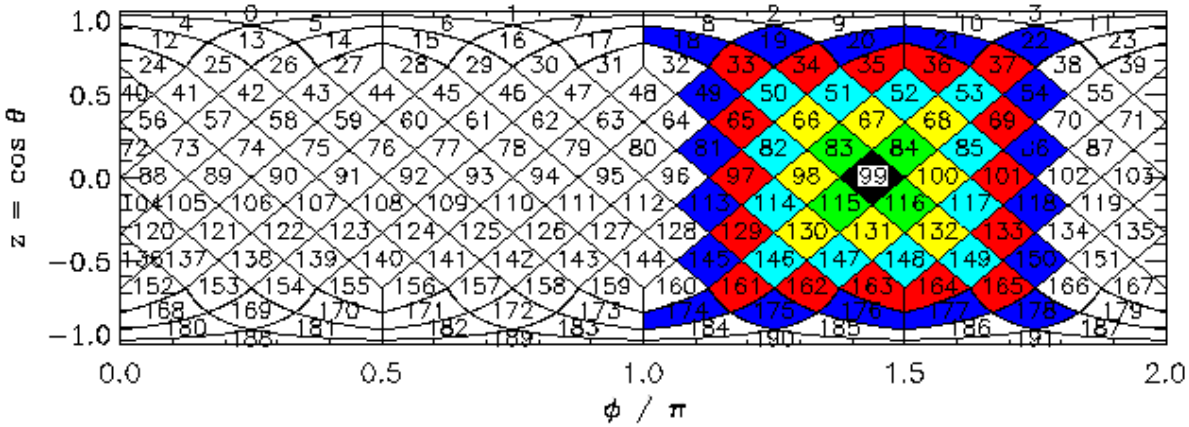

(a) ROI scheme, $N_{\text{side}} = 4$

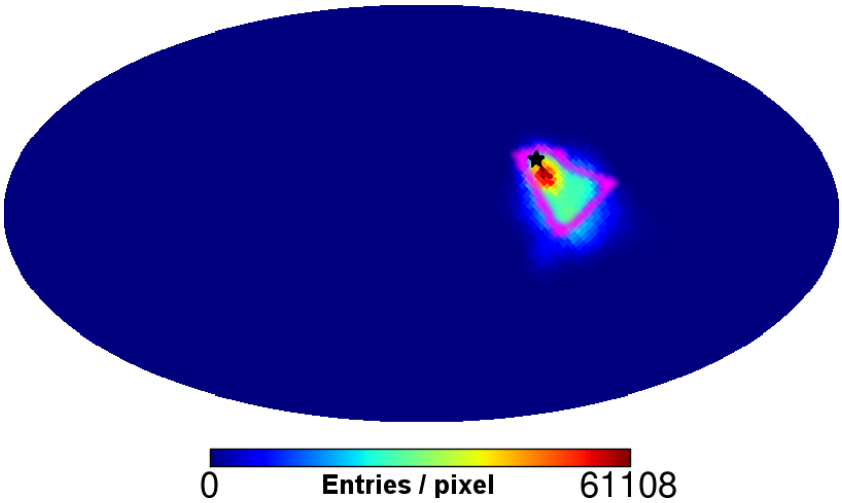

(b) ROI, $E \geq 8 \cdot 10^{18}$ eV, pure proton signal, Galactic coordinates

Figure 8.11.: a) Illustration how the ROI region is defined with Healpix N_{side} parameter =4. The black pixel with number 99 is the pixel where the average direction of all signal event points to. At a distance of $n_{\text{nbr}} = 1$ nearest neighbour the pixels directly attaching, i.e. NE, SE, SW and NE of the starting pixel, are added to the ROI. In this case these are the green pixels with numbers 84, 116, 115 and 83. Continuing at distance $n_{\text{nbr}} = 2$ all pixels attached to these pixels are included and so on. The corresponding colours to a nearest neighbour distance of $n_{\text{nbr}} = 2$, 3, 4 and 5 are yellow, light blue, red and dark blue. Each new ROI includes the previous ROIS. The ROI chosen for the analysis is the ROI with the highest SNR ratio as defined by equation 8.5.
b) Pure signal skymap, and ROI (in pink) in galactic coordinates in the case of a strong EGMF for a pure proton composition. The position of Centaurs A is marked with a black star. Within this ROI the respective SNR is maximised with $n_{\text{nbr}} = 10$. The structure of the ROI is due to the fact that it has been calculated in equatorial coordinates. Here the signal events are located closer to the south pole and the Healpix pixels have a more complicated structure closer to the poles (see at the top and at the bottom of **a)**).

Table 8.6.: Determined regions of interest (ROIs) as described in section 8.3.5. Due to the relatively low effect of even a strong EGMF on the direction of protons (see figure 8.10) the ROIs and their angular extend for both a weak and strong EGMF is similar. For comparison the equatorial coordinates of Centaurus A are $(\alpha, \delta) = (201°, -43°)$. The shift in coordinates can be explained by two factors. First, the Auger coverage rises towards the south leading to a higher SNR ratio. Second, the flux experiences a pull towards the galactic plane by the GMF as can be seen in the middle, left-hand side panel in figure 8.10. As the energy rises the ROIs move closer towards the position of Centaurus A. Due to the size of the ROIs the position of Centaurs A is included in the analysis as illustrated in figure 8.11.

Composition	EGMF strength / nG	Mean direction (α, δ) / (°,°)	Max. SNR at $n_{\mathrm{nbr,max}}$	Maximum ang. dist. / °	Needlet scales j
Energy $E \geq 8$ EeV					
Pure proton	0.001	(185, -56)	10	25	$2-5$
Pure proton	0.65	(185, -56)	10	25	$2-5$
Energy $E \geq 10$ EeV					
Pure proton	0.001	(189, -55)	9	22	$2-5$
Pure proton	0.65	(189, -55)	9	22	$2-5$
Energy $E \geq 12$ EeV					
Pure proton	0.001	(192, -54)	8	20	$2-5$
Pure proton	0.65	(192, -54)	8	20	$2-5$

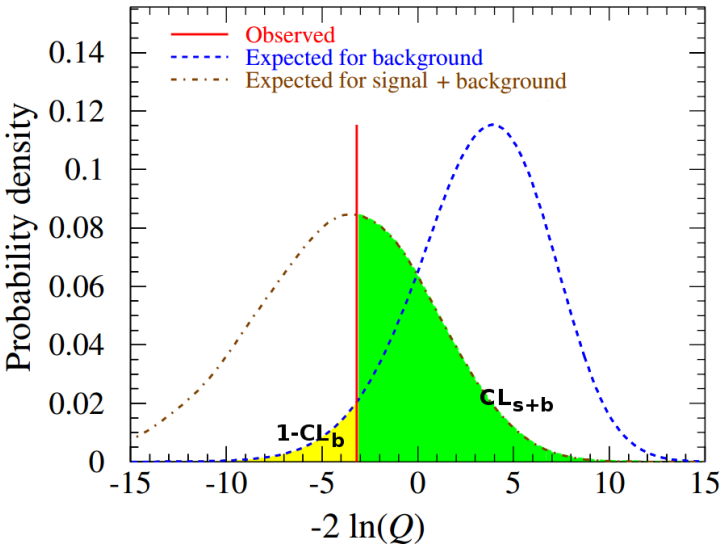

Figure 8.12.: Illustration of the CL_s method. Adapted from [123].

8.3.6. Analysis

Using the defined ROIs the Needlet analysis is applied to the data. The analysis is identical to the previously discussed results with one exception. When the S-value is calculated, only pixels in the ROI are included. As the search region is now defined by the ROI and does not extend over the whole sky, the used threshold T (see equation 5.5) is lowered[3] to 1.

The measured S-value, as well as an isotropic reference distribution, in the case of a weak EGMF (top) and a strong EGMF (bottom) and an energy threshold of 8 EeV, are shown on the left-hand side of figure 8.13. In both cases and in all other cases no significant deviation from isotropy was observed. Therefore we can use the simulated skymaps with varying signal fractions to obtain a limit on the flux from Centaurus A under the previously outlined conditions.

To establish the limits we use the CLs method, commonly used in high energy experiments (e.g. to exclude mass ranges for the Higgs boson at the LEP and LHC [121, 122] before its discovery.). In our case we need to distinguish between two hypotheses H_0 and H_s. H_0 is the null hypothesis, that the observed data is due to an isotropic (referred to as background) distribution. H_s is the hypothesis that the observed data is due to an isotropic background plus a contribution of a flux from Centaurus A (referred to as background plus signal) with a given signal fraction[4]. On the left-hand side of figure 8.13 the isotropic distribution (in blue) corresponds to the expected distribution of the S-value if H_0 is true and the signal distribution (in red) to the expected distribution if H_s is true.

[3]The expected limits worsen if $T = 3$ is used.

[4]Signal fraction here means the average fraction of events in the completely generated full sky test-skymaps.

To distinguish between the two hypotheses we use the likelihood ratio

$$Q = \frac{\mathcal{L}_{H_s}}{\mathcal{L}_{H_0}}, \tag{8.7}$$

as illustrated in figure 8.12. We built two distributions of this ratio by sampling random values from the simulated S-value distribution either in the case of isotropy or isotropy plus a given signal fraction and calculating the corresponding Q vale. An example of these distributions is shown on the right-hand side of figure 8.13 in the case of a weak and a strong EGMF on the top and bottom respectively. To exclude a given signal fraction at a given confidence level α one can calculate the probability to obtain the same or higher Q-value as the observed data from the distribution for isotropy and signal, $\mathrm{CL_{s+b}}$, as illustrated in figure 8.12. Conversely the probability $\mathrm{CL_b}$ to obtain the same or higher Q-value from the isotropic distribution can be similarly determined (see again figure 8.12). If the $\mathrm{CL_{s+b}}$ value is smaller than α one can say the hypothesis H_s is excluded at a confidence level $CL = 1 - \alpha$. This however leads to too stringent limits if both hypotheses largely overlap, i.e. near the sensitivity limit of the experiment [123]. A more conservative choice is to use the ratio

$$\mathrm{CL_s} = \frac{\mathrm{CL_{s+b}}}{\mathrm{CL_b}}, \tag{8.8}$$

where the confidence in the (combines) signal and background hypothesis is weighted with the confidence in the background (i.e. isotropy) hypothesis [123]. To exclude a given signal fraction we use a 95% confidence limit and hence require

$$\mathrm{CL_s} < 0.05\,. \tag{8.9}$$

On the contrary, if the observed data point is compatible with a pure isotropic arrival distribution but the $\mathrm{CL_s}$ is larger than 0.05 we cannot rule out that the given signal fraction of events from Centaurus A is present in the data. As an example we show the Q-value distributions and the observed data value for the largest possible signal fraction of 0.3%, which is still compatible with the data value on the right-hand side of figure 8.13. The figure shows the results for an assumed proton composition with a signal fraction of 0.3% and an energy threshold of 8 EeV in the case of a weak (top) and strong (bottom) EGMF. Consequently, MC data with a signal fraction of 0.4% and larger is not compatible with the observed value and can hence be excluded.

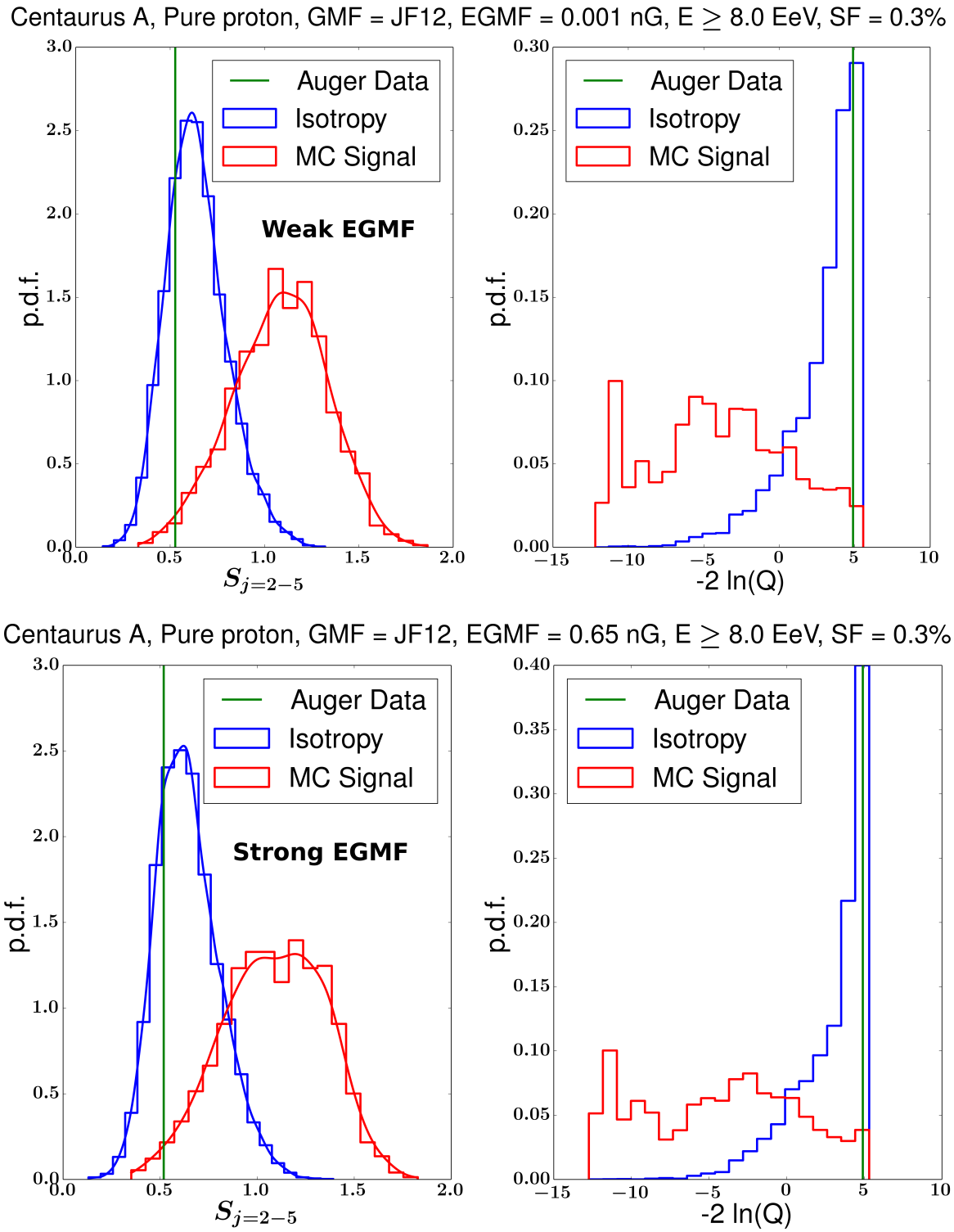

Figure 8.13.: CLs method applied to the ≥ 8 EeV data set for a weak (**top**) and a strong (**bottom**) EGMF. The two shown signal fractions are the largest (both 0.3%) which are compatible with the observed data (see table 8.5). As in both cases no deviation from isotropy was observed, the next larger (i.e. incompatible at a 95% C.L.) signal fraction can be interpreted as the limit on the flux from Centaurus A (0.4%) assuming the used GMF-lens and EGMF field strength and deflection model.

8.3.7. Results and Discussion

A summary of all obtained limits is shown in table 8.7 for energy thresholds 8, 10 and 12 EeV. The limit on the proton fractions is 0.4% regardless of EGMF strength and energy threshold. Within the Auger coverage with a maximum zenith angle of 80° this limit translates to a signal fraction of 0.7% due to the location of the Pierre Auger Observatory in the southern hemisphere. A comparison to previously established results is difficult as comparable analyses using the JF-12 model do not currently exist.

Of the two current UHECR observatories, the Pierre Auger Observatory and the Telescope Array, only the Pierre Auger Observatory has access to the sky region of Centaurus A. In case of the Auger observatory the expected number of events was compared to the observed number of events for energy thresholds ranging from 40 to 80 EeV and as a function of the angular distance to Centaurus A [35]. In contrast to the work described in this chapter, this analysis ([35]) makes no assumptions on the propagation of UHECRs and instead uses the observed data to define a ROI. The latest included events in the data set are from March 2014, which is only 3 months of more data in comparison to this work. As described in section 2.5, the largest observed excess of events was at an angular distance of 15° and for an energy threshold of 58 EeV (see right-hand side of figure 2.7 on page 17), with a penalized probability of 1.4% [35]. While the chance probability of this scenario is rather low it does not reach significance which is also the case in this work (with energies around 10 EeV).

Table 8.7.: Limits on the flux from Centaurus A using the CLs method at a confidence level of 95% as a function of the composition and the strength of the EGMF. The search is restricted to the ROI windows around the mean directions and to the Needlet scales listed in table 8.6. The limit is given in terms of the signal fraction either at Earth and also, on average, within the Auger coverage with a maximum zenith angle of 80°. Due to the position of the Pierre Auger Observatory the signal fraction is larger within the Auger coverage than averaged over the whole Earth. The included GMF field is described in section 2.4.1 and the derivation and usage of the lens obtained from the GMF model is described in section 8.3.3.

Composition	EGMF strength / nG	Limit of s.f. @95% C.L. at Earth	in Auger coverage
Energy $E \geq 8$ EeV, 19797 Events			
Proton	0.001	≤ 0.4 %	≤ 0.7 %
Proton	0.65	≤ 0.4%	≤ 0.7 %
Energy $E \geq 10$ EeV, 13195 Events			
Proton	0.001	≤ 0.4 %	≤ 0.7 %
Proton	0.65	≤ 0.4%	≤ 0.7 %
Energy $E \geq 12$ EeV, 9264 Events			
Proton	0.001	≤ 0.4 %	≤ 0.7 %
Proton	0.65	≤ 0.4%	≤ 0.7 %

9. Summary

Until today the origin of ultra-high energy cosmic rays (UHECRs) is unknown. The search for the origin of UHECRs is difficult as they are deflected by magnetic fields on their way to earth. This deflection is stronger the heavier the composition of the arriving cosmic rays is, leading to a largely isotropic distribution at earth.

In this work a Needlet Wavelet based analysis has been applied on the measured arrival directions of UHECRs at the Pierre Auger Observatory. The aim was to find any deviations in various angular sizes from a purely isotropic distribution of arrival directions. The analysis was applied to energies above the full trigger efficiency of the surface detector of the Pierre Auger Observatory. Two energy bins were analysed: $E = 4 - 8$ EeV and $E \geq 8$ EeV. In the case of energies $E \geq 8$ EeV a deviation of the expectation of pure isotropy was observed by the global anisotropy estimator with a chance probability of $p = 2.5 \times 10^{-3}$ (not accounting for the search in two energy bins).

The only significant deviation in the individual Needlet scales j was observed in the dipolar scale $j = 0$ for $E \geq 8$ EeV with only 0.0014% of isotropic reference skymaps possessing an equal or higher deviation from isotropy in this particular scale. No deviations from isotropy were observed in any other angular scale or energy.

Under the assumption of a dipole dominated flux the properties of the dipolar pattern were reconstructed. The dipolar pattern points towards a direction with a right ascension of $\alpha_d = 97^\circ \pm 16^\circ$ and a declination of $\delta_d = -39^\circ \pm 17^\circ$ and possesses an amplitude of $r = (6.8 \pm 1.6)\%$. Various data based cross-checks were performed to verify the robustness of the observed dipolar pattern. By relaxing the dominant dipole assumption it was found that a possible total of 0.5% percentage points of the observed dipole amplitude could be explained by the presence of a quadrupolar anisotropy.

Using the JF-12 model of the galactic magnetic field (GMF) the analysis was restricted to a portion of the sky where a possible signal from the active galactic nucleus closest to earth, Centaurus A, would be strongest in the case of a pure proton composition. No signal was observed, either in the case of a strong or a weak extra galactic magnetic field (EGMF) for energies $E \geq 8$ EeV, $E \geq 10$ EeV and $E \geq 12$ EeV. Due to the non-observation of a signal limits were set using the CLS method. The limit on the signal fraction at earth for a pure proton composition from Centaurus A under the assumption of the JF-12 GMF model and an otherwise isotropic distribution of arrival direction is 0.4% for all analysed energies and strengths of the EGMF.

A future application of the analysis used in this work to a subset of the lightest, and hence least deflected, UHECRs could significantly increase the change to observe further deviations from isotropy. One of the goals of the currently starting upgrade of the Pierre Auger Observatory is to achieve this capability. A requirement for this upgrade are efficient, robust and cost-effective light sensors with a sufficient dynamic

range. Silicon-Photomultipliers (SiPMs) are such sensors. In this work a technique to fully characterise their response to a wide variety of light pulses and to reconstruct the incident signal from their response was developed. This is an important requirement for their usage in the upgrade of the Pierre Auger Observatory or similar, future usage in the study of UHECRs.

Bibliography

[1] A. Letessier-Selvon and T. Stanev, "Ultrahigh energy cosmic rays," *Rev. Mod. Phys.* **83** (Sep, 2011) 907–942. http://link.aps.org/doi/10.1103/RevModPhys.83.907.

[2] J. Blümer, R. Engel, and J. R. Hörandel, "Cosmic rays from the knee to the highest energies," *Progress in Particle and Nuclear Physics* **63** no. 2, (2009) 293 – 338. http://www.sciencedirect.com/science/article/pii/S0146641009000362.

[3] K. Kotera and A. V. Olinto, "The astrophysics of ultrahigh-energy cosmic rays," *Annual Review of Astronomy and Astrophysics* **49** no. 1, (2011) 119–153, `http://dx.doi.org/10.1146/annurev-astro-081710-102620`. http://dx.doi.org/10.1146/annurev-astro-081710-102620.

[4] M. Longair, *High Energy Astrophysics*. Cambridge University Press, 2011.

[5] Pierre Auger Collaboration Collaboration, J. Abraham *et al.*, "Measurement of the depth of maximum of extensive air showers above 10^{18} eV," *Phys. Rev. Lett.* **104** (2010) 091101. http://link.aps.org/doi/10.1103/PhysRevLett.104.091101.

[6] The High Resolution Fly's Eye Collaboration Collaboration, R. U. Abbasi *et al.*, "Indications of Proton-Dominated Cosmic-Ray Composition above 1.6 EeV," *Physical Review Letters* **104** no. 16, (Apr., 2010) 161101, `arXiv:0910.4184 [astro-ph.HE]`. http://adsabs.harvard.edu/abs/2010PhRvL.104p1101A.

[7] K.-H. Kampert and P. Tinyakov, "Cosmic rays from the ankle to the cutoff," *Comptes Rendus Physique* **15** (2014) 318–328, `arXiv:1405.0575 [astro-ph.HE]`.

[8] B. Keilhauer, *Investigation of Atmospheric Effects on the Development of Extensive Air Showers and their Detection with the Pierre Auger Observatory*. Phd thesis, Universitaet Karlsruhe, Karlsruhe, 2003.

[9] Particle Data Group Collaboration, K. A. Olive *et al.*, "Review of Particle Physics," *Chin. Phys.* **C38** (2014) 090001.

[10] T. K. Gaisser, *Cosmic Rays and Particle Physics*. Cambridge University Press, 1990.

[11] K.-H. Kampert and A. Watson, "Extensive air showers and ultra high-energy cosmic rays: a historical review," *The European Physical Journal H* **37** no. 3, (2012) 359–412. http://dx.doi.org/10.1140/epjh/e2012-30013-x.

[12] E. Fermi, "On the origin of the cosmic radiation," *Phys. Rev.* **75** (Apr, 1949) 1169–1174. http://link.aps.org/doi/10.1103/PhysRev.75.1169.

[13] A. R. Bell, "The acceleration of cosmic rays in shock fronts – ii," *Monthly Notices of the Royal Astronomical Society* **182** no. 3, (1978) 443–455, `http://mnras.oxfordjournals.org/content/182/3/443.full.pdf+html`. http://mnras.oxfordjournals.org/content/182/3/443.abstract.

[14] R. D. Blandford and J. P. Ostriker, "Particle acceleration by astrophysical shocks," *The Astrophysical Journal Letters* **221** (Apr., 1978) L29–L32. http://adsabs.harvard.edu/abs/1978ApJ...221L..29B.

[15] A. M. Hillas, "The origin of ultra-high-energy cosmic rays," *Annual Review of Astronomy and Astrophysics* **22** no. 1, (1984) 425–444, `http://dx.doi.org/10.1146/annurev.aa.22.090184.002233`. http://dx.doi.org/10.1146/annurev.aa.22.090184.002233.

[16] T. Antoni, W. Apel, A. Badea, K. Bekk *et al.*, "Kascade measurements of energy spectra for elemental groups of cosmic rays: Results and open problems," *Astroparticle Physics* **24** no. 1–2, (2005) 1 – 25. http://www.sciencedirect.com/science/article/pii/S0927650505000691.

[17] R. L. Diehl, "Particle acceleration in cosmic sites. Astrophysics issues in our understanding of cosmic rays," *European Physical Journal D* **55** (Nov., 2009) 509–518, `arXiv:0902.4795 [astro-ph.HE]`. http://adsabs.harvard.edu/abs/2009EPJD...55..509D.

[18] P. Bhattacharjee, "Origin and propagation of extremely high energy cosmic rays," *Physics Reports* **327** (Mar., 2000) 109–247, `astro-ph/9811011`. http://adsabs.harvard.edu/abs/2000PhR...327..109B.

[19] R. M. Kulsrud and E. G. Zweibel, "On the origin of cosmic magnetic fields," *Reports on Progress in Physics* **71** no. 4, (2008) 046901. http://stacks.iop.org/0034-4885/71/i=4/a=046901.

[20] A. Achterberg, Y. A. Gallant, C. A. Norman, and D. B. Melrose, "Intergalactic Propagation of UHE Cosmic Rays," *ArXiv Astrophysics e-prints* (July, 1999) , `astro-ph/9907060`. http://adsabs.harvard.edu/abs/1999astro.ph..7060A.

[21] D. Harari, S. Mollerach, E. Roulet, and F. Sanchez, "Lensing of ultrahigh-energy cosmic rays in turbulent magnetic fields," *JHEP* **03** (2002) 045, `arXiv:astro-ph/0202362 [astro-ph]`.

[22] R. Jansson and G. R. Farrar, "The Galactic Magnetic Field," *The Astrophysical Journal Letters* **761** (Dec., 2012) L11, `arXiv:1210.7820 [astro-ph.GA]`. http://adsabs.harvard.edu/abs/2012ApJ...761L..11J.

[23] G. R. Farrar, "The Galactic Magnetic Field and Ultrahigh-Energy Cosmic Ray Deflections," *Comptes Rendus Physique* **15** (2014) 339–348, arXiv:1405.3680 [astro-ph.HE].

[24] D. Walz, *Constraining Models of the Extragalactic Cosmic Ray Origin with the Pierre Auger Observatory*. PhD thesis, RWTH Aachen University, Germany, 2016.

[25] T. Winchen, *The Principal Axes of the Directional Energy Distribution of Cosmic Rays Measured with the Pierre Auger Observatory*. PhD thesis, RWTH Aachen University, Germany, 2013. http://wwwo.physik.rwth-aachen.de/fileadmin/user_upload/www_physik/Personen/erdmann/Dissertation-Winchen.pdf.

[26] K. Dolag, D. Grasso, V. Springel, and I. Tkachev, "Constrained simulations of the magnetic field in the local Universe and the propagation of UHECRs," *JCAP* **0501** (2005) 009, arXiv:astro-ph/0410419 [astro-ph].

[27] K. Dolag, D. Grasso, V. Springel, and I. Tkachev, "Mapping deflections of extragalactic ultrahigh-energy cosmic rays in magnetohydrodynamic simulations of the local universe," *Journal of Experimental and Theoretical Physics Letters* **79** no. 12, (2004) 583–587. http://dx.doi.org/10.1134/1.1790011.

[28] M. S. Pshirkov, P. G. Tinyakov, and F. R. Urban, "New Limits on Extragalactic Magnetic Fields from Rotation Measures," *Physical Review Letters* **116** no. 19, (May, 2016) 191302, arXiv:1504.06546. http://adsabs.harvard.edu/abs/2016PhRvL.116s1302P.

[29] K. Dolag, M. Kachelriess, S. Ostapchenko, and R. Tomàs, "Lower Limit on the Strength and Filling Factor of Extragalactic Magnetic Fields," *The Astrophysical Journal Letters* **727** (Jan., 2011) L4, arXiv:1009.1782 [astro-ph.HE].

[30] The Pierre Auger Collaboration, P. Abreu, M. Aglietta, E. J. Ahn *et al.*, "Search for first harmonic modulation in the right ascension distribution of cosmic rays detected at the Pierre Auger Observatory," *Astroparticle Physics* **34** (Mar., 2011) 627–639, arXiv:1103.2721 [astro-ph.HE]. http://adsabs.harvard.edu/abs/2011APh....34..627P.

[31] The Pierre Auger Collaboration, A. Aab, P. Abreu, M. Aglietta *et al.*, "The Pierre Auger Observatory: Contributions to the 33rd International Cosmic Ray Conference (ICRC 2013)," *ArXiv e-prints* (July, 2013) , arXiv:1307.5059 [astro-ph.HE]. http://adsabs.harvard.edu/abs/2013arXiv1307.5059T.

[32] The Pierre Auger Collaboration, P. Abreu, M. Aglietta, M. Ahlers *et al.*, "Large-scale Distribution of Arrival Directions of Cosmic Rays Detected Above 10^{18} eV at the Pierre Auger Observatory," *The Astrophysical Journal, Supplement* **203** (Dec., 2012) 34, arXiv:1210.3736 [astro-ph.HE]. http://adsabs.harvard.edu/abs/2012ApJS..203...34P.

[33] The Pierre Auger Collaboration, P. Abreu, M. Aglietta, M. Ahlers *et al.*, "Constraints on the Origin of Cosmic Rays above 10^{18} eV from Large-scale Anisotropy Searches in Data of the Pierre Auger Observatory," *The Astrophysical Journal Letters* **762** (Jan., 2013) L13, arXiv:1212.3083 [astro-ph.HE]. http://adsabs.harvard.edu/abs/2013ApJ...762L..13P.

[34] The Pierre Auger Collaboration, A. Aab *et al.*, "Large Scale Distribution of Ultra High Energy Cosmic Rays Detected at the Pierre Auger Observatory With Zenith Angles up to 80°," *Astrophys. J.* **802** no. 2, (2015) 111, arXiv:1411.6953 [astro-ph.HE].

[35] The Pierre Auger Collaboration, A. Aab *et al.*, "The Pierre Auger Observatory: Contributions to the 34th International Cosmic Ray Conference (ICRC 2015)," *ArXiv e-prints* (2015) , arXiv:1509.03732 [astro-ph.HE]. https://inspirehep.net/record/1393211/files/arXiv:1509.03732.pdf.

[36] Telescope Array Collaboration, R. U. Abbasi *et al.*, "Indications of Intermediate-Scale Anisotropy of Cosmic Rays with Energy Greater Than 57 EeV in the Northern Sky Measured with the Surface Detector of the Telescope Array Experiment," *Astrophys. J.* **790** (2014) L21, arXiv:1404.5890 [astro-ph.HE].

[37] The Pierre Auger, Telescope Array Collaboration, A. Aab *et al.*, "Searches for large-scale anisotropy in the arrival directions of cosmic rays detected above energy of 10^{19} ev at the pierre auger observatory and the telescope array," *The Astrophysical Journal* **794** no. 2, (2014) 172. http://stacks.iop.org/0004-637X/794/i=2/a=172.

[38] J. R. Vázquez, J. Rosado, D. García-Pinto, and F. Arqueros, "The effect of the fluorescence yield selection on the energy scales of Auger, HiRes and TA," in *European Physical Journal Web of Conferences*, vol. 53 of *European Physical Journal Web of Conferences*, p. 10002. June, 2013. arXiv:1303.2945 [astro-ph.IM]. http://adsabs.harvard.edu/abs/2013EPJWC..5310002V.

[39] The Pierre Auger, Telescope Array Collaboration, R. U. Abbasi *et al.*, "Pierre Auger Observatory and Telescope Array: Joint Contributions to the 34th International Cosmic Ray Conference (ICRC 2015)," *ArXiv e-prints* (2015) , arXiv:1511.02103 [astro-ph.HE].

[40] M. Kachelrieß and P. Serpico, "The compton–getting effect on ultra-high energy cosmic rays of cosmological origin," *Physics Letters B* **640** no. 5–6, (2006) 225 – 229. http://www.sciencedirect.com/science/article/pii/S037026930600983X.

[41] D. Harari, S. Mollerach, and E. Roulet, "Anisotropies of ultrahigh energy cosmic rays diffusing from extragalactic sources," *Phys. Rev. D* **89** (Jun, 2014) 123001. http://link.aps.org/doi/10.1103/PhysRevD.89.123001.

[42] The Pierre Auger Collaboration, "The pierre auger cosmic ray observatory," *Nuclear Instruments and Methods in Physics Research Section A: Accelerators, Spectrometers, Detectors and Associated Equipment* **798** (2015) 172 – 213. http://www.sciencedirect.com/science/article/pii/S0168900215008086.

[43] A. Nelles, "Search for anomalies in cosmic air showers measured with the surface detector of the pierre auger observatory," masters thesis, RWTH Aachen University, Germany, 2010. https://web.physik.rwth-aachen.de/~hebbeker/theses/nelles_diploma.pdf.

[44] The Pierre Auger Collaboration, J. Abraham, P. Abreu, M. Aglietta *et al.*, "The fluorescence detector of the pierre auger observatory," *Nuclear Instruments and Methods in Physics Research Section A: Accelerators, Spectrometers, Detectors and Associated Equipment* **620** no. 2–3, (2010) 227 – 251. http://www.sciencedirect.com/science/article/pii/S0168900210008727.

[45] The Pierre Auger Collaboration, I. Allekotte, A. F. Barbosa, P. Bauleo *et al.*, "The surface detector system of the Pierre Auger Observatory," *Nuclear Instruments and Methods in Physics Research A* **586** (Mar., 2008) 409–420, `arXiv:0712.2832`. http://adsabs.harvard.edu/abs/2008NIMPA.586..409A.

[46] F. Arqueros, J. R. Hoerandel, and B. Keilhauer, "Air fluorescence relevant for cosmic-ray detection. summary of the 5th fluorescence workshop, el escorial 2007," *Nuclear Instruments and Methods in Physics Research Section A: Accelerators, Spectrometers, Detectors and Associated Equipment* **597** no. 1, (2008) 1 – 22. Proceedings of the 5th Fluorescence Workshop.

[47] The Pierre Auger Collaboration, X. Bertou, P. Allison, C. Bonifazi, P. Bauleo *et al.*, "Calibration of the surface array of the pierre auger observatory," *Nuclear Instruments and Methods in Physics Research Section A: Accelerators, Spectrometers, Detectors and Associated Equipment* **568** no. 2, (2006) 839 – 846. http://www.sciencedirect.com/science/article/pii/S0168900206013593.

[48] The Pierre Auger Collaboration, "Reconstruction of inclined air showers detected with the Pierre Auger Observatory," *Journal of Cosmology and Astroparticle Physics* **8** (Aug., 2014) 019, `arXiv:1407.3214 [astro-ph.HE]`. http://adsabs.harvard.edu/abs/2014JCAP...08..019T.

[49] The Pierre Auger Collaboration, J. Abraham, P. Abreu, M. Aglietta, E. J. Ahn *et al.*, "Trigger and aperture of the surface detector array of the Pierre Auger Observatory," *Nuclear Instruments and Methods in Physics Research A* **613** (Jan., 2010) 29–39, `arXiv:1111.6764 [astro-ph.IM]`. http://adsabs.harvard.edu/abs/2010NIMPA.613...29A.

[50] K. Kamata and J. Nishimura, "The lateral and the angular structure functions of electron showers," *Progress of Theoretical Physics Supplement* **6** (1958) 93–155,

http://ptps.oxfordjournals.org/content/6/93.full.pdf+html.
http://ptps.oxfordjournals.org/content/6/93.abstract.

[51] K. Greisen *Progress in Cosmic Ray Physics* **3** (1956) . https://archive.org/stream/progressincosmic031401mbp/progressincosmic031401mbp_djvu.txt.

[52] P. Sommers, "Cosmic ray anisotropy analysis with a full-sky observatory," *Astroparticle Physics* **14** (Jan., 2001) 271–286, astro-ph/0004016. http://adsabs.harvard.edu/abs/2001APh....14..271S.

[53] The Pierre Auger Collaboration, P. Abreu *et al.*, "The Pierre Auger Observatory I: The Cosmic Ray Energy Spectrum and Related Measurements," in *Proceedings of the 32nd International Cosmic Ray Conference (ICRC 2011)*. 2011. arXiv:1107.4809 [astro-ph.HE]. https://inspirehep.net/record/919725/files/arXiv:1107.4809.pdf.

[54] Pierre Auger Collaboration and C. Bonifazi, "The angular resolution of the Pierre Auger Observatory," *Nuclear Physics B Proceedings Supplements* **190** (May, 2009) 20–25, arXiv:0901.3138 [astro-ph.HE]. http://adsabs.harvard.edu/abs/2009NuPhS.190...20B.

[55] The Pierre Auger Collaboration, A. Aab, P. Abreu, M. Aglietta *et al.*, "The Pierre Auger Observatory Upgrade - Preliminary Design Report," *ArXiv e-prints* (Apr., 2016) , arXiv:1604.03637 [astro-ph.IM]. http://adsabs.harvard.edu/abs/2016arXiv160403637T.

[56] SensL, "J-series data sheet," 2016, last visited 08/2016. http://sensl.com/products/j-series/.

[57] J. Buss, "FACT - How stable are the silicon photon detectors?," in *Proceedings, 33rd International Cosmic Ray Conference (ICRC2013): Rio de Janeiro, Brazil, July 2-9, 2013*, p. 0683. http://www.cbpf.br/%7Eicrc2013/papers/icrc2013-0683.pdf.

[58] D. Renker and E. Lorenz, "Advances in solid state photon detectors," *Journal of Instrumentation* **4** no. 04, (2009) P04004. http://stacks.iop.org/1748-0221/4/i=04/a=P04004.

[59] Y. Du and F. Retière, "After-pulsing and cross-talk in multi-pixel photon counters," *Nuclear Instruments and Methods in Physics Research Section A: Accelerators, Spectrometers, Detectors and Associated Equipment* **596** no. 3, (2008) 396 – 401. http://www.sciencedirect.com/science/article/pii/S0168900208012643.

[60] F. Corsi, C. Marzocca, A. Perrotta, A. Dragone *et al.*, "Electrical characterization of silicon photo-multiplier detectors for optimal front-end design," in *2006 IEEE Nuclear Science Symposium Conference Record*, vol. 2, pp. 1276–1280. Oct, 2006.

[61] P. Buzhan, B. Dolgoshein, L. Filatov, A. Ilyin *et al.*, "Silicon photomultiplier and its possible applications," *Nuclear Instruments and Methods in Physics Research Section A: Accelerators, Spectrometers, Detectors and Associated Equipment* **504** no. 1–3, (2003) 48 – 52. http://www.sciencedirect.com/science/article/pii/S0168900203007496. Proceedings of the 3rd International Conference on New Developments in Photodetection.

[62] M. Petasecca, B. Alpat, G. Ambrosi, P. Azzarello *et al.*, "Thermal and electrical characterization of silicon photomultiplier," *IEEE Transactions on Nuclear Science* **55** no. 3, (June, 2008) 1686–1690.

[63] P. Eckert, H.-C. Schultz-Coulon, W. Shen, R. Stamen *et al.*, "Characterisation studies of silicon photomultipliers," *Nuclear Instruments and Methods in Physics Research A* **620** (Aug., 2010) 217–226, `arXiv:1003.6071 [physics.ins-det]`. http://adsabs.harvard.edu/abs/2010NIMPA.620..217E.

[64] A. Vacheret, G. Barker, M. Dziewiecki, P. Guzowski *et al.*, "Characterization and simulation of the response of multi-pixel photon counters to low light levels," *Nuclear Instruments and Methods in Physics Research Section A: Accelerators, Spectrometers, Detectors and Associated Equipment* **656** no. 1, (2011) 69 – 83. http://www.sciencedirect.com/science/article/pii/S0168900211014513.

[65] A. D. Guerra, N. Belcari, M. G. Bisogni, G. LLosa *et al.*, "Advantages and pitfalls of the silicon photomultiplier (sipm) as photodetector for the next generation of {PET} scanners," *Nuclear Instruments and Methods in Physics Research Section A: Accelerators, Spectrometers, Detectors and Associated Equipment* **617** no. 1–3, (2010) 223 – 226. http://www.sciencedirect.com/science/article/pii/S0168900209019056. 11th Pisa Meeting on Advanced DetectorsProceedings of the 11th Pisa Meeting on Advanced Detectors.

[66] T. Liu, J. Anderson, J. Freeman, S. Los *et al.*, "Proceedings of the 2nd international conference on technology and instrumentation in particle physics (tipp 2011) upgrade of the cms hadron outer calorimeter with sipms," *Physics Procedia* **37** (2012) 72 – 78. http://www.sciencedirect.com/science/article/pii/S1875389212016677.

[67] H. Anderhub, M. Backes, A. Biland, A. Boller *et al.*, "Fact—the first cherenkov telescope using a g-apd camera for tev gamma-ray astronomy," *Nuclear Instruments and Methods in Physics Research Section A: Accelerators, Spectrometers, Detectors and Associated Equipment* **639** no. 1, (2011) 58 – 61. http://www.sciencedirect.com/science/article/pii/S0168900210023466. Proceedings of the Seventh International Workshop on Ring Imaging Cherenkov Detectors.

[68] CTA Consortium Collaboration, M. Actis, G. Agnetta, F. Aharonian, A. Akhperjanian *et al.*, "Design concepts for the Cherenkov Telescope Array CTA: an advanced facility for ground-based high-energy gamma-ray astronomy," *Experimental Astronomy* **32** (Dec., 2011) 193–316, arXiv:1008.3703 [astro-ph.IM]. http://adsabs.harvard.edu/abs/2011ExA....32..193A.

[69] T. Niggemann, P. Assis, P. Brogueira, A. Bueno *et al.*, "Status of the Silicon Photomultiplier Telescope FAMOUS for the Fluorescence Detection of UHECRs," *Proceedings of the 33rd International Cosmic Ray Conference (ICRC 2013)* (2013) , arXiv:1502.00792 [astro-ph.IM]. http://adsabs.harvard.edu/abs/2015arXiv150200792N.

[70] S. M. Sze, *Physics of Semiconductor Devices*. Wiley-Interscience, 2007.

[71] A. N. Otte, *Observation of VHE Gamma-Rays from the Vicinity of magnetized Neutron Stars and Development of new Photon-Detectors for Future Ground based Gamma-Ray Detectors*. Phd thesis, Technische Universitaet Muenchen, Muenchen, 2007.

[72] J. Rennefeld, *Studien zur Eignung von Silizium Photomultipliern fuer den Einsatz im erweiterten CMS Detektor am SLHC*. Diploma thesis, RWTH Aachen University, Germany, 2010.

[73] A. L. Lacaita, F. Zappa, S. Bigliardi, and M. Manfredi, "On the bremsstrahlung origin of hot-carrier-induced photons in silicon devices," *IEEE Transactions on Electron Devices* **40** no. 3, (Mar, 1993) 577–582.

[74] Thorlabs, "Is200 data sheet." http://www.thorlabs.de.

[75] Hamamatsu Photonics, "S2281-photodiode data sheet," last visited 08/2016. https://www.hamamatsu.com/resources/pdf/ssd/s2281_series_kspd1044e.pdf.

[76] Phillips Scientific, "Ps 6945b-100 data sheet." http://www.phillipsscientific.com.

[77] Dycometal, "Cck-25-100 model data sheet." http://www.dycometal.com.

[78] Keithley, "6485 model data sheet." http://www.keithley.com.

[79] Aim and Thurlby Thandar Instruments, "models plh120-p, tga 1242, cpx 400 dual data sheets." http://www.tti-test.com.

[80] CAEN, "models qdc v965a, adc v1729, scaler v560ae, ltd v814b, fanin/fanout v925 data sheets." http://www.caen.it.

[81] LeCroy, "Waverunnter 1600 data sheet." http://www.teledynelecroy.com.

[82] N. Seguin-Moreau, "Latest generation of asics for photodetector readout," *Nuclear Instruments and Methods in Physics Research Section A: Accelerators, Spectrometers, Detectors and Associated Equipment* **718** (2013) 173 – 179. http://www.sciencedirect.com/science/article/pii/S0168900212014817. Proceedings of the 12th Pisa Meeting on Advanced DetectorsLa Biodola, Isola d'Elba, Italy, May 20 – 26, 2012.

[83] KETEK GmbH, "Pm3350 series data sheet," last visited 08/2016. http://www.ketek.net/products/sipm/pm3350/. http://www.ketek.net/products/sipm/pm3350/?no_cache=1&cid=5749&did=2251&sechash=1b16f9d1.

[84] Hamamatsu Photonics, "S10362-33 series data sheet," last visited 08/2016. http://www.datasheetlib.com/datasheet/707358/s10362-33_hamamatsu-photonics.html.

[85] C. R. Crowell and S. M. Sze, "Temperature dependence of avalanche multiplication in semiconductors," *Applied Physics Letters* **9** no. 6, (1966) 242–244. http://scitation.aip.org/content/aip/journal/apl/9/6/10.1063/1.1754731.

[86] R. Newman, "Visible light from a silicon $p - n$ junction," *Phys. Rev.* **100** (Oct, 1955) 700–703. http://link.aps.org/doi/10.1103/PhysRev.100.700.

[87] F. R. Schneider, T. R. Ganka, G. Şeker, E. Engelmann *et al.*, "Characterization of blue sensitive 3x3 mm2 sipms and their use in pet," *Journal of Instrumentation* **9** no. 07, (2014) P07027. http://stacks.iop.org/1748-0221/9/i=07/a=P07027.

[88] P. Hallen, "Determination of the recovery time of silicon photomultipliers," bachelor thesis, RWTH Aachen University, Germany, 2011. http://web.physik.rwth-aachen.de/~hebbeker/theses/hallen_bachelor.pdf.

[89] F. Scheuch, "Measurement and simulation of electrical properties of sipm photon detectors," masters thesis, RWTH Aachen University, Germany, 2012. http://web.physik.rwth-aachen.de/~hebbeker/theses/scheuch_master.pdf.

[90] L. Gruber, S. Brunner, J. Marton, and K. Suzuki, "Over saturation behavior of sipms at high photon exposure," *Nuclear Instruments and Methods in Physics Research Section A: Accelerators, Spectrometers, Detectors and Associated Equipment* **737** (2014) 11 – 18. http://www.sciencedirect.com/science/article/pii/S0168900213015520.

[91] D. Marinucci, D. Pietrobon, A. Balbi, P. Baldi *et al.*, "Spherical Needlets for CMB Data Analysis," *Mon. Not. Roy. Astron. Soc.* **383** (2008) 539, `arXiv:0707.0844 [astro-ph]`.

[92] D. Pietrobon, A. Amblard, A. Balbi, P. Cabella *et al.*, "Needlet Detection of Features in WMAP CMB Sky and the Impact on Anisotropies and Hemispherical Asymmetries," *Phys. Rev.* **D78** (2008) 103504, arXiv:0809.0010 [astro-ph].

[93] S. M. Feeney, M. C. Johnson, D. J. Mortlock, and H. V. Peiris, "First Observational Tests of Eternal Inflation: Analysis Methods and WMAP 7-Year Results," *Phys. Rev.* **D84** (2011) 043507, arXiv:1012.3667 [astro-ph.CO].

[94] R. Alves Batista, E. Kemp, R. M. de Almeida, and B. Daniel, "Wavelets Applied to the Detection of Point Sources of UHECRs," *Physicae Proc.* **1** (2010) 223, arXiv:1012.3645 [astro-ph.IM].

[95] R. Alves Batista, E. Kemp, and B. Daniel, "Detection of Point Sources in Cosmic Ray Maps Using the Mexican Hat Wavelet Family," *International Journal of Modern Physics E* **20** (2011) 61–66, arXiv:1201.2799 [astro-ph.IM].

[96] M. Plum, "Wavelet analysis of the arrival directions of ultra high energy cosmic rays at the pierre auger observatory," masters thesis, RWTH Aachen University, Germany, 2011. https://web.physik.rwth-aachen.de/~hebbeker/theses/plum_diploma.pdf.

[97] K. M. Górski, E. Hivon, A. J. Banday, B. D. Wandelt *et al.*, "HEALPix: A Framework for High-Resolution Discretization and Fast Analysis of Data Distributed on the Sphere," *The Astrophysical Journal* **622** (Apr., 2005) 759–771, astro-ph/0409513. http://adsabs.harvard.edu/abs/2005ApJ...622..759G.

[98] W. K, "Evaluation of active and passive shimming in magnetic resonance imaging," *Research and Reports in Nuclear Medicinel* **4** (Oct., 2014) 1–12. https://dx.doi.org/10.2147/RRNM.S46526.

[99] N. Schaeffer, "Efficient spherical harmonic transforms aimed at pseudospectral numerical simulations," *Geochemistry, Geophysics, Geosystems* **14** (Mar., 2013) 751–758, arXiv:1202.6522 [physics.comp-ph].

[100] T. C. and C. G., "A Practical Guide to Wavelet Analysis," *Bulletin of the American Meteorological Society* (Jan., 1998) . http://dx.doi.org/10.1175/1520-0477(1998)079⟨0061:APGTWA⟩2.0.CO;2.

[101] The IceCube Collaboration, "The IceCube Collaboration: contributions to the 30th International Cosmic Ray Conference (ICRC 2007)," *ArXiv e-prints* (Nov., 2007) , arXiv:0711.0353. http://adsabs.harvard.edu/abs/2007arXiv0711.0353T.

[102] D. Harari, S. Mollerach, and E. Roulet, "Effects of the galactic magnetic field upon large scale anisotropies of extragalactic cosmic rays," *Journal of Cosmology and Astroparticle Physics* **11** (Nov., 2010) 033, arXiv:1009.5891 [astro-ph.HE]. http://adsabs.harvard.edu/abs/2010JCAP...11..033H.

[103] O. Deligny, E. Armengaud, T. Beau, P. Da Silva *et al.*, "Angular power spectrum estimation of cosmic ray anisotropies with full or partial sky coverage," *Journal of Cosmology and Astroparticle Physics* **10** (Oct., 2004) 008, astro-ph/0404253. http://adsabs.harvard.edu/abs/2004JCAP...10..008D.

[104] C. B. Netterfield, P. A. R. Ade, J. J. Bock, J. R. Bond *et al.*, "A Measurement by BOOMERANG of Multiple Peaks in the Angular Power Spectrum of the Cosmic Microwave Background," *The Astrophysical Journal* **571** (June, 2002) 604–614, astro-ph/0104460. http://cdsads.u-strasbg.fr/abs/2002ApJ...571..604N.

[105] C. L. Bennett, D. Larson, J. L. Weiland, N. Jarosik *et al.*, "Nine-year Wilkinson Microwave Anisotropy Probe (WMAP) Observations: Final Maps and Results," *The Astrophysical Journal Supplement* **208** (Oct., 2013) 20, arXiv:1212.5225. http://adsabs.harvard.edu/abs/2013ApJS..208...20B.

[106] Planck Collaboration, P. A. R. Ade, N. Aghanim, Y. Akrami *et al.*, "Planck 2015 results. XVI. Isotropy and statistics of the CMB," *ArXiv e-prints* (June, 2015) , arXiv:1506.07135. http://adsabs.harvard.edu/abs/2015arXiv150607135P.

[107] IceCube Collaboration, Pierre Auger Collaboration, and Telescope Array Collaboration, "Search for correlations between the arrival directions of IceCube neutrino events and ultrahigh-energy cosmic rays detected by the Pierre Auger Observatory and the Telescope Array," *Journal of Cosmology and Astroparticle Physics* **1** (Jan., 2016) 037, arXiv:1511.09408 [astro-ph.HE]. http://adsabs.harvard.edu/abs/2016JCAP...01..037I.

[108] M. S. Pshirkov, P. G. Tinyakov, P. P. Kronberg, and K. J. Newton-McGee, "Deriving the Global Structure of the Galactic Magnetic Field from Faraday Rotation Measures of Extragalactic Sources," *The Astrophysical Journal Letters* **738** (Sept., 2011) 192, arXiv:1103.0814. http://adsabs.harvard.edu/abs/2011ApJ...738..192P.

[109] "Healpix documentation." http://healpix.sourceforge.net/documentation.php.

[110] R. Fisher, "Dispersion on a sphere," *Proceedings of the Royal Society of London A: Mathematical, Physical and Engineering Sciences* **217** no. 1130, (1953) 295–305, http://rspa.royalsocietypublishing.org/content/217/1130/295.full.pdf. http://rspa.royalsocietypublishing.org/content/217/1130/295.

[111] H.-P. Bretz, M. Erdmann, P. Schiffer, D. Walz *et al.*, "Parsec: A parametrized simulation engine for ultra-high energy cosmic ray protons," *Astroparticle Physics* **54** (2014) 110 – 117. http://www.sciencedirect.com/science/article/pii/S0927650513001874.

[112] P. Bigalke, "A method for searching for anisotropy in the arrival directions of cosmic nuclei traversing the galactic magnetic field," bachelor thesis, RWTH Aachen University, Germany, 2014.

http://wwwo.physik.rwth-aachen.de/fileadmin/user_upload/www_physik/Personen/erdmann/Bachelorthesis-Bigalke.pdf.

[113] J. P. Huchra, L. M. Macri, K. L. Masters, T. H. Jarrett *et al.*, "The 2MASS Redshift Survey - Description and Data Release," *The Astrophysical Journal Letters Supplements* **199** (Apr., 2012) 26, arXiv:1108.0669. http://adsabs.harvard.edu/abs/2012ApJS..199...26H.

[114] Pierre Auger Collaboration, J. Abraham *et al.*, "Astrophysical Sources of Cosmic Rays and Related Measurements with the Pierre Auger Observatory," in *31st International Cosmic Ray Conference (ICRC 2009) Lodz, Poland, July 7-15, 2009*. 2009. arXiv:0906.2347 [astro-ph.HE]. http://lss.fnal.gov/cgi-bin/find_paper.pl?conf-09-351.

[115] E. Hivon, K. M. Górski, C. B. Netterfield, B. P. Crill *et al.*, "Master of the cosmic microwave background anisotropy power spectrum: A fast method for statistical analysis of large and complex cosmic microwave background data sets," *The Astrophysical Journal* **567** no. 1, (2002) 2. http://stacks.iop.org/0004-637X/567/i=1/a=2.

[116] The Pierre Auger Collaboration, P. Abreu, M. Aglietta, E. J. Ahn *et al.*, "The effect of the geomagnetic field on cosmic ray energy estimates and large scale anisotropy searches on data from the Pierre Auger Observatory," *Journal of Cosmology and Astroparticle Physics* **11** (Nov., 2011) 022, arXiv:1111.7122 [astro-ph.IM]. http://adsabs.harvard.edu/abs/2011JCAP...11..022P.

[117] The Pierre Auger Collaboration, J. Abraham, P. Abreu, M. Aglietta *et al.*, "Atmospheric effects on extensive air showers observed with the surface detector of the Pierre Auger observatory," *Astroparticle Physics* **32** (Sept., 2009) 89–99, arXiv:0906.5497 [astro-ph.IM]. http://adsabs.harvard.edu/abs/2009APh....32...89P.

[118] G. L. H. Harris, M. Rejkuba, and W. E. Harris, "The Distance to NGC 5128 (Centaurus A)," *Publications of the Astron. Soc. of Australia* **27** (Oct., 2010) 457–462, arXiv:0911.3180. http://adsabs.harvard.edu/abs/2010PASA...27..457H.

[119] A. Keivani, G. R. Farrar, and M. Sutherland, "Magnetic deflections of ultra-high energy cosmic rays from Centaurus A," *Astroparticle Physics* **61** (Feb., 2015) 47–55, arXiv:1406.5249 [astro-ph.HE]. http://adsabs.harvard.edu/abs/2015APh....61...47K.

[120] "Galactic magnetic field lense download, last visited 08/2016." http://web.physik.rwth-aachen.de/Auger_MagneticFields/PARSEC/downloads.php.

[121] ALEPH Collaboration, DELPHI Collaboration, L3 Collaboration, OPAL Collaboration *et al.*, "Search for the Standard Model Higgs boson at LEP,"

Physics Letters B **565** (July, 2003) 61–75, hep-ex/0306033. http://adsabs.harvard.edu/abs/2003PhLB..565...61.

[122] CMS Collaboration, S. Chatrchyan *et al.*, "Combined results of searches for the standard model Higgs boson in pp collisions at $\sqrt{s} = 7$ TeV," *Phys. Lett.* **B710** (2012) 26–48, arXiv:1202.1488 [hep-ex].

[123] A. L. Read, "Presentation of search results: the cl s technique," *Journal of Physics G: Nuclear and Particle Physics* **28** no. 10, (2002) 2693. http://stacks.iop.org/0954-3899/28/i=10/a=313.

A. Appendix

A.1. List of Abbreviations

AGN	Active Galactic Nuclei
APS	Angular Power Spectrum
Auger	Pierre Auger Observatory
CDAS	Central Data Acquisition System
CMB	Cosmic Microwave Background
C.L.	Confidence Level
FOV	Field of View
GAPD	Geiger-Mode Avalanche Photodiode
GZK	Greisen-Zatsepin-Kuzmin-cutoff
(E)GMF	(Extra-) Galactic Magnetic Field
LDF	Lateral Density Function
NKG	Nishimura-Kamata-Greisen
PDE	Photon Detection Efficiency
PMT	Photomultiplier tube
PAO	Pierre Auger Observatory
PDF	Probability Density Function
ROI	Region of Interest
SD	Surface Detector
S.F.	Signal Fraction
SDP	Sower Detector Plane
SNR	Signal to Noise Ratio
SiPM	Silicon Photomultiplier
SNR	Supernova Remnant
SSD	Surface Scintillator Detectors
TA	Telescope Array
UHECR	Ultra-High Energy Cosmic Ray
UMD	Underground Muon Detector
VEM	Vertical Equivalent Muon
WCD	Water-Cherenkov detector

B. Appendix

B.1. Additional Plots: Benchmark Scenarios and Results

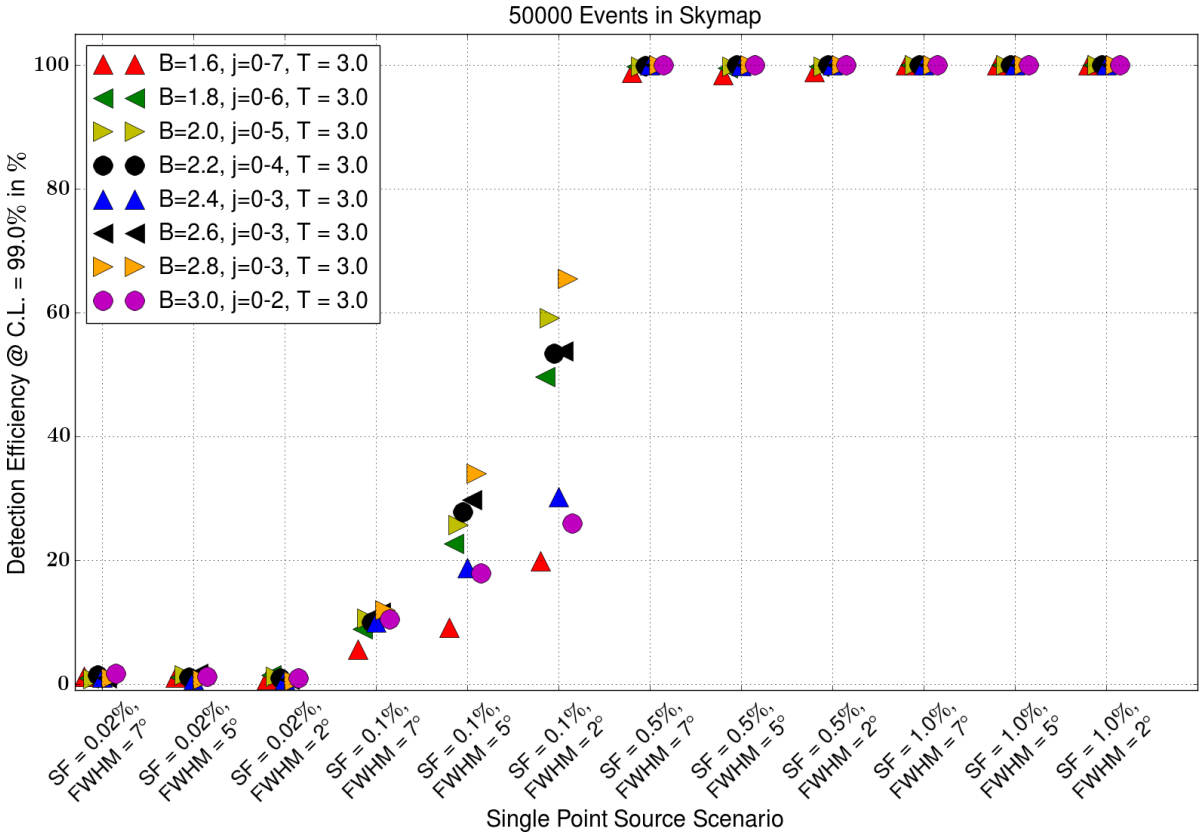
50000 Events in Skymap
B=1.6, j=0-7, T = 3.0
B=1.8, j=0-6, T = 3.0
B=2.0, j=0-5, T = 3.0
B=2.2, j=0-4, T = 3.0
B=2.4, j=0-3, T = 3.0
B=2.6, j=0-3, T = 3.0
B=2.8, j=0-3, T = 3.0
B=3.0, j=0-2, T = 3.0
Detection Efficiency @ C.L. = 99.0% in %
0
20
40
60
80
100
SF = 0.02%, FWHM = 7°
SF = 0.02%, FWHM = 5°
SF = 0.02%, FWHM = 2°
SF = 0.1%, FWHM = 7°
SF = 0.1%, FWHM = 5°
SF = 0.1%, FWHM = 2°
SF = 0.5%, FWHM = 7°
SF = 0.5%, FWHM = 5°
SF = 0.5%, FWHM = 2°
SF = 1.0%, FWHM = 7°
SF = 1.0%, FWHM = 5°
SF = 1.0%, FWHM = 2°
Single Point Source Scenario

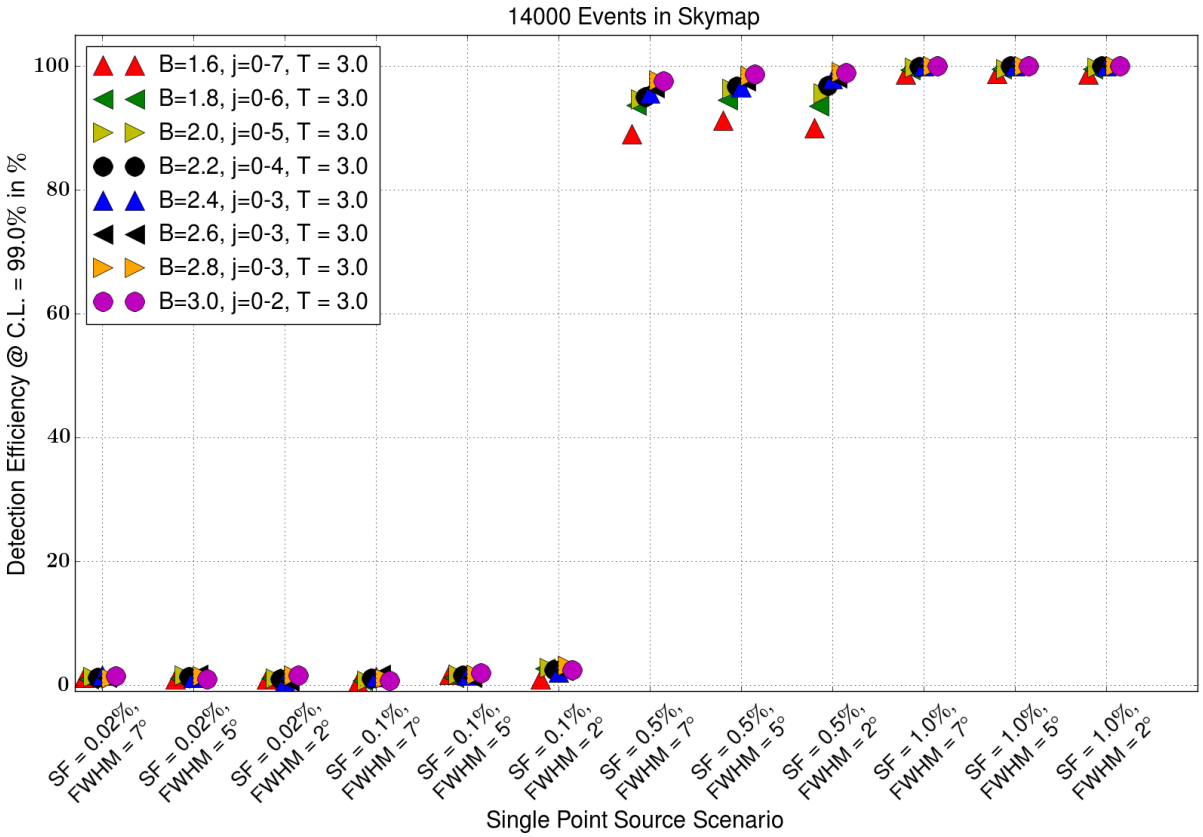
14000 Events in Skymap
B=1.6, j=0-7, T = 3.0
B=1.8, j=0-6, T = 3.0
B=2.0, j=0-5, T = 3.0
B=2.2, j=0-4, T = 3.0
B=2.4, j=0-3, T = 3.0
B=2.6, j=0-3, T = 3.0
B=2.8, j=0-3, T = 3.0
B=3.0, j=0-2, T = 3.0
Detection Efficiency @ C.L. = 99.0% in %
0
20
40
60
80
100
SF = 0.02%, FWHM = 7°
SF = 0.02%, FWHM = 5°
SF = 0.02%, FWHM = 2°
SF = 0.1%, FWHM = 7°
SF = 0.1%, FWHM = 5°
SF = 0.1%, FWHM = 2°
SF = 0.5%, FWHM = 7°
SF = 0.5%, FWHM = 5°
SF = 0.5%, FWHM = 2°
SF = 1.0%, FWHM = 7°
SF = 1.0%, FWHM = 5°
SF = 1.0%, FWHM = 2°
Single Point Source Scenario

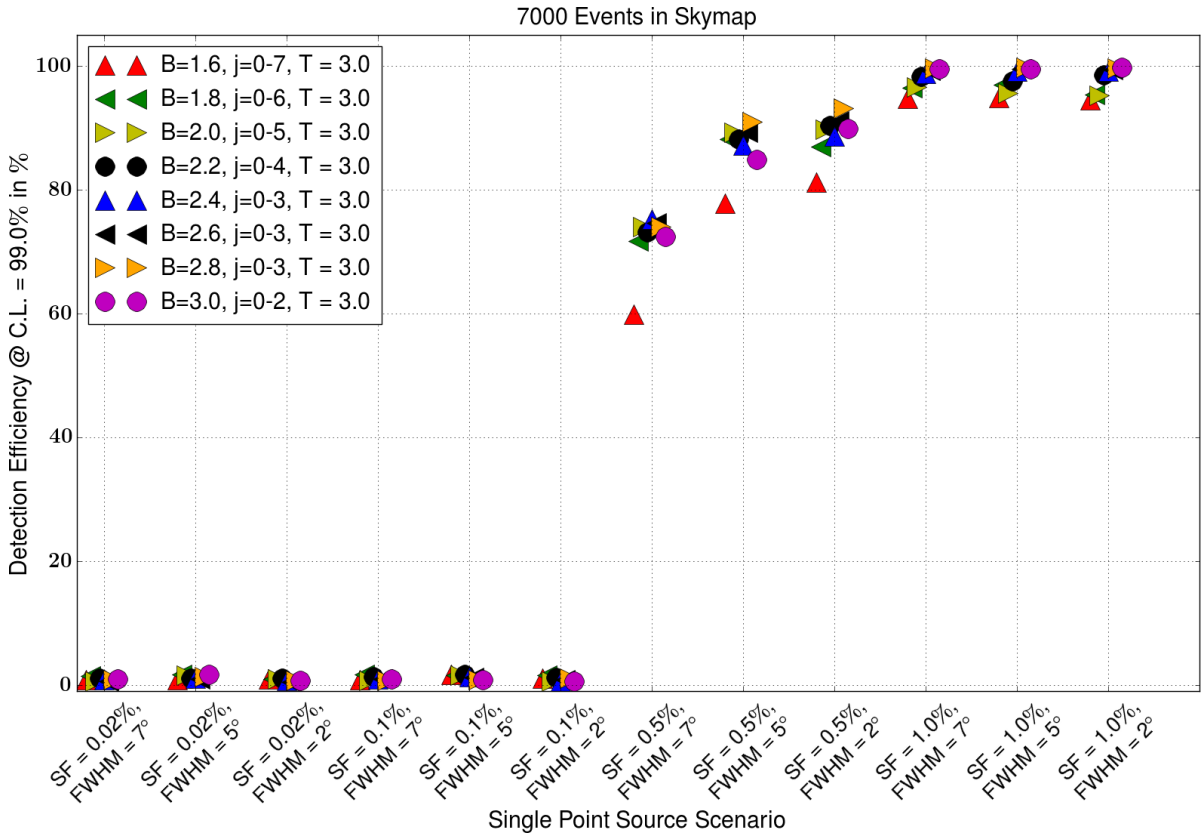
7000 Events in Skymap
B=1.6, j=0-7, T = 3.0
B=1.8, j=0-6, T = 3.0
B=2.0, j=0-5, T = 3.0
B=2.2, j=0-4, T = 3.0
B=2.4, j=0-3, T = 3.0
B=2.6, j=0-3, T = 3.0
B=2.8, j=0-3, T = 3.0
B=3.0, j=0-2, T = 3.0
Detection Efficiency @ C.L. = 99.0% in %
0
20
40
60
80
100
SF = 0.02%, FWHM = 7°
SF = 0.02%, FWHM = 5°
SF = 0.02%, FWHM = 2°
SF = 0.1%, FWHM = 7°
SF = 0.1%, FWHM = 5°
SF = 0.1%, FWHM = 2°
SF = 0.5%, FWHM = 7°
SF = 0.5%, FWHM = 5°
SF = 0.5%, FWHM = 2°
SF = 1.0%, FWHM = 7°
SF = 1.0%, FWHM = 5°
SF = 1.0%, FWHM = 2°
Single Point Source Scenario

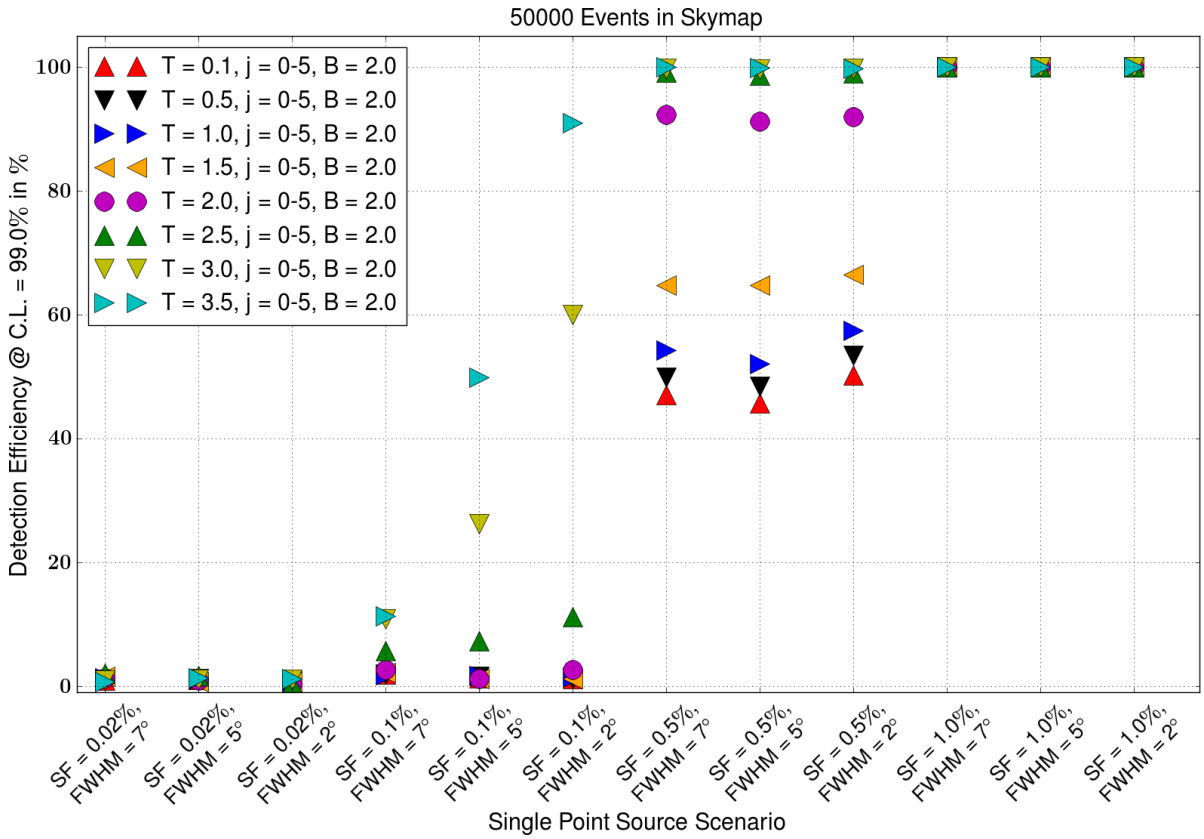
50000 Events in Skymap
T = 0.1, j = 0-5, B = 2.0
T = 0.5, j = 0-5, B = 2.0
T = 1.0, j = 0-5, B = 2.0
T = 1.5, j = 0-5, B = 2.0
T = 2.0, j = 0-5, B = 2.0
T = 2.5, j = 0-5, B = 2.0
T = 3.0, j = 0-5, B = 2.0
T = 3.5, j = 0-5, B = 2.0
Detection Efficiency @ C.L. = 99.0% in %
0
20
40
60
80
100
SF = 0.02%, FWHM = 7°
SF = 0.02%, FWHM = 5°
SF = 0.02%, FWHM = 2°
SF = 0.1%, FWHM = 7°
SF = 0.1%, FWHM = 5°
SF = 0.1%, FWHM = 2°
SF = 0.5%, FWHM = 7°
SF = 0.5%, FWHM = 5°
SF = 0.5%, FWHM = 2°
SF = 1.0%, FWHM = 7°
SF = 1.0%, FWHM = 5°
SF = 1.0%, FWHM = 2°
Single Point Source Scenario

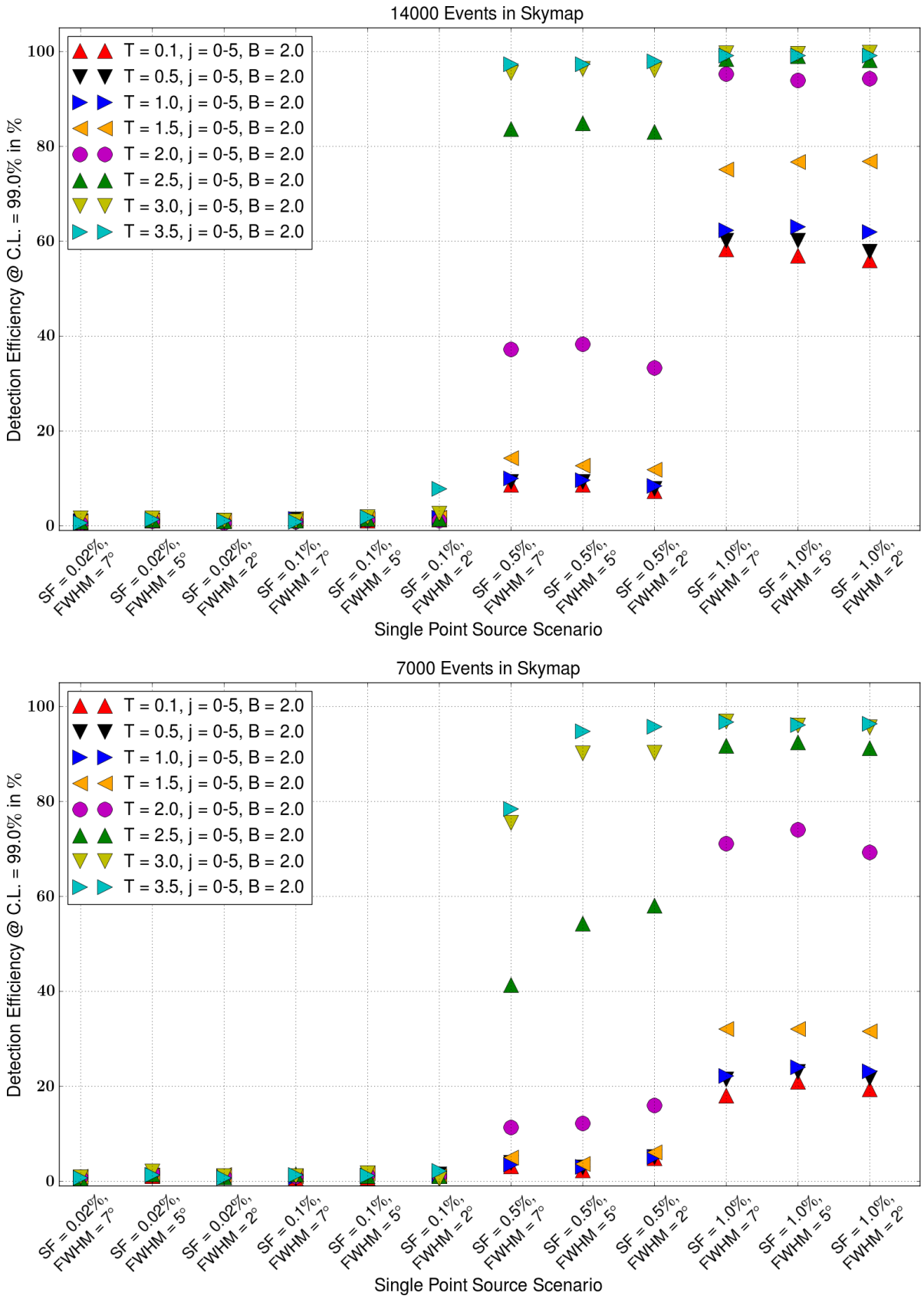

Figure B.1.: Sensitivity to the single point GMF source scenario in section 6.3.3. **Top 3:** Variable Needlet width B. **Bottom 3:** Variable threshold T.

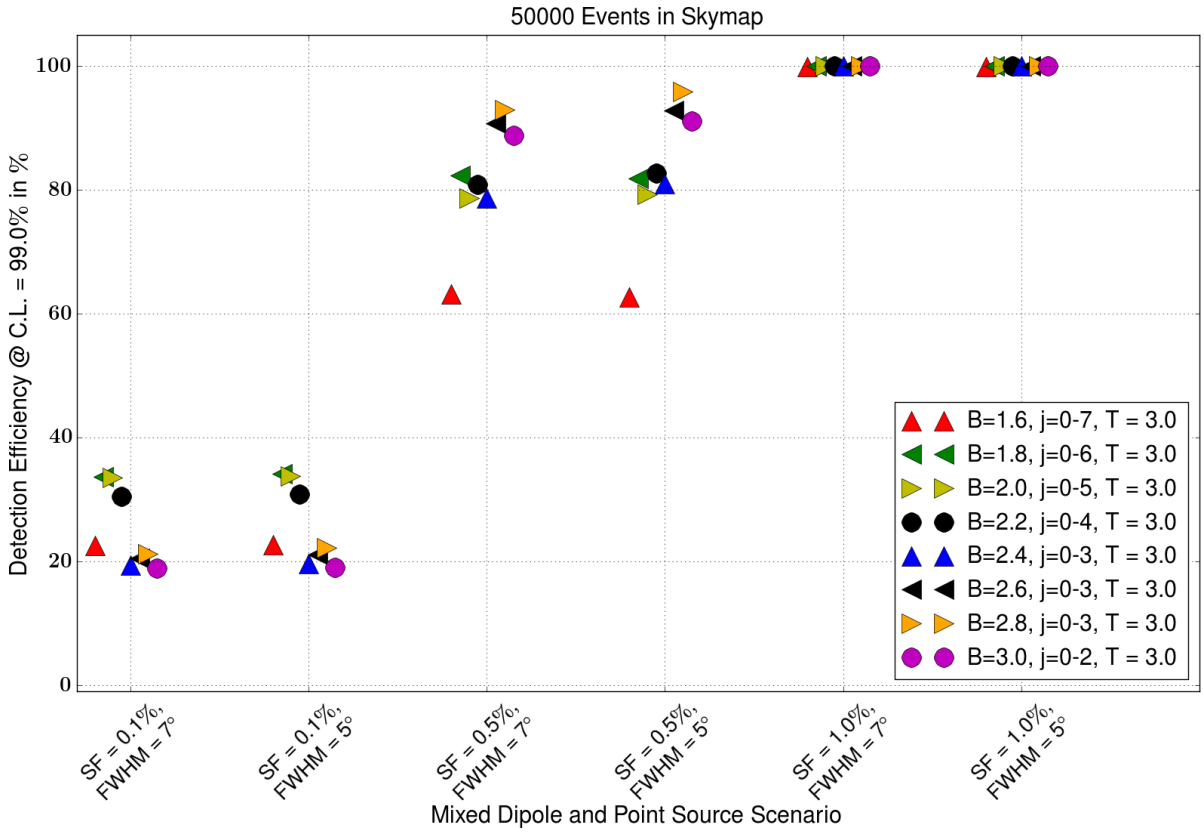
50000 Events in Skymap
Detection Efficiency @ C.L. = 99.0% in %
0
20
40
60
80
100
B=1.6, j=0-7, T = 3.0
B=1.8, j=0-6, T = 3.0
B=2.0, j=0-5, T = 3.0
B=2.2, j=0-4, T = 3.0
B=2.4, j=0-3, T = 3.0
B=2.6, j=0-3, T = 3.0
B=2.8, j=0-3, T = 3.0
B=3.0, j=0-2, T = 3.0
SF = 0.1%, FWHM = 7°
SF = 0.1%, FWHM = 5°
SF = 0.5%, FWHM = 7°
SF = 0.5%, FWHM = 5°
SF = 1.0%, FWHM = 7°
SF = 1.0%, FWHM = 5°
Mixed Dipole and Point Source Scenario

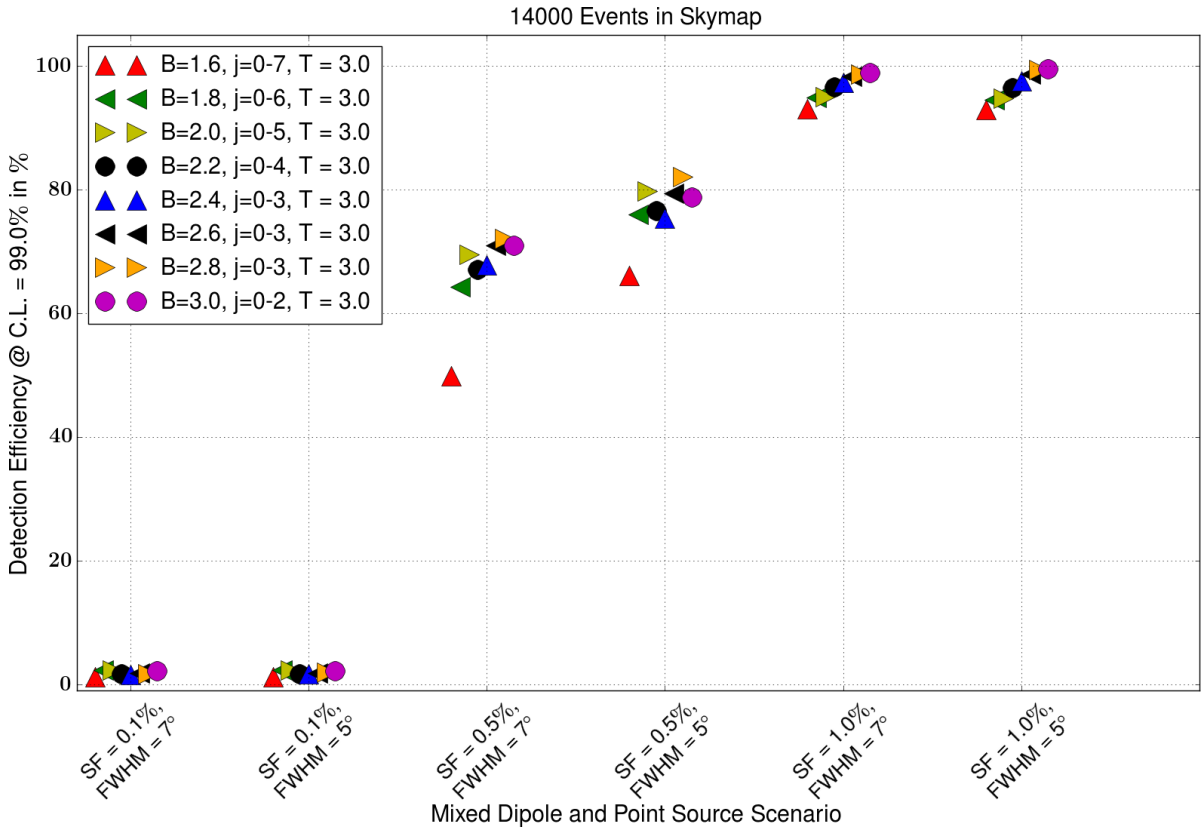
14000 Events in Skymap
Detection Efficiency @ C.L. = 99.0% in %
0
20
40
60
80
100
B=1.6, j=0-7, T = 3.0
B=1.8, j=0-6, T = 3.0
B=2.0, j=0-5, T = 3.0
B=2.2, j=0-4, T = 3.0
B=2.4, j=0-3, T = 3.0
B=2.6, j=0-3, T = 3.0
B=2.8, j=0-3, T = 3.0
B=3.0, j=0-2, T = 3.0
SF = 0.1%, FWHM = 7°
SF = 0.1%, FWHM = 5°
SF = 0.5%, FWHM = 7°
SF = 0.5%, FWHM = 5°
SF = 1.0%, FWHM = 7°
SF = 1.0%, FWHM = 5°
Mixed Dipole and Point Source Scenario

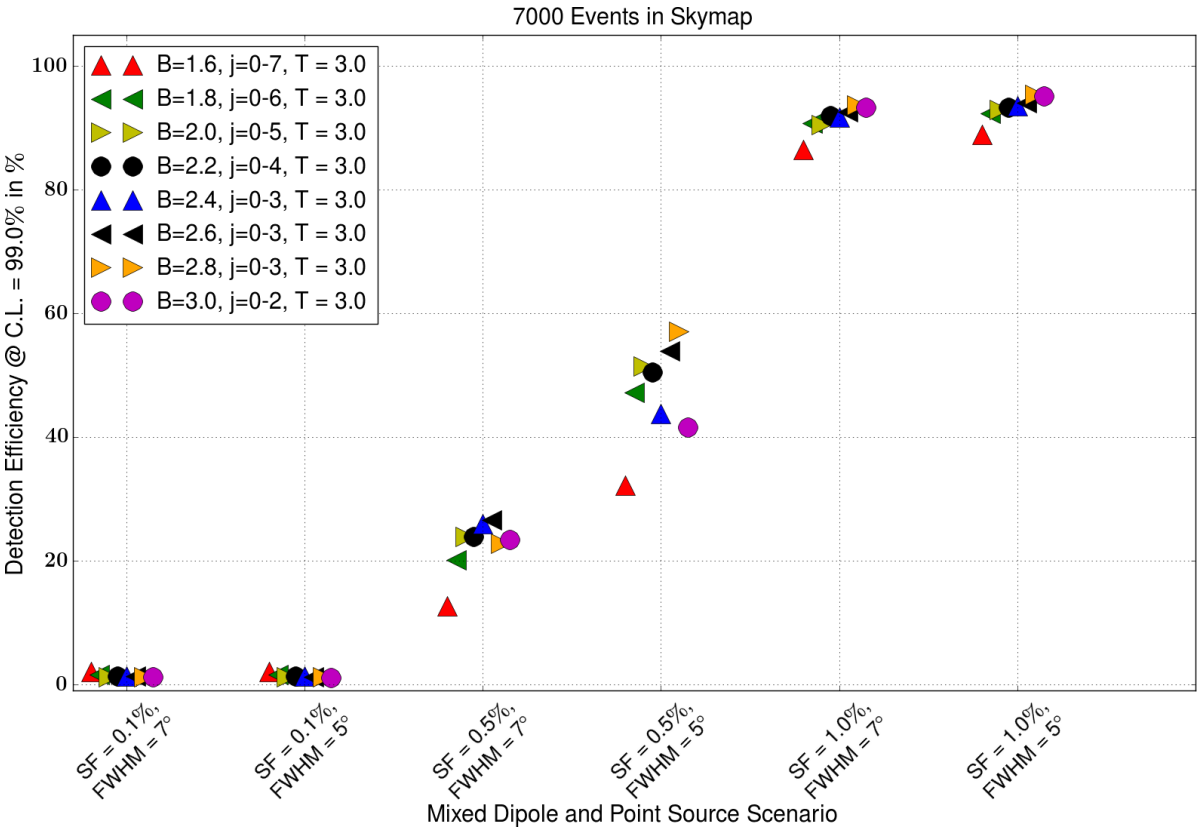
7000 Events in Skymap
B=1.6, j=0-7, T = 3.0
B=1.8, j=0-6, T = 3.0
B=2.0, j=0-5, T = 3.0
B=2.2, j=0-4, T = 3.0
B=2.4, j=0-3, T = 3.0
B=2.6, j=0-3, T = 3.0
B=2.8, j=0-3, T = 3.0
B=3.0, j=0-2, T = 3.0
Detection Efficiency @ C.L. = 99.0% in %
0
20
40
60
80
100
SF = 0.1%, FWHM = 7°
SF = 0.1%, FWHM = 5°
SF = 0.5%, FWHM = 7°
SF = 0.5%, FWHM = 5°
SF = 1.0%, FWHM = 7°
SF = 1.0%, FWHM = 5°
Mixed Dipole and Point Source Scenario

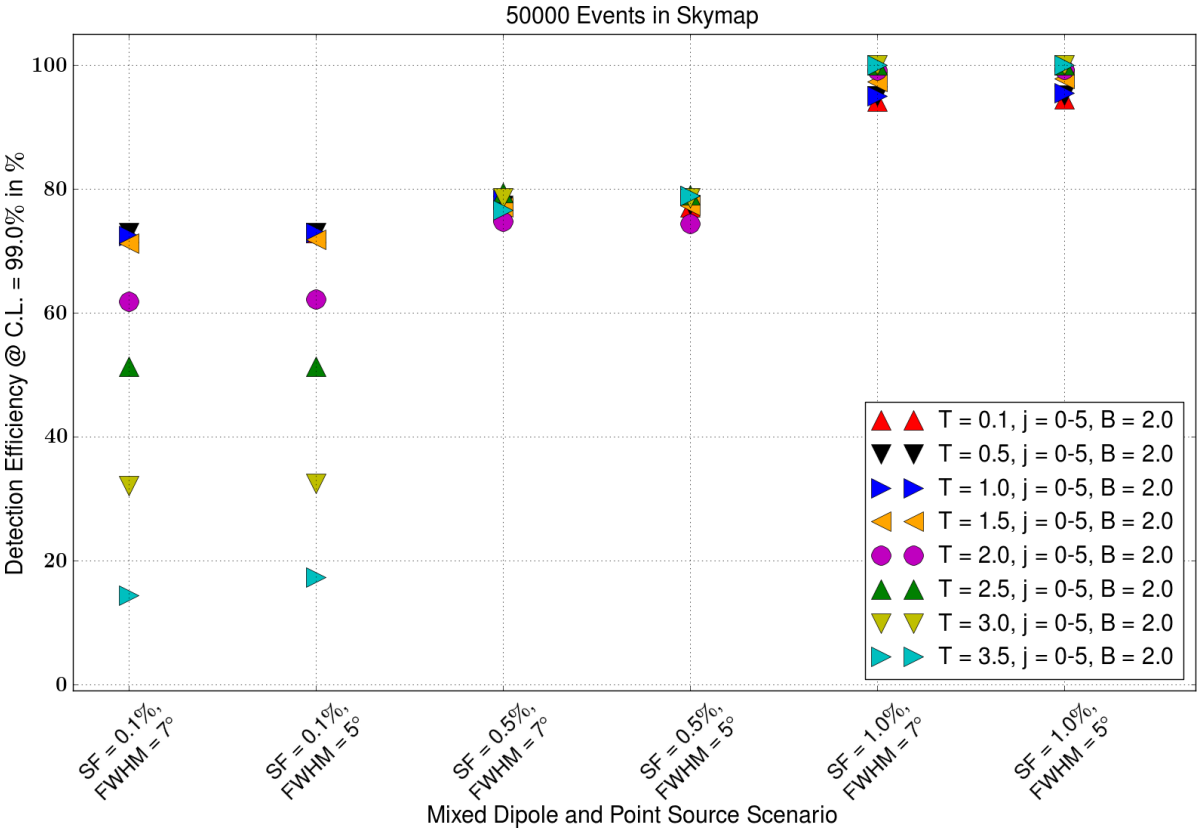
50000 Events in Skymap
T = 0.1, j = 0-5, B = 2.0
T = 0.5, j = 0-5, B = 2.0
T = 1.0, j = 0-5, B = 2.0
T = 1.5, j = 0-5, B = 2.0
T = 2.0, j = 0-5, B = 2.0
T = 2.5, j = 0-5, B = 2.0
T = 3.0, j = 0-5, B = 2.0
T = 3.5, j = 0-5, B = 2.0
Detection Efficiency @ C.L. = 99.0% in %
0
20
40
60
80
100
SF = 0.1%, FWHM = 7°
SF = 0.1%, FWHM = 5°
SF = 0.5%, FWHM = 7°
SF = 0.5%, FWHM = 5°
SF = 1.0%, FWHM = 7°
SF = 1.0%, FWHM = 5°
Mixed Dipole and Point Source Scenario

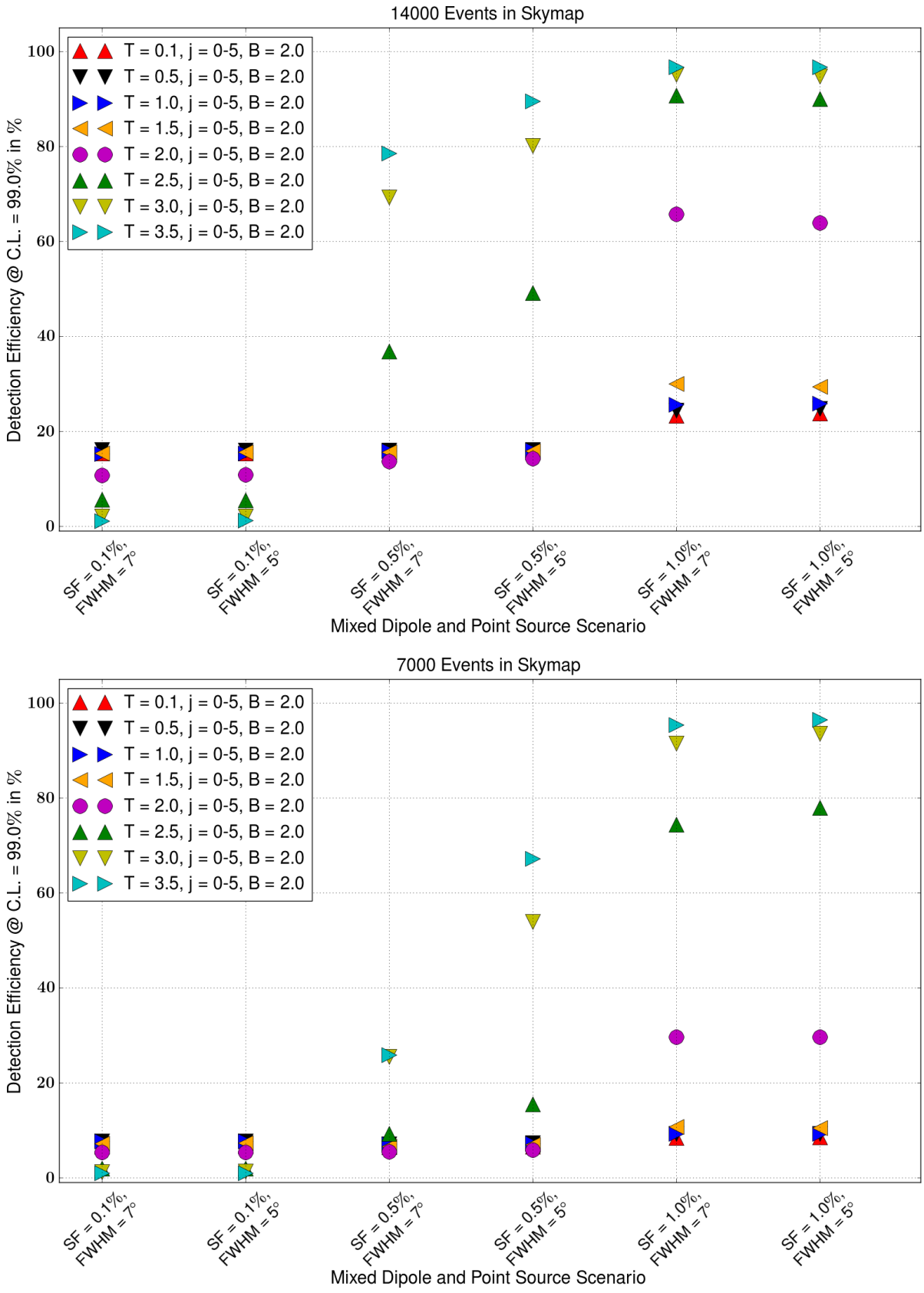

Figure B.2.: Sensitivity to the mixed dipole and point source scenario in section 6.3.4. **Top 3:** Variable Needlet width B. **Bottom 3:** Variable threshold T.

B.2. Additional Plots: Performance of the Angular Power Spectrum compared to the Needlet Wavelet Analysis

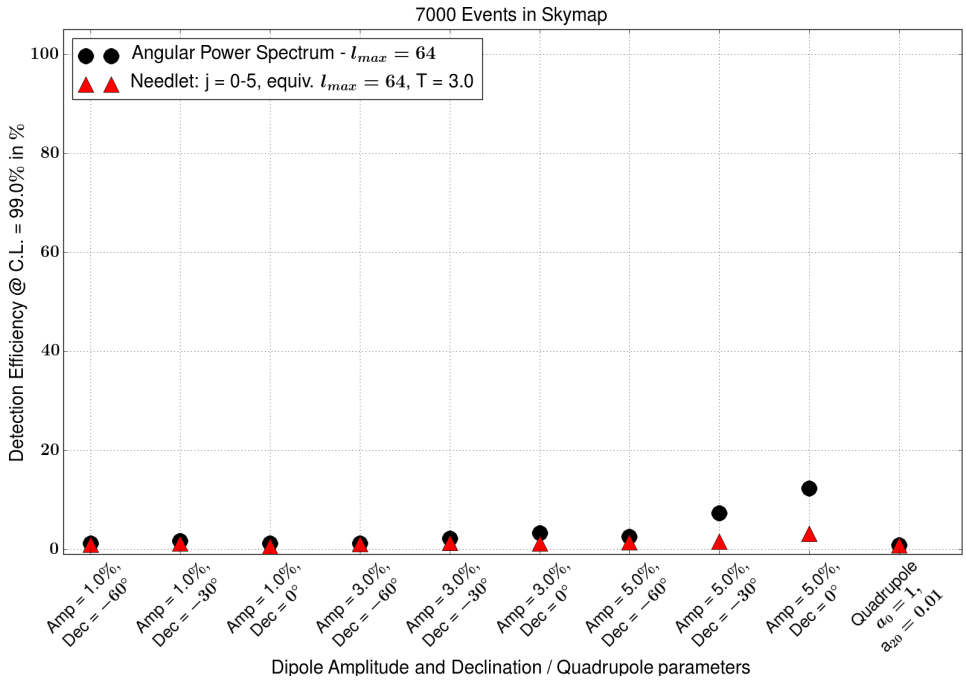

Figure B.3.: Sensitivity of the APS (black circles) and Needlet analysis (red triangles) to the dipole and quadrupole scenario described in section 6.3.1.

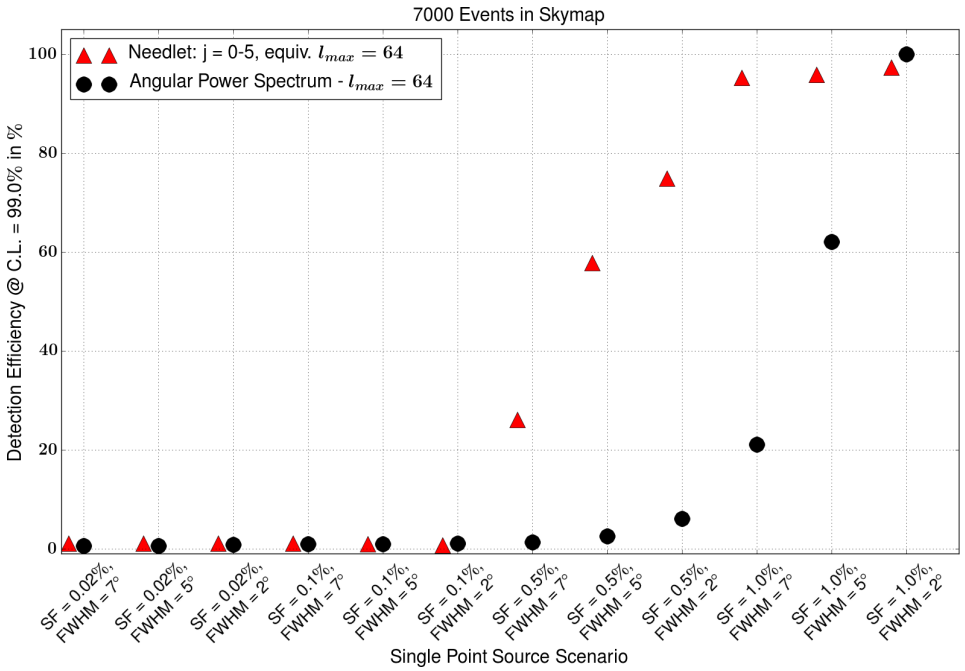

Figure B.4.: Sensitivity of the APS (black circles) and Needlet analysis (red triangles) to the single point source scenario described in section 6.3.2.

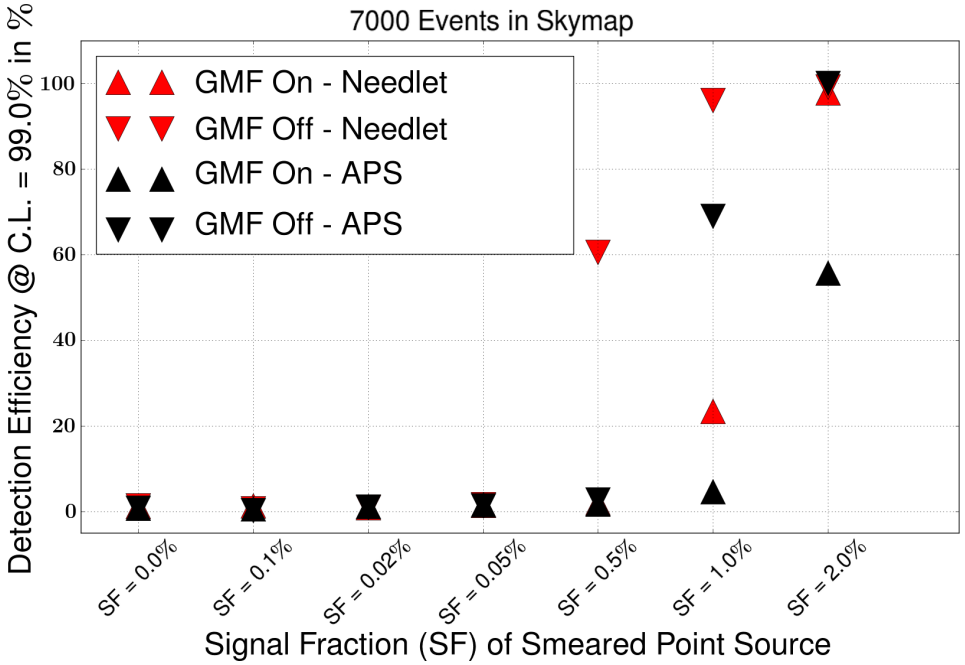

Figure B.5.: Sensitivity of the APS (black triangles) and Needlet analysis (red triangles) to the single point source smeared through the GMF scenario described in section 6.3.3.

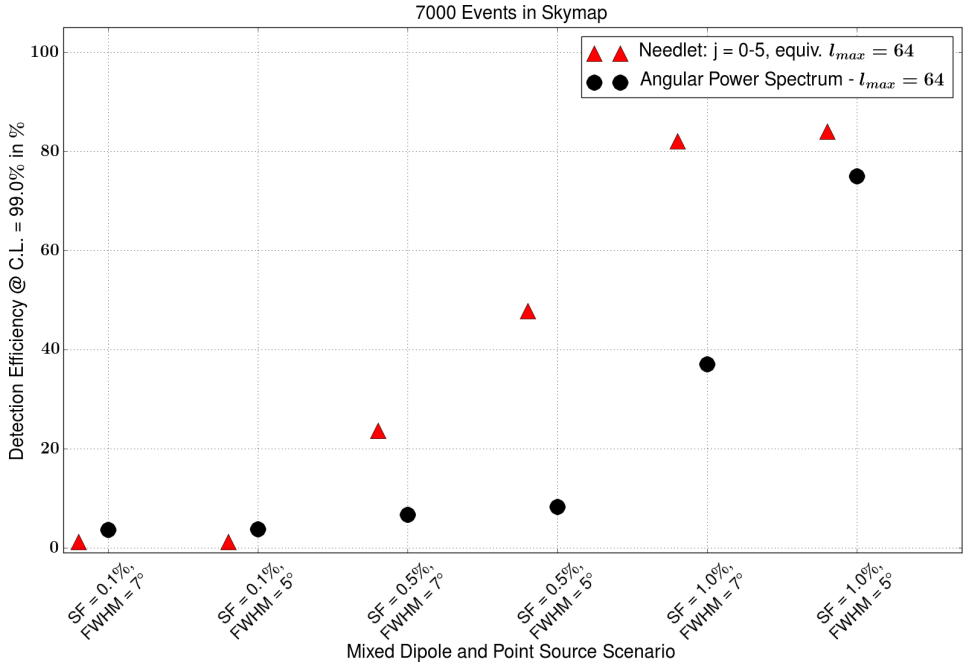

Figure B.6.: Sensitivity of the APS (black circles) and Needlet analysis (red triangles) to the mixed dipole and point source scenario described in section 6.3.4.

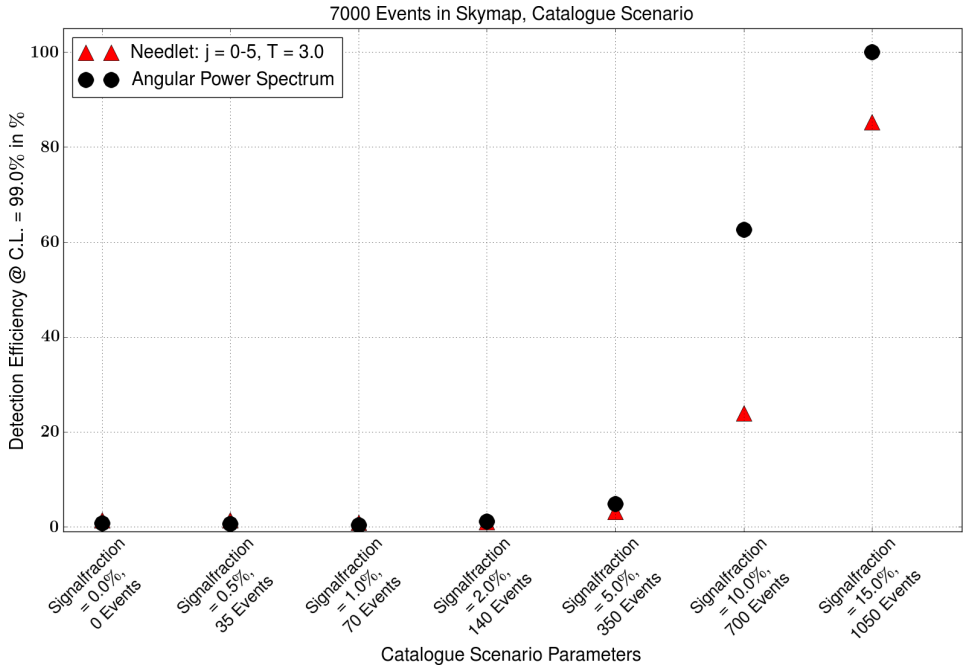

Figure B.7.: Sensitivity of the APS (black circles) and Needlet analysis (red triangles) to the catalogue scenario described in section 6.3.5.

B.3. Additional Plots: Auger Data Analysis

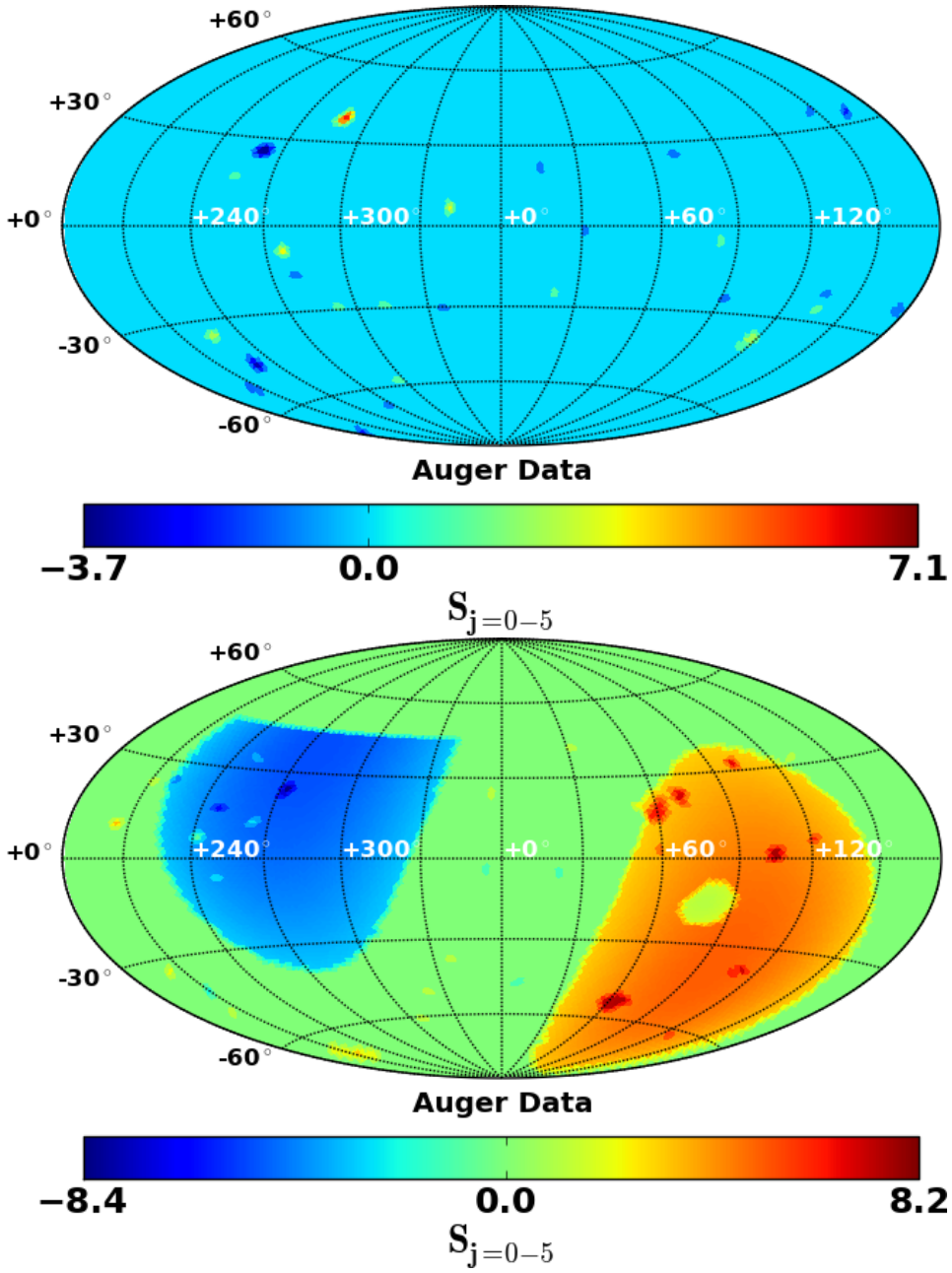

Figure B.8.: Reconstructed,thresholded and combined significance skymap $S_{j=0-5}$ for 4 EeV $< E <$ 8 EeV **(top)** and $E \geq$ 8 EeV **(bottom)**. The most prominent visible features are the dipole signature for $E \geq$ 8 EeV and a localised excess around $(\alpha, \delta) = (280°, -35°)$ for 4 EeV $< E <$ 8 EeV. However, the global significance of this local excess is low as shown in figure 8.2. On the other hand the global anisotropy estimator of $E \geq$ 8 EeV shows a hint of deviation from isotropy (see figure 8.3). The dipole-signature is further analysed and characterised in section 8.2.

Acknowledgements

An dieser Stelle möchte ich mich bei allen bedanken die mir diese Arbeit ermöglicht und mir dabei geholfen haben.

Zu aller erst möchte ich mich bei meinem Betreuer Prof. Dr. Hebbeker für die Gelegenheit bedanken überhaupt diese Arbeit durchgeführt haben zu können. Seine Anleitung, Ratschläge und Hinweise konnten meine Arbeit stets in eine bessere Richtung lenken und auch aus vermeintlichen Sackgassen helfen. Auch möchte ich mich für die Gelegenheiten bedanken meine Arbeit auf Meetings und Konferenzen auf der ganzen Welt zeigen zu können und eine Teleskopschicht vor Ort durchführen zu können.

Weiterhin möchte ich mich Prof. Dr. Christopher Wiebusch für die Begutachtung meiner Arbeit und die Anregungen und Diskussionen bei den Treffen in Bad Honnef bedanken.

Ein ganz besonderer Dank gilt meinen zwei (ehemaligen) Büro Kollegen Maurice Stephan und Christine Peters. Nicht nur fachlich sondern auch persönlich war es eine tolle Erfahrung mit euch zu Arbeiten. Danke für die tollen Jahre.

Meinen generellen Dank möchte ich der gesamten Auger Gruppe am Institut aussprechen. Die kollegiale Arbeitsweise und die regelmäßen Treffen und Diskussionen waren stets eine Hilfe und Anregung für meine Arbeit.

Gleiches gilt für die gesamte „Hallen Mannschaft“.

Ebenso möchte ich mich bei Matthias Plum für die Diskussionen über und die Starthilfe in sein altes Thema herzlich bedanken.

Ein großes Danke geht an meine Korrekturleser, Tim Niggemann, Matthias Plum und insbesondere Christine Peters für das Lesen der gesamten Arbeit.

C. Declaration of pre-released extracts

The following publications and internal notes of the Pierre Auger Collaboration contain pre-released extracts of this work. The used text from these publications has been written by the author of this thesis and was revised and copy-edited by the co-authors of the publications.

- T. Bretz, T. Hebbeker, M. Lauscher, L. Middendorf, T. Niggemann, J. Schumacher, M. Stephan, A. Bueno, S. Navas and A.G. Ruiz, *Dynamic range measurement and calibration of SiPMs*, Journal of Instrumentation, Volume 11, March 2016, (2016), URL: http://iopscience.iop.org/article/10.1088/1748-0221/11/03/P03009
  The results of chapter 4 have been published in the above reference. The chapter is based on this publication with some additions and modifications by the author of this work. The author of this work is the corresponding author of this publication. An additional and more detailed declaration has been added to the beginning of chapter 4.

- R. M. de Almeida, U. Giaccari, T. Hebbeker, M. Lauscher, J. R. T. de Mello Neto, J. S. de Oliveira and M. Plum, *Multiresolution anisotropy studies of UHECR detected by the Pierre Auger Observatory*, Internal Note of the Pierre Auger Collaboration GAP-2015-044 (2015)
  The internal note of the Pierre Auger Collaboration contains parts of chapter 2, 5, 7 and 8.

- R. M. de Almeida, T. Hebbeker, E. Kemp, M. Lauscher, J. R. T. de Mello Neto, J. S. de Oliveira and M. Plum, *On the sensitivities of Angular Power Spectrum and Needlet analysis to detect UHECRs flux anisotropies in multiple scales*, Internal Note of the Pierre Auger Collaboration GAP-2014-087 (2014)
  The internal note of the Pierre Auger Collaboration contains parts of chapter 6 and appendix B.

- M. Lauscher, M. Plum, *Analysis of the Arrival Direction of Cosmic Rays with the Needlet Wavelet*, Internal Note of the Pierre Auger Collaboration GAP-2013-082 (2013)
  The internal note of the Pierre Auger Collaboration contains parts of chapter 5.

The following publications based on work presented in this thesis are in preparation.

- A. Aab, et. al. (The Pierre Auger Collaboration), *Multi-resolution anisotropy studies of ultra-high energy cosmic rays detected at the Pierre Auger Observatory*, in preparation (2016)
  This publication will contain parts of chapter 2, 5, 7 and 8.